

**STRUCTURAL AND DYNAMICS STUDIES OF MICROTUBULE-  
ASSOCIATED TAU AND KIF5B ASSEMBLED WITH MICROTUBULES;  
NMR CRYSTALLOGRAPHY OF OXOVANADIUM (V) BIOINORGANICS:  
INSIGHTS FROM MAGIC ANGLE SPINNING NMR SPECTROSCOPY**

by

Mingyue Li

A dissertation submitted to the Faculty of the University of Delaware in partial fulfillment of the requirements for the degree of Doctor of Philosophy in Chemistry and Biochemistry

Fall 2016

© Fall 2016 Mingyue Li  
All Rights Reserved

**STRUCTURAL AND DYNAMICS STUDIES OF MICROTUBULE-  
ASSOCIATED TAU AND KIF5B ASSEMBLED WITH MICROTUBULES;  
NMR CRYSTALLOGRAPHY OF OXOVANADIUM (V) BIOINORGANICS:  
INSIGHTS FROM MAGIC ANGLE SPINNING NMR SPECTROSCOPY**

by

Mingyue Li

Approved:

\_\_\_\_\_

Murray Johnston, Ph.D.

Chair of the Department of Department of Chemistry and Biochemistry

Approved:

\_\_\_\_\_

George H. Watson, Ph.D.

Dean of the College of College Arts and Sciences

Approved:

\_\_\_\_\_

Ann L. Ardis, Ph.D.

Senior Provost for Graduate and Professional Education

I certify that I have read this dissertation and that in my opinion it meets the academic and professional standard required by the University as a dissertation for the degree of Doctor of Philosophy.

Signed:

---

Tatyana Polenova, Ph.D.  
Professor in charge of dissertation

I certify that I have read this dissertation and that in my opinion it meets the academic and professional standard required by the University as a dissertation for the degree of Doctor of Philosophy.

Signed:

---

Cecil Dybowski, Ph.D.  
Member of dissertation committee

I certify that I have read this dissertation and that in my opinion it meets the academic and professional standard required by the University as a dissertation for the degree of Doctor of Philosophy.

Signed:

---

Sharon Rozovsky, Ph.D.  
Member of dissertation committee

I certify that I have read this dissertation and that in my opinion it meets the academic and professional standard required by the University as a dissertation for the degree of Doctor of Philosophy.

Signed:

---

Antonina Roll-Mecak, Ph.D.  
Member of dissertation committee

## **ACKNOWLEDGMENTS**

Pursuing my Ph.D. has been a truly challenging, yet rewarding journey. I owe my sincerest gratitude to everyone who has supported and encouraged me along the way. Only with their support was I able to complete my thesis.

First, I want to express my gratitude to my Ph.D. advisor Prof. Tatyana Polenova for her continuous patience, support, motivation, and immense knowledge. Her guidance has greatly broadened my horizons and capabilities as a scientist. As my mentor, she has encouraged me to overcome the challenges of my research. Beyond research, she has also helped me to develop strong workplace ethics, which has been invaluable preparation for my career as a scientist.

I would also like to thank my other Ph.D. committee members: Prof. Cecil Dybowski and Prof. Sharon Rozovsky at the University of Delaware, and Dr. Antonina Roll-Mecak from the National Institutes of Health. It would not have been such a successful journey without their suggestions and support.

I want to thank all of our collaborators on various projects: Prof. Guy Lippens from CNRS-INSA Toulouse, Prof. John C. Williams from the Beckman Research Institute of City of Hope, Dr. Antonina Roll-Mecak from the National Institutes of Health, Prof. Amir Goldbourt from Tel Aviv University, Prof. Debbie C. Crans from Colorado State University, Prof. Frederique Pourpoint from the University of Lille 1, and Prof. Jean-Paul Amoureux from the University of Lille 1 and East China Normal University.

I also want to give my special thanks to Dr. Guangjin Hou, an NMR spectroscopist at the University of Delaware for many valuable discussions and suggestions. Guangjin taught me the fundamentals of NMR data acquisition. His involvement throughout the course of my Ph.D. has made it a very pleasant learning experience.

Furthermore, I want to express my profound appreciation to my colleagues in the Polenova lab. Jenna Yehl, a colleague in my graduate year, is a sincere friend in both research and daily life. Additionally, Dr. Si Yan was my first mentor on the microtubule project. I have also learned a great deal of biochemistry and NMR through collaboration with each person on the microtubule project team including Changmiao Guo, Jodi Kraus, Chunting Zhang and Wenfei Tian. Dr. Chris Suiter, Dr. Rupal Gupta, Dr. Caitlin Quinn, Dr. Xingyu Lu, Dr. Huilan Zhang, Maple (Mingzhang Wang), Manman Lu, Ryan W. Russell, and Luke Onisk have also all supported me and made my Ph.D. life much more joyful. A special thanks goes to Dr. Caitlin Quinn, Changmiao Guo, and others who took the time to proofread my thesis and keep me motivated during my thesis writing: this is much appreciated!

Finally, I am deeply indebted to my friends and family. My gratitude goes to all of my friends in the United States and China. I also want to thank my aunt Kejuan Wu for her deep trust in my abilities, and most importantly, her love. I want to express my sincerest appreciation to my parents. While I was writing my thesis, my mother flew from China to support me. Therefore, this thesis is dedicated to my parents for their unconditional love and continuous support.

*Dedicated to My Parents for Their Love*

## TABLE OF CONTENTS

LIST OF TABLES.....	xi
LIST OF FIGURES .....	xiii
LIST OF ABBREVIATIONS.....	xxiii
ABSTRACT.....	xxvi

### Chapter

1	MICROTUBULES AND MICROTUBULE-ASSOCIATED PROTEINS .....	1
1.1	Microtubules .....	3
1.1.1	Structure of Microtubules .....	3
1.1.2	Dynamic Instability of Microtubules .....	6
1.2	Microtubule-Associated Protein Tau .....	8
1.2.1	Biological Functions of Tau.....	8
1.2.2	Tau and Alzheimer's Disease .....	9
1.2.3	Domain Organization of Tau .....	10
1.2.4	Tau as an Intrinsically Disordered Protein.....	12
1.3	Microtubule-Associated Motor Protein Kinesin.....	12
1.3.1	Kinesin Superfamily and Conventional Kinesin.....	12
1.3.2	Kinesin Motor Domain Structure.....	15
1.3.3	Kinesin Processivity.....	19
1.4	Summary .....	21
	REFERENCES .....	23
2	OVERVIEW OF MAS NMR METHODS RELEVANT TO THE STRUCTURAL AND DYNAMICS STUDIES OF MICROTUBULE- ASSOCIATED PROTEINS AND MICROTUBULE ASSEMBLIES .....	29
2.1	Isotopic Labeling .....	30
2.2	MAS NMR Multidimensional Correlation Spectroscopy.....	32

2.2.1	Through-Space Correlation Spectra.....	32
2.2.2	Through-Bond Correlation Spectra.....	37
2.2.3	Proton-Detected and Fast MAS NMR.....	40
2.3	Studies of Dynamics of Protein Assemblies by MAS NMR Spectroscopy.....	43
2.3.1	Studies of Dynamics on the Nanosecond to Microsecond Timescale by Dipolar Coupling Measurement.....	45
2.3.2	Study of Dynamics on the Nanosecond to Microsecond Timescale by Cross Polarization in MAS NMR.....	47
2.4	Summary.....	49
	REFERENCES.....	51
3	INVESTIGATIONS OF CONFORMATIONAL AND DYNAMICS OF TAUF4 BINDING WITH MICROTUBULES.....	58
3.1	Introduction.....	58
3.2	Materials and Methods.....	60
3.2.1	Materials.....	60
3.2.2	Cosedimentation Assay of TauF4 with Microtubules.....	60
3.2.3	Transmission Electron Microscopy.....	61
3.2.4	MAS NMR Sample Preparation.....	62
3.2.5	MAS NMR Spectroscopy.....	62
3.2.6	Data Analysis.....	64
3.3	Results.....	66
3.3.1	Biochemical Characterization of TauF4 Binding to Microtubules.....	66
3.3.2	Conformation of TauF4 in Complex with Microtubules.....	66
3.3.3	Dynamics of TauF4 in Complex with Microtubules on Multiple Timescales.....	80
3.4	Discussion.....	93
3.5	Conclusions.....	94
	REFERENCES.....	95
4	STRUCTURAL STUDIES OF KIF5B MOTOR DOMAIN IN COMPLEX WITH MICROTUBULES BY MAS NMR.....	98

4.1	Introduction.....	98
4.2	Materials and Methods.....	99
4.2.1	Materials .....	100
4.2.2	Expression of Isotopically Labeled Kif5b (1-349) .....	101
4.2.3	Purification of Isotopically Labeled Kif5b (1-349) .....	102
4.2.4	Preparation of Kif5b for Solution NMR .....	104
4.2.5	Preparation of Paclitaxel-Stabilized Microtubules .....	104
4.2.6	Cosedimentation Assay.....	104
4.2.7	Morphological Characterization of Microtubules and Kif5b/MT Complexes.....	105
4.2.8	Preparation of U- <sup>13</sup> C, <sup>15</sup> N-Kif5b/Microtubule Assemblies for MAS NMR Studies .....	106
4.2.9	Preparation of ADP U- <sup>13</sup> C, <sup>15</sup> N Kif5b/MT Assemblies for MAS NMR Studies .....	108
4.2.10	Solution NMR Experiments.....	108
4.2.11	MAS NMR Experiments.....	109
4.3	Results and Discussion .....	110
4.3.1	Solution NMR Studies of U- <sup>15</sup> N-Kif5b .....	110
4.3.2	Preparation of Kif5b/MT Assemblies for MAS NMR Studies..	112
4.3.3	Morphological Characterization of MTs and Kif5b/MT Assemblies by TEM.....	117
4.3.4	MAS NMR Studies of U- <sup>15</sup> N, <sup>13</sup> C-Kif5b/MT Complexes.....	118
4.3.5	MAS NMR Studies of ADP Binding State of Kif5b in Complex with Microtubules .....	134
4.4	Conclusions and Future Perspectives.....	138
	REFERENCES .....	140
5	STRUCTURAL CHARACTERIATION OF OXOVANADIUM (V) BIOINORGANIC COMPOUNDS BY MULTINUCLEAR NMR SPECTROSCOPY AND DFT CALCULATIONS .....	142
5.1	Introduction.....	142
5.2	Materials and Experiments .....	147
5.2.1	Materials .....	147
5.2.2	<sup>51</sup> V, <sup>15</sup> N and <sup>13</sup> C MAS NMR Spectroscopy .....	148
5.2.3	Density Functional Theory (DFT) Calculations of NMR Parameters.....	151

5.3	Results and Discussions.....	152
5.3.1	$^{51}\text{V}$ , $^{15}\text{N}$ and $^{13}\text{C}$ Experimental NMR Parameters.....	152
5.3.2	Distance Determination of $^{51}\text{V}$ - $^{15}\text{N}$ by LA-REDOR Experiments .....	160
5.3.3	Geometry Derivation Combining DFT Calculations and NMR Parameters.....	162
5.4	Conclusions and Future Outlook .....	177
	REFERENCES .....	178
Appendix		
A	COPYRIGHT LETTERS.....	183

## LIST OF TABLES

Table 3.1:	Resonance Assignments of TauF4 Assembled on Polymerized Microtubules from J-Coupling-based 2D $^{13}\text{C}$ - $^{13}\text{C}$ CTUC-COSY Correlation Spectra and Comparison with Published Solution NMR Shifts .....	69
Table 3.2:	$^{13}\text{C}$ Resonance Assignments of 2D CORD Spectra Acquired at $-5\text{ }^{\circ}\text{C}$ ....	75
Table 3.3:	Residue Type Assignments from $^{13}\text{C}$ - $^{13}\text{C}$ CORD Spectra Acquired at $-8\text{ }^{\circ}\text{C}$ .....	78
Table 3.4:	Summary of Parameters of $^1\text{H}$ - $^{13}\text{C}^{\alpha}$ Cross Polarization Dynamics .....	88
Table 3.5:	$^1\text{H}$ - $^{13}\text{C}^{\alpha}$ Dipolar Coupling Constants for Four Sites Corresponding to Strong Crosspeaks Observed in 2D CORD Spectra Acquired at $-5\text{ }^{\circ}\text{C}$ ...	90
Table 3.6:	$^1\text{H}$ - $^{13}\text{C}$ Dipolar Order Parameters of Backbone $\text{C}^{\alpha}$ in TauF4/MT Assemblies at Different Temperatures. ....	92
Table 4.1:	Summary of Sample Preparation Details for Kif5b/MT Complex.....	107
Table 4.2:	Sensitivity in the MAS NMR Experiments for Different Kif5b/MT Complex Samples .....	115
Table 4.3:	Spin System Assignments and Secondary Structure Prediction Based on CORD, NCA, and NH-HETCOR Spectra of $\text{U-}^{13}\text{C}$ , $^{15}\text{N}$ -Kif5b/MT Complex.....	123
Table 5.1:	Experimental and Computed $^{51}\text{V}$ NMR Parameters for $[\text{VO}^{15}\text{NGlySalbz}]$ and $[\text{VO}^{15}\text{NGlySal}(\text{OCH}_3)]$ .....	155
Table 5.2:	Experimental and Computed $^{15}\text{N}$ NMR Parameters for $[\text{VO}^{15}\text{NGlySalbz}]$ and $[\text{VO}^{15}\text{NGlySal}(\text{OCH}_3)]$ .....	156
Table 5.3:	Experimental and Computed (BLYP/TZV) $^{13}\text{C}$ Isotropic Chemical Shifts for $[\text{VO}^{15}\text{NGlySalbz}]$ and $[\text{VO}^{15}\text{NGlySal}(\text{OCH}_3)]$ . The numbering of the carbon atoms is shown in Figure 5.1.....	159

Table 5.4:	Experimental and Computed $^{51}\text{V}$ NMR Parameters for $[\text{VO}^{15}\text{NGlySal}(\text{OCH}_3)]\cdot(\text{CH}_3\text{OH})$ as a Function of V---OHCH <sub>3</sub> Distance .....	169
Table 5.5:	Experimental and Computed $^{15}\text{N}$ NMR Parameters for $[\text{VO}^{15}\text{NGlySal}(\text{OCH}_3)]\cdot(\text{CH}_3\text{OH})$ as a Function of V---OHCH <sub>3</sub> Distance .....	174
Table 5.6:	Experimental and Computed $^{13}\text{C}$ NMR Parameters for $[\text{VO}^{15}\text{NGlySalbz}]$ and $[\text{VO}^{15}\text{NGlySal}(\text{OCH}_3)]$ .....	175

## LIST OF FIGURES

- Figure 1.1: The structure and dynamic instability of microtubules. a)  $\alpha\beta$  tubulin heterodimer and microtubule protofilament. b) Thirteen protofilaments associate laterally to form the hollow microtubule wall. c) A microtubule switches from the growing state to the shrinking state by polymerization and depolymerization. This is accompanied by the hydrolysis of GTP. The figure was originally published in reference<sup>13</sup>. Permission for reuse in this dissertation is granted by Nature Publishing Group, copyright 2008.....4
- Figure 1.2: The structure of an  $\alpha\beta$  tubulin heterodimer obtained by electron crystallography<sup>14</sup> generated with Pymol. (PDB ID code: 1TUB) The GDP in the exchangeable site (E-site) on  $\alpha$  tubulin is shown in orange, and the GTP in the non-exchangeable site (N-site) on  $\beta$  tubulin is shown in yellow. The anticancer drug taxol is localized on  $\beta$  tubulin near the lateral tubulin contact site and is shown in green. ....6
- Figure 1.3: a) Six Tau isoforms expressed in the adult brain are distinguished by the presence of zero, one, or two near N-terminus inserts N1 and N2, and repeat R2 from the microtubule assembly domain. This figure is adapted from reference<sup>46</sup>. b) Conformation of the longest of Tau isoform 2N4R determined by solution NMR. The overall Tau structure in solution is unfolded, with a few transient secondary structure elements, including  $\alpha$  helical propensity shown as a red cylinder,  $\beta$  strands shown as yellow arrows, and helices formed by poly-Proline sequences, shown as green boxes. An ensemble of 20 conformations is displayed in the background. Color-coding indicates the domain organization. The figure is reprinted with permission from reference<sup>54</sup> .....11

- Figure 1.4: (a) Fifteen subfamilies of the kinesin superfamily based upon phylogenetic analysis. (b) Domain organization of the kinesin superfamily. The motor domain is highly conserved among kinesin superfamily members. Based on the position of the motor domain, kinesins are categorized into three subfamilies: N-kinesin, M-kinesin, and C-kinesin. The figure was originally published in reference<sup>62</sup>. Permission for reuse in this dissertation is granted by Nature Publishing Group, copyright 2009..... 14
- Figure 1.5: The X-ray structure of Kif5b (PDB ID code: 1BG2). The  $\alpha$  helices are shown in green-cyan,  $\beta$  strands in blue, and loop regions in yellow. The ADP molecule is displayed as red sticks. The numbering is adapted from reference<sup>75</sup>..... 17
- Figure 1.6: The subdomain structure of nucleotide free Kif5b and the coordinated movement of subdomains in each step of the nucleotide cycle. a) The three subdomains of Kif5b are colored as follows: the Switch I&II subdomain is shown in cyan, the microtubule binding domain in green, and the P-loop subdomain in beige. b) The reorientation of subdomains along each step of nucleotide cycle. Upon binding with microtubules, the neck linker (in red) is docked in the ATP binding state, while the linker is undocked in the free and ADP-bound states. Figure is adapted from reference<sup>82</sup>. Permission for reuse in this dissertation is granted by John Wiley and Sons, copyright 2015..... 18
- Figure 1.7: The “hand over hand” walking mechanism of dimeric kinesin along a microtubule. The two kinesin motor domains are dimerized through the coiled coil region. In one step, the kinesin motor domain cycles through different nucleotide states as indicated. The figure was originally published in reference<sup>82</sup>. Permission for reuse in this dissertation is granted by John Wiley & Sons, copyright 2015.....20
- Figure 2.1: Protonation levels in a model protein  $\alpha$ -spectrin SH3 upon deuteration (PDB code ID: 1U06).<sup>36</sup> (a) Fully protonated protein. (b) Deuterated protein crystallized from 100% H<sub>2</sub>O with all exchangeable amide protons and protons of hydrated water molecules determined and refined in X-ray crystallography structure exhibited. (c) Deuterated protein crystallized from 10% H<sub>2</sub>O/90% D<sub>2</sub>O sample buffer. The protonation level is greatly reduced. On average, 21 protons contained in each protein molecule are displayed. (d) <sup>1</sup>H-<sup>1</sup>H dipolar couplings are strongly attenuated upon the incorporation of deuterons. The figure was originally published in reference<sup>31</sup>. Permission for reuse in this dissertation is granted by Elsevier, copyright 2012.....31

- Figure 2.2: (a) The general pulse diagram for 2D  $^{13}\text{C}$ - $^{13}\text{C}$  Combined  $\text{R}_{2n}^{\text{v}}$  Driven (CORD) correlation experiments. A series of composite RF pulses comprised of  $\text{R}_{2n}^{\text{v}}$  blocks are applied on the proton channel during the CORD mixing time. The RF pulse sequences correspond to: (b) Basic CORD building block spanning 6Tr (rotor period); (c)  $\text{CORD}_{\text{xix}}$  spanning 12Tr; (d)  $\text{CORD}_{\text{xy4}}$  spanning 24Tr. Rotor-synchronized  $\text{R}_{2n}^{\text{v}}$ -type symmetry sequences as the building blocks:  $\text{R}_{21}^1$  ( $\nu_{\text{H}}^1 = \nu_{\text{r}}$ ),  $\text{R}_{21}^2$  ( $\nu_{\text{H}}^1 = \nu_{\text{r}}$ ),  $\text{R}_{22}^2$  ( $\nu_{\text{H}}^1 = \nu_{\text{r}}/2$ ). The figure was originally published in reference<sup>52</sup>. Permission for reuse in this dissertation is granted by Elsevier, copyright 2013. (e) Pulse sequence for HETCOR with heteronuclear detection (e), and proton detection (f). Original figure courtesy of Dr. Xingyu Lu in Prof. Tatyana Polenova's group.....34
- Figure 2.3: The magnetization transfer pathways in heteronuclear correlation experiments: NCA, NCO, NCACX, NCOCX, and CONCACX. Original figure courtesy of Ryan Russell in Prof. Tatyana Polenova's research group.....36
- Figure 2.4: Comparison of 1D  $^{13}\text{C}$  CP-MAS spectra in (a) and (b) with INEPT spectrum in (c) of U- $^{13}\text{C}$ -isoleucine. In (a), CP-MAS with long mixing time (1.2 ms) yields the best sensitivity which also invokes long-range magnetization transfer. One bond transfer is obtained in CP-MAS with short contact time (12  $\mu\text{s}$ ) in (b) and INEPT in (c), evidenced by the absence of non-protonated CO signal. INEPT shows more uniform one-bond transfer than CP-MAS. Reprinted with permission from reference<sup>71</sup>. Copyright (2005) American Chemical Society. ....40
- Figure 2.5: Linear correlation of proton linewidth with rotor period (the inverse of MAS frequency) for selected residues in a model protein SH3 (deuterated with 10% back-exchanged amide proton). Rotor period is the inverse of the MAS frequency in kHz. The figure was originally published in reference<sup>29</sup>. Permission for reuse in this dissertation is granted by John Wiley and Sons, copyright 2006. ....42
- Figure 2.6: Solid state NMR methods for probing dynamic processes associated with proteins over a full and continuous range. The figure is adapted from reference<sup>80</sup>. Permission for reuse in this dissertation is granted by Elsevier, copyright 2005. ....44

- Figure 2.7: (a) Two-dimensional  $RN_n^V$  DIPSHIFT sequences for  $^1H$ - $^{13}C$ / $^{15}N$  heteronuclear dipolar recoupling. An RF irradiation comprised of  $RN_n^V$  symmetry pulses is applied on proton spins during the  $t_1$  evolution to reintroduce  $^1H$ - $^{15}N$  and  $^1H$ - $^{13}C$  dipolar coupling respectively. (b, c) Three-dimensional  $RN_n^V$  DIPSHIFT sequences for residue-specific  $^1H$ - $^{15}N$  and  $^1H$ - $^{13}C$  dipolar coupling measurements. (d) Backbone dynamics of CAP-Gly domain of dynactin captured by residue-specific  $^1H$ - $^{13}C$  dipolar order parameter, measured with the  $R16_3^2$  sequence. Reprinted with permission from reference<sup>86</sup>. Copyright (2011) American Chemical Society. ....47
- Figure 3.1: a) Domain organization and primary sequence of TauF4. Numbering is based on the longest adult Tau isoformer (441 residues). The R1, R2 and R3 repeat regions are defined by Lee et al.<sup>21</sup> The regions of high homology are underlined, and the less homologous regions are inter-repeats. b) SDS-PAGE gel of co-sedimentation assay of TauF4 with microtubules. The experimental TauF4 and tubulin dimer molar ratios are marked on the top of the gel. Tubulin and TauF4 protein bands are marked to the left of the gel. In the presence of taxol, microtubules are preassembled and stabilized, followed by the formation of TauF4/MT complexes. In the absence of taxol, TauF4 co-assembles with tubulin heterodimers to form TauF4/MT copolymer. c) Negatively stained TEM images of the microtubule filament (top); TauF4/MT complexes in the presence of taxol (middle); TauF4-promoted TauF4/MT bundles in the absence of taxol (bottom). “P” represents pellet; “S” represents supernatant. ....67
- Figure 3.2: Characteristic regions of J coupling-based 2D  $^{13}C$ - $^{13}C$  CTUC-COSY correlation MAS spectra of U- $^{13}C$ ,  $^{15}N$  TauF4/MT complexes at -5 °C and 19.96 T. a) Expansion showing sidechain carbon correlations. b) Expansion demonstrating  $C^\alpha$ - $C^\beta$  and  $C^\alpha$ - $C'$  correlations of residues whose  $C^\beta$  is within the chemical shift range of 45 - 10 ppm, and chemical shift of  $C^\alpha$  lies in the range of 65 - 50 ppm. c)  $C^\alpha$ - $C^\beta$  and  $C^\alpha$ - $C'$  correlations of Ser and Thr residues. All possible assignments based on solution NMR shifts are labeled.<sup>15</sup> The summary of assignments is listed in Table 3.1. The overlapping peaks may not contain all residues expected to be associated with the corresponding resonances. ....68
- Figure 3.3: Residues absent from J-coupling-based  $^{13}C$ - $^{13}C$  CTUC-COSY spectra, marked on the TauF4 domain organization. ....73

- Figure 3.4: Two-dimensional dipolar-based  $^{13}\text{C}$ - $^{13}\text{C}$  CORD correlation MAS spectra of U- $^{13}\text{C}$ ,  $^{15}\text{N}$  TauF4/MT complexes at  $-5\text{ }^\circ\text{C}$  and magnetic field strength of 19.96 T. Peak assignments are shown on the spectra and summarized in Table 3.2. The 1D  $^1\text{H}$ - $^{13}\text{C}$  cross polarization spectrum is displayed as a top trace; chemical shifts for  $\text{C}^\alpha$  resonances corresponding to strong cross peaks in the 2D spectrum are labeled.....74
- Figure 3.5: Two-dimensional dipolar-based  $^{13}\text{C}$ - $^{13}\text{C}$  CORD correlation MAS spectra of U- $^{13}\text{C}$ ,  $^{15}\text{N}$  TauF4/MT complex at  $-8\text{ }^\circ\text{C}$  and magnetic field strength of 19.96 T. a) Aliphatic region with synthetic peaks (orange) corresponding to  $\text{C}^\alpha$ - $\text{C}^\beta$  correlations are generated using solution NMR shifts. Sidechain peak assignments are labeled in blue. Ile  $\text{C}^\gamma$ - $\text{C}^\beta$  cross peak with multiple features is highlighted with grey box. b), c), and d)  $\text{C}^\alpha$ - $\text{C}^\beta$  correlations of residues 276-312 (orange) and  $^{260}\text{IGSTEN}^{265}$  motif (green) generated from solution NMR shifts mapped onto  $^{13}\text{C}$ - $^{13}\text{C}$  CORD spectra of U- $^{13}\text{C}$ ,  $^{15}\text{N}$  TauF4/MT complex. e), f), and g)  $\text{C}^\alpha$ - $\text{C}^\beta$  correlations of residues 276-312 (blue) generated from SHIFTX2-predicted chemical shifts from the reported conformation (PDB code: 2MZ7);  $\text{C}^\alpha$ - $\text{C}^\beta$  correlations of  $^{260}\text{IGSTEN}^{265}$  motif (red) in turn conformation generated from SHIFTX2-predicted chemical shifts of the I280-N285 turn from X-ray structure (PDB code 3MSU). Peaks that are missing or whose shifts disagree with the experimental MAS NMR data are labeled in blue and red. In the black and blue spectra, the contour level is set to 3X and 2X the noise level, respectively. ....77
- Figure 3.6: Temperature dependence of 1D  $^1\text{H}$ - $^{13}\text{C}$  cross-polarization (CCP) spectra of U- $^{13}\text{C}$ ,  $^{15}\text{N}$ -TauF4/MT complex, displayed for carbonyl, aromatic, and aliphatic regions. The spectra are scaled to the same number of scans. Note that the signal-to-noise ratio increases as the temperatures decreases. ....82
- Figure 3.7: Temperature dependence of 1D  $^1\text{H}$ - $^{15}\text{N}$  cross-polarization (NCP) and 1D  $^{15}\text{N}$ - $^{13}\text{C}^\alpha$  SPECIFIC-CP (DCP) spectra of U- $^{13}\text{C}$ ,  $^{15}\text{N}$ -TauF4/MT complex.....83
- Figure 3.8: Comparison of 1D a)  $^1\text{H}$ - $^{13}\text{C}$  INEPT, b)  $^{13}\text{C}$  single pulse, c)  $^1\text{H}$ - $^{13}\text{C}$  CP with  $^{13}\text{C}$  single pulse excitation and d)  $^1\text{H}$ - $^{13}\text{C}$  CP spectra of U- $^{13}\text{C}$ ,  $^{15}\text{N}$ -TauF4/MT complex at  $-5\text{ }^\circ\text{C}$ , displayed for carbonyl, aromatic, and aliphatic regions. ....84

Figure 3.9: Temperature dependence of 1D single pulse excitation $^{13}\text{C}$ NMR spectra of $\text{U-}^{13}\text{C}$ , $^{15}\text{N}$ -TauF4/MT complex, displayed for carbonyl, aromatic, and aliphatic regions. The spectra are scaled to the same number of scans. ....	85
Figure 3.10: Normalized magnetization in $^1\text{H-}^{13}\text{C}^\alpha$ cross-polarization experiments acquired for a series of temperatures as a function of variable contact times at -18, -8, -5, -3, 2, and 10 °C. Experimental data are shown as filled circles; best-fit curves are shown as solid lines.....	87
Figure 3.11: $^1\text{H-}^{13}\text{C}^\alpha$ dipolar lineshapes extracted at chemical shifts corresponding to strong cross peaks in $^{13}\text{C-}^{13}\text{C}$ CORD spectrum of $\text{U-}^{13}\text{C}$ , $^{15}\text{N}$ TauF4/MT complex, recorded at various temperatures ranging from -28 °C to 2 °C. The experimental and simulated lineshapes are shown as solid black and dashed orange lines, respectively.....	90
Figure 3.12: 1D $^1\text{H-}^{13}\text{C}$ cross polarization (CP) spectra of $\text{U-}^{13}\text{C}$ , $^{15}\text{N}$ -TauF4/MT complex before and after freezing, displayed for carbonyl, aromatic, and aliphatic regions. ....	91
Figure 4.1: The primary sequence of the first 349 amino acids of human kinesin Kif5b containing the conserved motor domain (1-349). The secondary structure, as determined by X-ray crystallography, is indicated from residue 3 to residue 325 (PDB ID code: 1BG2). Yellow, dark blue, and light blue represent random coil, $\beta$ sheet, and $\alpha$ helix secondary structures, respectively. Residues 325 to 349 are missing in the X-ray structure.....	100
Figure 4.2: Purification of Kif5b motor domain characterized by SDS-PAGE gel. Lane 1: before cell induction; 2: after protein expression; 3: cell lysate; 4: combined fractions from the first HisTrap column; 5: cleavage of His <sub>6</sub> -SMT3-tag by Ulp-1 protease; 6: combined fractions from the second HisTrap column; 7: His <sub>6</sub> -SMT3-tag; 8: molecular weight marker. ....	103
Figure 4.3: Overlay of 14.1 T solution HSQC spectra of $^{15}\text{N}$ -Kif5b prepared in different buffers. Blue: $^{15}\text{N}$ -Kif5b in Tris buffer (50 mM Tris, 100 mM NaCl, 1 mM EDTA, 1 mM DTT, pH 6.3). Black: $^{15}\text{N}$ -Kif5b in PIPES buffer (25 mM PIPES, 1 mM EGTA, 1 mM MgCl <sub>2</sub> , 1 mM DTT, 200 mM KCl, pH 6.8).....	112

Figure 4.4:	SDS-PAGE gel of co-sedimentation assays of Kif5b with microtubules under different conditions. For all experiments, the pellet is indicated by “P”, and supernatant is indicated by “S”. a) Co-sedimentation assays of Kif5b/MTs with different Kif5b to MT ratios as indicated at the top of the gel. b) Co-sedimentation assays of Kif5b/MTs with different Kif5b to MT ratios in the presence of 2 mM AMP-PNP. c) Co-sedimentation assays of Kif5b/MTs with different nucleotide conditions including nucleotide free, in the presence of 2mM ATP, and in the presence of 2 mM AMP-PNP. Control 1 is free microtubule; control 2 is free Kif5b. d) Semi-quantitative analysis of Kif5b binding with MTs in the presence of 1 mM ADP by co-sedimentation assay. The molar ratio of Kif5b to MTs is 3.6. e) The effect of 10% sucrose on the binding of Kif5b to MTs characterized by co-sedimentation assay. The control experiment is done in the absence of 10% sucrose. ....	114
Figure 4.5:	Negatively stained TEM images of free MTs and Kif5b/MT assemblies. a) A single MT filament. b) Microtubules. c) Kif5b/MT complex. d) ADP-Kif5b/MT complexes. e) Kif5b/MT assemblies after MAS. ....	118
Figure 4.6:	$^1\text{H}$ - $^{15}\text{N}$ cross polarization spectra of U- $^{15}\text{N}$ -Kif5b/MT assemblies at different temperatures. The sample temperatures are indicated in the spectra. Spectra were acquired at 14 kHz MAS, 19.96 T. ....	119
Figure 4.7:	$^{13}\text{C}$ - $^{13}\text{C}$ CORD correlation spectrum of U- $^{13}\text{C}$ , $^{15}\text{N}$ -Kif5b/MT assemblies acquired at an MAS frequency of 14 kHz, field strength of 19.96 T, and sample temperature of 17 °C. Spin systems belonging to Thr, Ser, Pro, Val, Ala, Leu and Ile regions are highlighted with different colors as indicated. The expansions of the corresponding regions are shown below the full spectrum. Note the unprecedented high spectral resolution. ....	121
Figure 4.8:	Spin system assignments of the $^{13}\text{C}$ - $^{13}\text{C}$ CORD correlation spectrum of U- $^{13}\text{C}$ , $^{15}\text{N}$ -Kif5b/MT assemblies acquired at an MAS frequency of 14 kHz, field strength of 19.96 T, and sample temperature of 17 °C. a) $\text{C}^\alpha$ - $\text{C}'$ correlation region of Glycine residues. b) Backbone $\text{C}^\alpha$ - $\text{C}^\beta$ correlation region. ....	122
Figure 4.9:	Chemical shift predictions from <i>SHIFTX2</i> based on the X-ray structure of Kif5b (PDB ID code: 4LNU) mapped onto the $^{13}\text{C}$ - $^{13}\text{C}$ CORD correlation spectrum of the U- $^{13}\text{C}$ , $^{15}\text{N}$ -Kif5b/MT complexes. Note the remarkable overall agreement between the experimental and computed shifts. ....	126

- Figure 4.10: Heteronuclear NCA correlation spectrum of U- $^{13}\text{C}$ ,  $^{15}\text{N}$ -Kif5b/MT assemblies at an MAS frequency of 14 kHz, magnetic field of 19.96 T, and sample temperature of 17 °C. Glycine spin systems are labeled, and the corresponding chemical shifts are summarized in Appendix B, Table 4.3..... 127
- Figure 4.11: Left: Proton-detected  $^{15}\text{N}$ - $^1\text{H}$  HETCOR spectrum of protonated U- $^{13}\text{C}$ ,  $^{15}\text{N}$ -Kif5b/MT assemblies acquired at an MAS frequency of 60 kHz and field strength of 19.96 T. Selected backbone and sidechain spin systems are labeled in the 2D spectrum. Right: One-dimensional  $^1\text{H}$  traces for four residues extracted from the 2D HETCOR spectrum are shown with the corresponding spin system and linewidth indicated..... 129
- Figure 4.12: Proton-detected  $^{15}\text{N}$ - $^1\text{H}$  HETCOR spectrum of perdeuterated and back-exchanged U- $^{13}\text{C}$ ,  $^{15}\text{N}$ ,  $^2\text{H}$ -Kif5b/MT assemblies acquired at an MAS frequency of 40 kHz and field strength of 19.96 T. Selected backbone and sidechain spin systems are labeled in the 2D spectrum. One-dimensional  $^1\text{H}$  traces extracted from the 2D HETCOR spectrum for four residues are shown with the corresponding spin system and linewidth indicated..... 131
- Figure 4.13: Overlay of  $^1\text{H}$ - $^{15}\text{N}$  HETCOR spectra of perdeuterated back exchanged U- $^{13}\text{C}$ ,  $^{15}\text{N}$ ,  $^2\text{H}$ -Kif5b/MT (blue) and fully protonated U- $^{13}\text{C}$ ,  $^{15}\text{N}$ ,  $^1\text{H}$ -Kif5b/MTs (black). An expansion indicating the appearance of new peaks in the protonated U- $^{13}\text{C}$ ,  $^{15}\text{N}$ ,  $^1\text{H}$ -Kif5b/MT sample is shown..... 132
- Figure 4.14: Overlay of NH-HETCOR spectra of  $^2\text{H}$ ,  $^{13}\text{C}$ ,  $^{15}\text{N}$ -Kif5b/MT complexes acquired at MAS frequency of 40 kHz, a) after spinning for 16 days (red); b) after rehydration by addition of sample buffer (green). The spectra acquired at the beginning of MAS experiments is shown in black in both plots. .... 133
- Figure 4.15. Homo- and heteronuclear correlation MAS NMR spectra of ADP-bound U- $^{13}\text{C}$ ,  $^{15}\text{N}$ -Kif5b/MT assemblies (black) overlaid with the apo Kif5b/MT complex (blue). a)  $^{15}\text{N}$ - $^{13}\text{C}$  NCA; b)  $^{13}\text{C}$ - $^{13}\text{C}$  CORD; c) Expansion of CORD spectrum, indicating chemical shift perturbations between the two samples. .... 135
- Figure 4.16: 1D  $^1\text{H}$ - $^{13}\text{C}$  cross polarization (CP) spectra of ADP-U- $^{13}\text{C}$ ,  $^{15}\text{N}$  Kif5b/MT complexes acquired at different temperatures, at MAS frequency of 14 kHz, 19.96 T. The relative sensitivity is indicated to the left of the spectra..... 136

Figure 4.17: Overlay of a) CORD and b) NCO correlation spectra of ADP-U- <sup>13</sup> C, <sup>15</sup> N-Kif5b/MT complex (sample #7) acquired at 17 °C (black) and -21 °C (blue) at 19.96 T, 14 kHz MAS.....	137
Figure 5.1: Molecular structure of vanadium compounds: (A) [VO <sup>15</sup> NGlySalbz], (B) [VO <sup>15</sup> NglySal(OCH <sub>3</sub> )], and (C) [VO( <sup>15</sup> NglySal)(OCH <sub>3</sub> )]·(CH <sub>3</sub> OH). The isotopically labeled <sup>15</sup> N is marked in the structure. The carbon atom numbering corresponds to that in Table 5.3. ....	147
Figure 5.2: Low-alpha, low-amplitude rotational echo adiabatic passage double resonance (LA-REDOR) pulse sequence. ....	150
Figure 5.3: <sup>51</sup> V MAS NMR spectra of (A) [VO <sup>15</sup> NGlySalbz] and (B) [VO( <sup>15</sup> NGlySal)(OCH <sub>3</sub> )]·(CH <sub>3</sub> OH) shown as a function of the MAS frequency. The experimental spectrum is displayed at the bottom, and simulated at the top of each panel. The MAS frequencies for the [VO <sup>15</sup> NGlySalbz] spectra are: top, $\nu_r = 15$ kHz; middle, $\nu_r = 13$ kHz; and bottom, $\nu_r = 10$ kHz. The MAS frequencies for the [VO( <sup>15</sup> NGlySal)(OCH <sub>3</sub> )]·(CH <sub>3</sub> OH) spectra are: top, $\nu_r = 20$ kHz; middle, $\nu_r = 17$ kHz; and bottom, $\nu_r = 13$ kHz. The best-fit parameters are indicated in Table 5.1. The spectra were acquired at the magnetic field of 9.4 T. ....	154
Figure 5.4: Experimental (solid line) and best-fit simulated (dashed line) ROCSA spectra for labeled <sup>15</sup> N atom in (A) [VO <sup>15</sup> NGlySalbz], and (B) [VO( <sup>15</sup> NGlySal)(OCH <sub>3</sub> )]·(CH <sub>3</sub> OH). The spectra were acquired at $\nu_R = 10$ kHz and a magnetic field of 14.1 T. The experimental and SIMPSON best-fit <sup>15</sup> N CSA parameters, as determined by the lowest RMSD, are shown in Table 5.2.....	157
Figure 5.5: <sup>13</sup> C CPMAS NMR spectra of (A) [VO <sup>15</sup> NGlySalbz] and (B) [VO( <sup>15</sup> NGlySal)(OCH <sub>3</sub> )]·(CH <sub>3</sub> OH) acquired at the magnetic field of 9.4 T. The experimental chemical shift assignments were derived from DFT calculations and are listed in Table 5.3. ....	158

- Figure 5.6: The LA-REDOR experimental data (filled circles) and simulated curves for (A)  $[\text{VO}^{15}\text{NGlySalbz}]$ , and (B)  $[\text{VO}^{15}\text{NGlySal}(\text{OCH}_3)] \cdot (\text{CH}_3\text{OH})$ . The LA-REDOR data were acquired at the magnetic field of 9.4 T. In (A), the simulated curves are depicted for  $D = 330$  Hz, 300 Hz, and 280 Hz, and the best-fit curve, as determined by the lowest RMSD, corresponds to  $D = 300 \pm 30$  Hz. In (B), simulated curves are shown for  $D = 320$  Hz, 280 Hz, and 260 Hz, and the best-fit curve corresponds to  $D = 280 \pm 40$  Hz. The simulations include the experimentally determined parameters describing the  $^{51}\text{V}$  and  $^{15}\text{N}$  EFG and CSA tensors:  $C_Q(^{51}\text{V})$ ,  $\eta_Q(^{51}\text{V})$ ,  $\delta_\sigma(^{51}\text{V})$ ,  $\eta_\sigma(^{51}\text{V})$ , and  $\delta_\sigma(^{15}\text{N})$ . ..... 161
- Figure 5.7: Correlation between calculated and experimental  $^{13}\text{C}$  isotropic chemical shifts in (A)  $[\text{VO}^{15}\text{NGlySal}(\text{OCH}_3)]$ , and (B)  $[\text{VO}^{15}\text{NGlySal}(\text{OCH}_3)] \cdot (\text{CH}_3\text{OH})$ . In (B), the correlation is shown for pentacoordinate  $[\text{VO}^{15}\text{NGlySalOCH}_3]$  and in (C) for hexacoordinate  $[\text{VO}^{15}\text{NGlySal}(\text{OCH}_3)] \cdot (\text{CH}_3\text{OH})$ . The empty and the filled circles represent all carbons and carbons with unambiguous chemical shift assignments, respectively. The linear fit equations are shown as legends on each graph. The isotropic shifts are summarized in Table 5.3. .... 165
- Figure 5.8: Structures of  $[\text{VO}^{15}\text{NglySal}(\text{OCH}_3)]$  and  $[\text{VO}^{15}\text{NglySal}(\text{OCH}_3)(\text{CH}_3\text{OH})]$  with  $\text{V} \cdots \text{OHCH}_3$  of different distances. Distances are marked in each structure. These structures are optimized with Gaussian09 at B3LYP/TZV theory level and are used for NMR parameters calculations. .... 167
- Figure 5.9: Image of the electrostatic potential (ESP) surfaces of  $[\text{VO}^{15}\text{NGlySal}(\text{OCH}_3)]$  (A) and  $[\text{VO}^{15}\text{NGlySal}(\text{OCH}_3)] \cdot (\text{CH}_3\text{OH})$  (B-F) generated in Gaussview from the total SCF density calculated by Gaussian at the BLYP/TZV level. For  $[\text{VO}^{15}\text{NGlySal}(\text{OCH}_3)] \cdot (\text{CH}_3\text{OH})$ , the ESP surfaces are plotted for structures where  $\text{V} \cdots \text{OHCH}_3$  distances were fixed at 2 Å (B), 2.27 Å (C), 2.5 Å (D), 3.7 Å (E), and 4.5 Å (F), and the geometries optimized. The regions of positive and negative charge are depicted in blue and red, respectively. The color legend is shown at the bottom. .... 172

## LIST OF ABBREVIATIONS

2Q-HORROR	Double quantum-homonuclear rotatory resonance
3D	Three-dimensional
AD	Alzheimer's disease
ADP	Adenosine diphosphate
AMP-PNP	Adenylyl-imidophosphate
CAP-Gly	Cytoskeleton-associated protein-glycine-rich
CODEX	Centerband-only detection of exchange
CORD	Combined $R_{2n}^V$ -driven
COSY	Correlation spectroscopy
CP	Cross polarization
CP-HETCOR	CP-based heteronuclear correlation
CSA	Chemical shift anisotropy
CTUC-COSY	Constant time, uniform sign correlation spectroscopy
CW	Continuous wave
DARR	Dipolar assisted rotational resonance
DFT	Density functional theory
DIFSHIFT	Dipolar chemical shift correlation
DMSO	Dimethyl sulfoxide
DREAM	Dipolar recoupling enhanced by amplitude modulation
EFG	Electric field gradient
EM	Electron microscopy
EPR	Electron paramagnetic resonance
GDP	Guanosine-5'-diphosphate
GMP-PNP	5'-guanylyl imidodiphosphate
GMPCPP	Guanosine-5'-[(alpha, beta)-methylene]triphosphate
GTP	Guanosine-5'-triphosphate
HETCOR	Heteronuclear correlation
HIV	Human immunodeficiency virus
HSQC	Heteronuclear single quantum correlation
IDP	Intrinsically disordered protein
INADEQUATE	Incredible natural abundance double quantum transfer experiment

INEPT	Insensitive nuclei enhanced polarization transfer
IPTG	Isopropyl beta-D-1-thiogalactopyranoside
KHC	Kinesin heavy chain
KLC	Kinesin light chain
LA-REDOR	Low alpha, low amplitude rotational echo double resonance
LB	Luria broth
LG-CP	Lee Goldberg cross polarization
MAP	Microtubule associated protein
MAP	Microtubule associated protein
MAS	Magic angle spinning
MIRROR	Mixed rotational and rotary resonance
MREV	Mansfield-Rhim-Elleman-Vaughn
MT	Microtubule
MTBR	Microtubule binding region
NFT	Neurofibrillary tangles
NIH	National Institutes of Health
NMR	Nuclear magnetic resonance
NUS	Non-uniform sampling
PAR	Proton assisted recoupling
PARIS	Phase-alternated recoupling irradiation
PBS	Phosphate buffered saline
PDB	Protein data bank
PDSD	Proton driven spin diffusion
PHF	Paired helical filament
PIPES	Piperazine-N,N'-bis(2-ethanesulfonic acid)
PLUQ	PACSYlite unified query
PRE	Paramagnetic resonance enhancement
PRR	Proline rich region
RAD	Radio frequency assisted diffusion
RCF	Relative centrifugal force
RDSD	R2nv-symmetry driven spin diffusion
REAPDOR	Rotational echo adiabatic passage double resonance
REDOR	Rotational echo double resonance
RF	Radio frequency
RFDR	Radio frequency driven recoupling
RMSD	Root mean square deviation
ROCSA	Recoupling of chemical shift anisotropy

SDS-PAGE	Sodium dodecyl sulfate polyacrylamide gel electrophoresis
SNR	Signal-to-noise ratio
SPE	Single pulse excitation
SPECIFIC-CP	Spectrally induced filtering in combination with cross polarization
T2R	Tubulin: stathmin-like domain of RB3 (RB3-SLD) complex
TEM	Transmission electron microscopy
TOBSY	Total through-bond correlation spectroscopy
TOCSY	Total correlation spectroscopy
VFB	Vanadium flow battery

## ABSTRACT

Magic angle spinning (MAS) NMR is an important technique in the structural and dynamics characterization of biomacromolecules and bioinorganic complexes, especially those which lack solubility or resist crystallization. The knowledge of structure and dynamics of biological systems is crucial to understanding their functions. As systems of interest become increasingly challenging regarding the molecular size and complexity, novel MAS NMR strategies for characterization of proteins and bioinorganic solids are developing rapidly. This thesis discusses the application of MAS NMR spectroscopy to study structure, dynamics, and chemical/biological functions in two classes of systems. The first is microtubules (MTs) and microtubule-associated proteins (MAPs); the second is vanadium(V)-containing bioinorganic solids.

The MAP Tau plays critical roles in regulating multiple MT activities in neurons through binding with MTs. The loss of Tau binding to microtubules is pathologically relevant to many neurodegenerative diseases including Alzheimer's disease (AD). I present an investigation into the conformation and dynamics of Tau assembled with polymerized MTs by MAS NMR spectroscopy. Our studies of TauF4, a functional fragment of Tau, demonstrate that, surprisingly, TauF4 remains disordered upon binding with MTs and is highly dynamic on a wide of range of timescales (nano- to milliseconds). To my knowledge, such remarkable mobility of a protein when bound to its partner is unique to TauF4 and is consistent with its function in regulation of MT polymerization dynamics.

The Microtubule-associated motor protein Kif5b is essential to intracellular transport and cell division. Determining Kif5b motor domain structure assembled with polymeric microtubules is crucial for understanding the mechanism of Kif5b translocation along MTs. The protocol for preparing Kif5b/MT assemblies as presented in the thesis is the first for MAS NMR studies. Our preliminary NMR studies of Kif5b/MTs demonstrate that Kif5b bound to microtubules is well-structured, and lay the methodological foundation for its 3D structure determination.

Vanadium bioinorganic solids have found diverse applications as catalysts and demonstrated potential utility as pharmaceuticals. Vanadium in its +5 oxidation state is diamagnetic and not amenable to conventional EPR and UV-vis characterizations but is well suited for solid-state NMR studies. In deriving the structures of vanadium (V)-containing bioinorganic compounds, we combine multinuclear NMR spectroscopy with density functional theory (DFT) calculations. This approach, termed NMR crystallography, is first validated in a structurally known compound ( $^{15}\text{N}$ -salicylideneglycinate)-(benzhydroxamate)oxovanadium(V) ( $\text{VO}(^{15}\text{NGlySal})\text{bz}$ ) and subsequently employed in the determination of the three-dimensional structure of (methoxo)( $^{15}\text{N}$ -salicylidene-glycinato)oxovanadium(V) (abbreviated as  $\text{VO}(^{15}\text{NGlySal})\text{OCH}_3(\text{CH}_3\text{OH})$ ) including the correct solvation state, which has not been reported previously. This work has expanded the application of NMR crystallography in the context of vanadium(V)-containing compounds.

## Chapter 1

### MICROTUBULES AND MICROTUBULE-ASSOCIATED PROTEINS

Microtubules (MTs) are a major type of cytoskeletal filaments extending throughout the cytoplasm in eukaryotic cells. They are broadly involved in a variety of essential cellular activities including cell structure maintenance, intracellular transport, cell migration and cell division.<sup>1,2</sup> MTs are recognized as “molecular machines” that drive cell movement, such as the motility of chromosomes during cell mitosis.<sup>3</sup> They also provide platforms for intracellular cargo transport, such as transport of vesicles, organelles, mRNA, and other macromolecular assemblies.<sup>4</sup> All of these MT functions are assisted by interactions with a class of microtubule-associated proteins (MAPs), which regulate MT assembly and dynamic instability.<sup>5</sup> A broad class of proteins involved in intracellular transport through movement along MT is motor proteins, which includes the kinesin and dynein superfamilies.<sup>4</sup> Due to their important biological functions, the malfunction of MTs and their related proteins is associated with many neurodegenerative disorders, such as Alzheimer’s disease, frontotemporal dementia, and Perry syndrome.<sup>6-9</sup>

Insights into structural and dynamics aspects of MT and MAPs at atomic resolution are crucial for understanding the regulatory mechanism of MAPs and their interactions with MTs, thus providing a basis for the therapeutic treatment of MT-related diseases. As *in vitro* MTs lack long-range order and are insoluble, many conventional biophysical techniques for structural characterization, such as X-ray crystallography, electron microscopy, and solution nuclear magnetic resonance (NMR)

spectroscopy are not well suited for the study of MAPs in complex with polymeric microtubules, particularly at atomic resolution. Moreover, proteins undergo dynamic processes on multiple timescales while fulfilling their functions, and dynamic information on timescales of nano- to milliseconds cannot be obtained by X-ray crystallography or cryo-electron microscopy (cryo-EM).

We have applied magic angle spinning (MAS) NMR to the study of MAPs assembled on microtubules. MAS NMR provides atomic level structural information and yields rich protein dynamics data. Over the past decade, our laboratory has developed novel MAS NMR strategies in combination with other biophysical techniques for the structural and dynamics characterization of MTs and MAPs. The first structure of a MAP, the CAP-Gly domain of dynactin, bound to polymeric microtubules, was successfully solved by MAS NMR with atomic resolution by our laboratory (PDB ID Code 2MPX).<sup>10</sup> The dynamics of free CAP-Gly and upon binding to microtubules were also investigated by MAS NMR over multiple timescales and the observed dynamics were demonstrated to play an important role in the biological function of CAP-Gly.<sup>11</sup>

We are interested in expanding our structural and dynamic studies to broader classes of microtubule-associated proteins and microtubule-based motor proteins in complex with microtubules. Our long-term goals are to understand the protein-protein interactions of MAPs and microtubules and the mechanisms underlying the transport of microtubule-based molecular motors along microtubules. Demonstrated throughout this thesis is the successful application of MAS NMR methods to the study of two classes of MAPs with distinct structural properties when bound to MTs: Tau, an intrinsically disordered protein, and the motor protein Kif5b, which is well ordered.

This chapter is a brief introduction to MTs, Tau, and kinesin in the context of their structure, dynamics, and functions.

## **1.1 Microtubules**

### **1.1.1 Structure of Microtubules**

Microtubules are hollow, filamentous polymers formed by the polymerization of tubulin heterodimers, comprised of  $\alpha$ -tubulin and  $\beta$ -tubulin subunits.<sup>12</sup> These  $\alpha\beta$ -tubulin heterodimers associate from head to tail to generate linear microtubule protofilaments. The lateral association of thirteen protofilaments yields a cylindrical microtubule with a diameter of 25 nm. Thus the microtubule is a polar structure with  $\alpha$ -tubulin at one end, named the “minus-end,” and  $\beta$ -tubulin at the other end, called the “plus-end”.<sup>13</sup> The schematic diagram in Figure 1.1 demonstrates the formation of microtubules from  $\alpha\beta$ -tubulin heterodimers. In mammalian cells, MTs are nucleated and organized in the centrosome. After nucleation, the MT minus-end is anchored in the centrosome with the plus-end growing out in cytoplasm and leading to cell cortex.<sup>3</sup> The polarity of microtubules is essential for their biological functions. The plus end of microtubules attaches to chromosomes or the nucleus and drives their movement during cell division.<sup>3</sup> The intracellular anterograde and retrograde transport is also determined by the polarity of the microtubule.

The polymerization of microtubules is powered by the hydrolysis of guanosine triphosphate (GTP), and each tubulin subunit contains one GTP binding site. The  $\alpha$ -tubulin GTP-binding site, termed the N-site, is located at the intermolecular interface within a tubulin heterodimer, and is non-exchangeable.<sup>14</sup> One magnesium ion binds tightly at the N-site and is responsible for stabilizing the  $\alpha\beta$ -tubulin heterodimer

structure.<sup>15</sup> The GTP bound on the surface of  $\beta$ -tubulin is partially exposed and hydrolysable, thus the  $\beta$ -tubulin GTP binding site is named the E-site (exchangeable site). The E-site GTP at the surface of unpolymerized tubulin heterodimers is hydrolyzed to GDP when the  $\alpha$ -tubulin from an incoming tubulin heterodimer is added to complete the GTP hydrolyzing pocket.

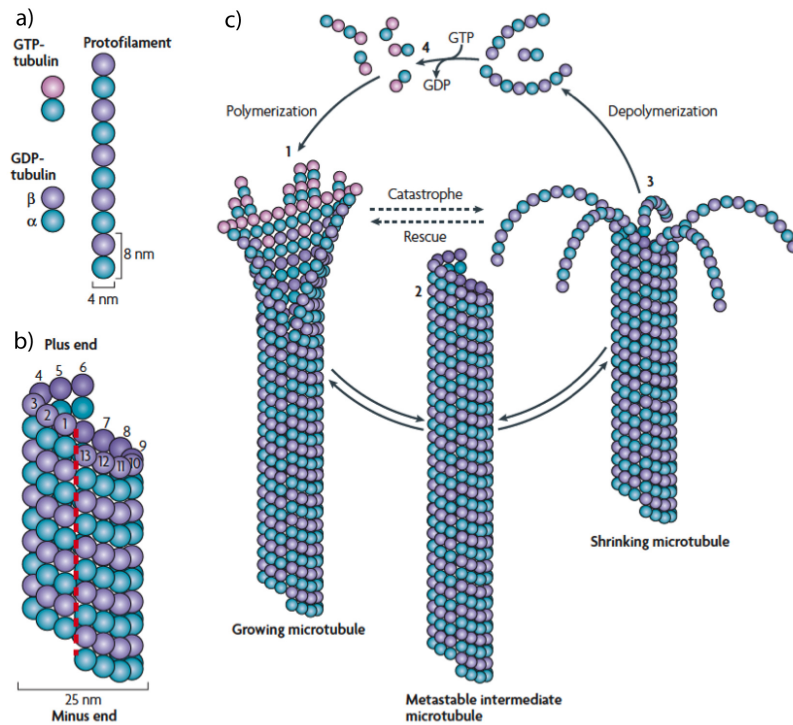


Figure 1.1: The structure and dynamic instability of microtubules. a)  $\alpha\beta$  tubulin heterodimer and microtubule protofilament. b) Thirteen protofilaments associate laterally to form the hollow microtubule wall. c) A microtubule switches from the growing state to the shrinking state by polymerization and depolymerization. This is accompanied by the hydrolysis of GTP. The figure was originally published in reference<sup>13</sup>. Permission for reuse in this dissertation is granted by Nature Publishing Group, copyright 2008.

Each  $\alpha$ -tubulin and  $\beta$ -tubulin subunit has a molecular weight of  $\sim 55$  kDa. Despite the fact that only 40% of the amino acid sequence is conserved, the globular structures of  $\alpha$ - and  $\beta$ - tubulin subunits are very similar, with each monomer being formed of a core of ten  $\beta$  strands flanked by twelve  $\alpha$  helices.<sup>14</sup> The tubulin structure is divided into three subdomains based on different functions: the nucleotide-binding domain at the N-terminus, an intermediate domain in the middle, and the C-terminal domain. The C-terminal domain tail is very acidic and highly flexible, and is responsible for interactions, through electrostatic forces, with MAPs, such as Tau.<sup>16</sup> The anti-cancer drug taxol, which inhibits the depolymerization of microtubules both *in vitro* and *in vivo*, binds to  $\beta$ -tubulin in the intermediate domain, close to the lateral contacts between protofilaments.<sup>14,17</sup>

Great progress has been made in the study of the tubulin heterodimer structure relevant to different functional states of microtubules. The monomeric  $\alpha\beta$  tubulin heterodimer structure in a straight conformation was first solved by electron crystallography (PDB ID code 1TUB), and represents the heterodimer structure in the stabilized microtubule.<sup>14</sup> The corresponding  $\alpha\beta$  tubulin structure with GTP bound at the N-site, GDP bound at the E-site and taxol bound to the intermediate domain is plotted in Figure 1.2. The dimeric  $\alpha\beta$  tubulin structure in complex with a stathmin family protein (referred to as T2R) determined by X-ray crystallography, represents the curved, destabilized form of microtubules.<sup>18</sup> High-resolution cryo-EM structures of microtubules in different nucleotide-binding states including GMPCPP-bound, GDP-, and taxol- stabilized GDP states have provided insight into the key structural conversions underlying microtubule shrinkage and growth.<sup>19</sup>

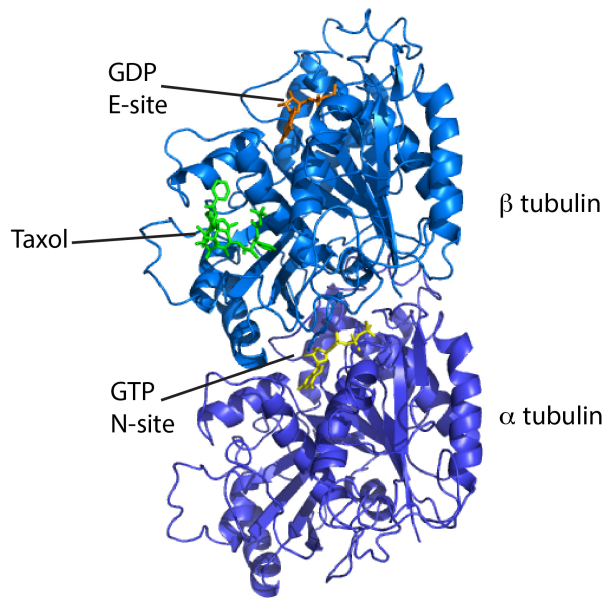


Figure 1.2: The structure of an  $\alpha\beta$  tubulin heterodimer obtained by electron crystallography<sup>14</sup> generated with Pymol. (PDB ID code: 1TUB) The GDP in the exchangeable site (E-site) on  $\alpha$  tubulin is shown in orange, and the GTP in the non-exchangeable site (N-site) on  $\beta$  tubulin is shown in yellow. The anticancer drug taxol is localized on  $\beta$  tubulin near the lateral tubulin contact site and is shown in green.

### 1.1.2 Dynamic Instability of Microtubules

The length, stability, and organization of microtubules change frequently to fulfill their functions in cells. Therefore, MTs are highly dynamic, and switch rapidly between growth and shrinkage both *in vitro* and *in vivo*. This non-equilibrium behavior exhibited by MTs is referred to as dynamic instability.<sup>20</sup> (illustrated in Figure 1.1) The dynamic switch from microtubule growth to shrinkage is called the “catastrophe,” and the opposite process is termed the “rescue”. Dynamic instability is coupled to the nucleotide state of tubulin at the plus end of the microtubule lattice. In a prevailing “GTP cap model”,<sup>21</sup> the microtubule is stabilized and tends to grow as

long as GTP-tubulin is at the plus end of microtubules, whereas the microtubule is unstable and tends to depolymerize when GDP-tubulin caps the end. Dynamic instability is very important for microtubules to fulfill their cellular functions. During metaphase and anaphase stages in cellular mitosis, the migration of chromosomes is induced by microtubule dynamics, and the segregation of chromosomes is directed by microtubule depolymerization.<sup>22</sup> MTs' vital role in cell division makes them an important candidate for anti-cancer therapies. For example, the anticancer drug taxol (paclitaxel) is used to prevent depolymerization of MT filaments, consequently inhibiting mitosis.<sup>23</sup> Other compounds that are promising in cancer treatment include the eleutherobin, epothilones, and their derivatives.<sup>24</sup>

In cells, the dynamic instability of MTs is highly regulated by interactions with MAPs, some of which stabilize and promote MT assembly while others destabilize and induce MT disassembly.<sup>5,25</sup> A class of structural MAPs, Tau, MAP2, and MAP4, are common "microtubule stabilizers" which bind with MT and promote MT polymerization.<sup>26</sup> Such processes are regulated by phosphorylation, and dysfunction of these proteins leads to a high frequency of microtubule dynamic instability.<sup>27</sup> In neurons, doublecortin counteracts MT depolymerization through stabilizing lateral contacts of MT protofilaments and preventing their outward bending.<sup>28</sup> The destabilization of microtubules is regulated by three classes of proteins via distinct mechanisms.<sup>24</sup> Katanin severs microtubules, generating a new end with GDP-tubulins exposed and causing microtubules to disassemble.<sup>29</sup> Stathmin enhances the frequency of GTP hydrolysis and increases the microtubule catastrophe rate.<sup>30</sup> Three members of the non-motile kinesin-13 family, Kif2a, Kif2b, and Kif2c, weaken the interaction between tubulin subunits and induce MT catastrophes.<sup>25</sup> Chapter 3 of this thesis

discusses our study of Tau, a microtubule assembly factor, and its interaction with microtubules.

## **1.2 Microtubule-Associated Protein Tau**

### **1.2.1 Biological Functions of Tau**

Tau predominantly functions as a MAP that facilitates the assembly of microtubules. The malfunction of Tau and formation of Tau aggregates have been implicated in many neurodegenerative diseases.<sup>31</sup> Recent studies have shown that Tau also plays important roles in cell signaling and regulation of enzymatic activities by interacting with its various binding partners, such as signaling molecules, kinases, and cytoskeletal proteins.<sup>32</sup> In this section, we highlight the microtubule-associated functions and intrinsic properties of Tau, and briefly describe its pathological role in Alzheimer's disease.

Tau is abundantly expressed in neurons, and it regulates diverse functions of neuronal microtubules.<sup>33</sup> One of Tau's primary functions is binding to microtubules and promoting microtubule growth, which is important for the maintenance of axon morphology and the longitudinal elongation of axons and dendrites.<sup>34,35</sup> In addition, Tau can promote the lateral association of microtubules during the formation of microtubule bundles, which is a crucial aspect of axonal growth.<sup>36</sup> Moreover, Tau stabilizes microtubules and regulates the dynamic instability of microtubules through suppression of the rapid switch between microtubule assembly and disassembly.<sup>37</sup> Specifically, in axons, Tau suppresses microtubule "treadmilling," a dynamic instability behavior only present in MTs wherein the growth rate of a MT at the plus end is equal to the shrinking rate at the minus end such that no net growth of MT is

observed.<sup>38</sup> By interfering with the binding of motor proteins to MTs, Tau governs microtubule-associated activities indirectly to regulate axonal transport.<sup>39</sup> The disruption of Tau's interaction with microtubules can cause neurodegenerative diseases referred as Tauopathies, including Alzheimer's disease, Pick's disease, some prion diseases, chronic traumatic encephalopathy, and several genetic forms of Parkinson's disease, to name a few.<sup>31,32</sup>

### **1.2.2 Tau and Alzheimer's Disease**

In its hyperphosphorylated and insoluble form, Tau is recognized as a major component of neurofibrillary tangles (NFTs), one of the pathological hallmarks of Alzheimer's disease.<sup>40</sup> The human brain contains six Tau isoforms, all of which have been identified in the NFTs of diseased patients' brains.<sup>41</sup> Under normal physiological conditions, Tau binds to and stabilizes microtubules via phosphorylation regulation.<sup>42</sup> In the longest Tau isoform, there are 85 sites (45 serines, 35 threonines, 5 tyrosines) where phosphorylation can potentially occur.<sup>43</sup> Every mole of Tau in a normal adult brain contains 2 to 3 moles of phosphate.<sup>44</sup> However, abnormal phosphorylation compromises Tau function and causes Tau to dissociate from microtubules. Consequently, microtubule disassembly is triggered, and Tau accumulates in the form of paired helical filaments (PHFs), the primary component of NFTs. About twenty-five aberrant phosphorylation sites linked to Tau aggregation have been identified.<sup>45</sup> In the diseased brain of a patient with Alzheimer's, Tau is about three- to four-fold more hyperphosphorylated than that of normal brain.<sup>44</sup> The exact pathological relevance of the hyperphosphorylation of Tau in Alzheimer's disease is still unclear.<sup>46</sup> The prevailing assumption is that the accumulation of Tau aggregates induced by hyperphosphorylation is responsible for the increase of cytotoxicity.<sup>47</sup> Other

pathological outcomes induced by hyperphosphorylation may include 1) synaptic malfunction due to the missorting of Tau in axons; 2) hampered degradation and cleavage of Tau; and 3) altered interaction of Tau with its interaction partners.<sup>46</sup> Therefore, the inhibition of Tau hyperphosphorylation has been a promising therapeutic strategy for the treatment of Alzheimer's disease. To date, three particular kinases (GSK3 $\beta$ , CDK5, and ERK2) have been specifically linked to Tau hyperphosphorylation and are the current targets for hyperphosphorylation inhibitors.<sup>48</sup>

### **1.2.3 Domain Organization of Tau**

Up to six different Tau isoforms are expressed at different stages of brain development.<sup>49</sup> In the adult human brain all six isoforms of Tau are expressed with molecular weight ranging from 37 to 45 kDa.<sup>50</sup> Signatures of Tau structure include three or four imperfect repeats near the C-terminus and zero, one or two N-terminal inserts near the N-terminus.<sup>46</sup> The domain organization of these six Tau isoforms is shown in Figure 1.3a. The isoforms are named by the number of N-terminal inserts and binding repeats they contain. For example, the longest Tau isoform 2N4R contains two N-terminal inserts and four binding repeats. The 2N4R isoform possesses two main functional domains: a microtubule assembly domain on the C-terminus and a projection domain on the N-terminus. The microtubule assembly domain is composed of the imperfect repeat regions annotated R1-R4 and a flanking region. As the name indicates, the main function of this domain includes binding with microtubule and promotion of microtubule assembly.<sup>51</sup> Each repeat motif contains 31 to 32 amino acids, with a highly conserved 18-amino-acid repeat region and a less homologous inter-repeat region of 13 or 14 amino acids. The proline-rich region upstream of the repeat region is also thought to promote microtubule assembly.<sup>51</sup>

Rather than forming proximal contact with the microtubule, the amino-terminal domain projects opposite to the microtubule surface, and thus is called the “projection domain”.<sup>52</sup> The projection domain has been shown to interact with adjacent microtubules and regulates the spacing between microtubules in axons and dendrites.<sup>53</sup>

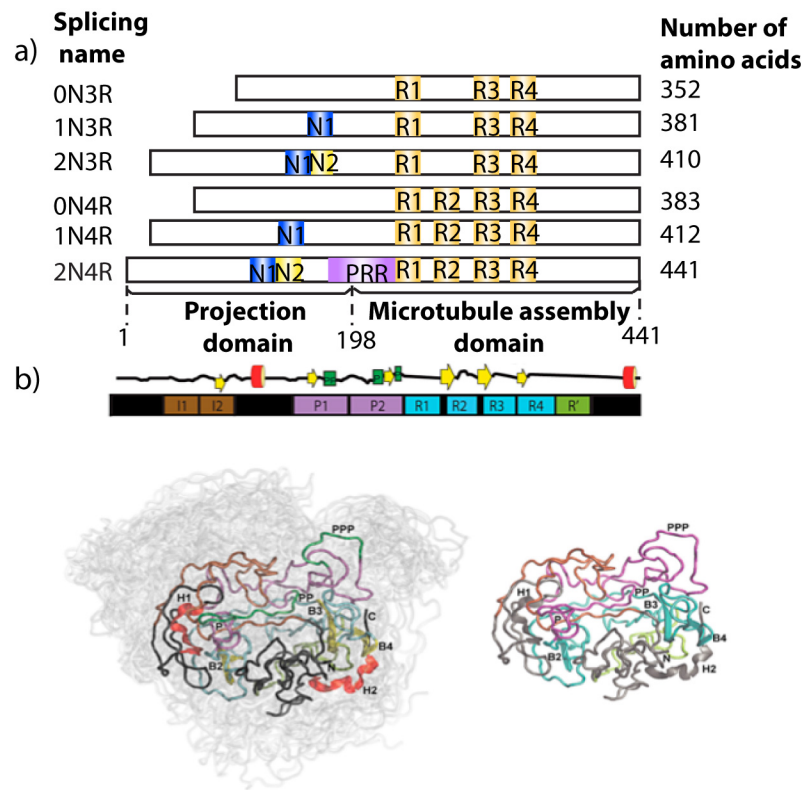


Figure 1.3: a) Six Tau isoforms expressed in the adult brain are distinguished by the presence of zero, one, or two near N-terminus inserts N1 and N2, and repeat R2 from the microtubule assembly domain. This figure is adapted from reference<sup>46</sup>. b) Conformation of the longest of Tau isoform 2N4R determined by solution NMR. The overall Tau structure in solution is unfolded, with a few transient secondary structure elements, including  $\alpha$  helical propensity shown as a red cylinder,  $\beta$  strands shown as yellow arrows, and helices formed by poly-Proline sequences, shown as green boxes. An ensemble of 20 conformations is displayed in the background. Color-coding indicates the domain organization. The figure is reprinted with permission from reference<sup>54</sup>.

#### **1.2.4 Tau as an Intrinsically Disordered Protein**

Given the prevalence of charged residues, Tau is overall hydrophilic and does not fold into stable secondary or tertiary structural elements.<sup>33,54,55</sup> Therefore, Tau belongs to a family of intrinsically disordered proteins (IDPs). The disordered property was first noticed by its high resistance to denaturation by heat or acid and its high solubility in water.<sup>56</sup> In addition, Tau is highly dynamic and occupies a much larger volume in solution compared to well-folded proteins of similar size.<sup>57</sup> There is no existing X-ray structure of Tau, as its intrinsically disordered nature precludes crystallization. The conformation of Tau at the residue-specific level has been characterized by solution NMR. More than 70% of full-length Tau is disordered, and the transiently ordered secondary structural elements exist in several small, discontinuous regions.<sup>54</sup> For example, two hexapeptides, <sup>275</sup>VQIINK<sup>280</sup> and <sup>306</sup>VQIVYK<sup>311</sup>, being the potential nuclei in forming Tau fibrous aggregates, have a strong  $\beta$  sheet propensity.<sup>58</sup> The transient elements of secondary structure are shown in Figure 1.3b. Paramagnetic relaxation enhancements (PRE) recorded by solution NMR suggest the presence of multiple conformations of Tau in solution.<sup>54</sup> An ensemble of 20 conformers calculated from PRE distance restraints is shown in Figure 1.3b. Despite a lack of compact structure, the amino-terminus tends to fold toward the carboxyl-terminus and forms a general turn structure in a “paperclip” shape.<sup>54,59</sup>

### **1.3 Microtubule-Associated Motor Protein Kinesin**

#### **1.3.1 Kinesin Superfamily and Conventional Kinesin**

Kinesins, a superfamily of microtubule-associated motor proteins, play essential roles in intracellular transport<sup>60-62</sup> and cell division<sup>63</sup> powered by the hydrolysis of ATP. In cells, motile kinesins transport numerous cargos including

organelles, vesicles, proteins, and mRNA to various destinations. They are crucial for cell functions, cell growth, and morphogenesis.<sup>62</sup> Kinesin motors are also involved in the motility of mitotic spindles and segregation of chromosomes at different stages of cell division.<sup>63</sup> Due to their important functions in mitosis, kinesins have become an emerging drug target for cancer therapeutic development.<sup>64</sup>

Since the initial discovery of conventional kinesin (kinesin-1), forty-five members of the kinesin superfamily (also known as Kifs) have been identified. Kinesins are classified into 15 subfamilies, termed Kinesin 1 to 14B, based upon phylogenetic analyses.<sup>60,61</sup> Members of the kinesin superfamily share a highly conserved motor domain. The 15 subfamilies are further subdivided into three classes based on the position of the motor domain: N-kinesins, C-kinesins and M-kinesins.<sup>62</sup> For these three classes, the motor domain is located at the amino terminus, at the carboxyl terminus, or in the middle of the protein respectively. The domain organization of the major Kifs is depicted in Figure. 1.4

Kifc2 and Kifc3, which drive microtubule minus-end-directed motility, belong to the C-kinesins subfamily. Kifc2 is ubiquitously expressed in dendrites.<sup>65</sup> Kif2a, belonging to the M-kinesin class, is non-motile and acts as a microtubule-destabilizing protein.<sup>62,66</sup> N-kinesins are primarily responsible for powering the microtubule plus end-directed motility. Kif5, the conventional kinesin, belongs to this family and includes three subtypes: Kif5a, Kif5b and Kif5c.<sup>67,68</sup> Kif5b is expressed ubiquitously in all cell types, whereas Kif5a and Kif5c are exclusively expressed in neurons. The Kif5 motors play essential roles in cargo transport on axons, including transport of synaptic vesicles, membrane organelles and mitochondria.<sup>69,70</sup>

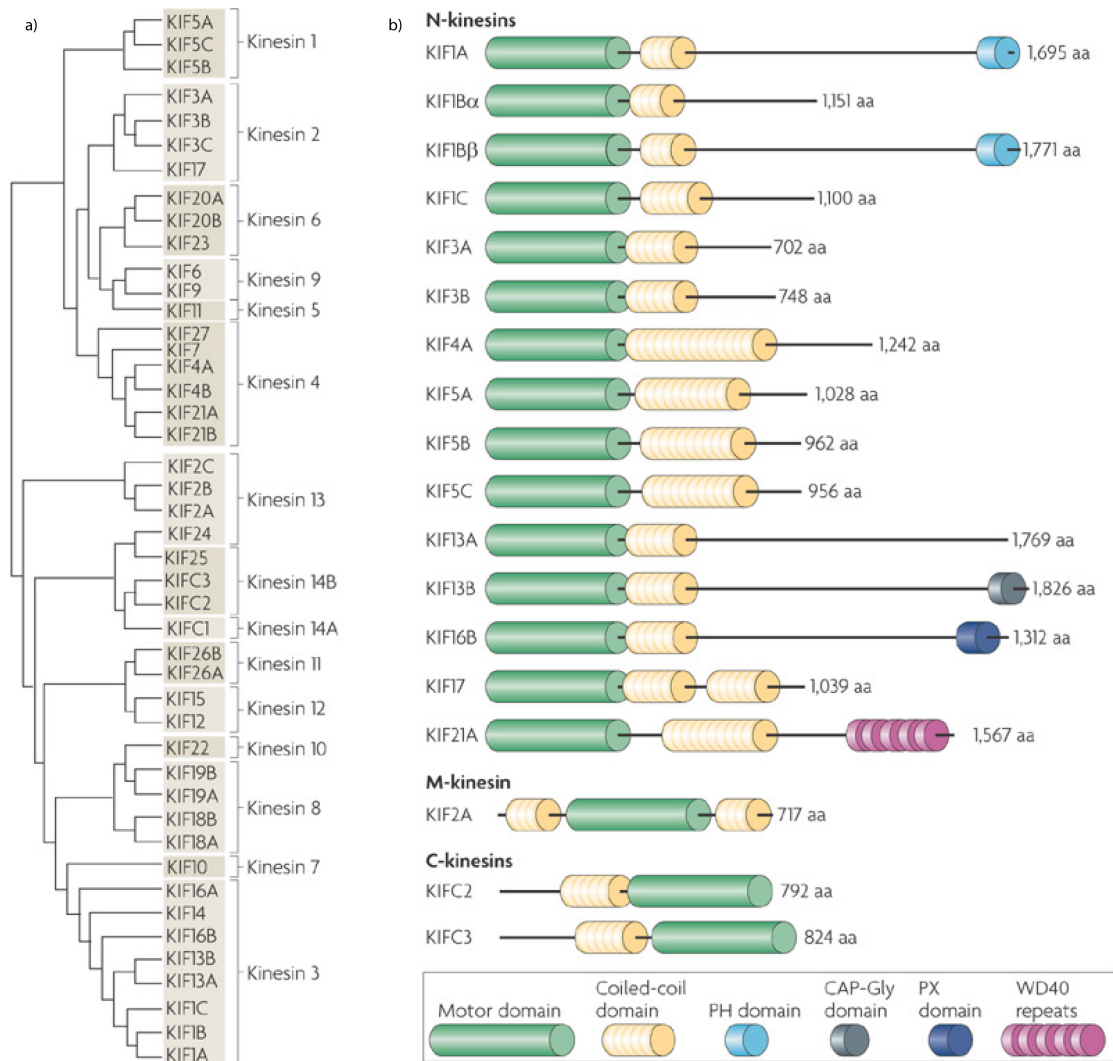


Figure 1.4: (a) Fifteen subfamilies of the kinesin superfamily based upon phylogenetic analysis. (b) Domain organization of the kinesin superfamily. The motor domain is highly conserved among kinesin superfamily members. Based on the position of the motor domain, kinesins are categorized into three subfamilies: N-kinesin, M-kinesin, and C-kinesin. The figure was originally published in reference<sup>62</sup>. Permission for reuse in this dissertation is granted by Nature Publishing Group, copyright 2009.

The kinesin superfamily can also be categorized into monomeric, homo- and heterodimeric motors. For instance, Kif1a, Kif1b $\alpha$  and Kif1b $\beta$  are monomeric motors due to their short-coiled coil regions.<sup>61</sup> Kif5 is one of the major dimeric motors, composed of two kinesin heavy chains (KHC) and two kinesin light chains (KLC). The KHC includes a motor domain at the NH<sub>2</sub>-terminus, which binds to a microtubule and harbors ATPase activity. Kif5 dimerizes through a coiled-coil stalk, which connects to a tail domain. The C-terminal region of the stalk and the tail domain both induce binding of KLC.<sup>71,72</sup> Kif5 can bind cargos through the tail domain and the carboxyl-terminal domains of the KLC.<sup>73</sup>

### **1.3.2 Kinesin Motor Domain Structure**

Since its discovery 30 years ago, conventional kinesin has been the most widely studied member of the kinesin superfamily.<sup>67</sup> This kinesin is the focus of studies described in chapter 4. Conventional kinesin is a homodimer of 960 amino acids per polypeptide chain. Each chain consists of a highly conserved motor domain on the N-terminus, which is the core for both ATPase activity and microtubule binding. Two motor domains dimerize through a coiled-coil stalk, which is linked to the tail domain. The binding and hydrolysis of ATP generates movement of the kinesin motor domain along microtubules accompanied by local structural changes. The key structural element that generates the movement is a ~14 - 18 amino acid neck linker at the C-terminal end of the motor domain. The structure of the motor domain has been extensively characterized by X-ray crystallography in both its isolated state<sup>74-76</sup> and bound to a tubulin heterodimer.<sup>77,78</sup> The structure of kinesin bound to polymeric microtubules has also been determined by cryo-EM.<sup>79,80</sup> These studies have greatly

advanced our understanding of the structural changes underlying the mechanism of mechanical movement.

The kinesin motor domain (1-349) forms an arrowhead-shaped structure, comprised of a core of eight parallel  $\beta$  strands surrounded by six  $\alpha$  helices.<sup>75</sup> The nucleotide-binding cleft, located near  $\alpha 6$  and  $\beta 2$  is open, as determined by the co-crystallization with MgADP. The kinesin motor domain structure is shown in Figure 1.5. A highly conserved phosphate-binding loop (P-loop) is found at the beginning of  $\alpha 2$ . Despite the fact that kinesin is only half the size of myosin, an actin-based motor, great structural similarity exists between the structural cores of these two proteins. Seven  $\beta$  strands (the strand  $\beta 5$  being the exception) and six  $\alpha$  helices align very well with myosin despite differences in amino acid sequence. This structural similarity suggests a similar mechanism for generating movement by motors from different families.<sup>75</sup> The neck linker, which drives the movement of kinesin, converts between mobile and docked states mediated by nucleotide exchange.<sup>81</sup> In free kinesin, the neck linker in its docked state is stabilized by a high concentration of lithium sulfate.<sup>74</sup> This structure, determined by X-ray crystallography (PDB ID code 1MKJ) also reveals the reorientation of  $\alpha 4$ , which forms the binding interface with microtubules.<sup>46</sup>

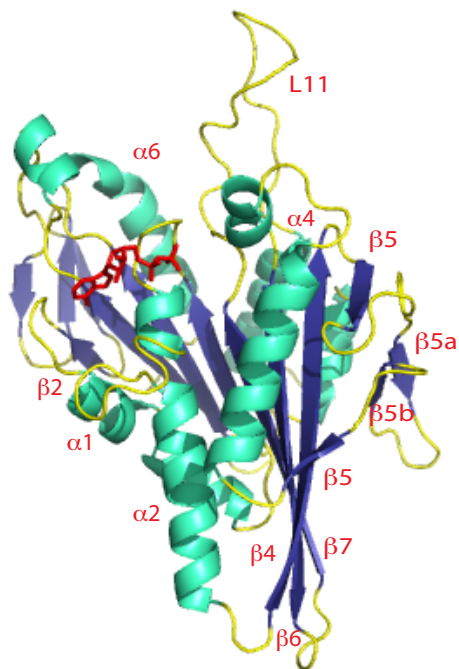


Figure 1.5: The X-ray structure of Kif5b (PDB ID code: 1BG2). The  $\alpha$  helices are shown in green-cyan,  $\beta$  strands in blue, and loop regions in yellow. The ADP molecule is displayed as red sticks. The numbering is adapted from reference<sup>75</sup>.

Recently, high resolution structures of kinesin bound to a tubulin heterodimer in ATP-like<sup>77</sup> and nucleotide-free states<sup>78</sup> were determined by X-ray crystallography (with resolution of 3.7 and 2.2 Å respectively). Three kinesin subdomains are identified subsequently, namely the Switch I&II subdomain, the tubulin-binding domain, and the P-loop subdomain, shown in Figure 1.6a.<sup>78</sup> As reported by Cao et al, helices  $\alpha 4$  and  $\alpha 5$ , together with the L12 loop and strands  $\beta 5a$ , and  $\beta 5b$  form the tubulin-binding domain. The Switch I&II and P-loop subdomains constitute the nucleotide-binding motif. On the basis of this structural information, the following

neck linker docking mechanism was proposed. The binding of ATP in the nucleotide-binding motif induces the reorientation of three subdomains shown in Figure 1.6b. It brings the P-loop and the Switch I&II subdomains together, and subsequently the first residue of the neck linker becomes buried, resulting in neck linker docking.<sup>78</sup> The coordinated movement of the three subdomains is thus required with neck linker being the key contributor to kinesin's movement.

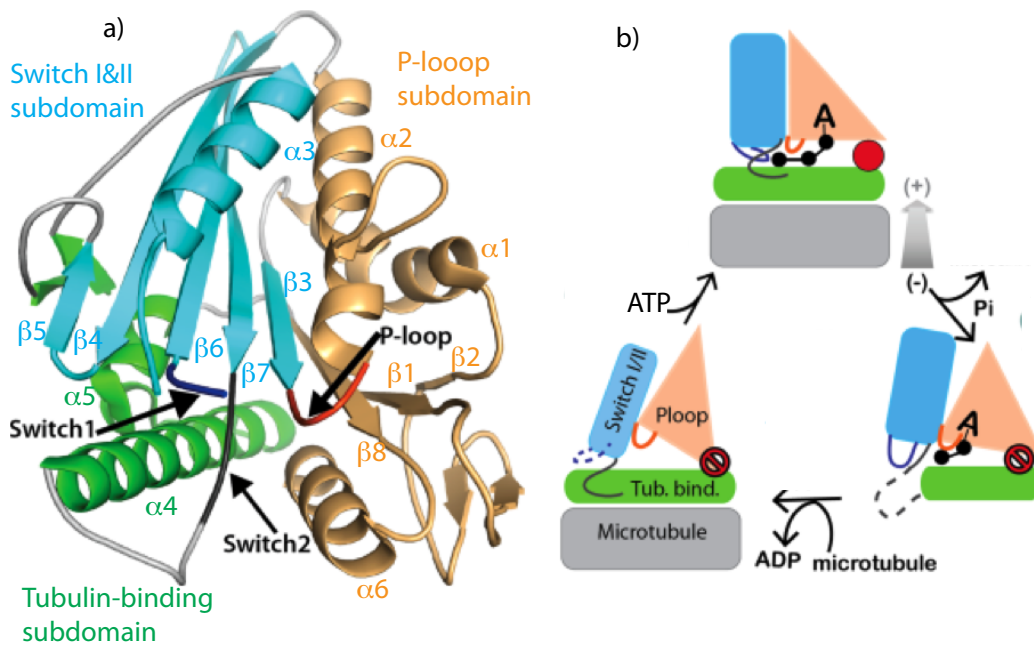


Figure 1.6: The subdomain structure of nucleotide free Kif5b and the coordinated movement of subdomains in each step of the nucleotide cycle. a) The three subdomains of Kif5b are colored as follows: the Switch I&II subdomain is shown in cyan, the microtubule binding domain in green, and the P-loop subdomain in beige. b) The reorientation of subdomains along each step of nucleotide cycle. Upon binding with microtubules, the neck linker (in red) is docked in the ATP binding state, while the linker is undocked in the free and ADP-bound states. Figure is adapted from reference<sup>82</sup>. Permission for reuse in this dissertation is granted by John Wiley and Sons, copyright 2015.

In parallel, the structures of the microtubule-bound kinesin motor domain in ATP-like and nucleotide-free states were determined by cryo-EM at resolutions of ~6-7 Å and 5-6 Å, respectively.<sup>78,79</sup> Comparison of the structure of the nucleotide-free kinesin motor domain bound to  $\alpha\beta$  tubulin (determined by X-ray crystallography) with the structure bound to polymeric microtubules (determined by cryo-EM), reveals that the protein backbones align to within an RMSD of 0.8 Å for  $\alpha$  helices and  $\beta$  sheets despite the differing resolution and state of tubulin oligomerization.<sup>82</sup> This further proves that the kinesin structure is similar when bound to tubulin heterodimer or polymeric microtubules.<sup>82</sup> The mechanism of movement induced by microtubule and nucleotide binding is inferred by comparison of the cryo-EM structures (free and ATP states) with that of ADP-bound state determined by X-ray crystallography. The binding of ATP causes the nucleotide-binding cleft to close and induces neck linker docking. Attachment to microtubules reopens the nucleotide-binding cleft and allows ADP to be released.<sup>80</sup>

### **1.3.3 Kinesin Processivity**

The conventional dimeric kinesin is a highly processive motor that can migrate on the surface of a microtubule for over 100 steps before detaching itself from the microtubule.<sup>83</sup> Kinesin hydrolyzes one ATP molecule per 8.2-nm step, which corresponds to the length of a tubulin heterodimer.<sup>84,85</sup> In the prevailing “hand-over-hand” stepping model, as shown in Figure 1.7,<sup>86,87</sup> the two heads of the kinesin dimer alternate between leading and trailing roles after each step. To start the walking cycle, the two kinesin heads in their waiting states are bound to the microtubule separated by 8.2 nm with ADP bound to the rear tethered head. Upon binding of ATP to the front head, the neck linker is immobilized onto the motor domain (docking), causing the

rear head to move toward the microtubule plus-end by 16 nm and attach to the next tubulin heterodimer and release the ADP. Subsequently, with ATP hydrolysis and detachment of the trailing head from MT, dimeric kinesin returns to its initial awaiting state and is ready to continue a new cycle. In contrast to the prevailing model, a more recent proposed model argues against the completion of tethered head movement and binding prior to ATP hydrolysis and suggests that the binding occurs subsequent to the hydrolysis, as described in reference<sup>88</sup>.

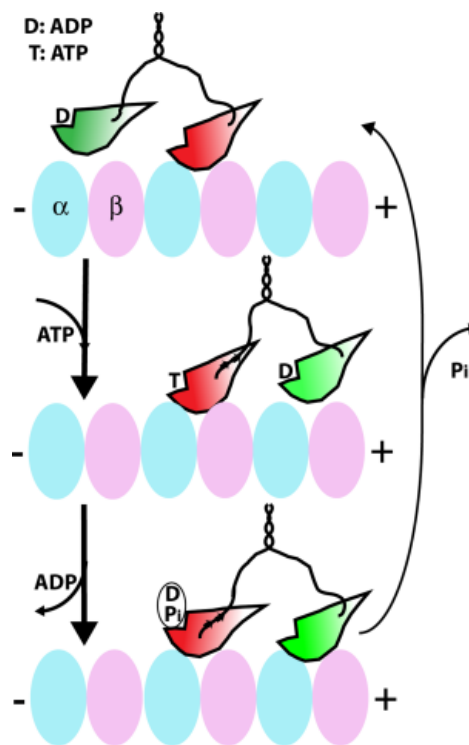


Figure 1.7: The “hand over hand” walking mechanism of dimeric kinesin along a microtubule. The two kinesin motor domains are dimerized through the coiled coil region. In one step, the kinesin motor domain cycles through different nucleotide states as indicated. The figure was originally published in reference<sup>82</sup>. Permission for reuse in this dissertation is granted by John Wiley & Sons, copyright 2015.

It is crucial that at least one kinesin head stays attached to the microtubule during the cycle so that it can accomplish multiple successive steps before detaching. Therefore, the precise coordination of movement and the nucleotide binding between the two heads is indispensable for kinesin processivity.<sup>89</sup> This mechanism is referred to as “alternating head catalysis”.<sup>90</sup> Both the ATP-bound and the free kinesin bind to microtubules more tightly than the ADP-bound kinesin,<sup>91</sup> thus the movement of the ADP-bound tethered head with subsequent ADP release and MT attachment should occur before ATP hydrolysis at the other head, which makes it tend to dissociate from the MT. The dwell time of kinesin binding to microtubules is slower than the forward stepping frequency to ensure that the dimeric motor remains associated to the microtubule.<sup>82,92</sup> The motor domain cycles through conformations during the nucleotide cycle (ATP-bound, nucleotide-free, and ADP-bound states).

#### **1.4 Summary**

Due to the biological importance of MAPs and their increasing prominence as drug targets for neurodegenerative disorders and cancers, we are interested in studying Tau and kinesin bound to microtubules to understand their structure and dynamics in the physiologically relevant states. Such studies provide the basis for the development of therapeutic strategies against the MAP-associated diseases. Although high-resolution investigations of conventional kinesin assembled with polymeric microtubules have become possible due to the recent revolutionary progress in cryo-EM enabling near low nanometer resolution,<sup>78,79</sup> there is still debate regarding the relevance of the structure under cryogenic conditions to the physiological states. More importantly, internal site-specific dynamics information cannot be gained by such studies; dynamics are crucial for function of these proteins, i.e. motions along the

microtubules. The intrinsically disordered and highly flexible nature of Tau has limited its structural characterization by X-ray crystallography or cryo-EM. Solution NMR is a popular tool for probing the conformation of Tau and its interaction with MTs; however, such studies are hampered by the disappearance of NMR signals due to the large size of the complex. In the next chapter we introduce MAS NMR methods for the study of structure and dynamics of MT and MAPs. Application of these methods to studies of Tau and kinesin are covered in chapters 3 and 4, respectively.

## REFERENCES

- (1) Hyams, S. J., Lloyd, W. C. *Microtubules*; Wiley-Liss, 1993.
- (2) Etienne-Manneville, S. *Annu. Rev. Cell Dev. Biol.* **2013**, *29*, 471.
- (3) Howard, J.; Hyman, A. A. *Nature* **2003**, *422*, 753.
- (4) Hirokawa, N. *Science* **1998**, *279*, 519.
- (5) Mandelkow, E.; Mandelkow, E. M. *Curr. Opin. Cell Biol.* **1995**, *7*, 72.
- (6) Farrer, M. J.; Hulihan, M. M.; Kachergus, J. M. *Nat. Genet.* **2009**, *41*, 163.
- (7) Baird, F. J.; Bennett, C. L. *J. Genet. Syndr. Gene. Ther.* **2013**, *4*, 203.
- (8) Augustinack, J. C.; Schneider, A.; Mandelkow, E. M.; Hyman, B. T. *Acta Neuropathol.* **2002**, *103*, 26.
- (9) Ghetti, B.; Oblak, A. L.; Boeve, B. F.; Johnson, K. A.; Dickerson, B. C.; Goedert, M. *Neuropathol. Appl. Neurobiol.* **2015**, *41*, 24.
- (10) Yan, S.; Guo, C.; Hou, G.; Zhang, H.; Lu, X.; Williams, J. C.; Polenova, T. *Proc. Natl. Acad. Sci. USA* **2015**, *112*, 14611.
- (11) Yan, S.; Zhang, H. L.; Hou, G. J.; Ahmed, S.; Williams, J. C.; Polenova, T. *J. Biol. Chem.* **2015**, *290*, 1607.
- (12) Desai, A.; Mitchison, T. J. *Annu. Rev. Cell Dev. Biol.* **1997**, *13*, 83.
- (13) Akhmanova, A.; Steinmetz, M. O. *Nat. Rev. Mol. Cell. Biol.* **2008**, *9*, 309.
- (14) Nogales, E.; Wolf, S. G.; Downing, K. H. *Nature* **1998**, *391*, 199.
- (15) Menendez, M.; Rivas, G.; Diaz, J. F.; Andreu, J. M. *J. Biol. Chem.* **1998**, *273*, 167.
- (16) Lefevre, J.; Chernov, K. G.; Joshi, V.; Delga, S.; Toma, F.; Pastre, D.; Curmi, P. A.; Savarin, P. *J. Biol. Chem.* **2011**, *286*, 3065.

- (17) Nogales, E.; Wolf, S. G.; Khan, I. A.; Luduena, R. F.; Downing, K. H. *Nature* **1995**, *375*, 424.
- (18) Gigant, B.; Curmi, P. A.; Martin-Barbey, C.; Charbaut, E.; Lachkar, S.; Lebeau, L.; Siavoshian, S.; Sobel, A.; Knossow, M. *Cell* **2000**, *102*, 809.
- (19) Alushin, G. M.; Lander, G. C.; Kellogg, E. H.; Zhang, R.; Baker, D.; Nogales, E. *Cell* **2014**, *157*, 1117.
- (20) Kirschner, M. W.; Mitchison, T. *Nature* **1986**, *324*, 621.
- (21) Mitchison, T.; Kirschner, M. *Nature* **1984**, *312*, 237.
- (22) McIntosh, J. R.; Volkov, V.; Ataulakhanov, F. I.; Grishchuk, E. L. *J. Cell Sci.* **2010**, *123*, 3425.
- (23) Yvon, A. M. C.; Wadsworth, P.; Jordan, M. A. *Mol. Biol. Cell* **1999**, *10*, 947.
- (24) Nogales, E. *Annu. Rev. Biochem.* **2000**, *69*, 277.
- (25) van der Vaart, B.; Akhmanova, A.; Straube, A. *Biochem. Soc. Trans.* **2009**, *37*, 1007.
- (26) Dehmelt, L.; Halpain, S. *Genome Biol.* **2005**, *6*, 204.
- (27) Drewes, G.; Ebner, A.; Mandelkow, E. M. *Trends Biochem. Sci.* **1998**, *23*, 307.
- (28) Moores, C. A.; Perderiset, M.; Kappeler, C. *EMBO J.* **2006**, *25*, 4448.
- (29) McNally, F. J.; Okawa, K.; Iwamatsu, A.; Vale, R. D. *J. Cell Sci.* **1996**, *109*, 561.
- (30) Howell, B.; Larsson, N.; Gullberg, M.; Cassimeris, L. *Mol. Biol. Cell* **1999**, *10*, 105.
- (31) Lee, V. M.; Goedert, M.; Trojanowski, J. Q. *Annu. Rev. Neurosci.* **2001**, *24*, 1121.
- (32) Morris, M.; Maeda, S.; Vossel, K.; Mucke, L. *Neuron* **2011**, *70*, 410.
- (33) Mandelkow, E. M.; Mandelkow, E. *Csh Perspect Med* **2012**, *2*.
- (34) Drubin, D. G.; Kirschner, M. W. *J. Cell Biol.* **1986**, *103*, 2739.

- (35) Weingarten, M. D.; Lockwood, A. H.; Hwo, S. Y.; Kirschner, M. W. *Proc. Natl. Acad. Sci. USA* **1975**, *72*, 1858.
- (36) Kanai, Y.; Takemura, R.; Oshima, T.; Mori, H.; Ihara, Y.; Yanagisawa, M.; Masaki, T.; Hirokawa, N. *J. Cell Biol.* **1989**, *109*, 1173.
- (37) Bunker, J. M.; Wilson, L.; Jordan, M. A.; Feinstein, S. C. *Mol. Biol. Cell* **2004**, *15*, 2720.
- (38) Panda, D.; Miller, H. P.; Wilson, L. *Proc. Natl. Acad. Sci. USA* **1999**, *96*, 12459.
- (39) Dixit, R.; Ross, J. L.; Goldman, Y. E.; Holzbaur, E. L. F. *Science* **2008**, *319*, 1086.
- (40) Blennow, K.; Bogdanovic, N.; Alafuzoff, I.; Ekman, R.; Davidsson, P. *J. Neural Transm.* **1996**, *103*, 603.
- (41) Goedert, M.; Spillantini, M. G.; Cairns, N. J.; Crowther, R. A. *Neuron* **1992**, *8*, 159.
- (42) Buee, L.; Bussiere, T.; Buee-Scherrer, V.; Delacourte, A.; Hof, P. R. *Brain Res. Brain Res. Rev.* **2000**, *33*, 95.
- (43) Hanger, D. P.; Anderton, B. H.; Noble, W. *Trends Mol. Med.* **2009**, *15*, 112.
- (44) Iqbal, K.; Liu, F.; Gong, C. X.; Grundke-Iqbal, I. *Curr. Alzheimer Res.* **2010**, *7*, 656.
- (45) Anderton, B. H.; Betts, J.; Blackstock, W. P. *Biochem. Soc. Symp.* **2001**, *73*.
- (46) Wang, Y.; Mandelkow, E. *Nat. Rev. Neurosci.* **2016**, *17*, 5.
- (47) Grundkeiqbal, I.; Iqbal, K.; Tung, Y. C.; Quinlan, M.; Wisniewski, H. M.; Binder, L. I. *Proc. Natl. Acad. Sci. USA* **1986**, *83*, 4913.
- (48) Mazanetz, M. P.; Fischer, P. M. *Nat. Rev. Drug Discov.* **2007**, *6*, 464.
- (49) Goedert, M.; Jakes, R. *EMBO J.* **1990**, *9*, 4225.
- (50) Goedert, M.; Spillantini, M. G.; Jakes, R.; Rutherford, D.; Crowther, R. A. *Neuron* **1989**, *3*, 519.
- (51) Gustke, N.; Trinczek, B.; Biernat, J.; Mandelkow, E. M.; Mandelkow, E. *Biochemistry* **1994**, *33*, 9511.

- (52) Hirokawa, N.; Shiomura, Y.; Okabe, S. *J. Cell Biol.* **1988**, *107*, 1449.
- (53) Chen, J.; Kanai, N.; Cowan, J. N.; Hirokawa, N. *Nature* **1992**, *360*, 674.
- (54) Mukrasch, M. D.; Bibow, S.; Korukottu, J.; Jeganathan, S.; Biernat, J.; Griesinger, C.; Mandelkow, E.; Zweckstetter, M. *Plos Biol.* **2009**, *7*, 399.
- (55) Schweers, O.; Schonbrunnhanebeck, E.; Marx, A.; Mandelkow, E. *J. Biol. Chem.* **1994**, *269*, 24290.
- (56) Cleveland, D. W.; Hwo, S. Y.; Kirschner, M. W. *J. Mol. Biol.* **1977**, *116*, 227.
- (57) Mylonas, E.; Hascher, A.; Bernado, P.; Blackledge, M.; Mandelkow, E.; Svergun, D. I. *Biochemistry* **2008**, *47*, 10345.
- (58) von Bergen, M.; Friedhoff, P.; Biernat, J.; Heberle, J.; Mandelkow, E. M.; Mandelkow, E. *Proc. Natl. Acad. Sci. USA* **2000**, *97*, 5129.
- (59) Jeganathan, S.; von Bergen, M.; Brutlach, H.; Steinhoff, H. J.; Mandelkow, E. *Biochemistry* **2006**, *45*, 2283.
- (60) Miki, H.; Okada, Y.; Hirokawa, N. *Trends Cell Biol.* **2005**, *15*, 467.
- (61) Hirokawa, N.; Noda, Y. *Physiol. Rev.* **2008**, *88*, 1089.
- (62) Hirokawa, N.; Noda, Y.; Tanaka, Y.; Niwa, S. *Nat. Rev. Mol. Cell. Biol.* **2009**, *10*, 682.
- (63) Wordeman, L. *Semin. Cell Dev. Biol.* **2010**, *21*, 260.
- (64) Rath, O.; Kozielski, F. *Nat. Rev. Cancer* **2012**, *12*, 527.
- (65) Saito, N.; Okada, Y.; Noda, Y.; Kinoshita, Y.; Kondo, S.; Hirokawa, N. *Neuron* **1997**, *18*, 425.
- (66) Homma, N.; Takei, Y.; Tanaka, Y.; Nakata, T.; Terada, S.; Kikkawa, M.; Noda, Y.; Hirokawa, N. *Cell* **2003**, *114*, 229.
- (67) Vale, R. D.; Reese, T. S.; Sheetz, M. P. *Cell* **1985**, *42*, 39.
- (68) Kanai, Y.; Okada, Y.; Tanaka, Y.; Harada, A.; Terada, S.; Hirokawa, N. *J. Neurosci.* **2000**, *20*, 6374.
- (69) Tanaka, Y.; Kanai, Y.; Okada, Y.; Nonaka, S.; Takeda, S.; Harada, A.; Hirokawa, N. *Cell* **1998**, *93*, 1147.

- (70) Toda, H.; Mochizuki, H.; Flores, R., 3rd *Genes Dev.* **2008**, *22*, 3292.
- (71) Diefenbach, R. J.; Mackay, J. P.; Armati, P. J.; Cunningham, A. L. *Biochemistry* **1998**, *37*, 16663.
- (72) Gyoeva, F. K.; Sarkisov, D. V.; Khodjakov, A. L.; Minin, A. A. *Biochemistry* **2004**, *43*, 13525.
- (73) Seiler, S.; Kirchner, J.; Horn, C.; Kallipolitou, A.; Woehlke, G.; Schliwa, M. *Nat. Cell Biol.* **2000**, *2*, 333.
- (74) Sindelar, C. V.; Budny, M. J.; Rice, S.; Naber, N.; Fletterick, R.; Cooke, R. *Nat. Struct. Biol.* **2002**, *9*, 844.
- (75) Kull, F. J.; Sablin, E. P.; Lau, R.; Fletterick, R. J.; Vale, R. D. *Nature* **1996**, *380*, 550.
- (76) Sack, S.; Muller, J.; Marx, A.; Thormahlen, M.; Mandelkow, E. M.; Brady, S. T.; Mandelkow, E. *Biochemistry* **1997**, *36*, 16155.
- (77) Gigant, B.; Wang, W. Y.; Dreier, B.; Jiang, Q. Y.; Pecqueur, L.; Pluckthun, A.; Wang, C. G.; Knossow, M. *Nat. Genet.* **2013**, *20*, 1001.
- (78) Cao, L. Y.; Wang, W. Y.; Jiang, Q. Y.; Wang, C. G.; Knossow, M.; Gigant, B. *Nat. Commun.* **2014**, *5*.
- (79) Atherton, J.; Farabella, I.; Yu, I. M.; Rosenfeld, S. S.; Houdusse, A.; Topf, M.; Moores, C. A. *Elife* **2014**, *3*, e03680.
- (80) Shang, Z.; Zhou, K.; Xu, C.; Csencsits, R.; Cochran, J. C.; Sindelar, C. V. *Elife* **2014**, *3*, e04686.
- (81) Rice, S.; Lin, A. W.; Safer, D. *Nature* **1999**, *402*, 778.
- (82) Wang, W. Y.; Cao, L. Y.; Wang, C. G.; Gigant, B.; Knossow, M. *Protein Sci.* **2015**, *24*, 1047.
- (83) Block, S. M.; Goldstein, L. S. B.; Schnapp, B. J. *Nature* **1990**, *348*, 348.
- (84) Coy, D. L.; Wagenbach, M.; Howard, J. *J. Biol. Chem.* **1999**, *274*, 3667.
- (85) Schnitzer, M. J.; Block, S. M. *Nature* **1997**, *388*, 386.
- (86) Asbury, C. L.; Fehr, A. N.; Block, S. M. *Science* **2003**, *302*, 2130.

- (87) Yildiz, A.; Tomishige, M.; Vale, R. D.; Selvin, P. R. *Science* **2004**, *303*, 676.
- (88) Milic, B.; Andreasson, J. O. L.; Hancock, W. O.; Block, S. M. *Proc. Natl. Acad. Sci. USA* **2014**, *111*, 14136.
- (89) Block, S. M. *Biophys. J.* **2007**, *92*, 2986.
- (90) Hackney, D. D. *Proc. Natl. Acad. Sci. USA* **1994**, *91*, 6865.
- (91) Cross, R. A. *Trends Biochem. Sci.* **2004**, *29*, 301.
- (92) Toprak, E.; Yildiz, A.; Hoffman, M. T.; Rosenfeld, S. S.; Selvin, P. R. *Proc. Natl. Acad. Sci. USA* **2009**, *106*, 12717.

## Chapter 2

### OVERVIEW OF MAS NMR METHODS RELEVANT TO THE STRUCTURAL AND DYNAMICS STUDIES OF MICROTUBULE-ASSOCIATED PROTEINS AND MICROTUBULE ASSEMBLIES

Proteins and protein assemblies perform many physiological roles in living cells, including maintaining cell structure, catalysis, cell signaling, and intracellular transport. Determining protein structure is fundamental to understanding their functions in various cellular processes. In addition to structure, protein dynamics have been recognized to be essential for different protein functions.<sup>1,2</sup> Magic angle spinning (MAS) NMR spectroscopy has become an important technique for structure determination and studies of dynamics of proteins and protein complexes that lack long-range order or do not crystallize. MAS NMR is well suited for the study of many biological systems, including large filamentous assemblies, such as bacteriophages,<sup>3-8</sup> the HIV capsid,<sup>9-12</sup> and the secretion system needles<sup>13,14</sup>. Non-crystalline amyloid fibrils<sup>15</sup> and membrane proteins embedded in lipids<sup>16-18</sup> have also been successfully characterized by MAS NMR techniques.

Microtubules (MTs) represent an important class of filamentous structures, and they are broadly involved in many physiological processes together with microtubule-associated proteins (MAPs), as described in chapter 1. MAPs regulate various functions of MTs through their binding and interactions with MTs, forming protein assemblies that are very large in size and insoluble. Knowledge of MAPs' structure and conformational dynamics is important to understanding their biological functions

and interactions with MTs. An overview of relevant MAS NMR methods that we apply for studies of MAP/MT assemblies is included in this chapter.

## 2.1 Isotopic Labeling

Isotopic labeling with magnetically active nuclei is required for NMR characterization of any biological systems. For proteins, uniform  $^{15}\text{N}$ ,  $^{13}\text{C}$  labeling is most commonly used, as it provides the most spectroscopic information in one sample. Protein expression is performed in minimal media containing  $^{13}\text{C}$ -glucose and  $^{15}\text{NH}_4\text{Cl}$  as carbon and nitrogen sources. The spectra of uniformly  $^{15}\text{N}$ ,  $^{13}\text{C}$ -labeled large proteins are often crowded and other labeling schemes are sometimes necessary to improve spectral resolution and reduce signal crowding. Alternative strategies include  $^{13}\text{C}$  sparse labeling,<sup>19-23</sup> amino acid-specific labeling,<sup>10,24</sup> and methyl group labeling.<sup>25-28</sup>

Protein deuteration is another labeling strategy for improving spectral resolution and has been widely applied in proton-detected MAS NMR spectroscopy.<sup>29-32</sup> The strong  $^1\text{H}$ - $^1\text{H}$  dipolar couplings in protein samples usually result in broadening of proton linewidths; therefore, protein deuteration with subsequent back-exchange of amide protons (proton dilution) is commonly used to suppress the strong  $^1\text{H}$ - $^1\text{H}$  dipolar couplings, thus reducing linewidths and as a result spectral overlap. Deuteration can be achieved by protein expression in  $\text{D}_2\text{O}$  minimal media using [ $^2\text{H}$ ,  $^{13}\text{C}$ ]-glucose as the sole carbon source.<sup>33</sup> The expressed protein incorporates deuterons into the exchangeable sites in backbone and sidechain positions. The back-exchange of amide and hydroxyl protons is then done by protein purification and subsequent dialysis in  $\text{H}_2\text{O}$  media. The percentage of amide protonation can be adjusted and controlled with appropriate  $\text{H}_2\text{O}/\text{D}_2\text{O}$  ratios (10% -40%) in dialysis buffer, which can further improve

the spectral resolution.<sup>29,34,35</sup> Visualization of different levels of protonation in a model protein SH3 is shown in Figure 2.1. In the case of a large, rigid protein, back-exchange of deuterons to protons in the hydrophobic core may be insufficient, rendering these positions undetectable. A protein unfolding and refolding process can improve the protonation level of the buried amide sites.<sup>33</sup>

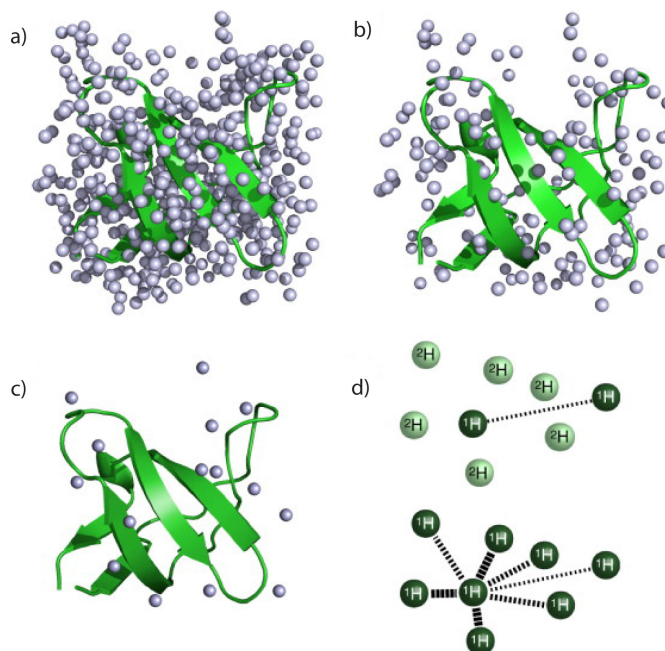


Figure 2.1: Protonation levels in a model protein  $\alpha$ -spectrin SH3 upon deuteration (PDB code ID: 1U06).<sup>36</sup> (a) Fully protonated protein. (b) Deuterated protein crystallized from 100% H<sub>2</sub>O with all exchangeable amide protons and protons of hydrated water molecules determined and refined in X-ray crystallography structure exhibited. (c) Deuterated protein crystallized from 10% H<sub>2</sub>O/90% D<sub>2</sub>O sample buffer. The protonation level is greatly reduced. On average, 21 protons contained in each protein molecule are displayed. (d) <sup>1</sup>H-<sup>1</sup>H dipolar couplings are strongly attenuated upon the incorporation of deuterons. The figure was originally published in reference<sup>31</sup>. Permission for reuse in this dissertation is granted by Elsevier, copyright 2012.

## 2.2 MAS NMR Multidimensional Correlation Spectroscopy

For MAS NMR studies of protein structure and dynamics, partial or full site-specific resonance assignments are the first step. These include spin system identification and sequential assignments. Spin system identification refers to the assignment of chemical shifts of backbone and sidechain carbons, nitrogens and protons belonging to a single residue, established through intraresidue correlations. The isotropic chemical shifts of each residue are likened to their “fingerprints” which include rich information on the secondary structure, torsion angle, dynamics, etc.<sup>37-39</sup> Sequential assignment refers to the link of different spin systems along the protein backbone by interresidue correlations. Both homo- and heteronuclear correlation experiments mediated by through-space (dipolar) and through-bond (scalar) couplings are generally acquired to establish these connections.

### 2.2.1 Through-Space Correlation Spectra

Magnetization can be transferred among atoms in close proximity by dipolar interactions. Dipolar-based homonuclear correlation experiments can establish both intra- and interresidue correlations, and are important for resonance assignment and determination of distance restraints. The conventional experiments for establishing homonuclear  $^{13}\text{C}$ - $^{13}\text{C}$  correlations include PDS (proton-driven spin diffusion),<sup>40</sup> DARR (dipolar-assisted rotational resonance),<sup>41</sup> RAD (RF-assisted diffusion),<sup>42</sup> RFDR (radio-frequency driven recoupling),<sup>43</sup> PAR (proton assisted recoupling),<sup>44</sup> 2Q-HORROR (double-quantum homonuclear rotary resonance),<sup>45</sup> and DREAM (dipolar recoupling enhanced by amplitude modulation),<sup>46</sup> etc. Among these homonuclear correlation techniques, the spin-diffusion-based experiments, such as PDS and DARR, have been the most widely employed, not only for resonance assignments, but

also for long-range distance determination.<sup>8,47,48</sup> However, the transfer efficiency and excitation band in PDSD/DARR experiments are usually limited, especially at MAS rates of 30 kHz and above.

In the last decade, several research groups including our laboratory have proposed a series of modified spin-diffusion-based pulse sequences specifically suitable for fast MAS frequencies, such as mixed rotational and rotary resonance (MIRROR),<sup>49</sup> phase-alternated recoupling irradiation (PARIS) and its variants,<sup>49,50</sup> and  $R_{2n}^V$ -symmetry driven spin diffusion (RDSD).<sup>51</sup> Recently, our laboratory developed another spin-diffusion-type pulse scheme, dubbed CORD (combined  $R_{2n}^V$  driven) for obtaining homonuclear correlations of spin pairs in spatial proximity, where spin diffusion is assisted by combined  $R_{2n}^V$  recoupling sequences in the mixing period, as shown in Figure 2.2.<sup>52</sup> CORD recoupling gives rise to broadband magnetization transfer across the spectral width, resulting in uniformly distributed peaks under both moderate and fast MAS (greater than 40 kHz) conditions. In addition, it allows for the detection of long-range distance correlations, due to its reduced sensitivity to dipolar truncation. Even at moderate MAS frequencies (10-30 kHz), CORD has proven to be advantageous to other methods as it enables detection of aromatic correlations, which are not available from other spin-diffusion-based experiments.<sup>12,53,54</sup>

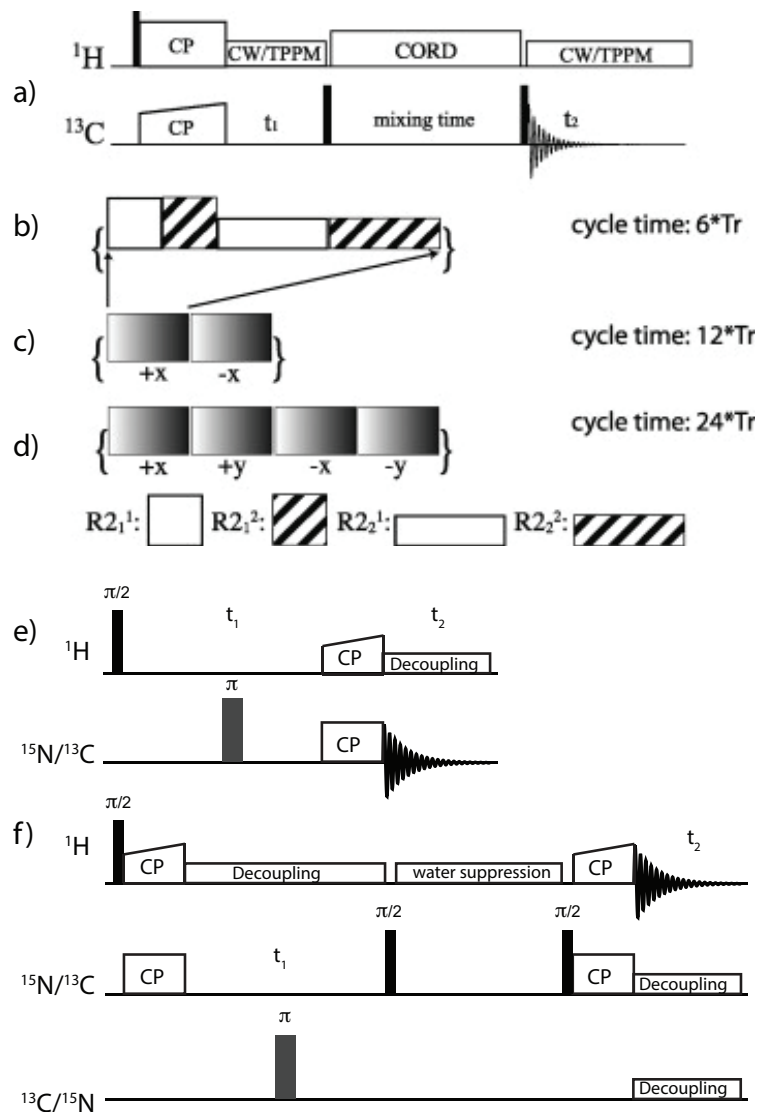


Figure 2.2: (a) The general pulse diagram for 2D  $^{13}\text{C}$ - $^{13}\text{C}$  Combined  $\text{R}_{2n}^{\text{V}}$  Driven (CORD) correlation experiments. A series of composite RF pulses comprised of  $\text{R}_{2n}^{\text{V}}$  blocks are applied on the proton channel during the CORD mixing time. The RF pulse sequences correspond to: (b) Basic CORD building block spanning  $6\text{Tr}$  (rotor period); (c) CORD<sub>xix</sub> spanning  $12\text{Tr}$ ; (d) CORD<sub>xy4</sub> spanning  $24\text{Tr}$ . Rotor-synchronized  $\text{R}_{2n}^{\text{V}}$ -type symmetry sequences as the building blocks:  $\text{R}_{2_1^1}$  ( $\nu^1_{\text{H}} = \nu_r$ ),  $\text{R}_{2_1^2}$  ( $\nu^1_{\text{H}} = \nu_r$ ),  $\text{R}_{2_2^2}$  ( $\nu^1_{\text{H}} = \nu_r/2$ ). The figure was originally published in reference<sup>52</sup>. Permission for reuse in this dissertation is granted by Elsevier, copyright 2013. (e) Pulse sequence for HETCOR with heteronuclear detection (e), and proton detection (f). Original figure courtesy of Dr. Xingyu Lu in Prof. Tatyana Polenova's group.

Heteronuclear correlations established through dipolar coupling are fundamental to MAS NMR studies of proteins. The combination of cross polarization (CP) and MAS has become the standard technique for obtaining solid state NMR spectra of low-gamma and/or dilute spins through heteronuclear polarization transfer.<sup>55</sup> The CP-based heteronuclear correlation (CP-HETCOR) experiment is commonly applied to correlate  $^1\text{H}$  with  $^{15}\text{N}/^{13}\text{C}$  through space in proteins. RF irradiation applied on both spins must meet the Hartmann-Hahn condition for efficient magnetization transfer,<sup>56</sup> and this will be described in more detail later. In the heteronuclear-detected CP-HETCOR experiment (Figure 2.2e), the chemical shift first evolves in the  $^1\text{H}$  dimension and the signal is detected on  $^{15}\text{N}/^{13}\text{C}$  spins. The proton-detected CP-HETCOR includes two CP transfer steps (Figure 2.2f), the chemical shift dimension of  $^{15}\text{N}/^{13}\text{C}$  evolves after the first CP step, and the magnetization is transferred to  $^1\text{H}$  for detection. The spectra in CP-HETCOR experiments are very sensitive to the sample homogeneity and quality. The dispersion of  $^1\text{H}$  and  $^{13}\text{C}/^{15}\text{N}$  chemical shifts also reflects the sample state (structured or unfolded or aggregated). Therefore,  $^1\text{H}$ - $^{15}\text{N}/^{13}\text{C}$  HETCOR spectra can be used to evaluate sample.

The dipolar-based heteronuclear correlation experiments (NCA, NCO, NCACX, and NCOCX) are used for protein sequential assignments in MAS NMR spectroscopy. Correlations including amide nitrogens are useful for establishing interresidue connectivities, as amide nitrogen(i) is connected to  $\text{C}^\alpha(\text{i})$  of the same residue and  $\text{C}'(\text{i}-1)$  belonging to the previous residue. The one bond  $\text{N}-\text{C}^\alpha$  or  $\text{N}-\text{C}'$  magnetization transfer is selectively performed by  $^{15}\text{N}$ - $^{13}\text{C}$  SPECIFIC CP experiments (spectrally induced filtering in combination with cross polarization).<sup>57</sup>  $^{15}\text{N}$ - $^{13}\text{C}$  multiple-bond contacts in NCACX and NCOCX are obtained by a homonuclear  $^{13}\text{C}$ -

$^{13}\text{C}$  spin-diffusion period (DARR or PDS) following the SPECIFIC-CP step. The polarization-transfer schemes for heteronuclear correlation experiments (NCA, NCO, NCACX, NCOCX, and CONCACX) are shown in Figure 2.3.

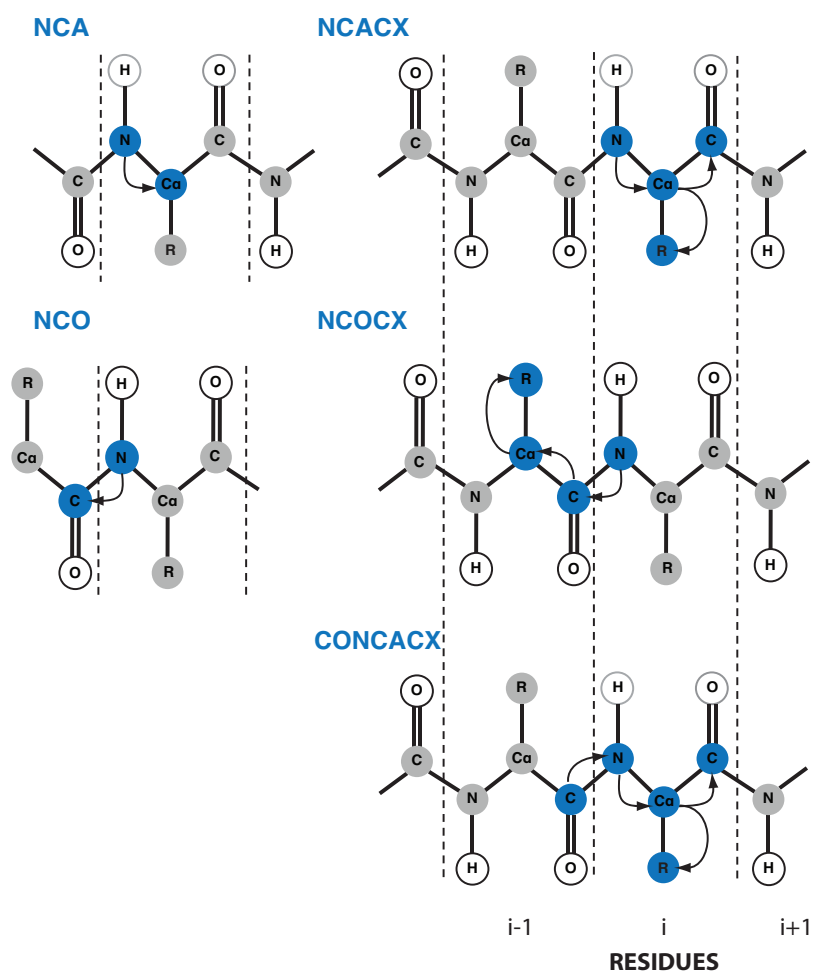


Figure 2.3: The magnetization transfer pathways in heteronuclear correlation experiments: NCA, NCO, NCACX, NCOCX, and CONCACX. Original figure courtesy of Ryan Russell in Prof. Tatyana Polenova's research group.

The two-dimensional NCA experiment can be used to evaluate the nitrogen/alpha carbon linewidth and sample quality before proceeding with higher-dimensional studies. The NCACX experiment establishes correlation between CA(i) and CX(i) and their respective backbone N(i), and the interresidue connectivity leading to sequential assignment can be obtained from NCOCX experiments as the same N(i) is correlated to CO(i-1) and CX(i-1) from the previous residue. Two-dimensional heteronuclear correlation NCACX and NCOCX experiments are often sufficient for the resonance assignment of backbone and sidechain signals of small proteins of approximate 60 residues.<sup>58</sup> Site-specific resonance assignments of several proteins with molecular weights ranging from 8 to 26 kDa were obtained using 3D versions of the NCACX and NCOCX experiments in combination with homonuclear correlation experiments in our laboratory.<sup>53,59-61</sup> The CONCACX experiment provides quasi-through-space transfer between two adjacent residues CO(i-1)-N(i)-CA(i)-CX(i). The N(i) or CA(i) evolution period can be eliminated to obtain 3D versions of such experiments. The 4D version of CONCACX further removes signal degeneracies, and is suitable for resonance assignment of large proteins.

### **2.2.2 Through-Bond Correlation Spectra**

In addition to through-space (dipolar coupling driven) correlation spectroscopy, through-bond, scalar coupling-driven correlation spectroscopy is another tool for structural investigations in solid-state NMR. Both homo- and heteronuclear through-bond correlation experiments are commonly utilized in solution NMR spectroscopy for establishing inter- and intra-residue correlations,<sup>62</sup> including COSY (correlation spectroscopy), TOCSY (total correlation spectroscopy), HSQC (heteronuclear single quantum correlation), and a suite of HNC0, HN(CA)CO, HNCA, HNCACB and

CBCA(CO)NH triple-resonance experiments. In solid-state MAS NMR experiments, correlation experiments based on J coupling transfers were initially considered impractical due to the relatively small magnitude of the J coupling compared to the strong dipolar interactions.<sup>48</sup> However, the performance of J coupling-based experiments has dramatically improved with the development of more effective decoupling strategies and increased MAS frequencies that lead to longer sample coherence times.<sup>63</sup> Through-bond correlation experiments are complementary to through-space correlation experiments in solid-state NMR spectroscopy and can provide unique structural information. Through-bond experiments are less sensitive to protein dynamics relative to dipolar-based experiments and, therefore, can be used for the detection of mobile residues.<sup>64</sup> Several solid-state J coupling-based sequences adapted from solution NMR experiments include INADEQUATE (incredible natural abundance double quantum transfer experiment),<sup>65,66</sup> COSY,<sup>67,68</sup> and TOBSY (total through-bond correlation spectroscopy)<sup>69</sup> experiments which are commonly applied for establishing homonuclear correlations.

For uniformly isotopically enriched protein samples, the presence of  $^{13}\text{C}$ - $^{13}\text{C}$  homonuclear J couplings often introduces line broadening and decreases spectral resolution. In the CTUC-COSY (constant time, uniform sign correlation spectroscopy) experiment, the magnetization transfer and the indirect evolution are combined into a single constant time period, thus the J-coupling broadening is greatly attenuated, leading to increased resolution without the loss of sensitivity for  $^{13}\text{C}$ - $^{13}\text{C}$  correlation spectra.<sup>70</sup> The CTUC-COSY experiment can be used to resolve congested peak regions for large protein and protein assemblies. By irradiating aliphatic residues with selective, shaped  $\pi$  pulses, aliphatic correlations can be established. Aliphatic-

carbonyl CTUC-COSY correlation spectra can be selectively acquired by applying hard  $\pi$  pulses instead.<sup>70</sup>

The refocused INEPT experiment (insensitive nuclei enhanced polarization transfer) adapted from solution NMR is commonly used for heteronuclear through-bond coherence transfer in rigid organic solids and proteins.<sup>68,71,72</sup>  $^1\text{H}$ - $^{13}\text{C}$  correlation experiments based on INEPT transfer demonstrate excellent selectivity for one-bond transfers, in addition to much more even intensity distribution compared to cross polarization, as shown for U- $^{13}\text{C}$ -isoleucine in Figure 2.4.<sup>71</sup> By utilizing INEPT and CTUC-COSY sequence units as building blocks, a suite of three-dimensional J coupling-based NCACO, NCOCA, and CANCO heteronuclear correlation experiments have been developed.<sup>68</sup> Strong sequential correlations are established even for heteronuclear correlations of  $^{15}\text{N}$ - $^{13}\text{CA}/^{13}\text{CO}$  with small J coupling constants. The spectral sensitivity of these experiments is comparable to their dipolar-driven counterparts.<sup>68</sup>

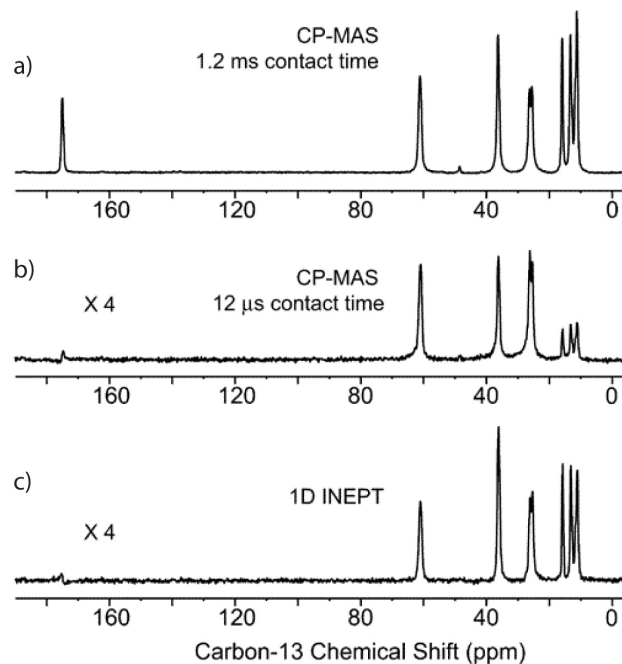


Figure 2.4: Comparison of 1D  $^{13}\text{C}$  CP-MAS spectra in (a) and (b) with INEPT spectrum in (c) of U- $^{13}\text{C}$ -isoleucine. In (a), CP-MAS with long mixing time (1.2 ms) yields the best sensitivity which also invokes long-range magnetization transfer. One bond transfer is obtained in CP-MAS with short contact time (12  $\mu\text{s}$ ) in (b) and INEPT in (c), evidenced by the absence of non-protonated CO signal. INEPT shows more uniform one-bond transfer than CP-MAS. Reprinted with permission from reference<sup>71</sup>. Copyright (2005) American Chemical Society.

### 2.2.3 Proton-Detected and Fast MAS NMR

Sensitivity enhancement in solid state NMR spectroscopy has been a vibrant field of research since the inception of the field, and especially with an increasing interest in the characterization of biomacromolecules and their assemblies. Due to the high gyromagnetic ratio ( $\gamma$ ) and nearly 100% natural abundance of  $^1\text{H}$ , the proton is the nucleus of choice for signal detection compared to heteronuclear detection of low  $\gamma$  nuclei ( $^{13}\text{C}$  and  $^{15}\text{N}$ ) in protein systems.<sup>73</sup> NMR sensitivity is proportional to  $\gamma^2$ , and therefore is greatly enhanced with proton-detection. However, direct detection of

protons in highly protonated biological samples is impractical under MAS frequencies slower than 60 kHz, due to the presence of strong  $^1\text{H}$ - $^1\text{H}$  dipolar couplings, which lead to severe  $^1\text{H}$  line broadening.<sup>74</sup> Over the past decade, advancements in the design of probes capable of delivering fast MAS frequencies (40-110 kHz, the regime in which  $^1\text{H}$  dipolar interactions start to be effectively attenuated by MAS) have greatly reduced the achievable  $^1\text{H}$  linewidth, which is inversely proportional to the spinning frequency as shown in Figure 2.5.<sup>29</sup> In combination with suitable proton dilution strategies during sample preparation, the  $^1\text{H}$ - $^1\text{H}$  homonuclear dipolar coupling can be averaged out efficiently in experiments carried out under MAS at frequencies higher than 40 kHz, which allows for proton detection with outstanding resolution and results in three-to-five-fold sensitivity enhancement compared to  $^{13}\text{C}$ -detected experiments. Thus far,  $^1\text{H}$ -detected studies that enable resonance assignment and structural determination have been carried out in several laboratories including ours, either in perdeuterated or fully protonated proteins.

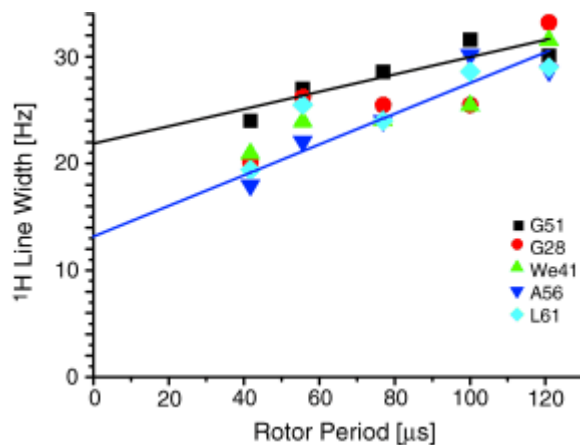


Figure 2.5: Linear correlation of proton linewidth with rotor period (the inverse of MAS frequency) for selected residues in a model protein SH3 (deuterated with 10% back-exchanged amide proton). Rotor period is the inverse of the MAS frequency in kHz. The figure was originally published in reference<sup>29</sup>. Permission for reuse in this dissertation is granted by John Wiley and Sons, copyright 2006.

High-resolution proton-detected experiments at moderate MAS (10-25 kHz) frequencies have been successfully presented on fully deuterated proteins with 100% or partial back-exchange of amide protons due to the high level of proton dilution.<sup>29,73,75</sup> The <sup>1</sup>H resolution in experiments at moderate spinning is remarkably improved for a deuterated protein with 10% back-exchange of amide protons, even without application of homonuclear decoupling.<sup>29</sup> Long-lived coherences in protein samples prepared with such extensive degrees of deuteration allow successful implementation of scalar coupling-based experiments, and the resultant resolution is comparable to that of solution experiments.<sup>75</sup> At an MAS frequency of 60 kHz, proton-detected spectra with high resolution and high sensitivity can be achieved for deuterated proteins with fully protonated amides at high magnetic fields (23.5 GHz) and this permits fast data acquisition for resonance assignment and structure

determination.<sup>76,77</sup> With fast MAS, proton-detected studies are also feasible on fully protonated proteins, and this was first successfully demonstrated on a small model protein GB1 (MW of 6 kDa) in an experiment carried out while spinning the sample at 40 kHz.<sup>74</sup> In an experiment carried out using an MAS frequency of 60 kHz, high-resolution proton-detected spectra of a fully protonated protein of ~20 kDa were acquired, permitting backbone assignments.<sup>78</sup>

### **2.3 Studies of Dynamics of Protein Assemblies by MAS NMR Spectroscopy**

Proteins are by no means static while fulfilling their biological functions, and structural components often undergo simultaneous dynamic processes, including backbone motions, subdomain reorientations, sidechain rotations, etc. These various motions have been correlated to multiple biological processes, such as protein folding, protein-protein and ligand-protein interactions, molecular recognition, allosteric regulation, and catalysis.<sup>79,80</sup> Understanding such dynamic behaviors in conjunction with static structure gives a comprehensive view of biological functions.

MAS NMR spectroscopy is a unique technique for probing protein dynamics, due to the broad range of timescales it can access, ranging from picoseconds to seconds and even days.<sup>79-81</sup> Multidimensional MAS NMR experiments provide insights into both the large-scale and site-specific dynamics of a protein molecule. Another advantage of MAS NMR is that it can capture protein dynamics over a wide range of temperatures from physiological to cryogenic conditions. Various MAS NMR methodologies allow the detection of protein dynamics over a continuous frequency range shown in Figure 2.6. Anisotropic interactions, including chemical shift anisotropy, electric field gradient, and heteronuclear H-X dipolar coupling are sensitive reporters of protein dynamics on broad timescales ranging from to pico- to

microseconds.<sup>80</sup> Several commonly applied measurements include  $^{13}\text{C}$  and  $^{15}\text{N}$   $T_1$  relaxation time measurements, which probe protein dynamics on the pico- to microsecond timescales.<sup>82-85</sup> Heteronuclear HX dipolar coupling is a sensitive probe of dynamics on timescales of nano- to microseconds.<sup>12,86,87</sup> The spin-lattice relaxation time constant in the rotating frame  $T_{1\rho}$  is a common tool for measuring molecular motions on the micro- to millisecond timescales.<sup>85,88</sup> To detect slower molecular dynamics over milliseconds to seconds, exchange experiments such as CODEX (centerband-only detection of exchange) can be applied.<sup>89-91</sup> In our studies, we specifically focus on the use of heteronuclear dipolar couplings to probe protein dynamics.

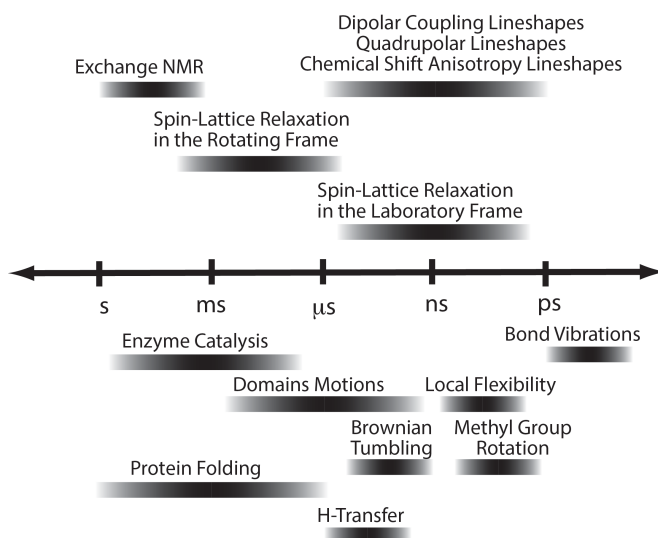


Figure 2.6: Solid state NMR methods for probing dynamic processes associated with proteins over a full and continuous range. The figure is adapted from reference<sup>80</sup>. Permission for reuse in this dissertation is granted by Elsevier, copyright 2005.

### 2.3.1 Studies of Dynamics on the Nanosecond to Microsecond Timescale by Dipolar Coupling Measurement

The dipolar coupling interaction of two nuclei depends on the internuclear distance and their relative motility. Typical dipolar coupling constants of  $^1\text{H}$ - $^{13}\text{C}$  and  $^1\text{H}$ - $^{15}\text{N}$  in the absence of motion are 22.7 kHz and 11.3 kHz, respectively.<sup>92,93</sup> The presence of motion on the timescale of the dipolar coupling results in dynamically reduced dipolar coupling strength, normally quantified by an order parameter  $S_D$  (which is the ratio of measured dipolar coupling to that in the limit of a static system (the so-called “rigid limit”)), which can be equal to or less than 1, depending on whether the corresponding bond vector is rigid or dynamic.<sup>12,92-94</sup> The accurate measurement of dipolar couplings is essential for the characterization of protein motions on nanosecond to microsecond timescales, the time range up to the inverse of the dipolar coupling constant. MAS averages anisotropic interactions including heteronuclear dipolar coupling, resulting in resolution enhancement with the loss of valuable dynamic information. Therefore many recoupling sequences have been developed for MAS conditions, including Lee-Goldburg cross polarization (LG-CP),<sup>95</sup> transverse-MREV (T-MREV),<sup>96</sup> and rotational-echo double resonance (REDOR)-based schemes<sup>97,98</sup>. Generally, these measurements are very sensitive to RF mismatches, or incompletely averaged heteronuclear interactions.<sup>48</sup>

RN-symmetry based recoupling sequences, originally developed by Levitt and coworkers, have been shown to reintroduce the desired anisotropic interactions, while suppressing others.<sup>99,100</sup> In our laboratory, we apply RN-symmetry based DIPSHIFT (dipolar chemical shift correlation) recoupling experiments for the measurement of  $^1\text{H}$ - $^{13}\text{C}$ / $^1\text{H}$ - $^{15}\text{N}$  dipolar couplings.<sup>86,98,101,102</sup> A train of rotor synchronized  $\text{RN}_n^y$  RF pulses is applied on the proton channel to reintroduce  $^1\text{H}$ - $^{13}\text{C}$ / $^1\text{H}$ - $^{15}\text{N}$  dipolar couplings, while

suppressing homonuclear dipolar coupling.  $N$ ,  $n$ , and  $v$  denote the symmetry numbers of the pulse sequence.  $RN_n^v$  is comprised of  $N/2$  pairs of  $\pi$  pulses with alternating phase shifts of  $\pi v/N$  and  $-\pi v/N$  radians, and the pulse length is  $n\tau_R/N$  with RF field strength of  $N\tau_R/2n$ . To obtain site-specific heteronuclear dipolar coupling information, a 3D version of  $RN_n^v$ -based DIPSHIFT is established by the incorporation of an NCO or NCA SPECIFIC CP sequence to obtain chemical shift correlations. The 2D and 3D  $RN_n^v$ -based DIPSHIFT sequences are shown in Figure 2.7.  $RN_n^v$  DIPSHIFT experiments are suited for the heteronuclear dipolar recoupling under fast MAS and have been successfully applied to fully protonated samples.<sup>12,86</sup> For example, the dynamic behavior of microtubule-associated protein CAP-Gly domain of dynactin captured by  $^1\text{H}$ - $^{13}\text{C}$  dipolar couplings shows a strong secondary structural dependence, and the corresponding residue-specific order parameters are mapped onto the tertiary structure, shown in Figure 2.7.

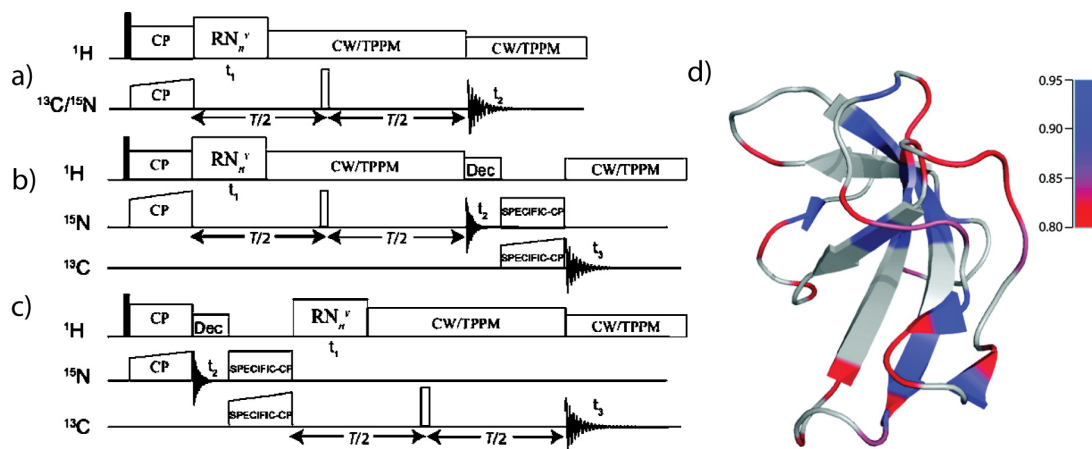


Figure 2.7: (a) Two-dimensional  $RN_n^V$  DIPSHIFT sequences for  $^1\text{H}$ - $^{13}\text{C}/^{15}\text{N}$  heteronuclear dipolar recoupling. An RF irradiation comprised of  $RN_n^V$  symmetry pulses is applied on proton spins during the  $t_1$  evolution to reintroduce  $^1\text{H}$ - $^{15}\text{N}$  and  $^1\text{H}$ - $^{13}\text{C}$  dipolar coupling respectively. (b, c) Three-dimensional  $RN_n^V$  DIPSHIFT sequences for residue-specific  $^1\text{H}$ - $^{15}\text{N}$  and  $^1\text{H}$ - $^{13}\text{C}$  dipolar coupling measurements. (d) Backbone dynamics of CAP-Gly domain of dynactin captured by residue-specific  $^1\text{H}$ - $^{13}\text{C}$  dipolar order parameter, measured with the  $R16_3^2$  sequence. Reprinted with permission from reference<sup>86</sup>. Copyright (2011) American Chemical Society.

### 2.3.2 Study of Dynamics on the Nanosecond to Microsecond Timescale by Cross Polarization in MAS NMR

Cross polarization (CP)<sup>103</sup> describes the magnetization transfer from abundant spins I (typically  $^1\text{H}$ ) to dilute spins X (typically  $^{13}\text{C}$  or  $^{15}\text{N}$  in proteins) in close proximity through heteronuclear dipolar interactions, as discussed earlier in this chapter. CP is an essential technique in MAS NMR spectroscopy for the signal detection of signals generated by the nuclei of low gyromagnetic ratios. The presence of strong  $^1\text{H}$ - $^1\text{H}$  dipolar interactions stimulates relaxation, rendering the spin-lattice relaxation time  $T_1$  of  $^1\text{H}$  shorter than that of dilute spins, thus the application of CP is advantageous for reducing experimental recycle delay. One-dimensional  $^1\text{H}$ - $^{13}\text{C}$  and  $^1\text{H}$ - $^{15}\text{N}$  spectra are generally recorded to evaluate the sample resolution and sensitivity

before proceeding with 2D and 3D experiments. Moreover, CP is the basis for establishing multi- dimensional correlation experiments.

The RF irradiation of proton ( $^1\text{H}$ ) and heteronuclei (X) in CP experiments on static sample must be carefully set to meet the Hartmann-Hahn matching condition.<sup>56</sup>

$$\gamma_H B_1(H) = \gamma_X B_1(X) \quad [2.1]$$

$B_1$  is the spin-lock field applied on the proton and X channels. Their nutation frequencies ( $\omega_1 = \gamma_H B_1$ ) are set to equal to achieve the Hartmann-Hahn condition under static conditions.

For samples spinning under MAS conditions, the Hartmann-Hahn condition depends on rotation frequency. RF irradiation on respective nuclei has to fulfill the following equation:

$$\gamma_H B_1(H) = \gamma_H B_1(X) \pm n\omega_r \quad [2.2]$$

where  $n = 1, 2$ . The difference in RF irradiation power should equal an integer multiple of the spinning frequency.

Theoretically, utilizing CP can give rise to sensitivity enhancement of up to  $\gamma_H/\gamma_X$ . However, the experimental signal intensity depends on proton relaxation time  $T_{1p}$  and the length of the spin lock (CP contact time). During the contact time, typically in the range of 0.02 ~ 3 ms, CP is mediated by the dipolar couplings between  $^1\text{H}$  and X, therefore the processes that disrupt dipolar interactions also interfere with CP transfer, for instance molecular motions. The inherent molecular motions partially average the dipolar coupling and reduce the rate of the CP transfer; thus in dynamic systems longer CP mixing times are generally necessary for maximum signal intensity. A variety of applications of CP for monitoring the dynamic behavior of polymers and proteins exist.<sup>94,104,105</sup>

The CP magnetization as a function of variable contact times can be used to determine the time constants  $T_{CH}$  and  $T_{1p}$ . The magnetization build-up is governed by the CP time constant  $T_{CH}$ , and the decay of magnetization is determined by  $^1H$   $T_{1p}$ . The magnetization is described by the equation<sup>106</sup>:

$$M(t) = M_0 [e^{-t/T_{HH}} - e^{-t/T_{CH}}] \left\{ \frac{T_{1p}}{T_{1p} - T_{CH}} \right\} \quad [2.3]$$

in which  $M_0$  represents the inherent total magnetization in the absence of spin-spin or spin-lattice relaxation effects. The time constant  $T_{HH}$  describes the relaxation of the spin-locked  $^1H$  nuclei in the rotating frame and is sensitive to molecular motion on the millisecond timescale.  $T_{CH}$  is a time constant of the magnetization transfer from the abundant  $^1H$  spins to the dilute spins. Fast motions interfere with the magnetization transfer and the corresponding  $T_{CH}$  is long, whereas in the presence of slow motions, the magnetization transfer is more efficient, therefore resulting in a shorter  $T_{CH}$ .

## 2.4 Summary

With the development of MAS NMR methodologies, MAS NMR can be used for the studies of challenging biological systems to answer complex biological questions. Such improvements include sample preparation protocols, probes capable of fast MAS, and new pulse sequences. In this chapter, the major MAS methods applied in the studies of MAPs assembled on MTs have been reviewed. Through-bond and through-space correlation experiments have been combined for the conformational study of the MAP TauF4 assembled with MT in chapter 3. In addition, dynamics of TauF4 on multiple timescales have been characterized to understand its interactions with MTs. Both heteronuclear-detected and proton-

detected experiments for homo- and heteronuclear correlations have been applied for the structural studies of the MAP kinesin assembled with MT in chapter 4.

## REFERENCES

- (1) Mccammon, J. A.; Gelin, B. R.; Karplus, M. *Nature* **1977**, *267*, 585.
- (2) Dyson, H. J.; Wright, P. E. *Chem. Rev.* **2004**, *104*, 3607.
- (3) Goldbourn, A.; Gross, B. J.; Day, L. A.; McDermott, A. E. *J. Am. Chem. Soc.* **2007**, *129*, 2338.
- (4) Lorieau, J. L.; Day, L. A.; McDermott, A. E. *Proc. Natl. Acad. Sci. USA* **2008**, *105*, 10366.
- (5) Abramov, G.; Morag, O.; Goldbourn, A. *J. Phys. Chem. B* **2011**, *115*, 9671.
- (6) Goldbourn, A.; Day, L. A.; McDermott, A. E. *J. Biol. Chem.* **2010**, *285*, 37051.
- (7) Purusottam, R. N.; Rai, R. K.; Sinha, N. *J. Phys. Chem. B* **2013**, *117*, 2837.
- (8) Sergeyev, I. V.; Bahri, S.; Day, L. A.; McDermott, A. E. *J. Chem. Phys.* **2014**, *141*, 22D533.
- (9) Han, Y.; Ahn, J.; Concel, J.; Byeon, I. J.; Gronenborn, A. M.; Yang, J.; Polenova, T. *J. Am. Chem. Soc.* **2010**, *132*, 1976.
- (10) Byeon, I. J.; Hou, G.; Han, Y.; Suiter, C. L.; Ahn, J.; Jung, J.; Byeon, C. H.; Gronenborn, A. M.; Polenova, T. *J. Am. Chem. Soc.* **2012**, *134*, 6455.
- (11) Chen, B.; Tycko, R. *Protein Sci.* **2010**, *19*, 716.
- (12) Lu, M.; Hou, G.; Zhang, H. *Proc. Natl. Acad. Sci. USA* **2015**, *112*, 14617.
- (13) Loquet, A.; Habenstein, B.; Lange, A. *Acc. Chem. Res.* **2013**, *46*, 2070.
- (14) Demers, J. P.; Habenstein, B.; Loquet, A.; Kumar Vasa, S.; Giller, K.; Becker, S.; Baker, D.; Lange, A.; Sgourakis, N. G. *Nat. Commun.* **2014**, *5*, 4976.
- (15) Meier, B. H.; Bockmann, A. *Curr. Opin. Struct. Biol.* **2015**, *30*, 43.
- (16) Tang, M.; Comellas, G.; Rienstra, C. M. *Acc. Chem. Res.* **2013**, *46*, 2080.

- (17) Brown, L. S.; Ladizhansky, V. *Protein Sci.* **2015**, *24*, 1333.
- (18) Naito, A.; Kawamura, I.; Javkhlantugs, N. *Annu. Rep. NMR Spectro.* **2015**, *86*, 333.
- (19) Hong, M. *J. Magn. Reson.* **1999**, *139*, 389.
- (20) LeMaster, D. M.; Kushlan, D. M. *J. Am. Chem. Soc.* **1996**, *118*, 9255.
- (21) Lundstrom, P.; Teilum, K.; Carstensen, T.; Bezsonova, I.; Wiesner, S.; Hansen, D. F.; Religa, T. L.; Akke, M.; Kay, L. E. *J. Biomol. NMR* **2007**, *38*, 199.
- (22) Castellani, F.; van Rossum, B.; Diehl, A.; Schubert, M.; Rehbein, K.; Oschkinat, H. *Nature* **2002**, *420*, 98.
- (23) Higman, V. A.; Flinders, J.; Hiller, M.; Jehle, S.; Markovic, S.; Fiedler, S.; van Rossum, B. J.; Oschkinat, H. *J. Biomol. NMR* **2009**, *44*, 245.
- (24) Kinsey, R. A.; Kintanar, A.; Oldfield, E. *J. Biol. Chem.* **1981**, *256*, 9028.
- (25) Lee, A. L.; Urbauer, J. L.; Wand, A. J. *J. Biomol. NMR* **1997**, *9*, 437.
- (26) Guo, C. Y.; Geng, C.; Tugarinov, V. *J. Biomol. NMR* **2009**, *44*, 167.
- (27) Goto, N. K.; Gardner, K. H.; Mueller, G. A.; Willis, R. C.; Kay, L. E. *J. Biomol. NMR* **1999**, *13*, 369.
- (28) Lichtenecker, R.; Ludwiczek, M. L.; Schmid, W.; Konrat, R. *J. Am. Chem. Soc.* **2004**, *126*, 5348.
- (29) Chevelkov, V.; Rehbein, K.; Diehl, A.; Reif, B. *Angew. Chem. Int. Ed.* **2006**, *45*, 3878.
- (30) Asami, S.; Reif, B. *Acc. Chem. Res.* **2013**, *46*, 2089.
- (31) Reif, B. *J. Magn. Reson.* **2012**, *216*, 1.
- (32) Andreas, L. B.; Le Marchand, T.; Jaudzems, K.; Pintacuda, G. *J. Magn. Reson.* **2015**, *253*, 36.
- (33) Tugarinov, V.; Kanelis, V.; Kay, L. E. *Nat. Protoc.* **2006**, *1*, 749.
- (34) Nieuwkoop, A. J.; Franks, W. T.; Rehbein, K.; Diehl, A.; Akbey, U.; Engelke, F.; Emsley, L.; Pintacuda, G.; Oschkinat, H. *J. Biomol. NMR* **2015**, *61*, 161.

- (35) Akbey, U.; Lange, S.; Franks, W. T.; Linser, R.; Rehbein, K.; Diehl, A.; van Rossum, B. J.; Reif, B.; Oschkinat, H. *J. Biomol. NMR* **2010**, *46*, 67.
- (36) Chevelkov, V.; Faelber, K.; Diehl, A.; Heinemann, U.; Oschkinat, H.; Reif, B. *J. Biomol. NMR* **2005**, *31*, 295.
- (37) Wishart, D. S.; Sykes, B. D. *J. Biomol. NMR* **1994**, *4*, 171.
- (38) Williamson, M. P. *Biopolymers* **1990**, *29*, 1428.
- (39) Fritzsching, K. J.; Yang, Y.; Schmidt-Rohr, K.; Hong, M. *J. Biomol. NMR* **2013**, *56*, 155.
- (40) Szeverenyi, N. M.; Sullivan, M. J.; Maciel, G. E. *J. Magn. Reson.* **1982**, *47*, 462.
- (41) Takegoshi, K.; Nakamura, S.; Terao, T. *Chem. Phys. Lett.* **2001**, *344*, 631.
- (42) Morcombe, C. R.; Gaponenko, V.; Byrd, R. A.; Zilm, K. W. *J. Am. Chem. Soc.* **2004**, *126*, 7196.
- (43) Bennett, A. E.; Rienstra, C. M.; Griffiths, J. M.; Zhen, W. G.; Lansbury, P. T.; Griffin, R. G. *J. Chem. Phys.* **1998**, *108*, 9463.
- (44) De Paepe, G.; Lewandowski, J. R.; Loquet, A.; Bockmann, A.; Griffin, R. G. *J. Chem. Phys.* **2008**, *129*.
- (45) Nielsen, N. C.; Bildsoe, H.; Jakobsen, H. J.; Levitt, M. H. *J. Chem. Phys.* **1994**, *101*, 1805.
- (46) Verel, R.; Ernst, M.; Meier, B. H. *J. Magn. Reson.* **2001**, *150*, 81.
- (47) Brown, S. P. *Macromol. Rapid Comm.* **2009**, *30*, 688.
- (48) Hou, G. J.; Suiter, C. L.; Yan, S.; Zhang, H. L.; Polenova, T. *Annu. Rep. NMR Spectro.* **2013**, *80*, 293.
- (49) Scholz, I.; Huber, M.; Manolikas, T.; Meier, B. H.; Ernst, M. *Chem. Phys. Lett.* **2008**, *460*, 278.
- (50) Weingarth, M.; Demco, D. E.; Bodenhausen, G.; Tekely, P. *Chem. Phys. Lett.* **2009**, *469*, 342.
- (51) Hou, G. J.; Yan, S.; Sun, S. J. *J. Am. Chem. Soc.* **2011**, *133*, 3943.

- (52) Hou, G. J.; Yan, S.; Trebosc, J.; Amoureux, J. P.; Polenova, T. *J. Magn. Reson.* **2013**, *232*, 18.
- (53) Yan, S.; Guo, C. M.; Hou, G. J.; Zhang, H. L.; Lu, X. Y.; Williams, J. C.; Polenova, T. *Proc. Natl. Acad. Sci. USA* **2015**, *112*, 14611.
- (54) Morag, O.; Sgourakis, N. G.; Baker, D.; Goldbourt, A. *Proc. Natl. Acad. Sci. USA* **2015**, *112*, 971.
- (55) Yannoni, C. S. *Acc. Chem. Res.* **1982**, *15*, 201.
- (56) Hartmann, S. R.; Hahn, E. L. *Phys. Rev.* **1962**, *128*, 2042.
- (57) Baldus, M.; Petkova, A. T.; Herzfeld, J.; Griffin, R. G. *Mol. Phys.* **1998**, *95*, 1197.
- (58) Pauli, J.; Baldus, M.; van Rossum, B.; de Groot, H.; Oschkinat, H. *Chembiochem* **2001**, *2*, 272.
- (59) Sun, S. J.; Butterworth, A. H.; Paramasivam, S.; Yan, S.; Lightcap, C. M.; Williams, J. C.; Polenova, T. *Can. J. Chem.* **2011**, *89*, 909.
- (60) Han, Y.; Ahn, J.; Concel, J.; Byeon, I. J. L.; Gronenborn, A. M.; Yang, J.; Polenova, T. *J. Am. Chem. Soc.* **2010**, *132*, 1976.
- (61) Sun, S. J.; Siglin, A.; Williams, J. C.; Polenova, T. *J. Am. Chem. Soc.* **2009**, *131*, 10113.
- (62) Cavanagh, J.; Fairbrother, W. J.; Palmer, A. G.; Rance, M.; Skelton, N. J. *Protein Nmr Spectroscopy: Principles and Practice, 2nd Edition* **2007**, 1.
- (63) Yan, S.; Suiter, C. L.; Hou, G. J.; Zhang, H. L.; Polenova, T. *Acc. Chem. Res.* **2013**, *46*, 2047.
- (64) Heise, H.; Hoyer, W.; Becker, S.; Andronesi, O. C.; Riedel, D.; Baldus, M. *Proc. Natl. Acad. Sci. USA* **2005**, *102*, 15871.
- (65) Carravetta, M.; Zhao, X.; Bockmann, A.; Levitt, M. H. *Chem. Phys. Lett.* **2003**, *376*, 515.
- (66) Lesage, A.; Bardet, M.; Emsley, L. *J. Am. Chem. Soc.* **1999**, *121*, 10987.
- (67) Mueller, L. J.; Elliott, D. W.; Leskowitz, G. M.; Struppe, J.; Olsen, R. A.; Kim, K. C.; Reed, C. A. *J. Magn. Reson.* **2004**, *168*, 327.

- (68) Chen, L. L.; Kaiser, J. M.; Lai, J. F.; Polenova, T.; Yang, J.; Rienstra, C. M.; Mueller, L. J. *Magn. Reson. Chem.* **2007**, *45*, S84.
- (69) Hardy, E. H.; Verel, R.; Meier, B. H. *J. Magn. Reson.* **2001**, *148*, 459.
- (70) Chen, L. L.; Olsen, R. A.; Elliott, D. W.; Boettcher, J. M.; Zhou, D. H. H.; Rienstra, C. M.; Mueller, L. J. *J. Am. Chem. Soc.* **2006**, *128*, 9992.
- (71) Elena, B.; Lesage, A.; Steuernagel, S.; Bockmann, A.; Emsley, L. *J. Am. Chem. Soc.* **2005**, *127*, 17296.
- (72) Lesage, A.; Emsley, L. *J. Magn. Reson.* **2001**, *148*, 449.
- (73) Paulson, E. K.; Morcombe, C. R.; Gaponenko, V.; Dancheck, B.; Byrd, R. A.; Zilm, K. W. *J. Am. Chem. Soc.* **2003**, *125*, 15831.
- (74) Zhou, D. H.; Shah, G.; Cormos, M.; Mullen, C.; Sandoz, D.; Rienstra, C. M. *J. Am. Chem. Soc.* **2007**, *129*, 11791.
- (75) Linser, R.; Fink, U.; Reif, B. *J. Magn. Reson.* **2008**, *193*, 89.
- (76) Lewandowski, J. R.; Dumez, J. N.; Akbey, U.; Lange, S.; Emsley, L.; Oschkinat, H. *J. Phys. Chem. Lett.* **2011**, *2*, 2205.
- (77) Knight, M. J.; Webber, A. L.; Pell, A. J. *Angew. Chem. Int. Ed.* **2011**, *50*, 11697.
- (78) Marchetti, A.; Jehle, S.; Felletti, M. *Angew. Chem. Int. Ed.* **2012**, *51*, 10756.
- (79) Krushelnitsky, A.; Reichert, D.; Saalwachter, K. *Acc. Chem. Res.* **2013**, *46*, 2028.
- (80) Krushelnitsky, A.; Reichert, D. *Prog. Nucl. Mag. Res. Sp.* **2005**, *47*, 1.
- (81) Watt, E. D.; Rienstra, C. M. *Anal. Chem.* **2014**, *86*, 58.
- (82) Lewandowski, J. R.; Sein, J.; Sass, H. J.; Grzesiek, S.; Blackledge, M.; Emsley, L. *J. Am. Chem. Soc.* **2010**, *132*, 8252.
- (83) Giraud, N.; Blackledge, M.; Goldman, M.; Bockmann, A.; Lesage, A.; Penin, F.; Emsley, L. *J. Am. Chem. Soc.* **2005**, *127*, 18190.
- (84) Chevelkov, V.; Diehl, A.; Reif, B. *J. Chem. Phys.* **2008**, *128*, 052316.
- (85) Lewandowski, J. R. *Acc. Chem. Res.* **2013**, *46*, 2018.

- (86) Hou, G.; Byeon, I. J.; Ahn, J.; Gronenborn, A. M.; Polenova, T. *J. Am. Chem. Soc.* **2011**, *133*, 18646.
- (87) Yang, J.; Tasayco, M. L.; Polenova, T. *J. Am. Chem. Soc.* **2009**, *131*, 13690.
- (88) Lewandowski, J. R.; Sass, H. J.; Grzesiek, S.; Blackledge, M.; Emsley, L. *J. Am. Chem. Soc.* **2011**, *133*, 16762.
- (89) Deazevedo, E. R.; Hu, W. G.; Bonagamba, T. J.; Schmidt-Rohr, K. *J. Am. Chem. Soc.* **1999**, *121*, 8411.
- (90) Krushelnitsky, A. G.; Hempel, G.; Reichert, D. *Bba-Proteins Proteom.* **2003**, *1650*, 117.
- (91) Reichert, D.; Pascui, O.; deAzevedo, E. R.; Bonagamba, T. J.; Arnold, K.; Huster, D. *Magn. Reson. Chem.* **2004**, *42*, 276.
- (92) Yao, X. L.; Hong, M. *J. Biomol. NMR* **2001**, *20*, 263.
- (93) Huster, D.; Schiller, J.; Arnold, K. *Magn. Reson. Med.* **2002**, *48*, 624.
- (94) Yan, S.; Zhang, H. L.; Hou, G. J.; Ahmed, S.; Williams, J. C.; Polenova, T. *J. Biol. Chem.* **2015**, *290*, 1607.
- (95) Hong, M.; Yao, X. L.; Jakes, K.; Huster, D. *J. Phys. Chem. B* **2002**, *106*, 7355.
- (96) Hohwy, M.; Jaroniec, C. P.; Reif, B.; Rienstra, C. M.; Griffin, R. G. *J. Am. Chem. Soc.* **2000**, *122*, 3218.
- (97) Gullion, T.; Schaefer, J. *J. Magn. Reson.* **1989**, *81*, 196.
- (98) Schanda, P.; Meier, B. H.; Ernst, M. *J. Magn. Reson.* **2011**, *210*, 246.
- (99) Kristiansen, P. E.; Carravetta, M.; van Beek, J. D.; Lai, W. C.; Levitt, M. H. *J. Chem. Phys.* **2006**, *124*, 234510.
- (100) Levitt, M. H. *J. Chem. Phys.* **2008**, *128*.
- (101) Hou, G. J.; Lu, X. Y.; Vega, A. J.; Polenova, T. *J. Chem. Phys.* **2014**, *141*.
- (102) Lu, X. Y.; Zhang, H. L.; Lu, M. M.; Vega, A. J.; Hou, G. J.; Polenova, T. *PCCP* **2016**, *18*, 4035.
- (103) Pines, A.; Shattuck, T. W. *J. Chem. Phys.* **1974**, *61*, 1255.

- (104) Conte, P.; Berns, A. E. *Anal. Sci.* **2008**, *24*, 1183.
- (105) Ando, S.; Harris, R. K.; Monti, G. A.; Reinsberg, S. A. *Magn. Reson. Chem.* **1999**, *37*, 709.
- (106) Silvestri, R. L.; Koenig, J. L. *Macromolecules* **1992**, *25*, 2341.

## Chapter 3

### INVESTIGATIONS OF CONFORMATIONAL AND DYNAMICS OF TAU F4 BINDING WITH MICROTUBULES<sup>1</sup>

#### 3.1 Introduction

The microtubule-associated protein (MAP) Tau, expressed abundantly in neurons, regulates diverse and essential aspects of MTs, including their assembly, dynamics, and polarity.<sup>1</sup> Tau regulates axonal transport through its role in MT assembly, and it equally interferes with the transport of motor proteins along MTs.<sup>2</sup> The loss of Tau binding leads to microtubule instability, and the misfolded aggregated Tau is a characteristic pathological agent of Alzheimer's disease (AD).<sup>3</sup>

Tau belongs to a family of intrinsically disordered proteins (IDP) and lacks a rigid secondary and tertiary structure in solution.<sup>4</sup> Studies of Tau protein fragments have identified its different functional regions, as described in Chapter 1. Recently, a fragment of Tau, Tau[208-324] or TauF4, spanning part of the proline-rich region PRR and the first three microtubule binding regions (MTBRs), was identified as binding tightly to MTs and assembling tubulin heterodimers into microtubules efficiently.<sup>5</sup> The primary sequence is shown in Figure 3.1a.

Several models for Tau binding to microtubules have been proposed in the past.<sup>6-9</sup> More recently, the molecular mechanism of Tau's role in MT assembly and

---

<sup>1</sup> The study presented in this chapter was conducted in collaboration with Professor Guy Lippens from CNRS-INSA Toulouse, France.

the resulting conformation of Tau at the microtubule surface have been a subject of intense interest. TauF4 binds to a single tubulin heterodimer (in the TR complex<sup>10</sup>) as a U-turn with an overhanging peptide in the first repeat; the latter peptide contributes to the binding when a second tubulin heterodimer is added.<sup>10</sup> Nevertheless, in the T2R complex of two tubulin heterodimers stabilized to a curvature conformation by the stathmin-derived helix, large parts of TauF4 remain highly mobile. The absence of <sup>13</sup>C chemical shift variations between the unbound and bound TauF4 argues against the fragment adopting any stable secondary structure at the surface of the curved tubulin constructs.<sup>10</sup> In contrast, a study by a combination of fluorescence correlation spectroscopy and acrylodan fluorescence screening suggested that Tau binds to similar soluble tubulin constructs with an apparent helical structure.<sup>11</sup> Another recent study proposed on the basis of solution NMR and mass spectrometry is that Tau binds to taxol-stabilized straight microtubule filaments through discontinuous and small groups of microtubule-binding residues.<sup>12</sup> Residues in between the microtubule binding sites are highly flexible, and full-length Tau would not fold into a unique well-defined structure upon binding to microtubules according to the study by Kadavath et al.<sup>12</sup> However, a distinct stretch of residues (Tau267-312) within the microtubule binding repeats was proposed to be stabilized a defined conformation upon binding to MTs (PDB code: 2MZ7).<sup>13</sup> So far, there has been no agreement on the conformation of Tau bound to microtubules, and often these studies are complicated by the large size of Tau/microtubule complexes and the highly dynamic nature of the interaction.

To probe the intriguing questions regarding the conformation of Tau assembled with polymerized microtubules and how its dynamic properties are regulated by microtubules, we have employed MAS NMR spectroscopy. This approach is not

limited to assemblies of small molecular weight and provides atomic level information regarding protein conformation. Moreover, MAS NMR investigations provide atomic-level resolution of the internal dynamics of Tau/MT complexes occurring over many decades of motional timescales.

## **3.2 Materials and Methods**

### **3.2.1 Materials**

Common chemicals were purchased from Fisher Scientific or Sigma-Aldrich. Lyophilized bovine brain tubulin was purchased from Cytoskeleton, Inc. Paclitaxel (taxol) was purchased from Alexis. Guanosine triphosphate (GTP) was purchased from MP Biomedicals. 400 mesh, formvar-coated copper grids, stabilized with evaporated carbon films, were purchased from Electron Microscopy Science.

U-<sup>13</sup>C, <sup>15</sup>N-enriched TauF4 was prepared by our collaborator Prof. Guy Lippens at CNRS-INSA in Toulouse, France. Expression of U-<sup>13</sup>C, <sup>15</sup>N-enriched TauF4 was carried out as described previously,<sup>14</sup> and the purification of TauF4 was performed as described before.<sup>15</sup>

### **3.2.2 Cosedimentation Assay of TauF4 with Microtubules**

Two approaches for preparation of TauF4/MT complexes were tested by co-sedimentation assay. In the first, the microtubules were polymerized from lyophilized tubulin and stabilized with paclitaxel. Tubulin was dissolved in BRB15 (Borisy resuspension buffer) buffer containing 15 mM PIPES (piperazine-N, N'-bis), 1 mM MgCl<sub>2</sub>, 1 mM EGTA (ethylene glycol-bis(beta-aminoethyl ether)-N, N, N', N'-tetraacetic acid), pH 6.8. The resulting solution was then clarified by ultracentrifugation at 100,000 rpm (435,400 g) for 10 minutes, in a Beckman Coulter

Optima MAX-XP ultracentrifuge with a TLA 120.2 rotor. The supernatant was polymerized with an equal volume of polymerization buffer (2 mM GTP, 15 mM PIPES, 20% DMSO). Paclitaxel was added to the mixture to a final concentration of 20  $\mu$ M. The mixture was incubated at 37 °C for 30 minutes. After incubation, the paclitaxel-stabilized microtubules were pelleted down at 40,000 rpm (108,900 g) to remove the unpolymerized tubulin in the supernatant. Then the microtubules were incubated with molar ratios of TauF4 to tubulin dimers 1:1 and 1:2 for 30 minutes. The supernatant and pellet were separated by ultracentrifugation at 45,000 rpm for 10 minutes. In the second approach, tubulin and TauF4 stock solution were prepared both in BRB15 buffer. Molar ratios of 1:1 and 1:2 were mixed, followed by adding of equal volume of polymerization buffer. After incubation at 37 °C for 30 minutes, the pellet was separated from the supernatant by ultracentrifugation at 45,000 rpm for 10 minutes. Aliquots of supernatant and pellet were loaded on SDS-gel for electrophoresis analysis. The pellets were saved for TEM characterization.

### **3.2.3 Transmission Electron Microscopy.**

The morphology of the MTs and TauF4/MT assemblies prepared by the above protocols was verified by transmission electron microscopy (TEM). Samples of 30  $\mu$ M microtubules or complexes were first stained with uranyl acetate (5% w/v), through deposition onto 400 mesh, formvar/carbon-coated copper grids and allowed to air dry for 40 – 60 minutes. TEM analysis was performed with a Zeiss Libra 120 transmission electron microscope operating at 120 kV.

### 3.2.4 MAS NMR Sample Preparation

Ten milligrams of lyophilized bovine tubulin were dissolved in BRB15 buffer (15 mM PIPES, 1 mM EGTA, 1 mM MgCl<sub>2</sub>, pH 6.8) and clarified with ultracentrifugation at 100,000 rpm (435,400 g) for 15 min at 4 °C in a Beckman Coulter Optima MAX-XP ultracentrifuge with a TLA 120.2 rotor. The resulting tubulin supernatant was polymerized by addition of an equal volume of polymerization buffer (15 mM PIPES, 2 mM GTP, 20% DMSO) in the presence of 20 μM paclitaxel. After incubation at 36 °C for 30 min, the supernatant and the pellet were separated by centrifugation at 45,000 rpm (88,200 g) for 15 min. The pellet containing paclitaxel-stabilized microtubules was saved and resuspended gently with 600 μL of BRB15 buffer. Twenty μM paclitaxel was usually used for stabilizing microtubules in solution. TauF4 stock (407 μM in BRB15 buffer) was added to the suspension of MTs to reach a final Tau/MT ratio of 1:2 with TauF4 and MTs concentrations of 64 μmol and 128 μmol, respectively. After incubation at room temperature for 2 hours, the pellet containing Tau/MT complex was separated from the supernatant by centrifugation at 60,000 rpm (156,800 g) for 10 min. The surface of the pellet was rinsed with BRB15 buffer to preclude non-specific binding. Approximately 12 mg of the pellet containing the sample, of which ca. 0.6 mg was U-<sup>13</sup>C, <sup>15</sup>N-TauF4 were transferred into a 1.9 mm Bruker rotor for subsequent MAS NMR experiments.

### 3.2.5 MAS NMR Spectroscopy

MAS NMR spectra were collected on a 19.96 T Bruker AVANCE III instrument. All experiments were acquired using a 1.9 mm triple-channel HCN probe. The Larmor frequencies were operated at 850.5 MHz (<sup>1</sup>H), 213.8 MHz (<sup>13</sup>C) and 86.2

MHz ( $^{15}\text{N}$ ), respectively. The MAS frequency was controlled to within  $\pm 10$  Hz by a Bruker MAS controller. The temperature was calibrated using KBr.<sup>16</sup>

The 2D  $^{13}\text{C}$ - $^{13}\text{C}$  CORD correlation spectra were acquired at an MAS frequency of 14 kHz, and sample temperature of  $-5$  °C and  $-8$  °C. The  $^1\text{H}$   $90^\circ$  pulse was  $2.2$   $\mu\text{s}$  long. The  $^1\text{H}$ - $^{13}\text{C}$  cross polarization employed a tangent-ramped pulse of 90-110% on the  $^{13}\text{C}$  resonance, the  $^1\text{H}$  RF field was 83 kHz, and the center of the ramp on the  $^{13}\text{C}$  resonance was 86 kHz. The cross polarization (CP) mixing time of 1 ms was utilized. During the CORD mixing time (50 ms), RF fields of 14 kHz and 7 kHz on the proton channel were used. The  $^1\text{H}$  decoupling field strength was 102 kHz during the  $t_2$  acquisition and  $t_1$  evolution periods.

The 2D  $^{13}\text{C}$ - $^{13}\text{C}$  CTUC-COSY  $\text{C}^\alpha$ - $\text{C}^\beta$  correlation spectra were acquired at  $-5$  °C and MAS frequency of 18 kHz.  $^1\text{H}$   $90^\circ$  pulse was  $2.2$   $\mu\text{s}$  long. The  $^1\text{H}$ - $^{13}\text{C}$  CP employed a tangent amplitude ramp of 90-110%, the  $^1\text{H}$  RF field was 71 kHz, and the center of the ramp on the  $^{13}\text{C}$  resonance was 86 kHz. Eighty-six kHz  $^{13}\text{C}$  hard pulses were used throughout the experiment for  $^{13}\text{C}$ - $^{13}\text{C}$  J coupling transfer, and the CW13 field for  $^1\text{H}$  decoupling during transfer was 102 kHz. The  $^1\text{H}$  decoupling power of 102 kHz was used during acquisition.

In  $^1\text{H}$ - $^{13}\text{C}$  CP dynamics study, 1D  $^1\text{H}$ - $^{13}\text{C}$  cross-polarization spectra with contact time varying from 0.05 to 5.0 ms were acquired for temperatures of 10, 2, -3, -5, -8, and -18 °C. The  $^1\text{H}$   $90^\circ$  pulse length was 1.8 - 2.3  $\mu\text{s}$  as optimized at different temperatures. A tangent amplitude ramp of 90-110% was used for  $^1\text{H}$ - $^{13}\text{C}$  CP. The  $^1\text{H}$  RF field was 80 - 100 kHz, and the center of the ramp on the  $^{13}\text{C}$  resonance was 60 - 70 kHz with the Hartmann-Hahn condition attained.  $^1\text{H}$  decoupling power of 110 - 120 kHz was applied during the acquisition. The magnetization was calculated as the

integral of area encompassing the C<sup>α</sup> region (65.0 - 45.0 ppm). The error bar of each data point was determined by the signal-to-noise ratio (SNR).

The 2D DIPSHIFT experiments were used for the <sup>1</sup>H-<sup>13</sup>C dipolar coupling measurements at the MAS frequency of 14 kHz and at various temperatures: 2.0, -3.0, -8.0, -18.0, and -28.0 °C respectively. The R12<sub>1</sub><sup>4</sup> DIPSHIFT dipolar recoupling period applied on the proton channel was incorporated in a basic <sup>1</sup>H-<sup>13</sup>C CP sequence after the spin lock. During the R12<sub>1</sub><sup>4</sup> block, the <sup>1</sup>H RF field strength was 84 kHz. The parameters related to CP and <sup>1</sup>H decoupling were set in the same fashion as described in the previous paragraph. Sixteen points in the indirect dimension were acquired.

In <sup>13</sup>C single-pulse-excitation and <sup>1</sup>H-<sup>13</sup>C INEPT experiments, <sup>13</sup>C 90° pulses of 2.6 - 2.8 μs were used, and <sup>1</sup>H decoupling power of 110 - 120 kHz was applied during acquisition. A recycle delay of 5 s was used in <sup>13</sup>C single-pulse-excitation experiments, and a recycle delay of 2 s was employed in <sup>1</sup>H-<sup>13</sup>C INEPT and the <sup>1</sup>H-<sup>13</sup>C CP based experiments.

<sup>1</sup>H-<sup>15</sup>N CP spectra were recorded with tangent-ramped pulse of 80-100% on <sup>15</sup>N resonance; the <sup>1</sup>H RF field was 70 kHz, and the center of the pulse on the <sup>15</sup>N resonance was 84 kHz. The magnetization transfer in <sup>15</sup>N-<sup>13</sup>C double CP experiments, from <sup>15</sup>N to <sup>13</sup>C was realized using SPECIFIC-CP with a tangent amplitude ramp (90%-110%), and the RF field strengths were 49 kHz, 35 kHz and 100 kHz for <sup>15</sup>N, <sup>13</sup>C and <sup>1</sup>H channels, respectively.

### 3.2.6 Data Analysis

Two-dimensional CTUC-COSY data were processed with NMRPipe.<sup>17</sup> A 90° shifted sine bell function was applied in both dimensions. In addition, a Lorentzian-to-Gaussian transformation function was applied in the direct dimension. 2D CORD data

at -5 °C and -8 °C were processed with Topspin by applying a Lorentzian-to-Gaussian transformation function in both dimensions. For the 2D DIPSHIFT spectra at various temperatures for  $^1\text{H}$ - $^{13}\text{C}$  dipolar coupling measurements, a 90° shifted sine bell function was applied in both dimensions. One-dimensional data were processed with MestReNova, with a Lorentzian line broadening of 50 Hz. The chemical shifts were referenced to the  $^{13}\text{C}$  methylene peak in solid adamantane (40.76 ppm) and  $^{15}\text{N}$  shift in solid  $^{15}\text{NH}_4\text{Cl}$  (39.2 ppm) acquired around the same time.

The magnetization of  $^1\text{H}$ - $^{13}\text{C}^\alpha$  cross polarization vs. contact time curve was fitted to the following function:

$$M(t) = M_1[e^{-t/T_{HH}} - e^{-t/T_{CH1}}] \left\{ \frac{T_{HH}}{T_{HH} - T_{CH1}} \right\} + M_2[e^{-t/T_{HH}} - e^{-t/T_{CH'}}] \left\{ \frac{T_{HH}}{T_{HH} - T_{CH'}} \right\} \quad [3.1]$$

$M_1$  and  $M_2$  describe the partial magnetization from each type of chemical environments undergoing motion.  $T_{CH1}$  and  $T_{CH'}$  describe the transfer of polarization from abundant  $^1\text{H}$  spins to the dilute  $^{13}\text{C}^\alpha$  spins in the chemical environments characterized by  $M_1$  and  $M_2$ , respectively.  $T_{HH}$  describes a drain, usually assumed to be the effect of spin-lattice relaxation of protons. The fraction of each environment is determined by  $M_1/M_1 + M_2$  and  $M_2/M_1 + M_2$  respectively.

At the temperatures of -8 °C, -18 °C, and -28 °C, dipolar coupling constants were obtained by numerical simulations of the dipolar line shapes using SIMPSON,<sup>18</sup> as described previously.<sup>19</sup> At the temperatures of -5 °C and 2 °C, the dipolar coupling constants were beyond the limit that can be determined accurately and therefore were not reported.

### 3.3 Results

#### 3.3.1 Biochemical Characterization of TauF4 Binding to Microtubules

Co-sedimentation assay of TauF4-microtubule interactions has corroborated that TauF4 (S208-S324) binds with microtubules both in the presence and the absence of MT-stabilizing taxol, as illustrated in Figure 3.1b. To prevent the non-specific association of TauF4,<sup>20</sup> a TauF4/tubulin heterodimer ratio of 1:2 was used for the MAS NMR sample. The TEM images indicate that the samples are homogeneous, and that TauF4 does not disrupt the morphology of the MT filaments, when MT is polymerized with taxol. When MTs are coassembled with TauF4, they form bundles, in agreement with the absence of the projection domain in this TauF4 fragment.<sup>5</sup> Previous studies have shown that Tau binding to preassembled MTs is reversible, while if incorporated into the microtubule during the MT polymerization process, the binding becomes irreversible.<sup>8</sup> Our current study focuses on the complex of TauF4 bound to pre-assembled microtubules stabilized by taxol.

#### 3.3.2 Conformation of TauF4 in Complex with Microtubules

J-coupling-based  $^{13}\text{C}$ - $^{13}\text{C}$  correlation spectra (CTUC-COSY)<sup>22</sup> acquired at -5 °C are displayed in Figure 3.2; these were used to identify the dynamic residues in TauF4 assembled on polymerized MTs. It is clear that many peaks overlap, resulting in major intensity variations for the observed correlations. The peak positions and the corresponding line widths are reported in Table 3.1. The modest chemical shift dispersion for certain residues is in agreement with solution NMR observations for the free TauF4.<sup>15</sup> An astonishing finding is that the synthetic spectrum generated from the  $\text{C}^{\alpha}$  and  $\text{C}^{\beta}$  solution chemical shifts overlays well with our experimental MAS NMR spectra, making it possible to assign certain cross peaks belonging to the  $\text{C}^{\alpha}$ - $\text{C}^{\beta}$

correlations tentatively; these are labeled on the spectra and summarized in Table 3.1. All assignment possibilities are labeled for each peak, but we do not exclude the possibility that some residues are missing due to conformational heterogeneity or dynamics.

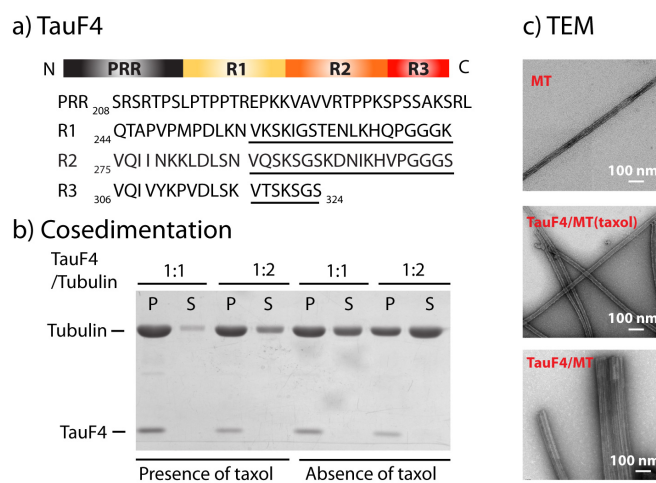


Figure 3.1: a) Domain organization and primary sequence of TauF4. Numbering is based on the longest adult Tau isoformer (441 residues). The R1, R2 and R3 repeat regions are defined by Lee et al.<sup>21</sup> The regions of high homology are underlined, and the less homologous regions are inter-repeats. b) SDS-PAGE gel of co-sedimentation assay of TauF4 with microtubules. The experimental TauF4 and tubulin dimer molar ratios are marked on the top of the gel. Tubulin and TauF4 protein bands are marked to the left of the gel. In the presence of taxol, microtubules are preassembled and stabilized, followed by the formation of TauF4/MT complexes. In the absence of taxol, TauF4 co-assembles with tubulin heterodimers to form TauF4/MT co-polymer. c) Negatively stained TEM images of the microtubule filament (top); TauF4/MT complexes in the presence of taxol (middle); TauF4-promoted TauF4/MT bundles in the absence of taxol (bottom). “P” represents pellet; “S” represents supernatant.

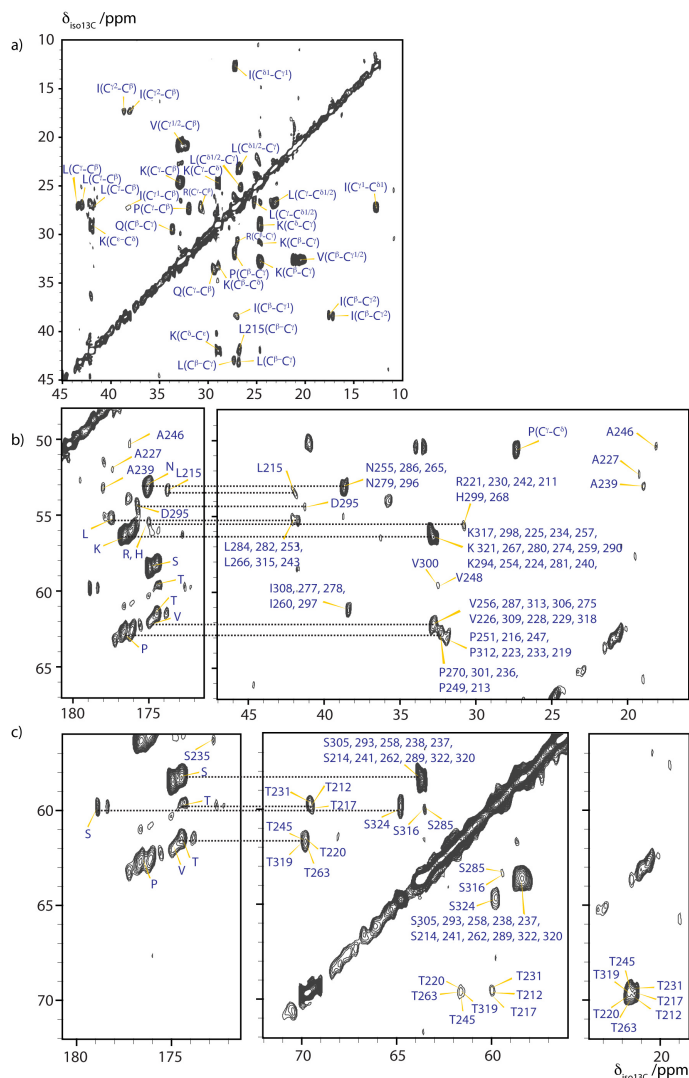


Figure 3.2: Characteristic regions of J coupling-based 2D  $^{13}\text{C}$ - $^{13}\text{C}$  CTUC-COSY correlation MAS spectra of U- $^{13}\text{C}$ ,  $^{15}\text{N}$  TauF4/MT complexes at  $-5\text{ }^\circ\text{C}$  and 19.96 T. a) Expansion showing sidechain carbon correlations. b) Expansion demonstrating  $\text{C}^\alpha\text{-C}^\beta$  and  $\text{C}^\alpha\text{-C}'$  correlations of residues whose  $\text{C}^\beta$  is within the chemical shift range of 45 - 10 ppm, and chemical shift of  $\text{C}^\alpha$  lies in the range of 65 - 50 ppm. c)  $\text{C}^\alpha\text{-C}^\beta$  and  $\text{C}^\alpha\text{-C}'$  correlations of Ser and Thr residues. All possible assignments based on solution NMR shifts are labeled.<sup>15</sup> The summary of assignments is listed in Table 3.1. The overlapping peaks may not contain all residues expected to be associated with the corresponding resonances.

Table 3.1: Resonance Assignments of TauF4 Assembled on Polymerized Microtubules from J-Coupling-based 2D  $^{13}\text{C}$ - $^{13}\text{C}$  CTUC-COSY Correlation Spectra and Comparison with Published Solution NMR Shifts

AA Type	Chemical Shifts (MAS NMR)		Peak Width		Residue	Chemical Shifts (Solution NMR)	
	C $\alpha$ (ppm)	C $\beta$ (ppm)	C $\alpha$ (ppm)	C $\beta$ (ppm)		C $\alpha$ (ppm)	C $\beta$ (ppm)
Asn	53.1	38.7	0.80	0.36	N255	53.3	38.7
					N265	53.4	38.6
					N279	53.0	38.9
					N286	53.3	38.8
					N296	53.3	38.6
Asp	54.4	41.3	0.99	0.26	D295	54.6	41.1
Leu	53.5	41.9	0.67	0.38	L215	53.0	41.8
Asp*	53.8	41.0	0.80	0.31	D252	54.0	41.0
					D283	53.8	41.0
					D314	53.5	40.8
His	55.9	30.4	0.70	0.32	H268	55.9	30.6
					H299	55.8	30.7
Leu	55.3	41.7	0.64	0.29	L243	55.1	42.1
					L253	55.3	41.9
					L266	55.4	42.1
					L282	55.1	42.4
					L284	55.1	41.6
					L315	55.3	41.6
Pro	63.0	31.9	1.04	0.44	P251	63.2	32.2
					P216	63.0	32.0
					P247	62.8	31.8
					P312	62.8	32.0
					P223	62.8	32.0
					P233	62.8	32.0
					P219	62.8	32.0
Pro	62.7	32.3	0.84	0.46	P249	63.0	32.2
					P213	63.3	32.2
					P236	63.0	32.2
					P301	63.6	32.0

					P270	63.6	32.0
Arg	55.6	30.8	0.96	0.34	R211	56.0	30.7
					R221	55.6	30.7
					R230	55.6	30.7
					R242	56.1	30.5
Ser	58.4	63.7	0.59	0.26	S214	58.2	63.8
					S237	58.4	63.6
					S238	58.2	63.9
					S241	58.4	63.6
					S258	58.4	63.9
					S262	58.4	63.9
					S289	58.6	63.8
					S293	58.4	63.9
					S305	58.3	64.0
					S320	58.2	64.0
					S322	58.4	63.9
Val	62.1	32.8	0.98	0.49	V226	61.8	32.8
					V228	62.2	32.8
					V229	62.1	32.6
					V256	62.7	32.6
					V275	62.3	32.6
					V287	63.0	32.6
					V306	62.3	32.8
					V309	61.8	32.8
					V313	62.3	32.8
					V318	62.7	32.7
Val	59.5	32.5	0.82	0.45	V248	59.7	32.5
					V300	59.5	32.6
Lys	56.4	32.8	0.60	0.38	K224	56.2	32.8
					K225	56.1	33.1
					K234	56.1	33.1
					K240	56.4	32.8
					K254	56.9	32.5
					K257	56.4	32.9
					K259	56.4	32.8
					K267	56.5	32.8
					K274	56.4	33.1

					K280	56.4	33.1
					K281	56.4	32.7
					K290	56.5	32.9
					K294	56.6	32.8
					K298	55.9	32.8
					K317	56.1	32.9
					K321	56.4	33.0
Thr	61.7	69.8	0.34	0.97	T220	61.8	69.8
					T245	61.5	69.8
					T263	62.2	69.6
					T319	61.8	70.0
Ile	61.2	38.4	0.85	0.30	I260	61.4	38.5
					I277	61.0	38.4
					I278	60.8	38.6
					I297	61.3	38.4
					I308	61.0	38.5
Ser	59.9	64.8	1.02	0.24	S324	59.9	64.9
Ser	60.0	63.5	0.64	0.21	S285	59.5	63.6
					S316	59.8	63.7
Thr	59.7	69.5	0.84	0.38	T231	59.7	69.6
					T212	59.9	69.8
					T217	60.0	69.8
Ala	52.2	19.2	0.95	0.22	A227	52.2	19.1
Ala	53.3	18.9	0.33	0.14	A239	52.7	18.8
Ala	50.4	18.1	0.81	0.24	A246	50.4	18.1
Gln*	55.7	29.3	0.70	0.64	Q244	55.9	29.4
					Q276	55.6	29.4
					Q288	56.1	29.3
					Q307	55.6	29.4

\*Peaks not displayed in Figure 3.2 because they are below the display contour level.

A227 and A239, the only two alanine residues which belong to the proline-rich region (PRR), show up as individual peaks, and point towards a substantial mobility of the PRR under these conditions. Likewise, A246, located in the beginning of R1 exhibits similar behavior. L215 also belongs to the PRR and appears in the spectra as a distinct peak, due to the presence of a proline downstream. The latter has a characteristic effect on its random coil  $^{13}\text{C}$  chemical shift values.<sup>23</sup> The same downstream-proline-induced shift is observed for the three T(P) (threonine-proline) motifs in the PRR, and for two valine residues, V248 in R1 and V300 in R2, with all of these showing up as a weak peak. In addition, two serine residues, S285 in R2 and S316 in R3, have unique chemical shifts in the solution spectrum of TauF4, and on this basis can be tentatively assigned in the CTUC-COSY spectrum, whereas the remaining eleven serine residues appear as one peak. We also see the resonance from S324, the last residue of the construct, as a surprisingly strong and broad peak. The line broadening suggests that this residue adopts multiple conformations and/or is dynamic. The presence of these individual residues highlights the dynamic nature of TauF4 when bound to the MT filament. The side chains also exhibit small chemical shift dispersions, and are therefore assigned by amino acid types shown in Figure 3.2a. Worth noticing is the presence of two distinct peaks of Ile  $\text{C}^\beta\text{-C}^{\gamma 2}$ , which indicates different local environments among the Ile residues.

The missing residues from the spectra are marked in the sequence in Figure 3.3; the lack of these peaks in the spectra could mean that they are rigid and have short  $T_2^*$  or that they are weak beyond detection because of conformational heterogeneity. Such is already the case for the unique Met250, in the first MTBR. This absence correlates well with the signal weakening when entering the first repeat, which was

observed by solution NMR in the TauF4 fragment in complex with T<sub>2</sub>R.<sup>10</sup> Tyr310, another unique residue in the third MTBR of TauF4, is absent in the present CTUC-COSY MAS NMR spectrum of TauF4 in complex with MTs. In the TR complex, this signal was severely broadened, but it became visible in the TauF4:T2R spectrum, and was at the center of the PHF6 fragment making the large amplitude sway movement. K311, as the sole lysine residue with a downstream proline, is equally absent from the CTUC-COSY spectrum. The absence of peaks for these residues in the CTUC-COSY spectra suggests that the PHF6 hexapeptide is immobilized or disordered when on a straight MT surface.

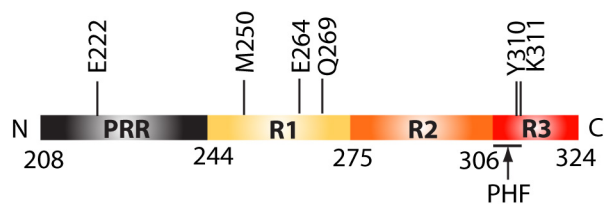


Figure 3.3: Residues absent from J-coupling-based <sup>13</sup>C-<sup>13</sup>C CTUC-COSY spectra, marked on the TauF4 domain organization.

Dipolar-based CORD<sup>24</sup> spectra were also acquired at the same temperature of -5 °C. As with the CTUC-COSY spectrum, we could not assign the peaks site-specifically, and have therefore assigned the residue types; these are labeled in Figure 3.4 and summarized in Table 3.2. Using PLUQ,<sup>25</sup> we have predicted the secondary structure of these residues to be a random coil. Some peaks are readily recognized to be missing or weak beyond detection compared with the J-based CTUC-COSY data set. Such is the case for L215, A227 and A239 in PRR, S285 in R2, and S316 in R3. More surprisingly, S324, which appears to be strong in J-based spectra, is absent from

the CORD spectra, highlighting the dynamic nature of the TauF4 C termini. Cross peaks corresponding to residue Y310 are not present in either the J-based or the dipolar-based CORD spectra at  $-5\text{ }^{\circ}\text{C}$ , but we observed diagonal peaks corresponding to the aromatic carbons  $\text{C}^{\gamma}$ ,  $\text{C}^{\delta 1/2}$  and  $\text{C}^{\epsilon 1/2}$  in the CORD spectra. The neighboring K311 is missing as well. Proline residues present in J-based COSY and CORD spectra at  $-5\text{ }^{\circ}\text{C}$  are in the all-*trans* conformation, and we do not find peaks corresponding to *cis*-Pro in this sample, contrary to a previous report.<sup>26</sup>

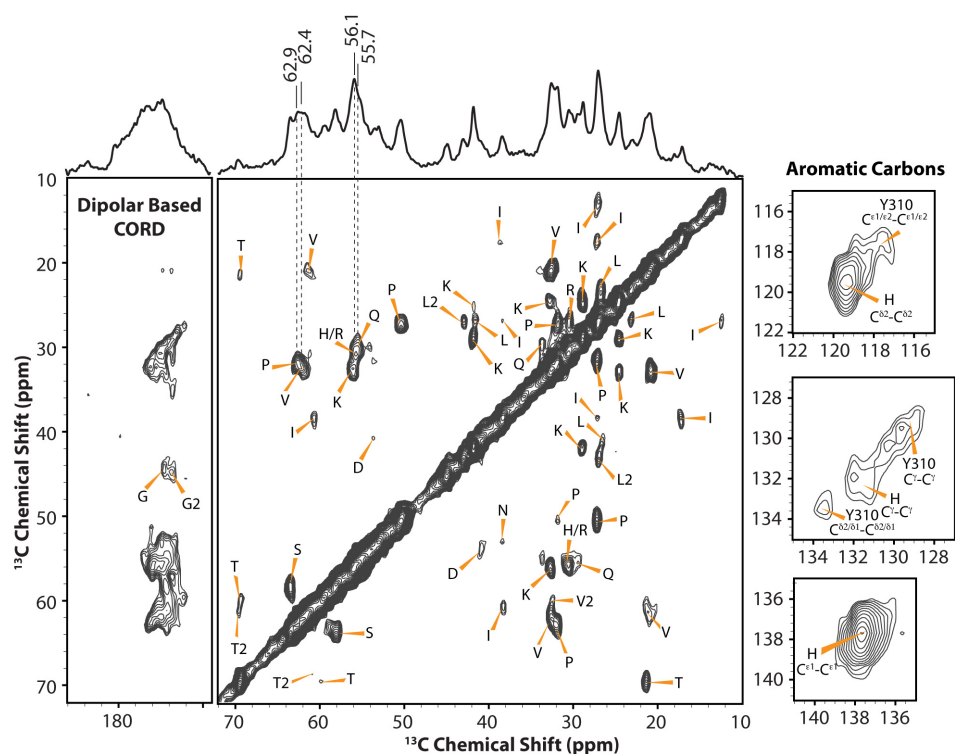


Figure 3.4: Two-dimensional dipolar-based  $^{13}\text{C}$ - $^{13}\text{C}$  CORD correlation MAS spectra of U- $^{13}\text{C}$ ,  $^{15}\text{N}$  TauF4/MT complexes at  $-5\text{ }^{\circ}\text{C}$  and magnetic field strength of 19.96 T. Peak assignments are shown on the spectra and summarized in Table 3.2. The 1D  $^1\text{H}$ - $^{13}\text{C}$  cross polarization spectrum is displayed as a top trace; chemical shifts for  $\text{C}^{\alpha}$  resonances corresponding to strong cross peaks in the 2D spectrum are labeled.

Table 3.2:  $^{13}\text{C}$  Resonance Assignments of 2D CORD Spectra Acquired at  $-5\text{ }^{\circ}\text{C}$

Residue Type	$\text{C}^{\alpha}$	$\text{C}^{\beta}$	$\text{C}^{\gamma 1}$	$\text{C}^{\gamma 2}$	$\text{C}^{\delta 1}$	$\text{C}^{\delta 2}$	$\text{C}^{\epsilon}$	$\text{C}'$	Conformation
T1	59.8	69.3		21.3					Coil
T2	61.0	69.6		21.3					Coil
S1	58.2	63.5							Coil
V1	62.3	32.0	20.9*						Coil
V2	59.6	32.2							Coil
P1	62.9	31.7	27.2		50.5				Coil
K1	56.1	32.5	24.6		29.0		42.0		Coil
H1	56.0	30.4	131.8			119.4	137.7		Coil
R1	56.0	30.5	27.0						Coil
Q1	55.7	29.5	33.7						Coil
I1	60.7	38.3	27.2	17.4	12.5				Coil
D1	53.7	40.7							Coil
N1	52.6	38.8							Coil
L1		41.6	26.7		23.5*				Coil/Helix
L2		43.0	26.8						Coil
G1	44.4							174.6	Coil
G2	44.8							173.8	Coil
Y310			129.6		133.4*		117.5		/

The CORD spectra acquired at  $-8\text{ }^{\circ}\text{C}$  are shown in Figure 3.5a. Interestingly, there are many more cross peaks and generally the lines are significantly broader, both for backbone and sidechain carbons, than in the CORD spectra at  $-5\text{ }^{\circ}\text{C}$ . This finding indicates that at  $-8\text{ }^{\circ}\text{C}$ , TauF4 on the MT surface is less dynamic than at higher temperature, thereby rendering dipolar-based transfers more efficient. By comparison with the synthetic spectra generated using the  $\text{C}^{\alpha}$ - $\text{C}^{\beta}$  chemical shifts from free TauF4 in solution, we find that within the  $\text{C}^{\alpha}$ - $\text{C}^{\beta}$  correlation region, the chemical shift dispersion agrees very well with that of free TauF4. Moreover, the sidechain carbons of the same residue types also tend to have similar chemical shifts and give rise to one broad intense peak, suggesting similar chemical environments. The broad peaks

originate from conformational heterogeneity and/or intermediate timescale motions present at lower temperature. Despite the peak overlap, we were able to assign the spin systems, and the sidechain assignments are summarized in Table 3.3. The reported shifts are measured at the center of the peaks, and represent the average shifts of multiple residues of the same type. Interestingly, we can assign a second proline group that is absent in the CORD spectra at -5 °C. The residues in this group are likely P218 and/or P232 in PRR as their chemical shifts are distinct vis-à-vis other prolines due to the influence of a C-terminal Pro residue (vide supra). A Glu C<sup>β</sup>-C<sup>γ</sup> cross peak, corresponding to Glu222 in PRR and/or Glu264 in R1, is present in the spectra at -8 °C; this resonance was not observed in the spectra at -5 °C shown in Figure 3.4. In line with J-coupling-based experiment at -5 °C, the Ile C<sup>β</sup>-C<sup>γ2</sup> cross peak also shows multiple features, suggesting different chemical environments.

The cross peak of Y310 located in the paired helical filament (PHF) hexapeptide, is still missing in the spectra at -8 °C. When the temperature is as low as -28 °C, the C<sup>α</sup>-C<sup>β</sup> correlation appears in the CORD spectrum (results not shown). Taken together, these results suggest that Y310 is disordered, albeit it is difficult to say unequivocally, whether the disorder is static or dynamic.

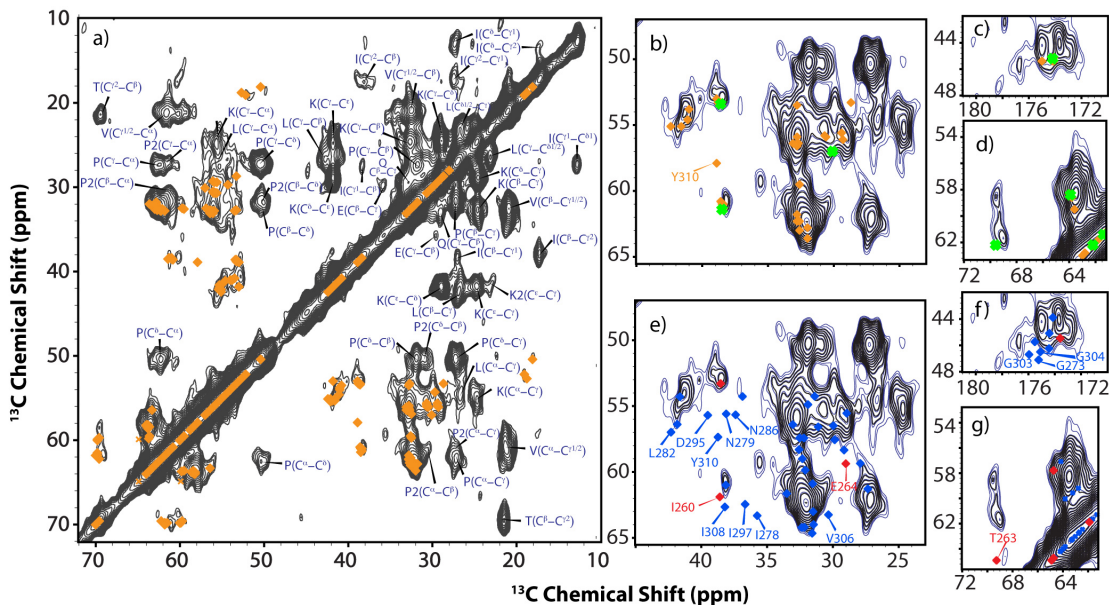


Figure 3.5: Two-dimensional dipolar-based  $^{13}\text{C}$ - $^{13}\text{C}$  CORD correlation MAS spectra of U- $^{13}\text{C}$ ,  $^{15}\text{N}$  TauF4/MT complex at  $-8^\circ\text{C}$  and magnetic field strength of 19.96 T. a) Aliphatic region with synthetic peaks (orange) corresponding to  $\text{C}^\alpha$ - $\text{C}^\beta$  correlations are generated using solution NMR shifts. Sidechain peak assignments are labeled in blue. Ile  $\text{C}^{\gamma 2}$ - $\text{C}^\beta$  cross peak with multiple features is highlighted with grey box. b), c), and d)  $\text{C}^\alpha$ - $\text{C}^\beta$  correlations of residues 276-312 (orange) and  $^{260}\text{IGSTEN}^{265}$  motif (green) generated from solution NMR shifts mapped onto  $^{13}\text{C}$ - $^{13}\text{C}$  CORD spectra of U- $^{13}\text{C}$ ,  $^{15}\text{N}$  TauF4/MT complex. e), f), and g)  $\text{C}^\alpha$ - $\text{C}^\beta$  correlations of residues 276-312 (blue) generated from SHIFTX2-predicted chemical shifts from the reported conformation (PDB code: 2MZ7);  $\text{C}^\alpha$ - $\text{C}^\beta$  correlations of  $^{260}\text{IGSTEN}^{265}$  motif (red) in turn conformation generated from SHIFTX2-predicted chemical shifts of the I280-N285 turn from X-ray structure (PDB code 3MSU). Peaks that are missing or whose shifts disagree with the experimental MAS NMR data are labeled in blue and red. In the black and blue spectra, the contour level is set to 3X and 2X the noise level, respectively.

Table 3.3: Residue Type Assignments from  $^{13}\text{C}$ - $^{13}\text{C}$  CORD Spectra Acquired at  $-8$  °C

Residue Type	$\text{C}^\alpha$	$\text{C}^\beta$	$\text{C}^{\gamma 1}$	$\text{C}^{\gamma 2}$	$\text{C}^{\delta 1}$	$\text{C}^{\delta 2}$	$\text{C}^\epsilon$
Pro	62.5	32.0	27.4		50.3		
Pro2	61.5	30.8	27.3		50.4		
Leu	55.1	41.6	26.6	23.1*			
Ile		38.4	27.0	17.3	12.8		
Val		32.5	20.9*				
Lys		32.7	24.7				41.7
Glu		29.8	35.9				
Gln		29.1	33.1				
Thr		69.5	21.5				

When TauF4 binds to a single tubulin heterodimer, a turn-like conformation centered on peptide  $^{260}\text{IGSTEN}^{265}$  in the middle of R1 repeat was reported to be present. To investigate whether TauF4 stretches along the microtubule, adopts a turn structure, or is in an equilibrium between both states, we compared our experimental chemical shifts with the predicted chemical shifts of this stretch of residues that would adopt either coil or turn conformation. We used the solution shifts of the  $^{260}\text{IGSTEN}^{265}$  stretch from the free state, similar to the coil shifts predicted by the *ncIDP* library<sup>27</sup> based on the primary sequence. In parallel, the  $\text{C}^\alpha$ ,  $\text{C}^\beta$  shifts of this peptide in a turn conformation were predicted with SHIFTX2<sup>28</sup> from the I280-N285 motif in the citrate synthase from *Francisella tularensis* (PDB code 3MSU). Shifts of both conformations are mapped onto our experimental CORD spectra at  $-8$  °C in Figure 3.5b-g. It is clear that the experimental chemical shifts for Tau on polymerized straight MT are consistent with coil conformation of this stretch, while turn

conformation does not appear to be adopted as predicted shifts for I260, T263 and E264 lie outside of the cross-peak regions in the MAS NMR spectra. We note that the random coil conformation in the context of *ncIDP* predictions may not be a single conformer but may represent the ensemble average over many rapidly exchanging conformers. This observation is not in contradiction with prior results from solution NMR on TauF4 bound to a single or two curved tubulin heterodimers.<sup>10</sup> When tubulin adopts a straight conformation as in the microtubules, the sway movement proposed for TauF4 on T2R might contribute to straightening the tubulin molecules and consequently result in a more extended conformation on the microtubule surface.

We have also examined the conformation of the MT-binding motif Tau(267-312) in the TauF4 assembled with polymerized microtubules. We have mapped the solution NMR shifts<sup>15</sup> of this strand in free TauF4 onto the CORD MAS NMR spectra of TauF4 assembled on MTs recorded at -8 °C. As shown in Figure 4b-4d, the shifts corresponding to most of the residues of free Tau(267-312) in solution overlay very well onto the experimental spectra of the TauF4/MT assembly, indicating that the Tau(267-312) motif adopts similar conformation(s) upon binding with polymerized MTs. When we predict the chemical shifts by SHIFTX2 from the recent solution NMR structure of Tau(267-312) interacting with MTs (PDB code: 2MZ7) and map those onto the CORD spectra of TauF4/MT assembly reported here (Figure 3.5e-g), to our surprise, there is no agreement: peaks for 12 out of 45 residues, including G273, I278, N279, I282, N286, D295, I297, G303, G304, V306, I308, and Y310, map onto empty regions of the CORD spectrum. These residues are spread across the sequence, with five of them residing in  $\alpha$ -helices, according to the solution NMR findings.<sup>13</sup> G303, G304 and V306 found to form a hairpin structure show poor agreement, too.

This result indicates that, when TauF4 is bound to the MT surface, it is unlikely that the Tau(267-312) motif adopts a unique conformation. The presence of multiple conformations of Tau as an alternative to a unique conformation binding with MT was already mentioned in the interpretation of the solution NMR study.<sup>13</sup>

### 3.3.3 Dynamics of TauF4 in Complex with Microtubules on Multiple Timescales

The results discussed above suggest that TauF4 remains dynamic on the microtubule surface, and the timescales of motions are temperature-dependent. First, 1D  $^1\text{H}$ - $^{13}\text{C}$  CP and  $^1\text{H}$ - $^{15}\text{N}$  CP spectra of TauF4/MT complex, which are sensitive to dynamics on nano- to low microsecond timescales, exhibit strong temperature dependences, as illustrated in Figure 3.6 and Figure 3.7. In all data sets, the sensitivity increases as the temperature is decreased, while the resolution deteriorates with the highest extent of broadening occurring at  $-28\text{ }^\circ\text{C}$ . Second, at  $-5\text{ }^\circ\text{C}$ , the scalar-based spectra exhibit a greater number of well-resolved resonances compared with the dipolar-based spectra shown in Figure 3.8. Finally, we have observed that TauF4 exhibits considerable mobility on slower, millisecond timescales at temperatures higher than  $-8\text{ }^\circ\text{C}$ , as evidenced by the loss of the  $^{15}\text{N}$ - $^{13}\text{C}^\alpha$  SPECIFIC-CP signal. (See Figure 3.7.) This loss of signal associated with dynamics has also prevented us from acquiring 2D and 3D heteronuclear dipolar correlation spectra. These results indicate that above  $-8\text{ }^\circ\text{C}$ , TauF4 is dynamic on timescales from nano- to milliseconds and, upon lowering the temperature, the protein motions are slowed and multiple conformers are detectable, giving rise to inhomogeneous peak broadening.

To investigate further the extent of dynamics occurring on the time scales of  $^1\text{H}$ - $^{13}\text{C}$  cross polarization, we have acquired  $^{13}\text{C}$  direct-excitation experiments as a function of temperature; these are shown in Figure 3.9. In the range of  $-5\text{ }^\circ\text{C}$  to  $10\text{ }^\circ\text{C}$ ,

the overall direct-excitation spectral envelope is similar to that in CPMAS spectra, with CPMAS spectra being broader. Furthermore, the sensitivity of the CPMAS experiment is lower compared with that of the direct-excitation measurement. These observations indicate that i) a significant fraction of the protein is mobile, giving rise to signal in the direct-excitation spectra; ii) a fraction of the protein is rigid on these timescales, resulting in the CP-based signal. Interestingly, unlike CPMAS spectra, the resolution and sensitivity of direct-excitation spectra are not temperature-dependent.

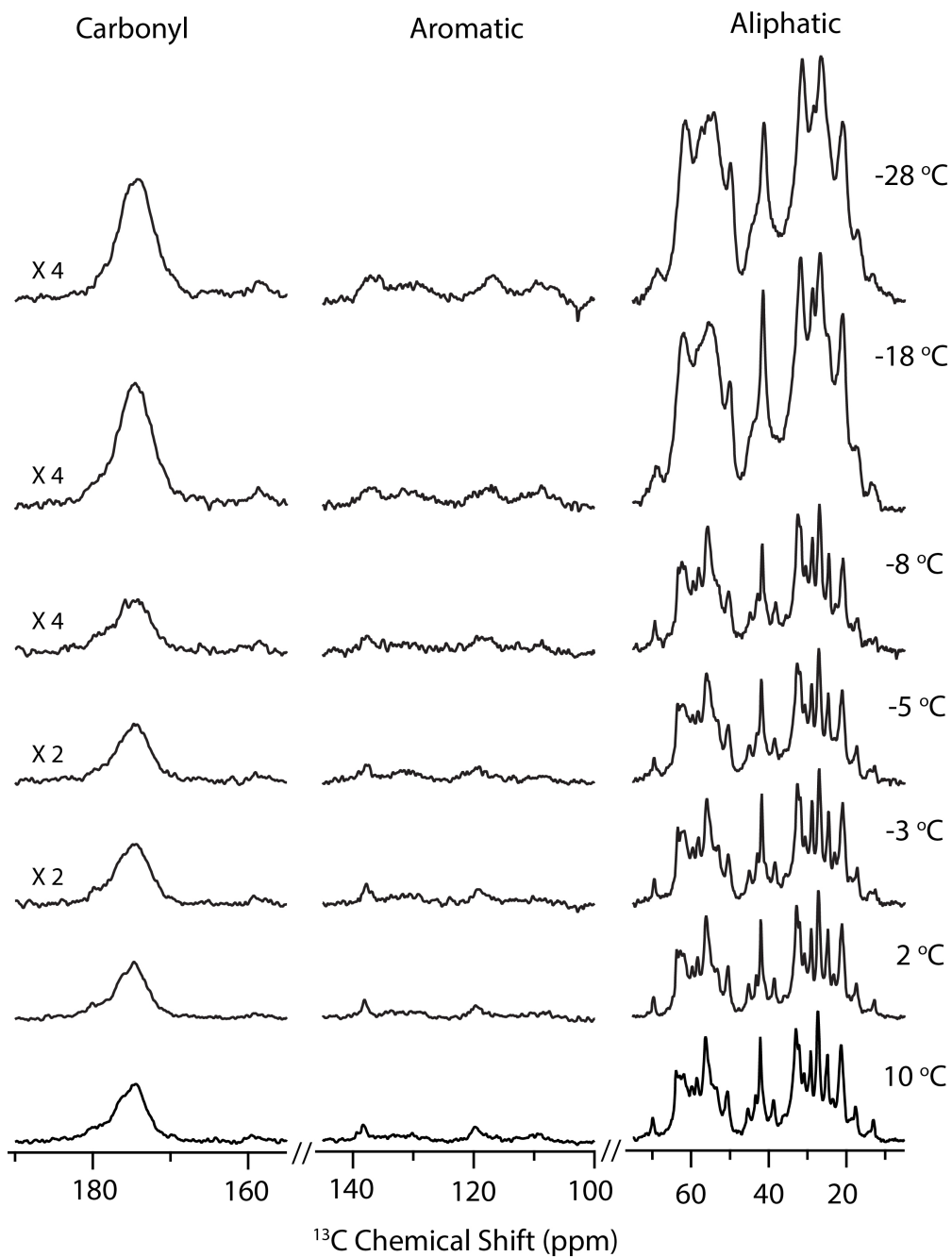


Figure 3.6: Temperature dependence of 1D  $^1\text{H}$ - $^{13}\text{C}$  cross-polarization (CCP) spectra of  $\text{U-}^{13}\text{C}, ^{15}\text{N}$ -TauF4/MT complex, displayed for carbonyl, aromatic, and aliphatic regions. The spectra are scaled to the same number of scans. Note that the signal-to-noise ratio increases as the temperatures decreases.

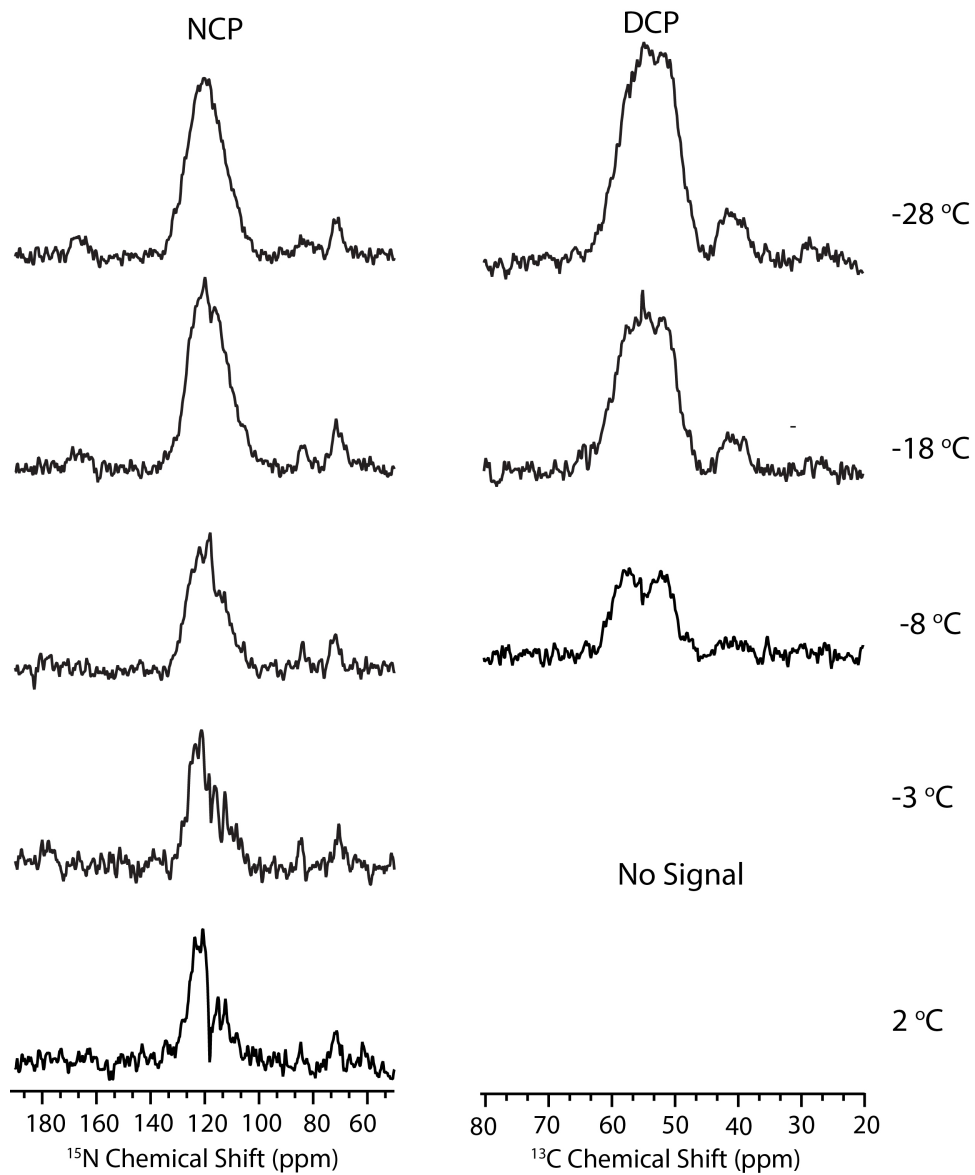


Figure 3.7: Temperature dependence of 1D  $^1\text{H}$ - $^{15}\text{N}$  cross-polarization (NCP) and 1D  $^{15}\text{N}$ - $^{13}\text{C}^\alpha$  SPECIFIC-CP (DCP) spectra of U- $^{13}\text{C}$ ,  $^{15}\text{N}$ -TauF4/MT complex.

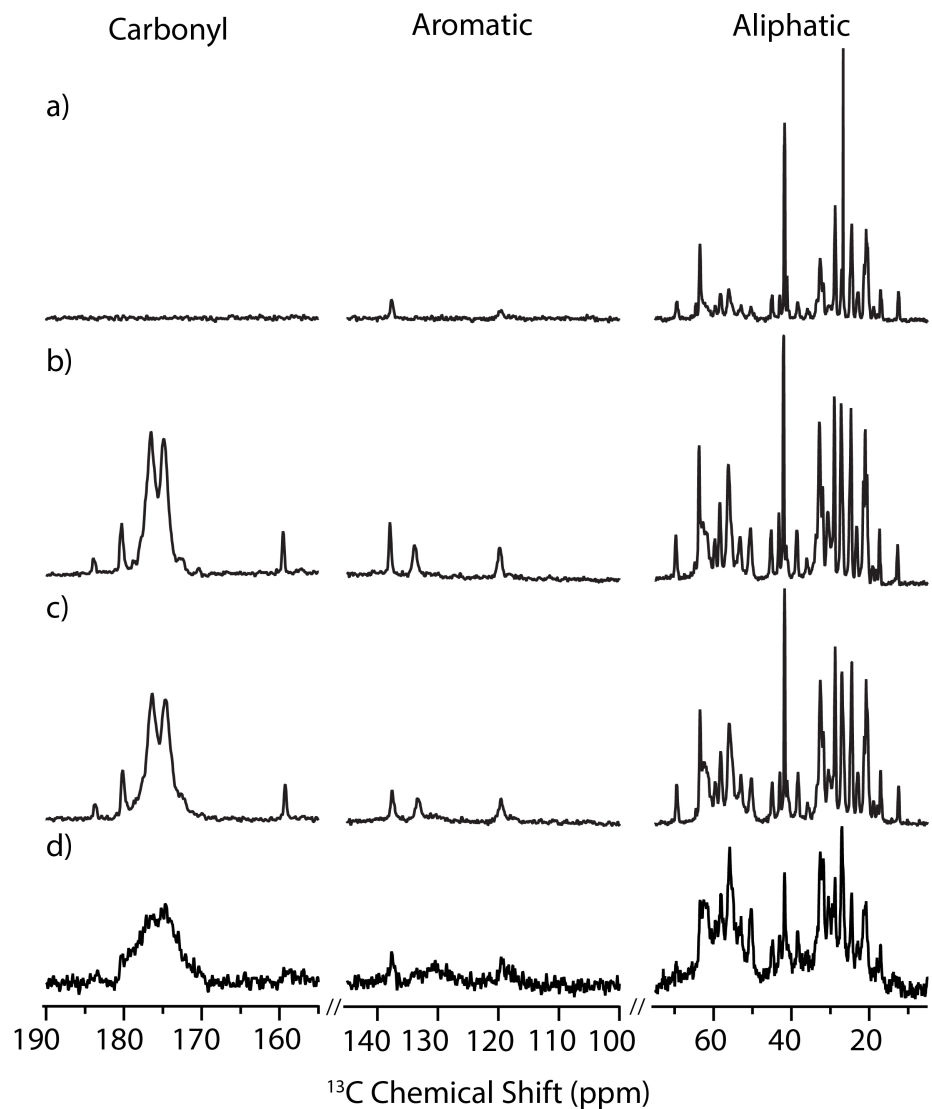


Figure 3.8: Comparison of 1D a)  $^1\text{H}$ - $^{13}\text{C}$  INEPT, b)  $^{13}\text{C}$  single pulse, c)  $^1\text{H}$ - $^{13}\text{C}$  CP with  $^{13}\text{C}$  single pulse excitation and d)  $^1\text{H}$ - $^{13}\text{C}$  CP spectra of  $\text{U-}^{13}\text{C}$ ,  $^{15}\text{N}$ -TauF4/MT complex at  $-5^\circ\text{C}$ , displayed for carbonyl, aromatic, and aliphatic regions.

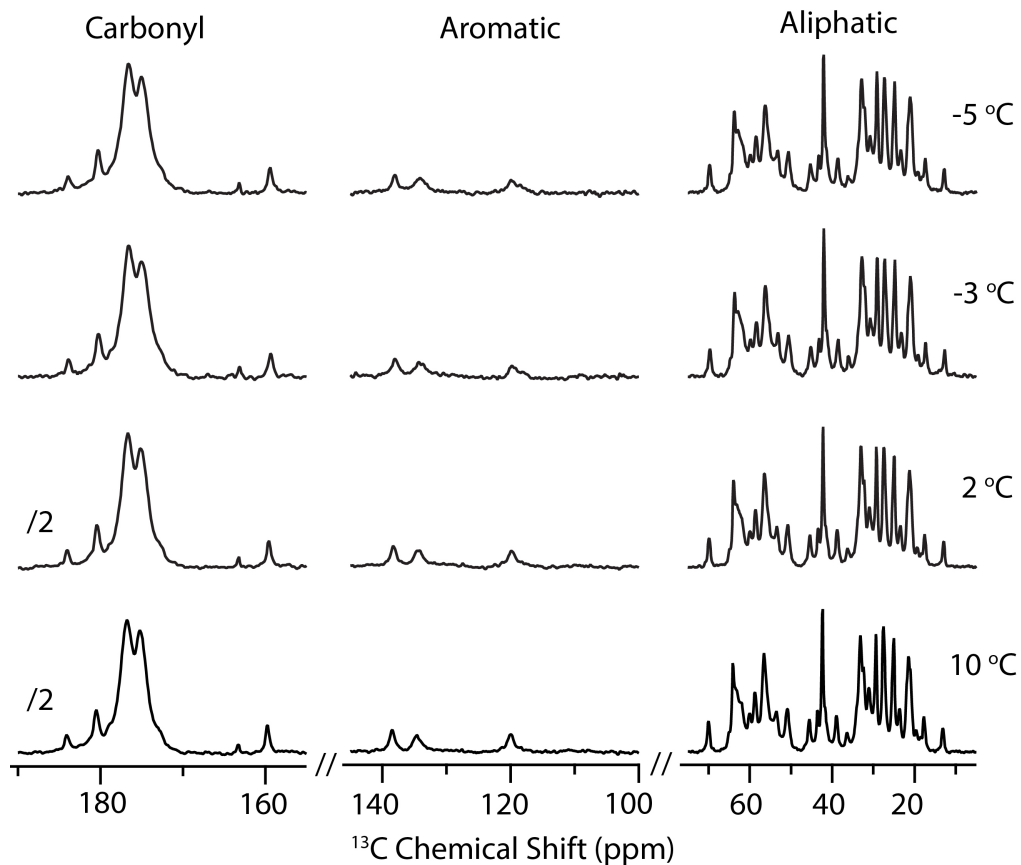


Figure 3.9: Temperature dependence of 1D single pulse excitation  $^{13}\text{C}$  NMR spectra of  $\text{U-}^{13}\text{C}$ ,  $^{15}\text{N}$ -TauF4/MT complex, displayed for carbonyl, aromatic, and aliphatic regions. The spectra are scaled to the same number of scans.

Additional information on the motional modes of TauF4 bound to polymerized MTs comes from the qualitative analysis of  $^1\text{H}$ - $^{13}\text{C}$  cross polarization dynamics. In Figure 3.10, the magnetization is plotted as a function of CP contact time. Note that such analysis is qualitative as it is performed assuming a greatly simplified model including no loss of magnetization to other processes. The time constant  $T_{\text{CH}}$  describes the buildup of magnetization and is sensitive to the protein motions. Short and long  $T_{\text{CH}}$  correspond to restricted and mobile groups, respectively.  $T_{\text{HH}}$ , also

written as  $^1\text{H } T_{1\rho}$ , characterizes the decay of the magnetization in the latter part of the profile due to the decay of spin locked  $^1\text{H}$  nuclei in the rotating frame. By fitting these curves, we obtain the  $T_{\text{HH}}$  and  $T_{\text{CH}}$  values, summarized in Table 3.4. The results indicate that at  $-18\text{ }^\circ\text{C}$  and  $-8\text{ }^\circ\text{C}$ , the CP buildup is characterized by a single  $T_{\text{CH}}$  of  $0.05\text{ ms}$ , corresponding to an average dipolar coupling constant of  $20\text{ kHz}$ . At these temperatures, the TauF4 motion is restricted. At  $-5\text{ }^\circ\text{C}$  and above, the magnetization buildup times increase, and fitting the curves requires a second  $T_{\text{CH}}$  around  $0.5\text{ to }0.8\text{ ms}$ , which corresponds to a faster motion with an average dipolar coupling of  $1 - 2\text{ kHz}$ . This temperature appears to be associated with a transition in the dynamic behavior. Important to note is that the restricted motion characterized by the  $T_{\text{CH}}$  of  $0.05\text{ ms}$  is also present throughout the entire temperature range of  $-18\text{ }^\circ\text{C}$  to  $10\text{ }^\circ\text{C}$  where the experiments were conducted, albeit its population monotonically decreases as a function of temperature. The observed dynamic profiles consisting of two pronounced environments, restricted and mobile, appear to be unique vis-à-vis other proteins, including microtubule-associated protein CAP-Gly as well as its complex with EB1 and assembly with polymerized microtubules studied by us previously.<sup>29</sup> We speculate that this behavior may be closely related to Tau being intrinsically disordered.

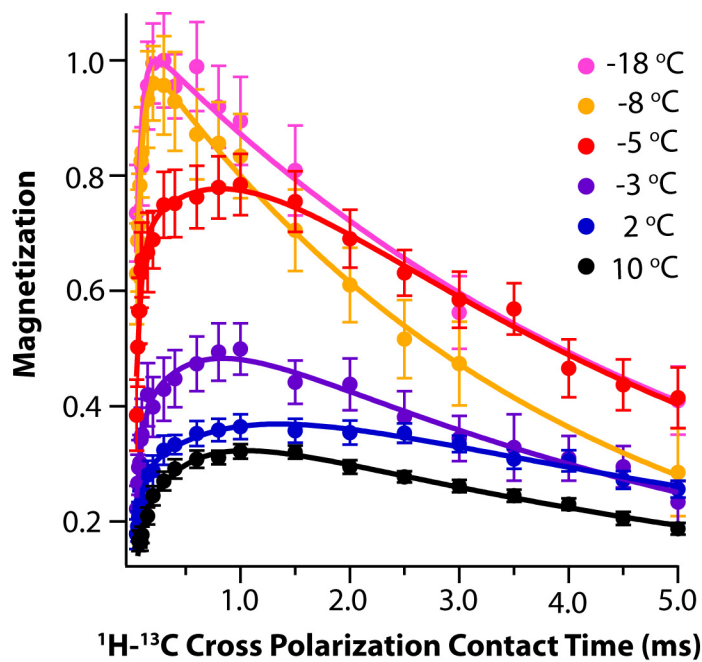


Figure 3.10: Normalized magnetization in  $^1\text{H}\text{-}^{13}\text{C}^\alpha$  cross-polarization experiments acquired for a series of temperatures as a function of variable contact times at -18, -8, -5, -3, 2, and 10 °C. Experimental data are shown as filled circles; best-fit curves are shown as solid lines.

Table 3.4: Summary of Parameters of  $^1\text{H}$ - $^{13}\text{C}^\alpha$  Cross Polarization Dynamics

$T/^\circ\text{C}$	$T_{\text{HH}}/\text{ms}$	$T_{\text{CH1}}/\text{ms}$	Percentage	$T_{\text{CH}'}/\text{ms}$	Percentage
10	6.7 $\pm 0.5$	0.06 $\pm 0.009$	46.2%	0.47 $\pm 0.08$	53.8%
2	8.1 $\pm 1.1$	0.05 $\pm 0.004$	58.7%	0.82 $\pm 0.2$	41.3%
-3	5.5 $\pm 0.7$	0.05 $\pm 0.009$	61.0%	0.50 $\pm 0.2$	39.0%
-5	5.1 $\pm 1.0$	0.05 $\pm 0.006$	66.3%	0.79 $\pm 0.4$	33.7%
-8	3.8 $\pm 0.1$	0.05 $\pm 0.001$	100.0%	N/A	0%
-18	5.3 $\pm 0.5$	0.05 $\pm 0.005$	100.0%	N/A	0%

Another NMR parameter that reports on the nano- to microsecond timescale dynamics is the  $^1\text{H}$ - $^{13}\text{C}^\alpha$  dipolar interaction, which can be measured site specifically using methods developed by us and by others.<sup>19,30-37</sup> The presence of motions occurring on the timescales of dipolar coupling dynamically average the dipolar tensor to a reduced value. To determine the  $^1\text{H}$ - $^{13}\text{C}^\alpha$  dipolar interactions in TauF4 as a function of temperature, we have employed RN symmetry sequences<sup>35,36</sup> incorporated into 2D sequences (we could not conduct 3D experiments in a residue-resolved mode because the  $^{15}\text{N}$ - $^{13}\text{C}$  double CP experiment could not be executed, as discussed in the preceding sections). There is considerable overlap in the corresponding 2D spectra. Despite this overlap, we have been able to extract dipolar lineshapes for four  $\text{C}^\alpha$  peaks: 62.9 ppm, 62.4 ppm, 56.1 ppm, and 55.7 ppm. Each peak at the above four chemical shifts corresponds to strong cross peaks in the CORD spectra at -5 °C (see Figure 3.4). The lineshapes are shown in Figure 3.11, and the corresponding dipolar coupling constants are summarized in Table 3.5. At the temperatures of -8 °C, -18 °C and -28 °C the average dipolar couplings are very similar: 18.3 kHz, 18.3 kHz and 18.7 kHz, respectively. These dipolar coupling constants translate into dipolar order parameters of 0.81, 0.81 and 0.83, indicating that the dynamics are restricted under these conditions. If the internal mobility of the backbone is treated according to the diffusion-in-a-cone model,<sup>38</sup> these order parameters translate into the diffusion cone angles between 19.7° and 20.9°, corresponding to small-amplitude motions. At temperatures above -8 °C, the dipolar lineshapes become considerably narrower, and a strong central peak emerges, whereas the intensity of the broad component is greatly attenuated.

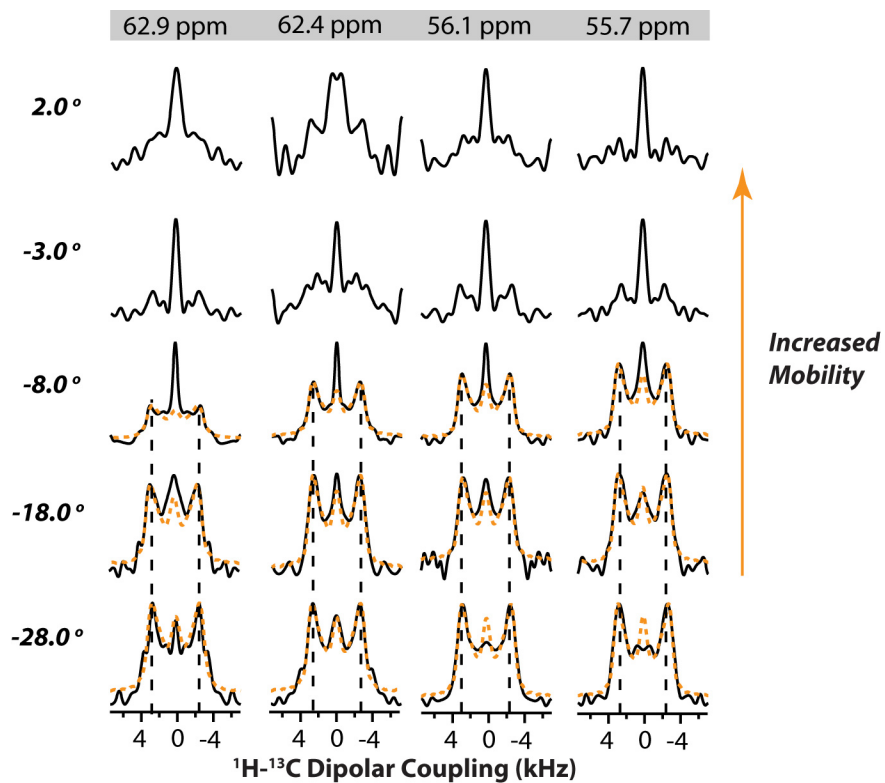


Figure 3.11:  $^1\text{H}$ - $^{13}\text{C}^\alpha$  dipolar lineshapes extracted at chemical shifts corresponding to strong cross peaks in  $^{13}\text{C}$ - $^{13}\text{C}$  CORD spectrum of U- $^{13}\text{C}$ ,  $^{15}\text{N}$  TauF4/MT complex, recorded at various temperatures ranging from  $-28\text{ }^\circ\text{C}$  to  $2\text{ }^\circ\text{C}$ . The experimental and simulated lineshapes are shown as solid black and dashed orange lines, respectively.

Table 3.5:  $^1\text{H}$ - $^{13}\text{C}^\alpha$  Dipolar Coupling Constants for Four Sites Corresponding to Strong Crosspeaks Observed in 2D CORD Spectra Acquired at  $-5\text{ }^\circ\text{C}$ .

$^1\text{H}$ - $^{13}\text{C}$ Dipolar Coupling Constant (kHz)			
Freq. /ppm	$-28\text{ }^\circ\text{C}$	$-18\text{ }^\circ\text{C}$	$-8\text{ }^\circ\text{C}$
62.9	18.3	18.1	18.1
62.4	18.6	18.3	18.3
56.1	18.8	18.0	18.3
55.7	19.3	18.7	18.6

For the temperatures of  $-8\text{ }^{\circ}\text{C}$  and below, we have extracted dipolar lineshapes and calculated corresponding order parameters for the region containing  $\text{C}^{\alpha}$  chemical shifts (50.0 - 64.0 ppm). The results are summarized in Table 3.6. Interestingly, the order parameters are overall very similar (the average value is  $0.82\pm 0.01$ ) and indicate restricted dynamics. The stability of the complex subjected to magic angle spinning and temperature cycling is checked by a 1D carbon cross-polarization acquired before and after experiments as shown in Figure 3.12. The complex is surprisingly stable, as demonstrated by the consistent sensitivity and resolution before and after MAS.

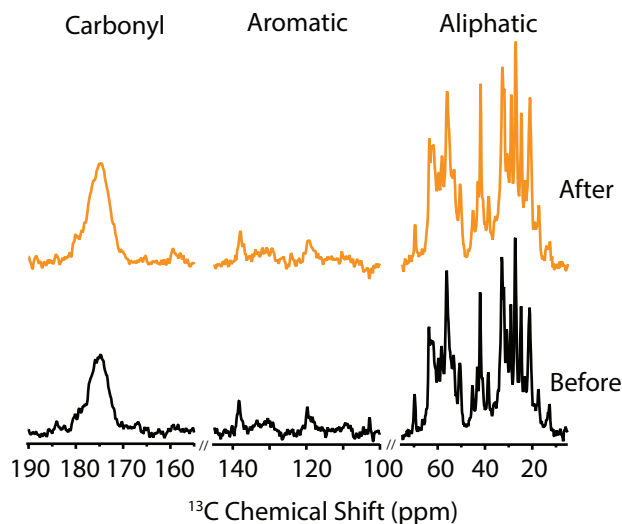


Figure 3:12: 1D  $^1\text{H}$ - $^{13}\text{C}$  cross polarization (CP) spectra of  $\text{U-}^{13}\text{C}$ ,  $^{15}\text{N}$ -TauF4/MT complex before and after freezing, displayed for carbonyl, aromatic, and aliphatic regions.

Table 3.6:  $^1\text{H}$ - $^{13}\text{C}$  Dipolar Order Parameters of Backbone  $\text{C}^\alpha$  in TauF4/MT Assemblies at Different Temperatures.

$^1\text{H}$ - $^{13}\text{C}$ Dipolar Order Parameter S							
Freq. /ppm	-28 °C	-18 °C	-8 °C	Freq. /ppm	-28 °C	-18 °C	-8 °C
63.9	0.90	0.79	0.74	57.9	0.83	0.83	0.82
63.7	0.84	0.78	0.73	57.8	0.83	0.82	0.83
63.6	0.81	0.74	0.74	57.6	0.82	0.81	0.82
63.4	0.81	0.78	0.78	57.4	0.81	0.81	0.81
63.2	0.84	0.82	0.79	57.3	0.81	0.81	0.82
63.1	0.83	0.79	0.79	57.1	0.82	0.79	0.81
62.9	0.81	0.80	0.80	56.9	0.82	0.79	0.80
62.7	0.81	0.82	0.79	56.8	0.82	0.80	0.82
62.5	0.82	0.81	0.79	56.6	0.82	0.81	0.83
62.4	0.82	0.81	0.81	56.4	0.82	0.80	0.83
62.2	0.81	0.81	0.82	56.2	0.83	0.79	0.82
62.0	0.81	0.81	0.79	56.1	0.83	0.79	0.81
61.9	0.81	0.80	0.80	55.9	0.83	0.81	0.81
61.7	0.82	0.80	0.80	55.7	0.85	0.82	0.82
61.5	0.82	0.81	0.81	55.6	0.84	0.82	0.81
61.4	0.83	0.80	0.82	55.4	0.83	0.82	0.81
61.2	0.83	0.79	0.82	55.2	0.83	0.81	0.81
61.0	0.82	0.80	0.81	55.1	0.82	0.81	0.81
60.8	0.82	0.82	0.81	54.9	0.82	0.82	0.82
60.7	0.82	0.82	0.81	54.7	0.83	0.83	0.82
60.5	0.82	0.82	0.81	54.5	0.83	0.82	0.82
60.3	0.82	0.80	0.82	54.4	0.82	0.82	0.81
60.2	0.81	0.79	0.83	54.2	0.82	0.81	0.82
60.0	0.81	0.80	0.83	54.0	0.81	0.81	0.83
59.8	0.81	0.81	0.83	53.9	0.82	0.83	0.82
59.7	0.82	0.80	0.83	53.7	0.83	0.83	0.81
59.5	0.82	0.78	0.83	53.5	0.83	0.81	0.82
59.3	0.81	0.79	0.83	53.4	0.82	0.81	0.82
59.1	0.82	0.81	0.82	53.2	0.82	0.81	0.84
59.0	0.82	0.82	0.82	53.0	0.82	0.81	0.82
58.8	0.82	0.82	0.83	52.8	0.82	0.82	0.81
58.6	0.82	0.81	0.83	52.7	0.82	0.82	0.83
58.5	0.82	0.81	0.83	52.5	0.83	0.81	0.82
58.3	0.82	0.81	0.83	52.3	0.83	0.82	0.80
58.1	0.83	0.82	0.82	50.5	0.82	0.78	0.82

### 3.4 Discussion

Our results indicate that TauF4 likely does not fold into a well-defined structure upon binding to polymerized microtubules, and appears to retain its IDP character, which may be advantageous for the diffusion of Tau along the microtubule surface.<sup>39</sup> Secondary structure analysis suggests TauF4 in complex with a MT adopts an average random coil assembly over exchanging conformations. At temperatures above -8 °C, TauF4 retains flexibility upon binding with MTs, over timescales from nano- to milliseconds, as evidenced by a limited number of resonances in the dipolar-based CORD spectra, numerous strong peaks in scalar-based correlation spectra, reduced <sup>1</sup>H-<sup>13</sup>C dipolar coupling constants, and cross polarization dynamics. Interestingly, no major structural perturbations are associated with the binding of TauF4 to microtubules, as the chemical shifts of the bound and the free state in solution are very similar. This fact suggests an electrostatic interaction to be a main driving force for the binding of TauF4 to polymerized microtubules, in agreement with prior findings for TauF4 bound with T2R.<sup>10</sup>

The <sup>260</sup>IGSTEN<sup>265</sup> motif in the R1 repeat, which adopts a characteristic U-turn conformation when bound to a single tubulin heterodimer,<sup>10</sup> does not adopt this particular conformation when TauF4 interacts with the straight MT surface. It is already the case when TauF4 interacts with T2R.<sup>10</sup> The PHF6 peptide at the C-terminus of TauF4, which shows increased mobility when bound with T2R, is either static or dynamically disordered in the complex of TauF4 with polymeric microtubules.

The lack of a well-folded structure in TauF4 bound to polymerized microtubules is directly correlated with its unusual mobility occurring on timescales of nano- to milliseconds. These dynamics are observed in multiple experiments. From -

28 °C to -8 °C, TauF4 motions are mainly restricted to timescales of nano- to microseconds. A unique observation is the sharp protein dynamics transition between -8 °C to -5 °C, during which TauF4 becomes highly mobile on the surface of MTs. Such hierarchical protein dynamics within a wide range of temperatures (from 160 K and below to 250K and above) has been recently described by Lewandowski et al.<sup>40</sup> Our results reveal a dynamics transition occurring at -5 °C, associated with large-scale motions occurring on slower timescales. We speculate that this extensive mobility is an essential attribute of Tau's function of regulating the microtubule assembly dynamics and is necessary for the efficient sampling of microtubule surface by Tau.

### **3.5 Conclusions**

In this study, we demonstrate, using MAS NMR spectroscopy, that TauF4 does not undergo a disorder-to-order transition upon microtubule binding, does not adopt a single folded structure, but remains disordered. Moreover, TauF4 displays unusual dynamic behavior on timescales from nano- to milliseconds, and is strongly temperature-dependent. Remarkably, due to the dynamic nature of the Tau/MT assembly, the binding to polymerized MTs does not induce chemical shift perturbations in the residues at the interface or distal residues (no allosteric effects) suggesting electrostatic interactions as the main driving force for the tight interaction between Tau and microtubules. Our MAS NMR approach for atomic-resolution analysis of structure and dynamics of Tau assembled with polymeric microtubules is applicable to other microtubule-associated proteins possessing intrinsic disorder. More broadly, MAS NMR spectroscopy can be used to study assemblies of other IDPs with their folded partners, which are important for a variety of biological processes.

## REFERENCES

- [1] Drechsel, D. N.; Hyman, A. A.; Cobb, M. H.; Kirschner, M. W. *Mol. Biol. Cell* **1992**, *3*, 1141.
- [2] Morris, M.; Maeda, S.; Vossel, K.; Mucke, L. *Neuron* **2011**, *70*, 410.
- [3] Brunden, K. R.; Trojanowski, J. Q.; Lee, V. M. *Nat. Rev. Drug Discov.* **2009**, *8*, 783.
- [4] Cleveland, D. W.; Hwo, S. Y.; Kirschner, M. W. *J. Mol. Biol.* **1977**, *116*, 227.
- [5] Fauquant, C.; Redeker, V.; Landrieu, I. et al. *J. Biol. Chem.* **2011**, *286*, 33358.
- [6] Al-Bassam, J.; Ozer, R. S.; Safer, D.; Halpain, S.; Milligan, R. A. *J. Cell Biol.* **2002**, *157*, 1187.
- [7] Kar, S.; Fan, J.; Smith, M. J.; Goedert, M.; Amos, L. A. *The EMBO journal* **2003**, *22*, 70.
- [8] Makrides, V.; Massie, M. R.; Feinstein, S. C.; Lew, J. *Proc. Natl. Acad. Sci.* **2004**, *101*, 6746.
- [9] Santarella, R. A.; Skiniotis, G.; Goldie, K. N. et al. *J. Mol. Biol.* **2004**, *339*, 539.
- [10] Gigant, B.; Landrieu, I.; Fauquant, C. et al. *J. Am. Chem. Soc.* **2014**, *136*, 12615.
- [11] Li, X. H.; Culver, J. A.; Rhoades, E. *J. Am. Chem. Soc.* **2015**, *137*, 9218.
- [12] Kadavath, H.; Hofele, R. V.; Biernat, J. et al. *Proc. Natl. Acad. Sci.* **2015**, *112*, 7501.
- [13] Kadavath, H.; Jaremko, M.; Jaremko, L.; Biernat, J.; Mandelkow, E.; Zweckstetter, M. *Angew. Chem. Int. Ed.* **2015**, *54*, 10347.
- [14] Amniai, L.; Barbier, P.; Sillen, A.; Wieruszkeski, J. M.; Peyrot, V.; Lippens, G.; Landrieu, I. *FASEB J.* **2009**, *23*, 1146.

- [15] Sibille, N.; Huvent, I.; Fauquant, C. et al. *Proteins* **2012**, *80*, 454.
- [16] Thurber, K. R.; Tycko, R. *J. Magn. Reson.* **2009**, *196*, 84.
- [17] Delaglio, F.; Grzesiek, S.; Vuister, G. W.; Zhu, G.; Pfeifer, J.; Bax, A. *J. Biomol. NMR* **1995**, *6*, 277.
- [18] Bak, M.; Rasmussen, J. T.; Nielsen, N. C. *J. Magn. Reson.* **2000**, *147*, 296.
- [19] Hou, G.; Byeon, I. J.; Ahn, J.; Gronenborn, A. M.; Polenova, T. *J. Am. Chem. Soc.* **2011**, *133*, 18646.
- [20] Ackmann, M.; Wiech, H.; Mandelkow, E. *J. Biol. Chem.* **2000**, *275*, 30335.
- [21] Lee, G.; Neve, R. L.; Kosik, K. S. *Neuron* **1989**, *2*, 1615.
- [22] Chen, L. L.; Olsen, R. A.; Elliott, D. W.; Boettcher, J. M.; Zhou, D. H. H.; Rienstra, C. M.; Mueller, L. J. *J. Am. Chem. Soc.* **2006**, *128*, 9992.
- [23] Wishart, D. S.; Bigam, C. G.; Holm, A.; Hodges, R. S.; Sykes, B. D. *J. Biomol. NMR* **1995**, *5*, 67.
- [24] Hou, G. J.; Yan, S.; Trebosc, J.; Amoureux, J. P.; Polenova, T. *J. Magn. Reson.* **2013**, *232*, 18.
- [25] Fritzsche, K. J.; Yang, Y.; Schmidt-Rohr, K.; Hong, M. *J. Biomol. NMR* **2013**, *56*, 155.
- [26] Jinwal, U. K.; Koren, J.; Borysov, S. I. et al. *J. Neurosci.* **2010**, *30*, 591.
- [27] Tamiola, K.; Acar, B.; Mulder, F. A. *J. Am. Chem. Soc.* **2010**, *132*, 18000.
- [28] Han, B.; Liu, Y. F.; Ginzing, S. W.; Wishart, D. S. *J. Biomol. NMR* **2011**, *50*, 43.
- [29] Yan, S.; Zhang, H. L.; Hou, G. J.; Ahmed, S.; Williams, J. C.; Polenova, T. *J. Biol. Chem.* **2015**, *290*, 1607.
- [30] Byeon, I. J. L.; Hou, G. J.; Han, Y. et al. *J. Am. Chem. Soc.* **2012**, *134*, 6455.
- [31] Schanda, P.; Huber, M.; Boisbouvier, J.; Meier, B. H.; Ernst, M. *Angew. Chem. Int. Edit.* **2011**, *50*, 11005.
- [32] Schanda, P.; Meier, B. H.; Ernst, M. *J. Am. Chem. Soc.* **2010**, *132*, 15957.

- [33] Tollinger, M.; Sivertsen, A. C.; Meier, B. H.; Ernst, M.; Schanda, P. *J. Am. Chem. Soc.* **2012**, *134*, 14800.
- [34] Ivanir-Dabora, H.; Nimerovsky, E.; Madhu, P. K.; Goldbourt, A. *Chem. Eur. J.* **2015**, *21*, 10778.
- [35] Levitt, M. H. In *Encyclopedia of Nuclear Magnetic Resonance*; Grant, M. D., Harris, K. R., Eds.; John Wiley & Sons, Ltd, : Chichester, 2002; Vol. 9, p 165.
- [36] Carravetta, M.; Eden, M.; Zhao, X.; Brinkmann, A.; Levitt, M. H. *Chem. Phys. Lett.* **2000**, *321*, 205.
- [37] Hong, M.; Gross, J. D.; Rienstra, C. M.; Griffin, R. G.; Kumashiro, K. K.; Schmidt-Rohr, K. *J. Magn. Reson.* **1997**, *129*, 85.
- [38] Lorieau, J. L.; Day, L. A.; McDermott, A. E. *Proc. Natl. Acad. Sci.* **2008**, *105*, 10366.
- [39] Hinrichs, M. H.; Jalal, A.; Brenner, B.; Mandelkow, E.; Kumar, S.; Scholz, T. *J. Biol. Chem.* **2012**, *287*, 38559.
- [40] Lewandowski, J. R.; Halse, M. E.; Blackledge, M.; Emsley, L. *Science* **2015**, *348*, 578.

## Chapter 4

### STRUCTURAL STUDIES OF KIF5B MOTOR DOMAIN IN COMPLEX WITH MICROTUBULES BY MAS NMR<sup>2</sup>

#### 4.1 Introduction

Conventional kinesin (also referred to as kinesin), the first member of the kinesin superfamily to be discovered, is a microtubule-associated motor protein that drives microtubule plus-end transport toward the periphery of the cell.<sup>1</sup> Due to its important roles in cell mitosis and intracellular transport, kinesin is an emerging target for the development of anti-cancer therapeutics.<sup>2</sup> Moreover, kinesin is a highly processive motor protein and serves as a chemomechanical model for understanding molecular motor movement. Therefore, understanding the structural and dynamic bases of its interaction with microtubules is critical to unraveling kinesin's biological mechanism.

The structures of kinesin in different nucleotide states at atomic resolution are indispensable to understanding the stepping mechanism of the protein along microtubules. The structure of kinesin bound to an  $\alpha/\beta$  tubulin heterodimer in free and ATP-binding states has recently been determined by X-ray crystallography.<sup>3,4</sup> Cryo-

---

<sup>2</sup> The study presented in this chapter was conducted in collaboration with Professor John C. Williams from the Beckman Research Institute of City of Hope and Dr. Antonina Roll-Mecak from National Institutes of Health.

electron microscopy (cryo-EM) also has been successfully applied in the structural determination of the kinesin motor domain in complexes with polymeric microtubules in all nucleotide-binding states with a resolution of 5 ~ 9 Å.<sup>5-7</sup> Despite existing studies by X-ray crystallography and cryo-EM, critical dynamics information underlying kinesin subdomain reorientation and domain movement is lacking. Knowledge of dynamics is crucial for understanding long-range transport mediated by local motions within the motor. To answer these questions, we have pursued MAS NMR characterization of kinesin's structure and dynamics on microtubules. In this chapter we describe the foundational studies that established the feasibility of MAS NMR analysis of kinesin/microtubule assemblies at atomic resolution. Specifically, we discuss the sample preparation protocols of kinesin//MT complexes compatible with MAS NMR spectroscopy. We present preliminary structural studies of kinesin/MT complexes in the nucleotide-free and ADP-bound states. This is the first atomic-level study of a kinesin motor protein-microtubule complex by MAS NMR.

## **4.2 Materials and Methods**

The conventional kinesin Kif5b motor domain construct includes N-terminal residues 1-349 consisting of the highly conserved motor domain and the neck linker. Kif5b is a monomer, with a molecular weight of 39.3 kDa. The primary sequence and secondary structure as determined by X-ray crystallography are shown in Figure 4.1. This work represents the first successful expression and purification of Kif5b (1-349) for MAS NMR characterization.

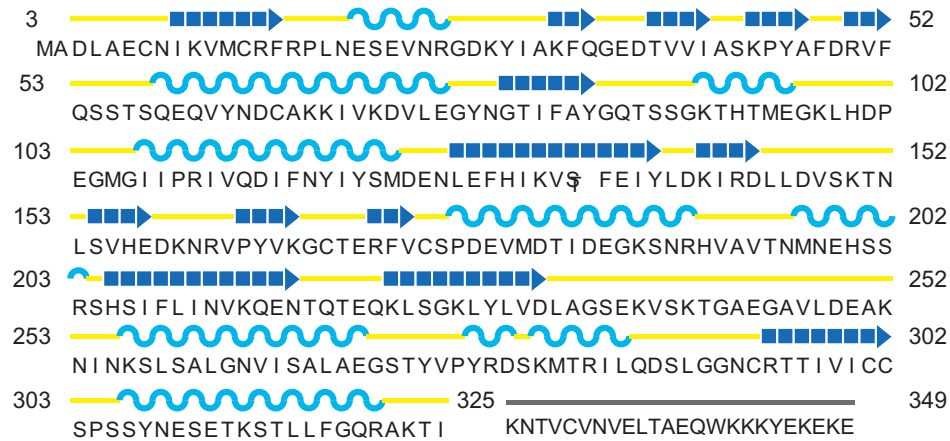


Figure 4.1: The primary sequence of the first 349 amino acids of human kinesin Kif5b containing the conserved motor domain (1-349). The secondary structure, as determined by X-ray crystallography, is indicated from residue 3 to residue 325 (PDB ID code: 1BG2). Yellow, dark blue, and light blue represent random coil,  $\beta$  sheet, and  $\alpha$  helix secondary structures, respectively. Residues 325 to 349 are missing in the X-ray structure.

#### 4.2.1 Materials

Common chemicals were purchased from Fisher Scientific or Sigma-Aldrich.  $^{15}\text{NH}_4\text{Cl}$ ,  $\text{U-}^{13}\text{C}_6$  glucose,  $\text{U-}^{13}\text{C}_6$ ,  $\text{D}_7$  glucose, and 99.8%  $\text{D}_2\text{O}$  were purchased from Cambridge Laboratories, Inc. EDTA-free protease inhibitor tablets were obtained from Roche. Chromatographic columns were purchased from GE Healthcare. Lyophilized bovine brain tubulin was purchased from Cytoskeleton, Inc. Paclitaxel (taxol) was purchased from Alexis. Guanosine triphosphate (GTP) was purchased from MP Biomedicals. Four hundred mesh copper grids coated with formvar and stabilized with evaporated carbon films were purchased from Electron Microscopy Science.

The human Kif5b motor domain construct optimized for expression in *E.coli* BL21 (DE3) was prepared by our collaborator Professor John C. Williams at the

Beckman Institute of City of Hope. This construct contains Kif5b motor domain (1-349) with a His<sub>6</sub>-SMT3 Tag fused to the N-terminus (in the form of His<sub>6</sub>-SMT3-Kif5b). The His<sub>6</sub>-Ulp1 protease construct was provided by Dr. Christopher Lima from the Weill Medical College at Cornell University.

#### **4.2.2 Expression of Isotopically Labeled Kif5b (1-349)**

U-<sup>13</sup>C, <sup>15</sup>N-enriched Kif5b was prepared according to the method described by Marley et al.<sup>8</sup> In brief, *E. coli* cells containing the recombinant protein construct were cultured in 2 L of fresh Luria broth (LB) medium supplemented with 0.03 mg/mL of kanamycin, and grown at 35 – 37 °C in an incubator shaker. When the OD<sub>600</sub> reached 1.2 – 1.6, cells were pelleted down by centrifugation at 4,000 g for 25 min, followed by washing with M9 minimal media containing no nitrogen or carbon sources. After pelleting again, cells were resuspended in 1 L of M9 minimal medium containing 2 g of <sup>15</sup>NH<sub>4</sub>Cl, 4 g of U-<sup>13</sup>C<sub>6</sub> glucose (for <sup>15</sup>N-enriched Kif5b, natural abundance D-glucose was used instead), basal vitamins, 0.1 mM CaCl<sub>2</sub>, and 2 mM MgSO<sub>4</sub>. Cells were incubated for 1 hour at 25 °C, after which IPTG was added to a final concentration of 0.8 mM for induction. Protein expression proceeded overnight at 25 °C and cells were harvested by centrifugation at 4,000 g for 25 min at 4 °C and the cell pellet was resuspended in 1x PBS buffer and stored at -80 °C.

U-<sup>2</sup>H, <sup>13</sup>C, <sup>15</sup>N-Kif5b was expressed in M9 media prepared in 99.8% D<sub>2</sub>O and supplemented with U-<sup>13</sup>C<sub>6</sub>, D<sub>7</sub> glucose and <sup>15</sup>NH<sub>4</sub>Cl. Cells were first grown in 25 mL of LB media overnight at 37 °C. Cells were then harvested and resuspended in 50 mL M9 minimal media (in H<sub>2</sub>O) to give a starting OD of about 1. After growth at 37 °C to an OD of ~1.5, cells were pelleted down by centrifugation at 4,000 g for 20 mins, followed by resuspension in 75 mL of M9 media (in 70% D<sub>2</sub>O). When the OD

reached ~2.9, cells were harvested at 4,000 g for 20 min and transferred into 150 mL M9 media (99.8% D<sub>2</sub>O). Natural abundance D-glucose and <sup>15</sup>NH<sub>4</sub>Cl were used as the carbon and nitrogen sources in all the M9 minimal media for the adaptation steps described above. After growth overnight, the cells were pelleted and transferred into 900 mL of minimal media (99.8% D<sub>2</sub>O). The induction culture was incubated at 37 °C until the OD reached 1.1, at which point the temperature of the shaker was lowered to 18 °C for expression. When the OD reached ~1.2 expression was induced with IPTG at a final concentration of 0.8 mM. Expression proceeded for 20 hrs at 18 °C and cells were harvested at 4,000 g for 30 min, and stored at -80 °C.

#### **4.2.3 Purification of Isotopically Labeled Kif5b (1-349)**

Natural abundance, U-<sup>15</sup>N-enriched, U-<sup>13</sup>C,<sup>15</sup>N-enriched and U-<sup>2</sup>H,<sup>13</sup>C,<sup>15</sup>N-enriched Kif5b were purified according to the same protocol. Cells were thawed on ice, followed by the addition of one tablet of EDTA-free protease inhibitor and DTT (200 mM) to a final concentration of 1 mM. The cells were lysed by homogenization under the pressure of 10 psi for 14–16 cycles at 4 °C, and the cell debris was pelleted by centrifugation at 15,000 rpm (27,000 g) for 30 min at 4 °C. The supernatant was filtered through a 0.2 mm filter and applied to a 5 mL HisTrap Ni-affinity column. Subsequently, the target recombinant protein was eluted with a 120 to 240 mM imidazole gradient (1x PBS, 1 mM DTT, pH 7.4). Fractions containing the target protein were combined and incubated overnight with the His<sub>6</sub>-Ulp-1 enzyme to cleave the His<sub>6</sub>-SMT3-tag. Subsequently, imidazole was diluted (to less than 10 mM) by diafiltration over a 30 kDa membrane in an Amicon stir unit (from EMD Millipore). The resulting solution was loaded onto a 5 mL HisTrap Ni-affinity column after clarification by centrifugation at 4,000g for 10 mins. Kif5b was eluted with 80 mM

imidazole buffer. The protein was exchanged into PIPES buffer (25 mM PIPES, 1 mM EGTA, 1 mM MgCl<sub>2</sub>, 1 mM DTT, 200 mM KCl, pH 6.8). The purity of the protein was assessed by SDS-PAGE gel, as shown in Figure 4.2.

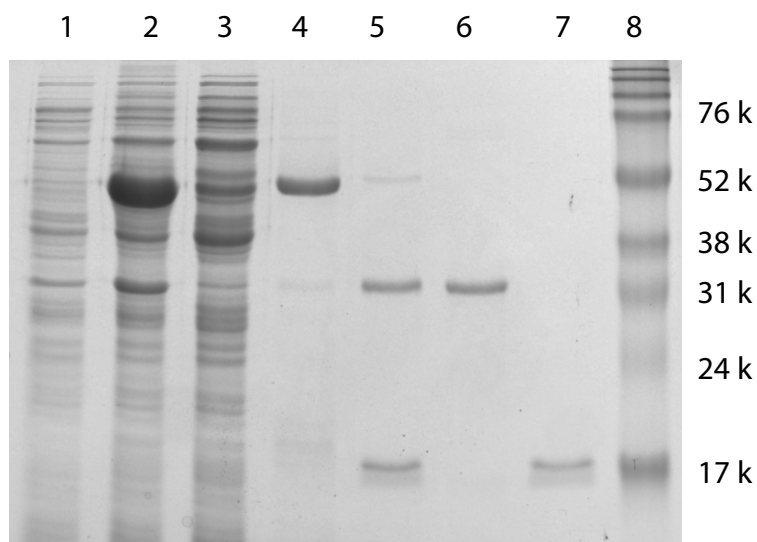


Figure 4.2: Purification of Kif5b motor domain characterized by SDS-PAGE gel. Lane 1: before cell induction; 2: after protein expression; 3: cell lysate; 4: combined fractions from the first HisTrap column; 5: cleavage of His<sub>6</sub>-SMT3-tag by Ulp-1 protease; 6: combined fractions from the second HisTrap column; 7: His<sub>6</sub>-SMT3-tag; 8: molecular weight marker.

The typical yield for natural abundance Kif5b from LB rich media is about 5 mg/L. For uniformly <sup>15</sup>N-labeled and for <sup>13</sup>C, <sup>15</sup>N doubly labeled Kif5b, the yield is about 8-10 mg/L in M9 minimal media. The yield of perdeuterated <sup>13</sup>C, <sup>15</sup>N-Kif5b is around 3-4 mg/L in D<sub>2</sub>O M9 minimal media.

#### **4.2.4 Preparation of Kif5b for Solution NMR**

<sup>15</sup>N-Kif5b was expressed and purified according to the protocol described above. <sup>15</sup>N-Kif5b was prepared with two different buffer conditions for solution NMR studies. The Tris buffer (pH = 6.3) contained 50 mM Tris (Tris(hydroxymethyl)aminomethane), 100 mM NaCl, 1 mM EDTA, 1 mM DTT, and the PIPES buffer (pH = 6.8) contained 25 mM PIPES, 1 mM EGTA, 1 mM MgCl<sub>2</sub>, 1 mM DTT, 200 mM KCl. About 500 μL sample containing 2.9 mg of <sup>15</sup>N-Kif5b with a final concentration of 0.15 mM and 50 μL D<sub>2</sub>O (10%) was used for solution NMR measurements.

#### **4.2.5 Preparation of Paclitaxel-Stabilized Microtubules**

Lyophilized tubulin was dissolved in BRB80 buffer (80 mM PIPES, 1 mM MgCl<sub>2</sub>, 1 mM EGTA, pH 6.8), and clarified with ultracentrifugation at 100,000 rpm (435,400 g) for 10 minutes, in a Beckman Coulter Optima MAX-XP ultracentrifuge with a TLA 120.2 rotor. The resulting tubulin supernatant was polymerized in the presence of 25 μM paclitaxel by addition of an equal volume of 2x polymerization mix buffer (2 mM GTP, 160 mM PIPES, 20% (v/v) DMSO). After incubation for 30 minutes at 37 °C, the supernatant and pellet were separated by centrifugation at 40,000 rpm (108,900 g) for 10 min. The pellet containing paclitaxel-stabilized microtubules was saved and resuspended gently to a desired concentration for subsequent studies. The concentration of paclitaxel used for stabilizing microtubules in solution was typically 20-25 μM.

#### **4.2.6 Cosedimentation Assay**

MT filaments were prepared according to the protocol described above. Kif5b stock solution was clarified at 100,000 rpm (435,400 g) for 10 minutes before use.

Generally, Kif5b and MT stocks were co-incubated for about 30 minutes to form the Kif5b/MT complex. Subsequently the supernatant and pellet were separated by ultracentrifugation at 40,000 rpm (108,900 g). Aliquots of the supernatant (S) and pellet (P) were loaded onto SDS-PAGE gel for electrophoresis analysis.

To determine the optimum ratio of Kif5b to MTs for efficient binding, MTs were freshly prepared and mixed with various concentrations of Kif5b to final Kif5b/MTs ratio of 1:1, 2:1, and 11:1. The final concentration of MTs was 11  $\mu$ M for all trials, and the final Kif5b concentrations were 12.7  $\mu$ M, 25.4  $\mu$ M and 127  $\mu$ M, respectively. The optimal binding ratio was found to be 2:1, as further discussed below.

To assess the effects of different nucleotides on binding, a Kif5b:MT molar ratio of 2:1 was used with final concentrations of MTs and Kif5b of 11  $\mu$ M and 25.4  $\mu$ M, respectively. The final concentration of nucleotide (ATP or AMP-PNP) was 2 mM. For the semi-quantitative analysis of Kif5b binding with MTs in the presence of 1 mM ADP, the final concentrations of Kif5b and MTs used were 18  $\mu$ M and 5  $\mu$ M, respectively, to reach a final molar ratio of 3.6 during incubation. The binding of Kif5b/MTs in the presence of 10% sucrose was also examined. A 50% (w/v) sucrose stock was added to the Kif5b/MT complex suspension to reach a final concentration of 10%. The final concentrations of Kif5b and MTs used were 37.4  $\mu$ M and 18.2  $\mu$ M with a molar ratio close to 2:1.

#### **4.2.7 Morphological Characterization of Microtubules and Kif5b/MT Complexes**

The morphology of microtubules and Kif5b/MT complexes was characterized by transmission electron microscopy (TEM). TEM analysis was performed with a

Zeiss Libra 120 transmission electron microscope operating at 120 kV. Samples of 5–10  $\mu\text{M}$  microtubules or complexes were stained with uranyl acetate (5% w/v), deposited onto 400-mesh, formvar/carbon-coated copper grids and air-dried for 40–60 min.

#### **4.2.8 Preparation of U- $^{13}\text{C}$ , $^{15}\text{N}$ -Kif5b/Microtubule Assemblies for MAS NMR Studies**

In total, six batches of Kif5b/MT assemblies were prepared for MAS NMR studies. The NMR samples were prepared by cosedimentation following a general protocol. The rotor packing procedures for NMR samples were modified for each sample with respect to the centrifugation speed, centrifugation time, packing method, and sucrose conditions. Details for individual sample preparations are summarized in Table 4.1.

Paclitaxel-stabilized microtubules were freshly prepared with 14 mg of bovine tubulin, according to the protocol described above. The polymeric microtubules were gently resuspended with U- $^{15}\text{N}$ ,  $^{13}\text{C}$  kinesin stock solution with 25  $\mu\text{M}$  paclitaxel for stabilization of MTs. The mixture was incubated at room temperature for 30 min followed by ultracentrifugation at 60,000 rpm (156,800 g) for 15 min. The centrifugation step was repeated in seven increments, and the supernatant was removed after each step, to collect the total sample into a single centrifuge tube. The pellet was transferred into Bruker thin wall 3.2 mm rotor. 42 mg of hydrated U- $^{15}\text{N}$ ,  $^{13}\text{C}$  Kif5b/MT complexes were packed per rotor.

Table 4.1: Summary of Sample Preparation Details for Kif5b/MT Complex

Number	Sample	Centrifugation		Centrifugation Time	Sucrose	ADP	Packing method	Spectra Quality	Sample Stability
		Rotor size (mm)	Speed for Packing (RCF)						
1	<sup>15</sup> N-Kif5b/MT	3.2 (regular)	108,900 g	10 mins*4	N	N	Pipette tips	High resolution	Stable
2	<sup>13</sup> C, <sup>15</sup> N-Kif5b/MT	3.2 (regular)	108,900 g	10 mins*4	N	N	Pipette tips	High resolution	Stable
3	<sup>13</sup> C, <sup>15</sup> N-Kif5b/MT	3.2 (thin wal)	156,800 g	10 mins*7	N	N	Pipette tips	High resolution	Stable
4	<sup>13</sup> C, <sup>15</sup> N-Kif5b/MT	1.3	352,700 g	2 hrs	Y	N	Pipette tips	High resolution	Rotor crashed overnight
5	<sup>2</sup> H, <sup>13</sup> C, <sup>15</sup> N-Kif5b/MT	1.9	352,700 g	2 hrs	Y	N	Pipette tips	High resolution	Deteriorated over MAS
6	<sup>13</sup> C, <sup>15</sup> N-Kif5b/MT	1.9	352,700 g*	1 hr	Y	N	Rotor packing tool**	Low resolution	-
7	<sup>13</sup> C, <sup>15</sup> N-Kif5b/MT	1.9	435,400 g	1 hr	Y	Y	Pipette tips	Low resolution	-
8	<sup>13</sup> C, <sup>15</sup> N-Kif5b/MT	1.9	352,700 g	1 hr	Y	Y	Rotor packing tool*	Low resolution	-

\*Done in a swing bucket ultracentrifuge (Colburn Laboratory), 4/7 indicates the number of steps/aliquots to combine the sample into a single centrifuge tube

\*\*A 1.9 mm rotor packing tool originally designed by Prof. Patrick Van der Wel from the University of Pittsburgh with slight modification by our lab.

Table 4.1: Summary of Sample Preparation Details for Kif5b/MT Complex (continued)

Number	Sample	Concentration of Kif5b stock (mg/mL)	Tubulin dimer concentration (mg/mL)	Kif5b/MT molar ratio	Total Sample Mass (mg)	Estimated Mass Labeled Kif5b (mg)
1	<sup>15</sup> N-Kif5b/MT	2.86	2.50	3.20	28.80	1.60
2	<sup>13</sup> C, <sup>15</sup> N-Kif5b/MT	3.20	2.50	3.58	27.10	1.40
3	<sup>13</sup> C, <sup>15</sup> N-Kif5b/MT	2.80	2.50	3.13	42.00	2.70
4	<sup>13</sup> C, <sup>15</sup> N-Kif5b/MT	3.64	2.50	4.08	4.40	0.90
5	<sup>2</sup> H, <sup>13</sup> C, <sup>15</sup> N-Kif5b/MT	2.30	3.30	1.95	10.00	1.40
6	<sup>13</sup> C, <sup>15</sup> N-Kif5b/MT	2.84	4.00	1.99	16.00	1.90
7	<sup>13</sup> C, <sup>15</sup> N-ADP-Kif5b/MT	3.60	2.50	4.03	8.90	1.40
8	<sup>13</sup> C, <sup>15</sup> N-ADP-Kif5b/MT	2.84	4.00	1.99	16.10	1.80

#### 4.2.9 Preparation of ADP U-<sup>13</sup>C, <sup>15</sup>N Kif5b/MT Assemblies for MAS NMR Studies

An ADP stock solution (40 mM) was added to the Kif5b stock solution (91.6 μM) in a buffer (25 mM PIPES, 1 mM EGTA, 1 mM MgCl<sub>2</sub>, 100 mM KCl, 1mM DTT, pH 6.8) to reach a final concentration of 1 mM ADP, and was stored on ice at 4°C overnight. The ADP-Kif5b/MT complex was prepared following the protocol described above.

#### 4.2.10 Solution NMR Experiments

Two-dimensional <sup>1</sup>H-<sup>15</sup>N HSQC spectra of <sup>15</sup>N-Kif5b were acquired on a 14.1 T Bruker AVANCE spectrometer equipped with a triple-resonance inverse detection (TXI) probe. The Larmor frequencies were 600.1 MHz (<sup>1</sup>H) and 60.8 MHz (<sup>15</sup>N). The sample temperature was maintained at 4°C.

#### 4.2.11 MAS NMR Experiments

MAS NMR spectra of U- $^{13}\text{C}$ ,  $^{15}\text{N}$ -Kif5b/MT were acquired on a 19.96 T Bruker AVANCE III instrument with a 3.2 mm EFree HCN probe. The Larmor frequencies were 850.4 MHz ( $^1\text{H}$ ), 213.8 MHz ( $^{13}\text{C}$ ), and 86.2 MHz ( $^{15}\text{N}$ ). The MAS frequency of 14 kHz was maintained within  $\pm 10$  Hz by a Bruker MAS controller. The temperature was calibrated for this probe with KBr<sup>9</sup> and the sample temperature was maintained within  $\pm 0.5$  °C in all experiments using a Bruker temperature controller.

The typical  $90^\circ$  pulse lengths were 2.9-3.0  $\mu\text{s}$  for  $^1\text{H}$ , 3.0-3.2  $\mu\text{s}$  for  $^{13}\text{C}$ , and 4.0-4.2 for  $^{15}\text{N}$ . The  $^1\text{H}$ - $^{13}\text{C}$  and  $^1\text{H}$ - $^{15}\text{N}$  cross polarization (CP) step employed a linear amplitude ramp of 80-100%, and a  $^1\text{H}$  RF field of 86 kHz. The center of the ramp on the  $^{13}\text{C}$  or  $^{15}\text{N}$  was matched to the first spinning sideband of the Hartmann-Hahn condition. 1D  $^1\text{H}$ - $^{15}\text{N}$  CP spectra were acquired at 27 °C, 22 °C, 17 °C, 12 °C, and 7 °C. For CORD (combined  $\text{R}2_n^v$ -driven)  $^{13}\text{C}$ - $^{13}\text{C}$  correlation experiments, RF fields of 14 kHz and 7 kHz on the proton channel were used during the CORD mixing time (50 ms). In the NCA experiment, magnetization was transferred from  $^{15}\text{N}$  to  $^{13}\text{C}^\alpha$  using a 4.9 ms SPECIFIC-CP sequence with a tangent amplitude ramp (90%-110%), and RF field strengths of 48 kHz, 36 kHz and 85 kHz for  $^{15}\text{N}$ ,  $^{13}\text{C}$ , and  $^1\text{H}$  channels, respectively. A  $^1\text{H}$  decoupling field strength of 80-90 kHz was used during acquisition for all heteronuclear-detected experiments.

Proton-detected MAS NMR spectra of the U- $^{13}\text{C}$ ,  $^{15}\text{N}$ -Kif5b/MT complexes were acquired with a 1.3 mm HCN probe on the same 19.96 T Bruker AVANCE III spectrometer at an MAS frequency of 60 kHz. Sample temperature was maintained at 17 °C (which accounted for an additional 40 °C heating from MAS). A  $90^\circ$  pulse of 1.72  $\mu\text{s}$  was used on the proton channel. In the 2D proton-detected heteronuclear correlation (NH-HETCOR) experiment, a tangent amplitude ramp of 90-110% was

employed during cross polarization. The  $^1\text{H}$  RF field was 156 kHz and the  $^{15}\text{N}$  field was 99 kHz at the center of the ramp. Low power saturation (5 kHz) was applied for water signal suppression. A  $^1\text{H}$  decoupling power of 15 kHz was used during acquisition.

Proton-detected NH-HETCOR spectra of perdeuterated U- $^{13}\text{C}$ ,  $^{15}\text{N}$ ,  $^2\text{H}$ -Kif5b in complex with microtubules were acquired with a 1.9 mm HCN probe at an MAS frequency of 40 kHz. The sample temperature was maintained at 17 °C (which includes 40 °C additional heating from MAS). A 3.3  $\mu\text{s}$   $^1\text{H}$  90° pulse was used.  $^1\text{H}$ - $^{15}\text{N}$  cross polarization employed a tangent amplitude ramp of 90-110%, the  $^1\text{H}$  RF field was 57 kHz and the  $^{15}\text{N}$  RF field was 88 kHz at the center of the ramp.

MAS NMR spectra of ADP-U- $^{15}\text{N}$ ,  $^{13}\text{C}$ -Kif5b/microtubule complex were acquired with a 1.9 mm HCN probe at an MAS frequency of 14 kHz. The sample temperature was first maintained at 17±0.3 °C and then lowered to -21±0.3 °C. Typical  $^1\text{H}$ ,  $^{13}\text{C}$ , and  $^{15}\text{N}$  90° pulses of 3  $\mu\text{s}$ , 3  $\mu\text{s}$ , and 3.6  $\mu\text{s}$  were applied. The  $^1\text{H}$ - $^{13}\text{C}$  and  $^1\text{H}$ - $^{15}\text{N}$  CP spectra were recorded with a linear amplitude ramp of 80-100% and the  $^1\text{H}$  RF field were set to 69 and 62 kHz respectively. The center of the ramp on the  $^{13}\text{C}$  or  $^{15}\text{N}$  was Hartmann-Hahn matched to the first spinning sideband. Homonuclear CORD and heteronuclear NCA and NCO correlation spectra were acquired with the previously described experimental parameters.

## **4.3 Results and Discussion**

### **4.3.1 Solution NMR Studies of U- $^{15}\text{N}$ -Kif5b**

Prior to MAS NMR studies of Kif5b, we have performed its solution NMR characterization, to corroborate that the protein is folded and assess the efficiency of

isotopic labeling. Resonance assignments based on solution NMR datasets can also support the resonance assignments in the solid state.  $^1\text{H}$ - $^{15}\text{N}$  HSQC spectra of U- $^{15}\text{N}$ -Kif5b with different buffer conditions are shown in Figure 4.3. The presence of NMR signals in these spectra indicates that Kif5b was successfully isotopically enriched in minimal media. Under both buffer conditions, the number of detected signals is much lower than the number of amino acids in the sequence, and (not surprisingly) the spectral lines are considerably broadened. This line broadening can be explained by the large size of Kif5b (39.3 kDa), which results in slower tumbling rates in solution, and thus shorter NMR signal relaxation times. The relatively few observed signals likely arise from flexible sidechains and dynamic regions of Kif5b.

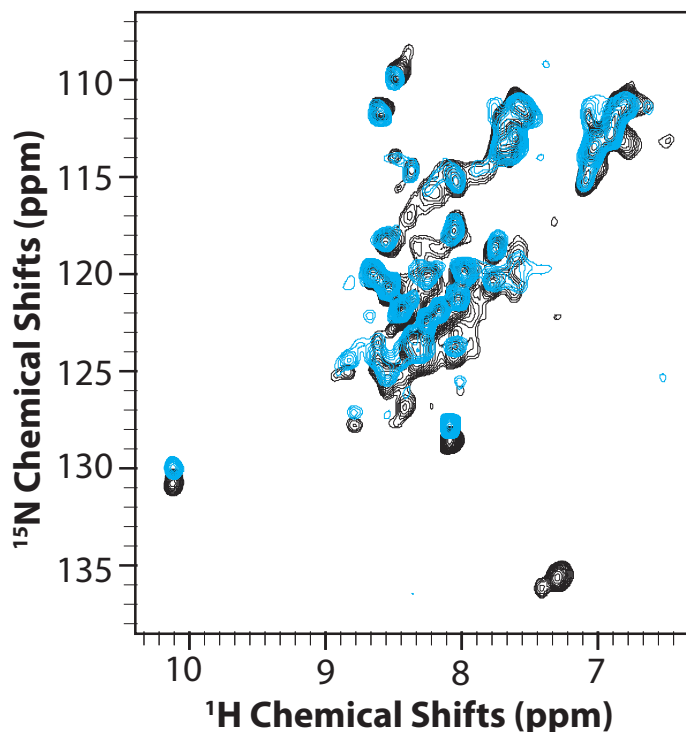


Figure 4.3: Overlay of 14.1 T solution HSQC spectra of  $^{15}\text{N}$ -Kif5b prepared in different buffers. Blue:  $^{15}\text{N}$ -Kif5b in Tris buffer (50 mM Tris, 100 mM NaCl, 1 mM EDTA, 1 mM DTT, pH 6.3). Black:  $^{15}\text{N}$ -Kif5b in PIPES buffer (25 mM PIPES, 1 mM EGTA, 1 mM  $\text{MgCl}_2$ , 1 mM DTT, 200 mM KCl, pH 6.8)

#### 4.3.2 Preparation of Kif5b/MT Assemblies for MAS NMR Studies

Before one can obtain valuable MAS NMR data, sample conditions compatible with MAS NMR must first be established. The Kif5b sample buffer condition (25 mM PIPES, 1mM EGTA, 1mM  $\text{MgCl}_2$ , 200 mM KCl, 1 mM DTT, pH 6.8) was selected based on prior X-ray crystallography and electron microscopy studies.<sup>11</sup> Under such conditions, Kif5b is stable at 4°C for two weeks, before it starts to precipitate. In the formation of the Kif5b/MT complexes, the PIPES buffer concentration may affect the stability of microtubules as shown in our laboratory by Dr. Si Yan.<sup>12</sup> In our studies,

the depolymerization of MTs is not observed under such buffer conditions, as confirmed by the SDS-PAGE assay.

The formation of the Kif5b/MT complexes under different conditions is evaluated by a cosedimentation assay to determine the optimal molar ratio of Kif5b to MT for preparation of NMR samples. The optimal binding of Kif5b to paclitaxel-stabilized microtubules is determined by varying the Kif5b/MT ratios, as shown in Figure 4.4a. The proportion of Kif5b co-sedimented into the pellet was found to increase as the molar ratio of Kif5b/MT is decreased from 2:1 to 1:1. When the molar ratio is decreased from 2:1 to 11:1, the proportion of bound Kif5b does not increase dramatically. This result indicates that the surface of the microtubules has been largely decorated by Kif5b at a molar ratio of Kif5b/MT around 2:1. A similar trend is observed in the presence of a non-hydrolyzable ATP analog AMP-PNP, as shown in Figure 4.4b. We conclude that a molar ratio of Kif5b/MT around 2:1 is optimal in the preparation of Kif5b/MT complexes for MAS NMR studies.

The binding affinity of Kif5b for MTs in the presence of the nucleotides ATP, AMP-PNP, and ADP was estimated, and the corresponding co-sedimentation assay results are shown in Figure 4.4c and 4.4d. The presence of 2 mM ATP reduces the binding of Kif5b to MTs. The binding and hydrolysis of ATP may cause Kif5b to detach from the MT lattice. Kif5b binds to MTs with similar affinity in both the nucleotide-free state and in the presence of 2 mM AMP-PNP. A semi-quantitative analysis of Kif5b binding with tubulin shows that Kif5b and MTs form a complex with a 1:1 ratio in the presence of 1 mM ADP. In the following, Kif5b/MT complexes in both their free and ADP-bound states were examined by MAS NMR spectroscopy.

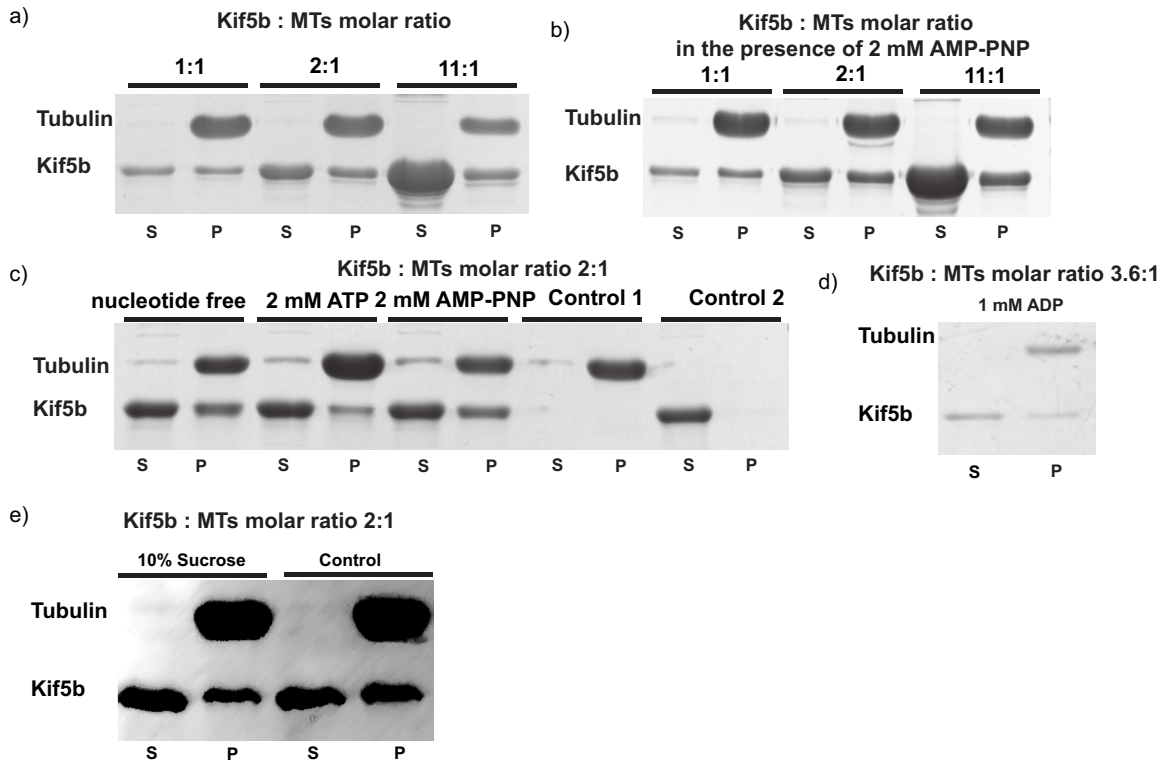


Figure 4.4: SDS-PAGE gel of co-sedimentation assays of Kif5b with microtubules under different conditions. For all experiments, the pellet is indicated by “P”, and supernatant is indicated by “S”. a) Co-sedimentation assays of Kif5b/MTs with different Kif5b to MT ratios as indicated at the top of the gel. b) Co-sedimentation assays of Kif5b/MTs with different Kif5b to MT ratios in the presence of 2 mM AMP-PNP. c) Co-sedimentation assays of Kif5b/MTs with different nucleotide conditions including nucleotide free, in the presence of 2mM ATP, and in the presence of 2 mM AMP-PNP. Control 1 is free microtubule; control 2 is free Kif5b. d) Semi-quantitative analysis of Kif5b binding with MTs in the presence of 1 mM ADP by co-sedimentation assay. The molar ratio of Kif5b to MTs is 3.6. e) The effect of 10% sucrose on the binding of Kif5b to MTs characterized by co-sedimentation assay. The control experiment is done in the absence of 10% sucrose.

Table 4.2: Sensitivity in the MAS NMR Experiments for Different Kif5b/MT Complex Samples

Number	Sample	Temp	Rotor	MAS freq.	Experiment	NS	S/N		
1	<sup>15</sup> N-Kif5b/MT	27 °C	3.2 mm	14 kHz	NCP	2048	N 30.4		
		22 °C			NCP	2048	N 33.5		
		17 °C			NCP	2048	N 35.8		
		12 °C			NCP	2048	N 42.3		
2	<sup>13</sup> C, <sup>15</sup> N-Kif5b/MT	17 °C	3.2 mm	14 kHz	DARR	512	CO 25.4	CA 18.8	CX 26
					NCP	256	N 10.9		
3	<sup>13</sup> C, <sup>15</sup> N-Kif5b/MT	17 °C	3.2 mm	14 kHz	NCP	128	N 15.4		
					CORD	288	CO 42.8	CA 30.2	CX 46.8
					NCA	2048	CA 17.9		
					NCACX	2048	CO 9.6	CA 7.4	CX 4.5
4	<sup>13</sup> C, <sup>15</sup> N-Kif5b/MT	17 °C	1.3 mm	60 kHz	NH-HETCOR	192	H 97		
5	<sup>2</sup> H, <sup>13</sup> C, <sup>15</sup> N-Kif5b/MT	17 °C	1.9 mm	40 kHz	NH-HETCOR	128	H 83		
					CH-HETCOR	512	CO 16	CA 20	CX 12
					CANH	256	H 12.2		
					CCP	128	CO 8	CA 10.9	CX 6.5
					NCP	128	N 10.1		
6	<sup>13</sup> C, <sup>15</sup> N-Kif5b/MT	17 °C	1.9 mm	14 kHz	NCP	128	N 10.5		
					CCP	1024	CO 23.6	CA 17.5	CX 32.1
					CORD	512	CO 34	CA 24	CX 37.9
					NCA	2048	CA 11		
		17 °C	1.9 mm	14 kHz	NCP	128	N 9.8		
					CCP	1024	CO 37	CA 62.3	CX 62.3
					CORD	400	CO 29	CA 22.6	CX 34.5

					NCA	1728		CA 11.9	
7	$^{13}\text{C}, ^{15}\text{N}$ -ADP-Kif5b/MT	17 °C	1.9 mm	14 kHz	CORD	512	CO 22.6	CA 16.6	CX 23.8
		-21 °C	1.9 mm	14 kHz	NCO	2400	CO 18		
					CORD	224	CO 27.5	CA 20.9	CX 20.9
					NCO	512	CO 16.7		
					NCA	1024		CA 18.8	
					NCOCX	3072	CO 15.6	CA 11	CX 5
8	$^{13}\text{C}, ^{15}\text{N}$ -ADP-Kif5b/MT	17 °C	1.9 mm	14 kHz	CCP	256	CO 14	CA 16.9	CX 23.1
					NCP	128	N 8.5		
					CORD	400	CO 22.4	CA 17.6	CX 27.3
					NCA	3072		CA 20	

A further consideration for MAS NMR sample preparation is sample stability during magic angle spinning. Because the Kif5b/MT complex has a higher density than the buffer, the complex could sediment on the rotor wall during MAS, which may cause phase separation and sample dehydration during long periods of spinning. To prevent phase separation, 10% sucrose was used in the last step of sample pelleting. Co-sedimentation assay results shown in Figure 4e suggest that the presence of 10% sucrose does not affect the binding of Kif5b to MTs and can be used to prevent phase separation.

The experimental details for preparation of MAS NMR samples, concerning the rotor size, stock solution concentration, molar ratio of Kif5b to MTs, centrifugation speed, centrifugation time, sucrose condition, and ADP condition are summarized in Table 4.1. Assessment of sample quality based on resolution of the corresponding NMR spectra is also included in the table. The sensitivity of NMR experiments for each sample is listed in Table 4.2. The challenges encountered during sample preparation are further discussed in the section 4.3.4.

### **4.3.3 Morphological Characterization of MTs and Kif5b/MT Assemblies by TEM**

Homogeneous and stable protein samples are required to obtain high-resolution MAS NMR spectra. Negatively stained transmission electron micrographs were used for morphological characterization of samples. TEM images of microtubules, Kif5b/MT complexes, ADP-Kif5b/MT complexes and Kif5b/MT complexes after MAS are shown in Figure 4.5. Long, homogenous, well-defined microtubule filaments, without any signs of the depolymerization at their ends were consistently

observed under all conditions, indicating that the morphology of microtubules was well-preserved during the binding of Kif5b and ADP-Kif5b, as well as during MAS NMR experiments.

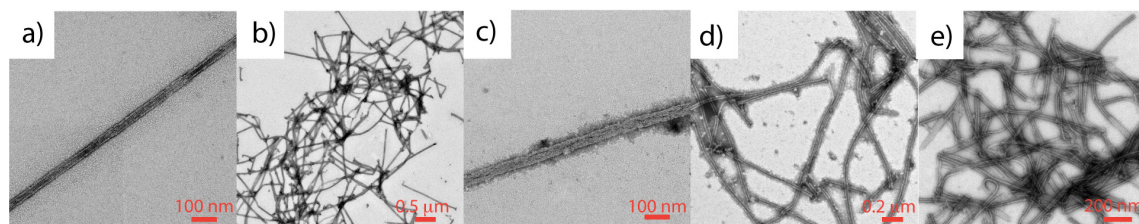


Figure 4.5: Negatively stained TEM images of free MTs and Kif5b/MT assemblies. a) A single MT filament. b) Microtubules. c) Kif5b/MT complex. d) ADP-Kif5b/MT complexes. e) Kif5b/MT assemblies after MAS.

#### 4.3.4 MAS NMR Studies of U-<sup>15</sup>N, <sup>13</sup>C-Kif5b/MT Complexes

The only NMR study of Kif5b reported to date only included 1D <sup>31</sup>P-NMR studies of ADP-bound kinesin, from which limited information was obtained.<sup>10</sup> As we demonstrate in the remainder of this chapter, with the rigorous sample preparation protocols in hand, we have obtained unprecedented-quality MAS NMR data on kinesin/microtubule assemblies, setting the stage for their atomic-resolution structure determination and the characterization of their dynamics.

The first step in our studies is to establish the temperature required for the MAS NMR experiments. Temperature is a critical parameter for obtaining high-quality spectra with optimal sensitivity and resolution. One-dimensional <sup>1</sup>H-<sup>15</sup>N CP spectra of U-<sup>15</sup>N-Kif5b/MTs at temperatures ranging from 7 °C to 27 °C are shown in Figure 4.6. The 1D <sup>1</sup>H-<sup>15</sup>N CP spectra possess very high resolution and are promising for 2D correlation studies. The sensitivity increases by approximately 16% when the

temperature is decreased from 27 °C to 7 °C, although the resolution deteriorates. The optimum balance of sensitivity and resolution is achieved at an experimental temperature of 17 °C. For subsequent NMR experiments, a sample temperature of 17 °C was used.

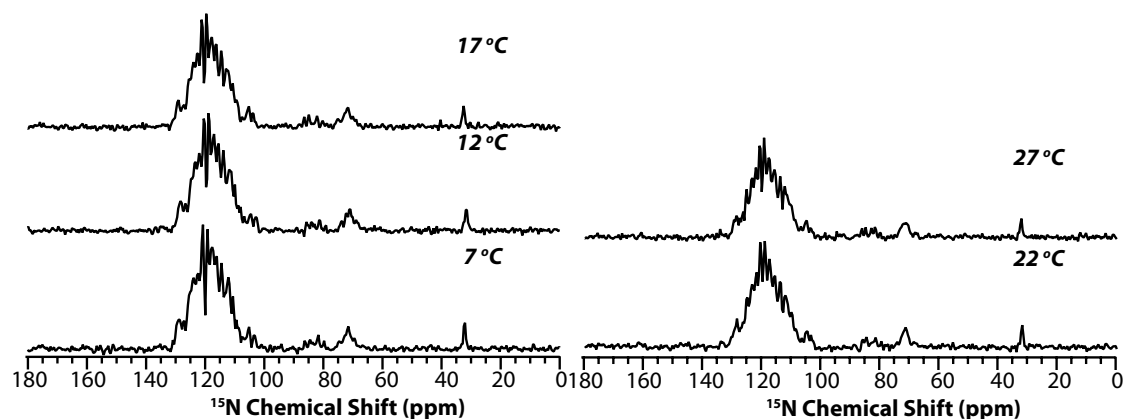


Figure 4.6:  $^1\text{H}$ - $^{15}\text{N}$  cross polarization spectra of U- $^{15}\text{N}$ -Kif5b/MT assemblies at different temperatures. The sample temperatures are indicated in the spectra. Spectra were acquired at 14 kHz MAS, 19.96 T.

The  $^{13}\text{C}$ - $^{13}\text{C}$  CORD correlation spectrum of U- $^{15}\text{N}$ ,  $^{13}\text{C}$ -Kif5b/MTs, shown in Figure 4.7, exhibits remarkable resolution and broad chemical shift dispersion. The Thr, Ser, Pro, Val, Ala, Leu and Ile regions of the spectrum (highlighted in color) can be easily identified. This clearly indicates that Kif5b is well-structured upon binding with MTs. The spin systems of Gly, Thr, Ser, Val, Ile, Ala are tentatively assigned and labeled in Figure 4.8. Corresponding chemical shifts and secondary structure as predicted by PLUQ<sup>13</sup> are summarized in Table 4.3. *SHIFTX2* can accurately predict the backbone and sidechain carbon atoms chemical shifts based on protein structure.<sup>14</sup> The spectrum generated from backbone carbon shifts predicted by *SHIFTX2* based on

the Kif5b/tubulin heterodimer X-ray structure (PDB ID code: 4LNU) is overlaid with the experimental CORD spectra and shown in Figure 4.9. The observed peak patterns are consistent in the experimental and predicted spectra, and even though the predicted chemical shifts are not in perfect agreement with experiment, the results allow one to make resonance assignments of a number of peaks by inspection. Even though not quantitative, the agreement between experimental and computed chemical shifts is remarkable (to within the expected *SHIFTX2* error) and that Kif5b is well-folded upon binding with MTs under MAS conditions, and adopts a conformation similar to that of the free Kif5b bound to tubulin heterodimer.

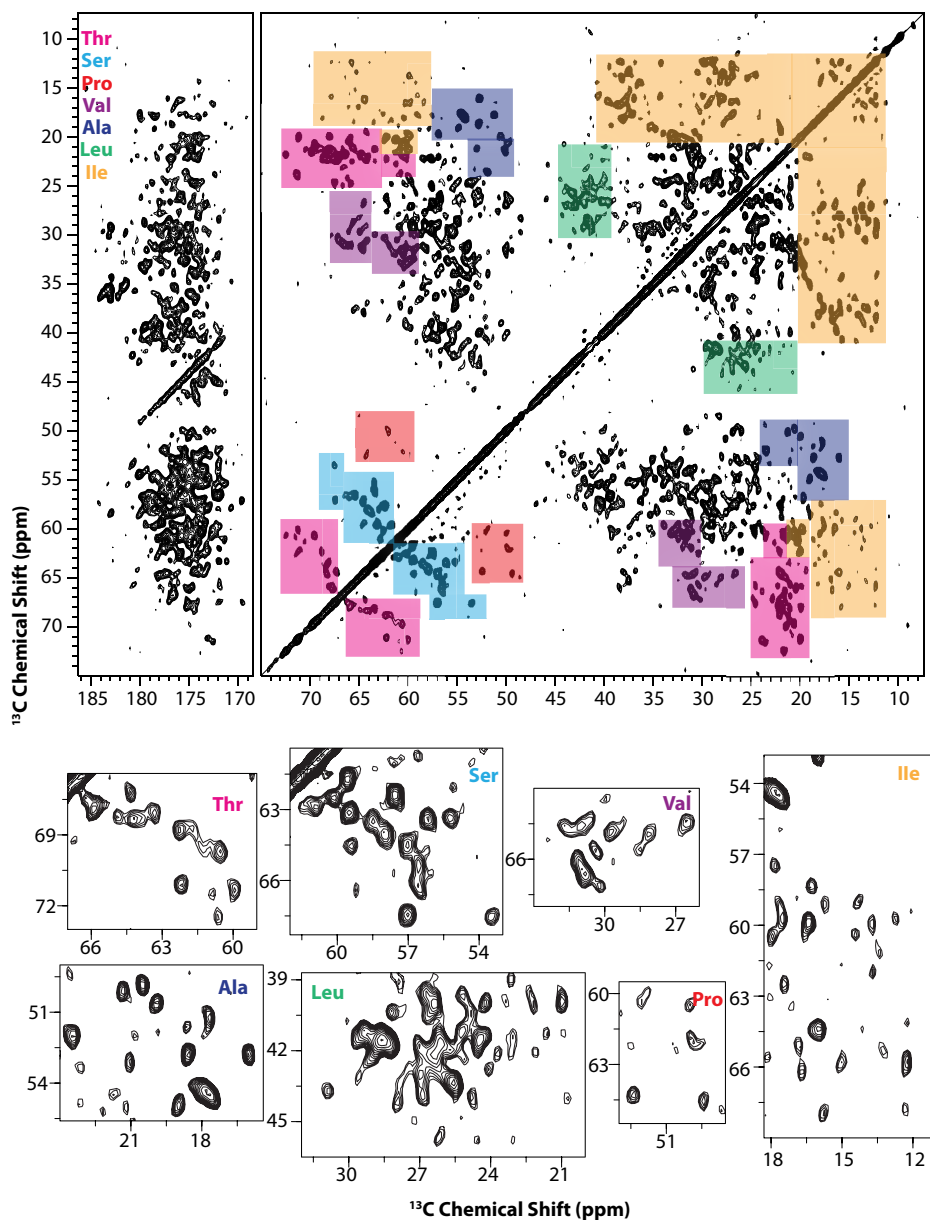


Figure 4.7.  $^{13}\text{C}$ - $^{13}\text{C}$  CORD correlation spectrum of  $\text{U-}^{13}\text{C}$ ,  $^{15}\text{N}$ -Kif5b/MT assemblies acquired at an MAS frequency of 14 kHz, field strength of 19.96 T, and sample temperature of 17 °C. Spin systems belonging to Thr, Ser, Pro, Val, Ala, Leu and Ile regions are highlighted with different colors as indicated. The expansions of the corresponding regions are shown below the full spectrum. Note the unprecedented high spectral resolution.

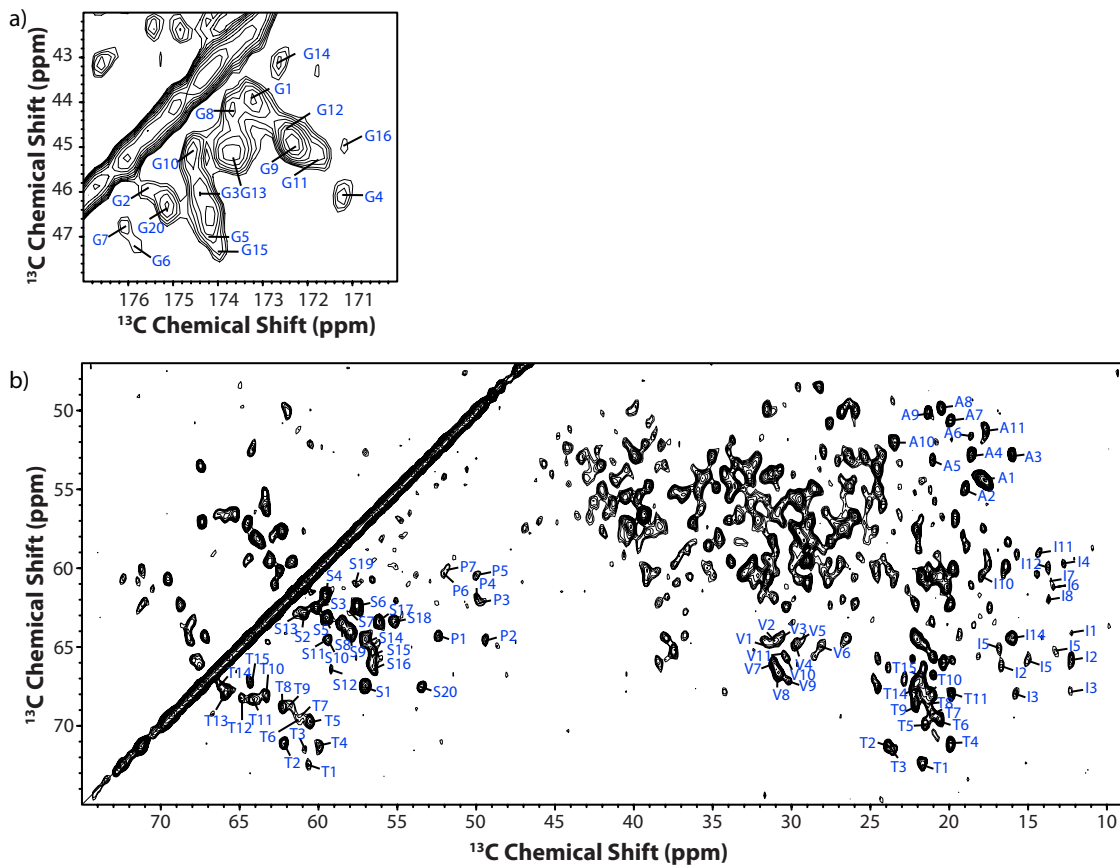


Figure 4.8: Spin system assignments of the  $^{13}\text{C}$ - $^{13}\text{C}$  CORD correlation spectrum of  $\text{U-}^{13}\text{C}$ ,  $^{15}\text{N}$ -Kif5b/MT assemblies acquired at an MAS frequency of 14 kHz, field strength of 19.96 T, and sample temperature of 17  $^\circ\text{C}$ . a)  $\text{C}^\alpha$ - $\text{C}'$  correlation region of Glycine residues. b) Backbone  $\text{C}^\alpha$ - $\text{C}^\beta$  correlation region.

Table 4.3: Spin System Assignments and Secondary Structure Prediction Based on  
CORD, NCA, and NH-HETCOR Spectra of U-<sup>13</sup>C, <sup>15</sup>N-Kif5b/MT  
Complex

Spin System Number	Residue Type	N	C $\alpha$	C'	HN	Secondary Structure
1	Gly	102.9	43.9	173.2	8.0	Coil
2	Gly	103.5	45.9	175.5	8.6	Coil
3	Gly		45.9	174.4		Coil
4	Gly	110.6	45.9	171.2	8.9	Coil
5	Gly	104.1	47.0	174.1	8.2	Coil
6	Gly	104.3	47.2	175.9		Helix
7	Gly	105.2	46.7	176.1		Coil
8	Gly	105.1	44.1	173.7	7.7	Coil
9	Gly	105.3	44.9	172.4		Coil
10	Gly	105.1	45.1	174.6	8.5	Coil
11	Gly	112.4	45.4	171.7		Coil
12	Gly	111.7	44.7	172.4		Coil
13	Gly	114.1	45.0	173.7		Coil
14	Gly	110.6	43.2	172.6		Coil
15	Gly	110.1	47.4	174.0	9.0	Coil
16	Gly	112.1	44.9	171.2		Coil
17	Gly	108.4	45.2			Coil
18	Gly	108.4	44.5			Coil
19	Gly	103.7			7.3	NA
20	Gly	109.7	46.3	175.1	8.1	Coil
Spin System Number	Residue Type	C $\alpha$	C $\beta$	C $\gamma$		Secondary Structure
1	Thr	60.7	72.4	21.8		sheet/coil
2	Thr	62.3	71.2	23.9		sheet/coil
3	Thr	60.9	71.5	23.5		sheet
4	Thr	59.9	71.3	19.9		sheet/coil
5	Thr	60.5	69.6	21.5		sheet
6	Thr	61.2	69.6	20.6		coil
7	Thr	61.0	69.4	21.0		coil
8	Thr	62.3	68.8	21.4		coil/sheet
9	Thr	61.7	68.7	22.2		coil
10	Thr	63.4	68.1	21.1		coil
11	Thr	64.2	68.3	19.9		coil
12	Thr	64.9	68.2			Helix
13	Thr	65.9	67.9			Helix
14	Thr	66.2	67.5	22.1		Helix
15	Thr	64.3	67.2	21.9		Helix
Spin System Number	Residue Type	C $\alpha$	C $\beta$			Secondary Structure
1	Ser	57.0	67.5			Sheet
2	Ser	60.9	62.9			Helix/coil
3	Ser	60.1	62.5			Helix/coil
4	Ser	59.6	61.7			coil

5	Ser	59.5	63.1				coil
6	Ser	57.6	62.4				coil
7	Ser	57.9	62.9				coil
8	Ser	58.5	63.5				coil
9	Ser	58.0	64.0				coil
10	Ser	59.4	64.5				coil
11	Ser	59.6	64.6				coil
12	Ser	59.2	66.4				coil
13	Ser	61.4	62.9				Helix
14	Ser	57.0	64.5				Coil/sheet
15	Ser	56.6	65.4				Coil/sheet
16	Ser	56.6	66.2				Sheet/coil
17	Ser	56.2	63.4				Coil
18	Ser	55.2	63.4				Coil
19	Ser	57.6	61.1				Coil
20	Ser	53.5	67.5				N/A
Spin System Number	Residue Type	C $\alpha$	C $\beta$	C $\gamma$ 1	C $\gamma$ 2	C $\delta$ 1	Secondary Structure
1	Iie	64.1	34.0	28.9	15.8	12.3	Helix
2	Iie	65.8	36.9	29.4	16.8	12.3	Helix
3	Iie	67.8	38.3	29.8	18.3	12.3	Helix
4	Iie	59.7	39.5	27.0	15.0	12.8	Sheet
5	Iie	65.3	37.5	28.6	15.3	13.1	Helix
6	Iie	61.2	37.4	30.5	16.9	13.3	Helix
7	Iie	60.9	38.9		16.7	13.5	Sheet
8	Iie	62.0	38.4	27.0	18.0	13.7	Coil
9	Iie		38.1	29.5	16.3	14.1	Helix
10	Iie	60.4	36.3	27.4	18.1	14.4	Sheet
11	Iie	59.0	40.8	28.2		14.3	Sheet
12	Iie	59.9				13.7	Coil
13	Iie			26.6	16.5	11.3	Coil
14	Ile	64.4			16.0		Helix
Spin System Number	Residue Type	C $\alpha$	C $\delta$ 1				Secondary Structure
1	Pro	64.3	52.4				coil
2	Pro	64.6	49.4				coil
3	Pro	62.1	49.6				coil
4	Pro	62.0	49.8				coil
5	Pro	60.5	50.0				coil
6	Pro	60.4	52.0				coil
7	Pro	59.9	51.8				bridge
Spin System Number	Residue Type	C $\alpha$	C $\beta$				Secondary Structure
1	Ala	54.5	17.7				Helix
2	Ala	54.9	19.0				Helix/coil
3	Ala	52.8	16.0				Helix
4	Ala	52.8	18.6				coil
5	Ala	53.1	21.0				coil
6	Ala	51.6	18.6				coil

7	Ala	50.6	19.9	sheet/coil
8	Ala	49.8	20.5	sheet/coil
9	Ala	50.1	21.3	sheet/coil
10	Ala	52.0	23.4	sheet
11	Ala	51.2	17.7	coil
Spin System Number	Residue Type	C $\alpha$	C $\beta$	Secondary Structure
1	Val	64.7	31.6	helix/coil
2	Val	64.6	31.0	helix
3	Val	64.4	30.7	coil
4	Val	64.9	29.8	helix
5	Val	64.5	29.2	helix
6	Val	65.0	28.1	helix
7	Val	66.0	31.1	helix
8	Val	66.6	30.8	helix
9	Val	67.1	30.2	helix
10	Val	66.8	30.3	helix
11	Val	65.5	30.4	helix

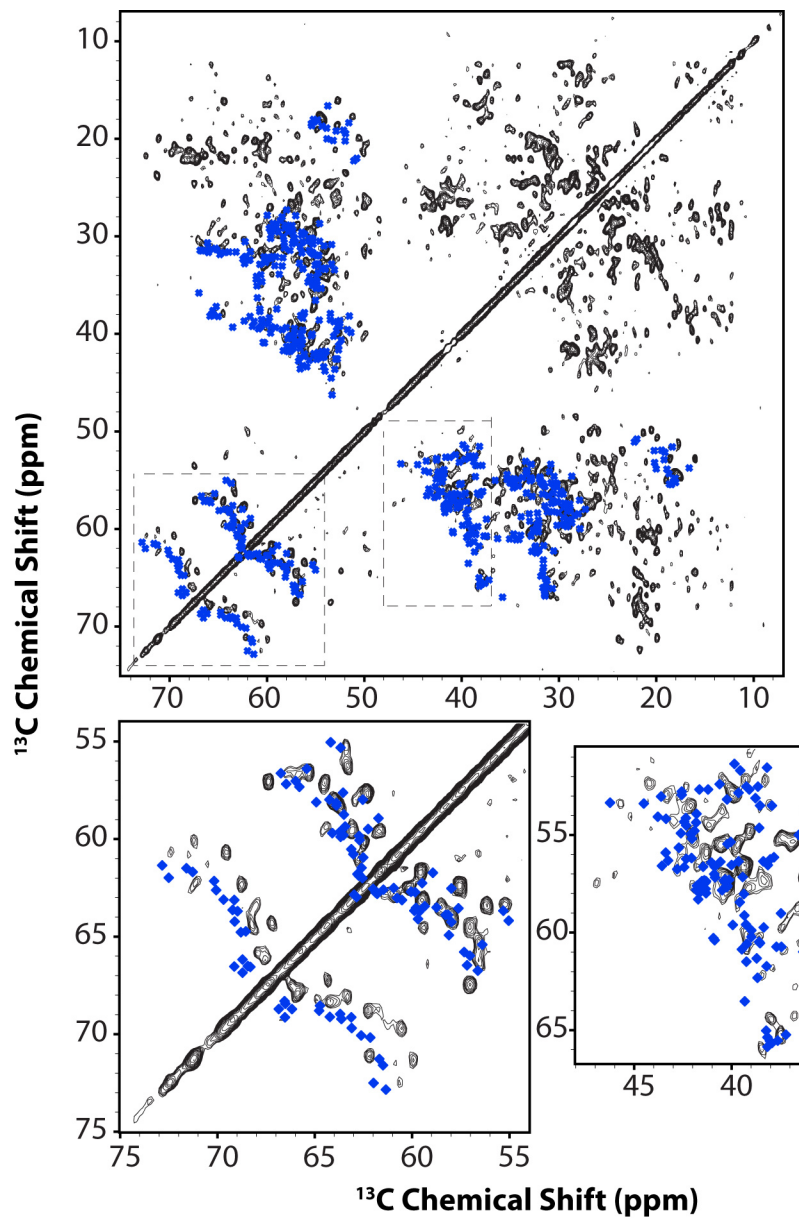


Figure 4.9: Chemical shift predictions from *SHIFTX2* based on the X-ray structure of Kif5b (PDB ID code: 4LNU) mapped onto the  $^{13}\text{C}$ - $^{13}\text{C}$  CORD correlation spectrum of the U- $^{13}\text{C}$ ,  $^{15}\text{N}$ -Kif5b/MT complexes. Note the remarkable overall agreement between the experimental and computed shifts.

Heteronuclear NCA correlation spectra of U- $^{15}\text{N}$ ,  $^{13}\text{C}$ -Kif5b/MTs also show remarkable resolution, as demonstrated in Figure 4.10. The glycine residues around 45 ppm are readily distinguished and well-dispersed. Eighteen of twenty glycine spin systems are detected, and the corresponding chemical shifts are reported in Table 4.3. We are able to count 125 isolated peaks, which only account for one third of the total expected resonances. There are several possible explanations for missing resonances, such as signal overlap and/or low sensitivity of the spectrum. Therefore, three- or four dimensional correlation experiments and more sensitive data acquisition methods are required for full resonance assignments of Kif5b in complex with MTs. Residues dynamic on the micro- to millisecond timescales would also not be visible in the spectra, so we will pursue scalar-based correlation experiments to detect those.

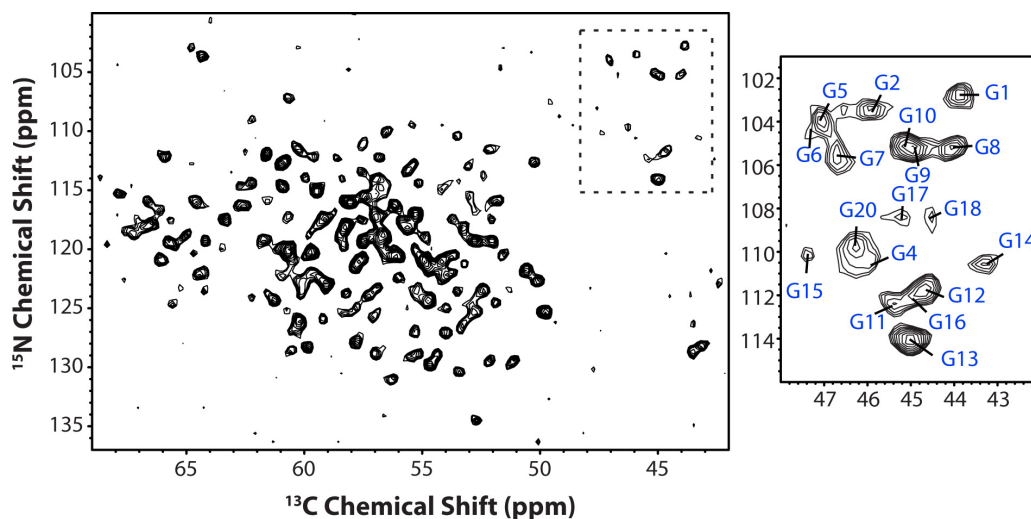


Figure 4.10: Heteronuclear NCA correlation spectrum of U- $^{13}\text{C}$ ,  $^{15}\text{N}$ -Kif5b/MT assemblies at an MAS frequency of 14 kHz, magnetic field of 19.96 T, and sample temperature of 17 °C. Glycine spin systems are labeled, and the corresponding chemical shifts are summarized in Appendix B, Table 4.3.

As discussed in Chapter 2, in MAS NMR spectroscopy, proton detection significantly improves the experimental sensitivity due to the high gyromagnetic ratio of the proton. However, the  $^1\text{H}$  resonances are broadened by strong  $^1\text{H}$ - $^1\text{H}$  dipolar coupling at MAS frequencies below 20 kHz. Resolution in the proton dimension can be greatly improved by spinning the sample faster than 40 kHz, which results in partially averaged  $^1\text{H}$ - $^1\text{H}$  dipolar couplings. This is achieved with the fast magic angle spinning probes and small rotors.

Proton-detected  $^{15}\text{N}$ - $^1\text{H}$  HETCOR spectra of U- $^{13}\text{C}$ ,  $^{15}\text{N}$ -Kif5b/MT assemblies packed in a 1.3 mm rotor were acquired at 60 kHz MAS and are shown in Figure 4.11. The sensitivity is greatly enhanced relative to heteronuclear detection. The signal-to-noise ratio (SNR) for 1D  $^1\text{H}$ - $^{15}\text{N}$  CP is about 5 with 128 scans. When the signal is transferred back to the proton for detection by a second  $^{15}\text{N}$ - $^1\text{H}$  CP step, the sensitivity is greatly enhanced, yielding an SNR of 47 with 64 scans.

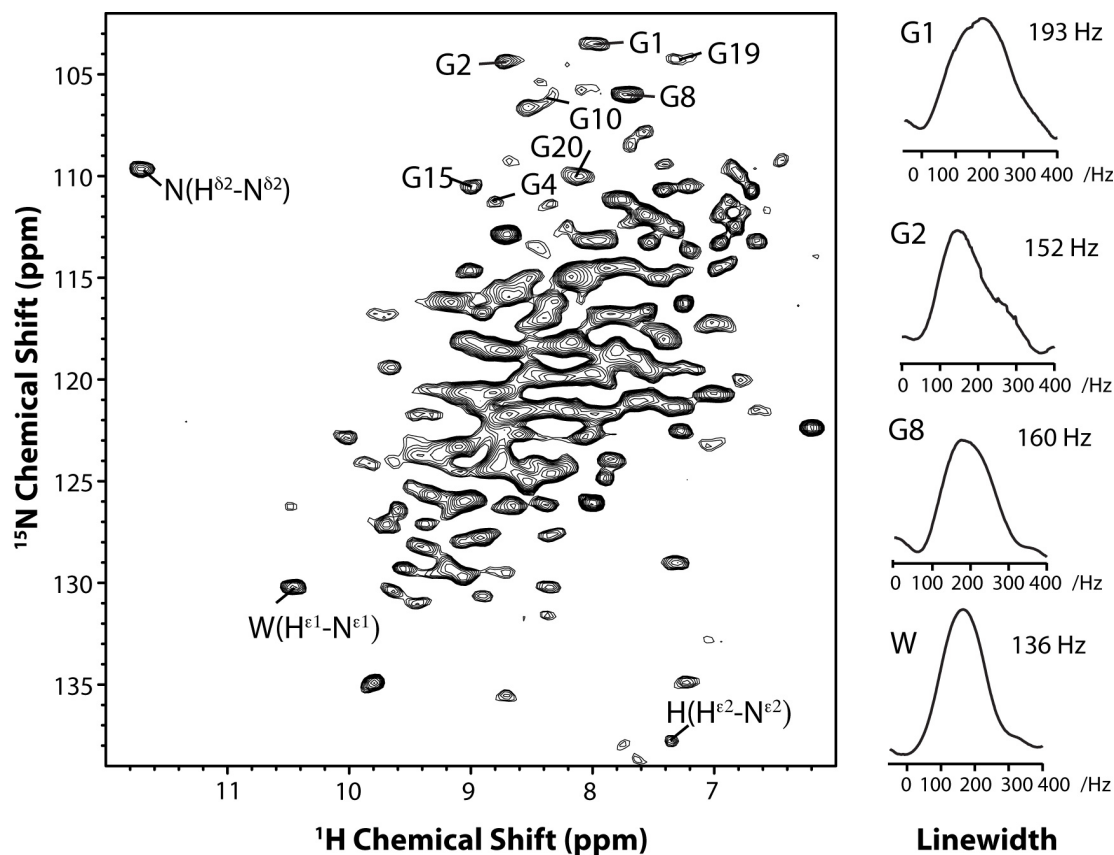


Figure 4.11: Left: Proton-detected  $^{15}\text{N}$ - $^1\text{H}$  HETCOR spectrum of protonated U- $^{13}\text{C}$ ,  $^{15}\text{N}$ -Kif5b/MT assemblies acquired at an MAS frequency of 60 kHz and field strength of 19.96 T. Selected backbone and sidechain spin systems are labeled in the 2D spectrum. Right: One-dimensional  $^1\text{H}$  traces for four residues extracted from the 2D HETCOR spectrum are shown with the corresponding spin system and linewidth indicated.

$^{15}\text{N}$ - $^1\text{H}$  HETCOR spectra of Kif5b show remarkable resolution.  $^{15}\text{N}$ - $^1\text{H}$  correlations from both protein sidechains and backbone are present in the spectra. Peaks with nitrogen chemical shifts of about 105 ppm are typically glycine residues. Eight glycine spin systems are assigned with the corresponding chemical shifts summarized in Table 4.3. The tentatively assigned sidechain correlations of His  $\text{N}^{\epsilon 2}$ -

$H^{\epsilon 2}$ , Trp  $N^{\epsilon 1}$ - $H^{\epsilon 1}$  and Asn  $N^{\delta 2}$ - $H^{\delta 2}$  are also labeled in the spectrum (Figure 4.11). Considerable peak overlap is observed from 115 ppm to 130 ppm in the nitrogen dimension. Peak widths are evaluated by only considering isolated peaks. The linewidths of resolved peaks range from 80 Hz to 260 Hz in the proton dimension, with an average value of 136 Hz.  $^1H$  1D slices corresponding to four spin systems are shown in Figure 4.11.

An additional factor for improvement of spectral resolution is protein perdeuteration, which can dilute the strong  $^1H$ - $^1H$  dipolar coupling and further narrow the proton linewidths. Perdeuterated  $U$ - $^{13}C$ ,  $^{15}N$ ,  $^2H$ -Kif5b was expressed in  $D_2O$ , and subsequent purification was carried out in protonated media and backbone amide protons are fully back-exchanged. A  $^{15}N$ - $^1H$  HETCOR spectrum of perdeuterated back exchanged  $U$ - $^{13}C$ ,  $^{15}N$ ,  $^2H$ -Kif5b/MTs is shown in Figure 4.12 and an overlay with protonated  $U$ - $^{13}C$ ,  $^{15}N$ -Kif5b/MTs is displayed in Figure 4.13. The spectrum of perdeuterated  $U$ - $^{13}C$ ,  $^{15}N$ ,  $^2H$ -Kif5b/MTs has better resolution, with sensitivity comparable to fully protonated  $U$ - $^{13}C$ ,  $^{15}N$ -Kif5b/MTs. The first 1D slice in the  $^{15}N$ - $^1H$  HETCOR spectrum of  $U$ - $^{13}C$ ,  $^{15}N$ ,  $^2H$ -Kif5b/MTs has an SNR of 83 with 128 scans. The proton linewidths of isolated peaks range from 84 Hz to 120 Hz, with an average value of 100 Hz. The  $^1H$  1D slices corresponding to four spin systems are shown on right side with the corresponding linewidth indicated.

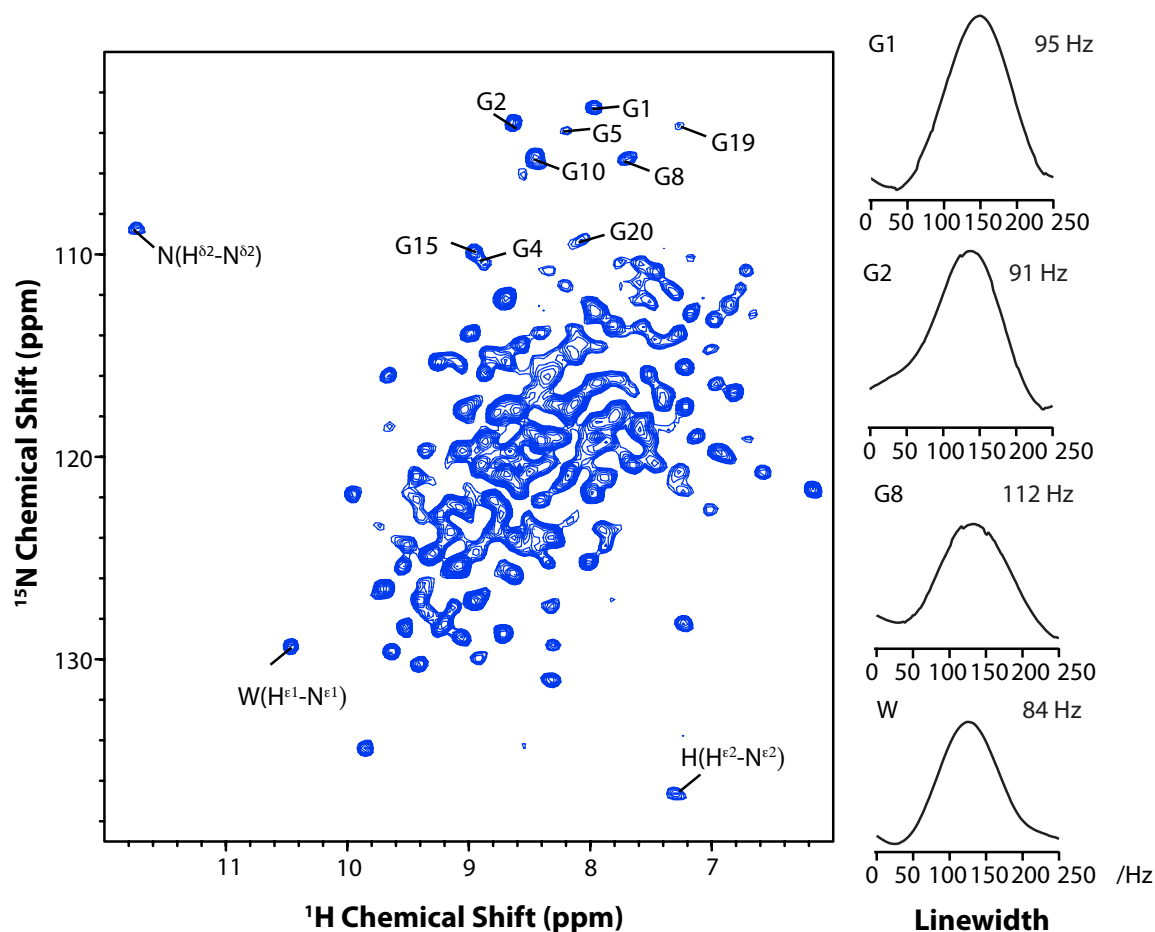


Figure 4.12: Proton-detected  $^{15}\text{N}$ - $^1\text{H}$  HETCOR spectrum of perdeuterated and back-exchanged  $\text{U-}^{13}\text{C}$ ,  $^{15}\text{N}$ ,  $^2\text{H}$ -Kif5b/MT assemblies acquired at an MAS frequency of 40 kHz and field strength of 19.96 T. Selected backbone and sidechain spin systems are labeled in the 2D spectrum. One-dimensional  $^1\text{H}$  traces extracted from the 2D HETCOR spectrum for four residues are shown with the corresponding spin system and linewidth indicated.

Despite back-exchange of amide protons in the perdeuterated protein, it is possible that amide proton sites from the hydrophobic core are not entirely back-exchanged and may not be detected in the  $^{15}\text{N}$ - $^1\text{H}$  HETCOR spectra. However, for a fully protonated protein, both the hydrophobic core and hydrophilic regions of the

protein can be detected. Additional peaks are observed in the  $^{15}\text{N}$ - $^1\text{H}$  HETCOR spectrum of the protonated  $\text{U-}^{13}\text{C},^{15}\text{N}$ -Kif5b/MT complexes, suggesting that these resonances likely arise from the hydrophobic core of Kif5b.

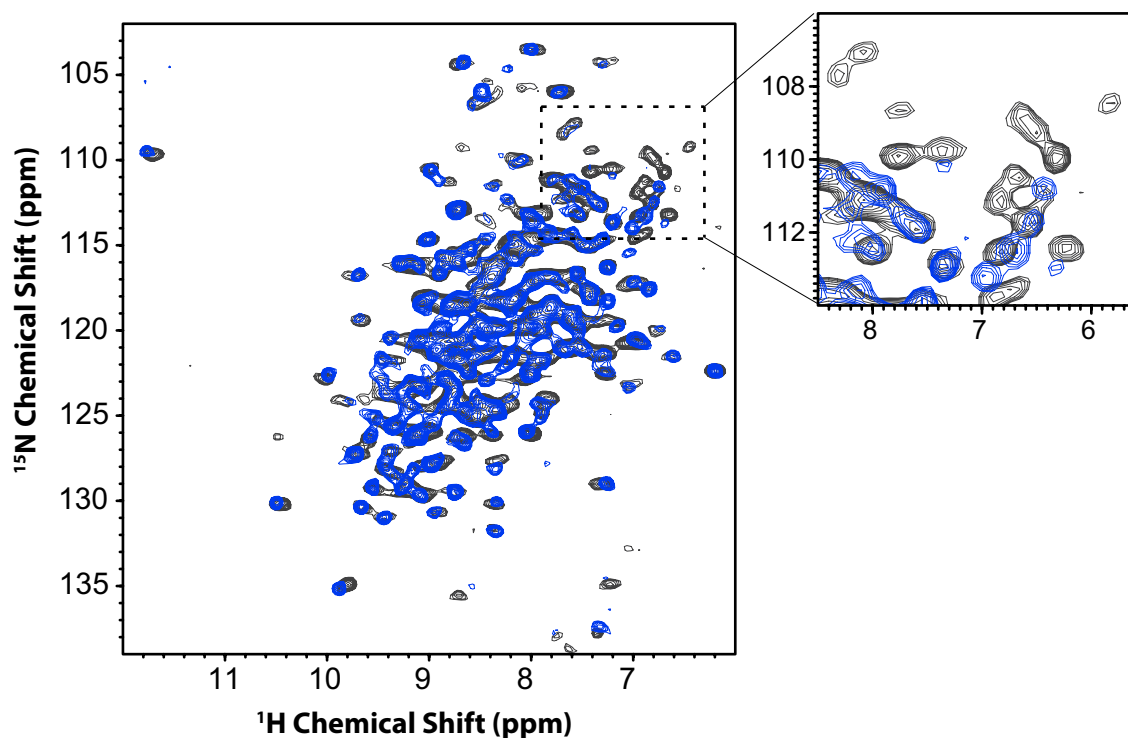


Figure 4.13: Overlay of  $^1\text{H}$ - $^{15}\text{N}$  HETCOR spectra of perdeuterated back exchanged  $\text{U-}^{13}\text{C},^{15}\text{N},^2\text{H}$ -Kif5b/MT (blue) and fully protonated  $\text{U-}^{13}\text{C},^{15}\text{N},^1\text{H}$ -Kif5b/MTs (black). An expansion indicating the appearance of new peaks in the protonated  $\text{U-}^{13}\text{C},^{15}\text{N},^1\text{H}$ -Kif5b/MT sample is shown.

Given the sensitivity and the overall unprecedented high quality of these 2D datasets, proton-detected experiments in combination with fast MAS appear very promising for future acquisition of three-dimensional experiments and resonance assignments. However, sample integrity under fast MAS may be problematic. We

observed, based on  $^{15}\text{N}$ - $^1\text{H}$  HETCOR spectra, that spectral quality deteriorates dramatically during the course of a 16-day-long experiment with sample spinning at 40 kHz, as shown in Figure 4.14a. We observed phase separation of the sample upon opening the rotor. The addition of buffer for rehydration did not restore the prior resolution, as shown in Figure 4.14b. We conclude that, under the current sample conditions, fast MAS is detrimental to Kif5b/MT complexes, and an alternative sample preparation method that prevents phase separation needs to be developed. One possible solution as suggested by our collaborator, Dr. Antonina Roll-Mecak from the NIH (National Institutes of Health), is to use GMPCPP-stabilized MTs in the formation of Kif5b/MT complexes, as GMPCPP-stabilized MTs are more rigid and may exhibit better tolerance under fast MAS.

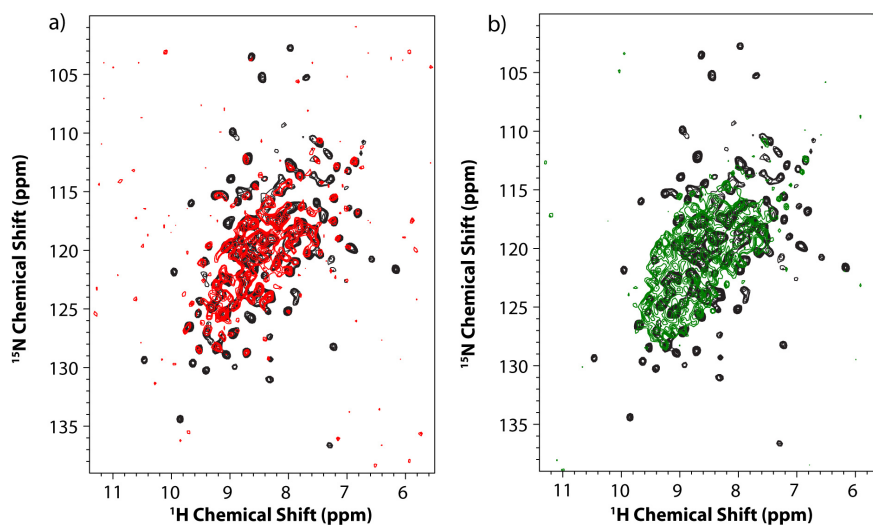


Figure 4.14: Overlay of NH-HETCOR spectra of  $^2\text{H}$ ,  $^{13}\text{C}$ ,  $^{15}\text{N}$ -Kif5b/MT complexes acquired at MAS frequency of 40 kHz, a) after spinning for 16 days (red); b) after rehydration by addition of sample buffer (green). The spectra acquired at the beginning of MAS experiments is shown in black in both plots.

Another important consideration for future studies of Kif5b is that in our early work the U-<sup>13</sup>C, <sup>15</sup>N-Kif5b/MT complex exhibited batch-to-batch variation in spectral quality (i. e., data acquired on the sample packed in a 3.2 mm rotor (sample #3 in Table 4.1) is significantly better than the sample packed in a 1.9 mm rotor (sample #6 in Table 4.1)) This may be due to modification of the sample preparation protocol for the 1.9 mm rotor, as shown in Table 4.1.

#### **4.3.5 MAS NMR Studies of ADP Binding State of Kif5b in Complex with Microtubules**

The ADP-U-<sup>13</sup>C, <sup>15</sup>N-Kif5b/MT complexes were prepared following the protocol reported in an X-ray crystallography study<sup>15</sup>, in which ADP was co-crystallized with Kif5b. The actual incorporation of ADP in the Kif5b/MT complex was not evaluated before MAS NMR experiments. For future studies of the ADP-Kif5b/MT complex, acquiring 1D <sup>31</sup>P single pulse excitation (SPE) or <sup>1</sup>H-<sup>31</sup>P CPMAS spectra is recommended to confirm successful incorporation of ADP molecule.

Both homonuclear (CORD) correlation spectra and heteronuclear (NCA) correlation spectra of the ADP-U-<sup>13</sup>C, <sup>15</sup>N-Kif5b/MT complexes were acquired. Overlays with free Kif5b in complex with microtubules are shown in Figure 4.15. Both chemical shift perturbations and linewidth changes are observed in spectra of the ADP-U-<sup>13</sup>C, <sup>15</sup>N-Kif5b/MT complex. This indicates that ADP may cause both structural and dynamic changes of Kif5b in complex with MTs. As mentioned above, we observed differences in batch-to-batch reproducibility of spectral quality in our earlier studies, and therefore definitive conclusions are difficult at this stage when comparing the spectra of Kif5b in free and ADP-bound states.

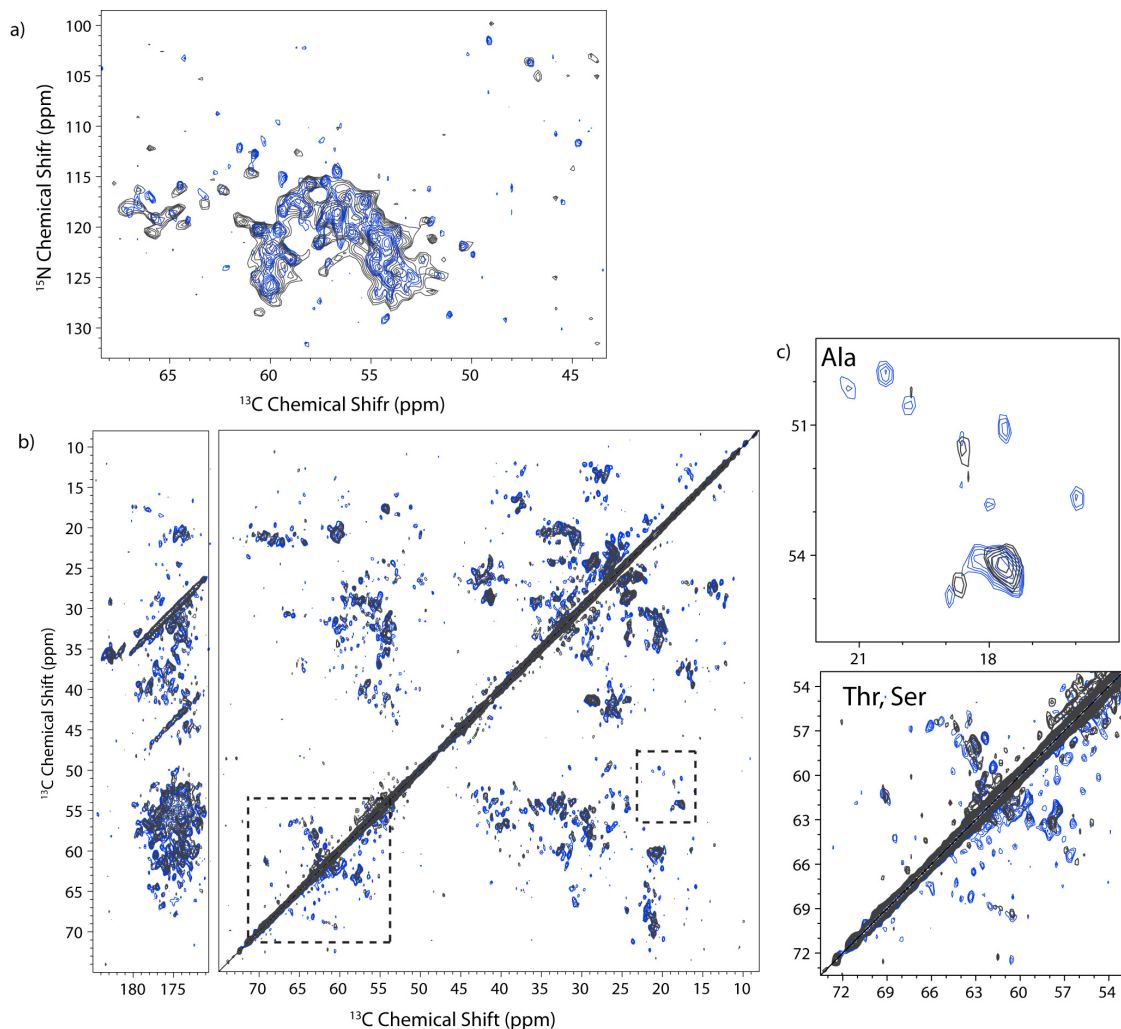


Figure 4.15. Homo- and heteronuclear correlation MAS NMR spectra of ADP-bound U- $^{13}\text{C}$ ,  $^{15}\text{N}$ -Kif5b/MT assemblies (black) overlaid with the apo Kif5b/MT complex (blue). a)  $^{15}\text{N}$ - $^{13}\text{C}$  NCA; b)  $^{13}\text{C}$ - $^{13}\text{C}$  CORD; c) Expansion of CORD spectrum, indicating chemical shift perturbations between the two samples.

Similar to U- $^{13}\text{C}$ ,  $^{15}\text{N}$ -Kif5b/MT complexes, the sensitivity of the MAS NMR experiments on ADP-U- $^{13}\text{C}$ ,  $^{15}\text{N}$ -Kif5b/MT complexes is also a challenge. In prior work in our laboratory, a sample temperature of  $-27\text{ }^{\circ}\text{C}$  had been used successfully for the studies of CAP-Gly in complex with MTs, yielding spectra with both high

sensitivity and resolution.<sup>16</sup>  $^1\text{H}$ - $^{13}\text{C}$  CPMAS spectra of Kif5b from 17 °C to -21 °C are plotted in Figure 4.16. Though sensitivity is enhanced by about 50% when the temperature is dropped to -21 °C, the spectral resolution deteriorates. This is further confirmed by comparing the  $^{13}\text{C}$ - $^{13}\text{C}$  CORD correlation spectra and NCO correlation spectra acquired at -21 °C with those acquired at 17 °C shown in Figure 4.17. We conclude that low temperatures ( $< 0^\circ$ ) are not ideal for the study of Kif5b/MT complexes.

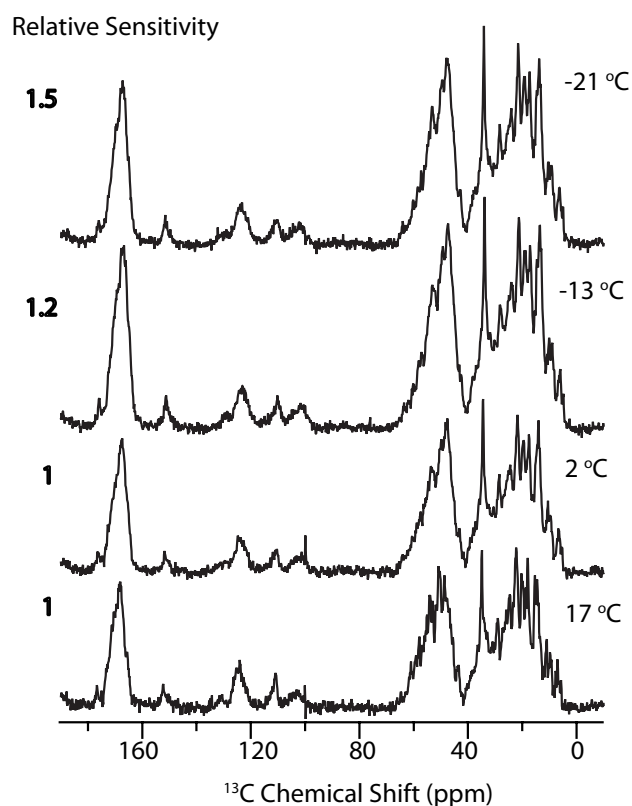


Figure 4.16: 1D  $^1\text{H}$ - $^{13}\text{C}$  cross polarization (CP) spectra of ADP-U- $^{13}\text{C}$ ,  $^{15}\text{N}$  Kif5b/MT complexes acquired at different temperatures, at MAS frequency of 14 kHz, 19.96 T. The relative sensitivity is indicated to the left of the spectra.

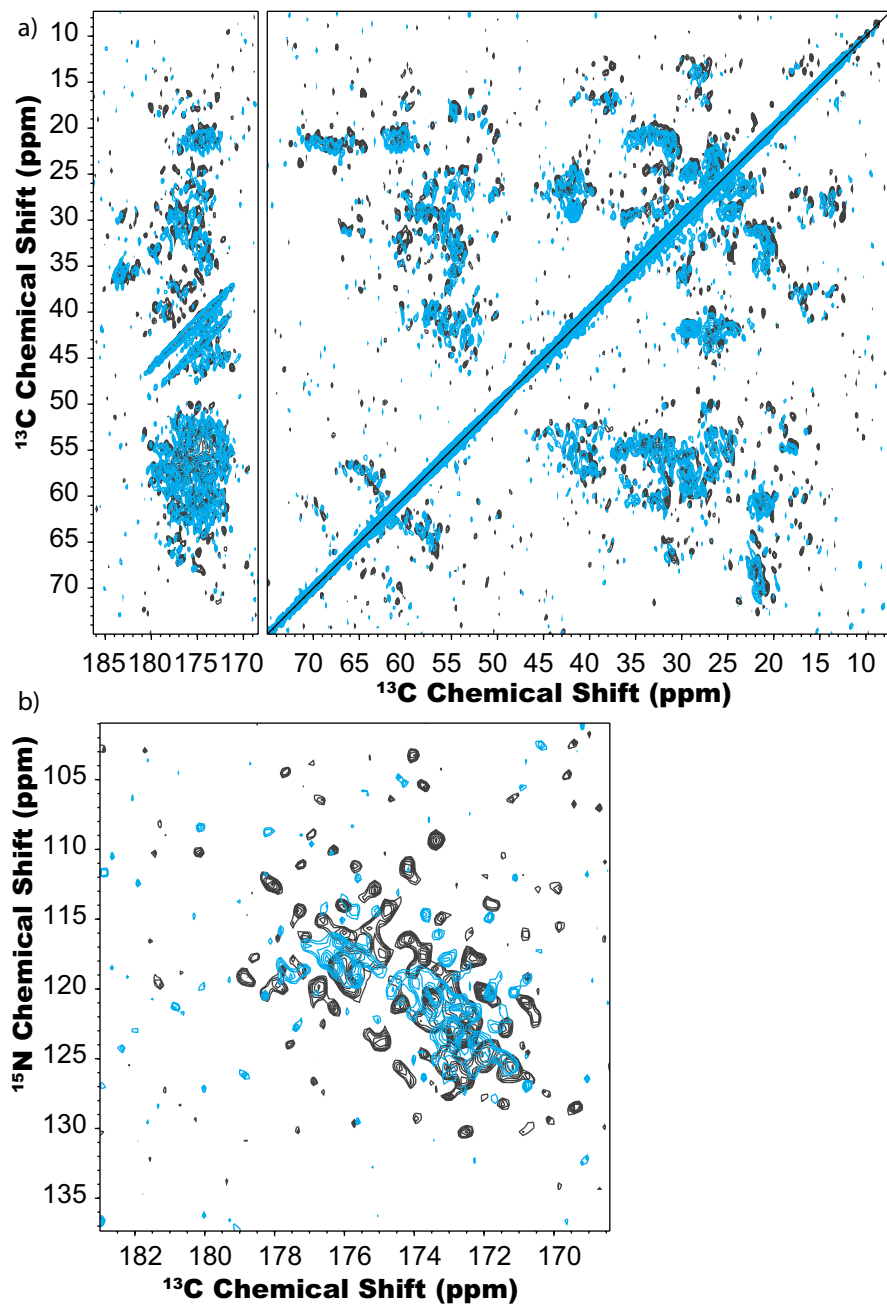


Figure 4.17: Overlay of a) CORD and b) NCO correlation spectra of ADP-U- $^{13}\text{C}$ ,  $^{15}\text{N}$ -Kif5b/MT complex (sample #7) acquired at 17 °C (black) and -21 °C (blue) at 19.96 T, 14 kHz MAS.

#### 4.4 Conclusions and Future Perspectives

We have established the sample preparation protocol appropriate to MAS NMR studies of Kif5b/MT complexes. This enabled us to acquire the first sets of 2D homo- and heteronuclear correlation MAS NMR spectra of Kif5b/MT complexes. The data exhibit remarkable resolution and broad chemical shift dispersion. This indicates that Kif5b is well-structured upon binding with MT, which is further confirmed by comparison with chemical shifts predicted by *SHIFTX2*. This is an important step toward future structural and dynamics studies of the Kif5b/MT complexes by MAS NMR spectroscopy.

Moreover, proton detection combined with fast MAS potentially presents a powerful approach for the study of Kif5b/MTs assemblies with greatly improved sensitivity and resolution, as demonstrated by this work. The addition of the proton dimension provides a third well-resolved atomic type (in addition to  $^{13}\text{C}$  and  $^{15}\text{N}$ ) to facilitate future resonance assignments and structure determination. However, one caveat is that spinning at fast MAS for several days is detrimental to the sample, and further optimization of sample preparation protocol is needed.

To date, the data acquired have been limited to two-dimensional correlation spectra, precluding site-specific resonance assignments of Kif5b. To acquire three-dimensional data sets, non-uniform sampling<sup>17-20</sup> (25% data sampling) is currently being applied, and enables the acquisition of a 3D NCACX dataset within two weeks. In addition, both resolution and sensitivity enhancement can be achieved by using high magnetic field (1 GHz) and fast MAS (up to 110 kHz) in combination with proton-detected experiments. With new experimental strategies and instrumentation developments, our preliminary work is promising for future determination of the 3D

structure of Kif5b in complex with MTs by MAS NMR, as well as for gaining insights into its dynamics at the atomic-level.

## REFERENCES

- (1) Hirokawa, N. *Science* **1998**, *279*, 519.
- (2) Rath, O.; Kozielski, F. *Nat. Rev. Cancer*. **2012**, *12*, 527.
- (3) Gigant, B.; Wang, W.; Dreier, B.; Jiang, Q.; Pecqueur, L.; Pluckthun, A.; Wang, C.; Knossow, M. *Nat. Struct. Mol. Biol.* **2013**, *20*, 1001.
- (4) Cao, L. Y.; Wang, W. Y.; Jiang, Q. Y.; Wang, C. G.; Knossow, M.; Gigant, B. *Nat. Commun.* **2014**, *5*.
- (5) Atherton, J.; Farabella, I.; Yu, I. M.; Rosenfeld, S. S.; Houdusse, A.; Topf, M.; Moores, C. A. *eLife* **2014**, *3*, e03680.
- (6) Shang, Z.; Zhou, K.; Xu, C.; Csencsits, R.; Cochran, J. C.; Sindelar, C. V. *eLife* **2014**, *3*, e04686.
- (7) Sindelar, C. V.; Downing, K. H. *Proc. Natl. Acad. Sci. USA* **2010**, *107*, 4111.
- (8) Marley, J.; Lu, M.; Bracken, C. *J. Biomol. NMR* **2001**, *20*, 71.
- (9) Thurber, K. R.; Tycko, R. *J. Magn. Reson.* **2009**, *196*, 84.
- (10) Suzuki, Y.; Tanokura, M.; Shimizu, T. *Eur. J. Biochem.* **1998**, *257*, 466.
- (11) Rice, S.; Lin, A. W.; Safer, D. *Nature* **1999**, *402*, 778.
- (12) Yan, S., University of Delaware, 2014.
- (13) Fritzsche, K. J.; Yang, Y.; Schmidt-Rohr, K.; Hong, M. *J. Biomol. NMR* **2013**, *56*, 155.
- (14) Han, B.; Liu, Y.; Ginzinger, S. W.; Wishart, D. S. *J. Biomol. NMR* **2011**, *50*, 43.
- (15) Sindelar, C. V.; Budny, M. J.; Rice, S.; Naber, N.; Fletterick, R.; Cooke, R. *Nat. Struct. Biol.* **2002**, *9*, 844.

- (16) Yan, S.; Guo, C. M.; Hou, G. J.; Zhang, H. L.; Lu, X. Y.; Williams, J. C.; Polenova, T. *Proc. Natl. Acad. Sci. USA* **2015**, *112*, 14611.
- (17) Paramasivam, S.; Suiter, C. L.; Hou, G.; Sun, S.; Palmer, M.; Hoch, J. C.; Rovnyak, D.; Polenova, T. *J. Phys. Chem. B* **2012**, *116*, 7416.
- (18) Palmer, M. R.; Wenrich, B. R.; Stahlfeld, P.; Rovnyak, D. *J. Biomol. NMR* **2014**, *58*, 303.
- (19) Rovnyak, D.; Frueh, D. P.; Sastry, M.; Sun, Z. Y. J.; Stern, A. S.; Hoch, J. C.; Wagner, G. *J. Magn. Reson.* **2004**, *170*, 15.
- (20) Suiter, C. L.; Paramasivam, S.; Hou, G. J.; Sun, S. J.; Rice, D.; Hoch, J.; Rovnyak, D.; Polenova, T. *J. Biomol. NMR* **2014**, *59*, 57.

## Chapter 5

### STRUCTURAL CHARACTERIZATION OF OXOVANADIUM (V) BIOINORGANIC COMPOUNDS BY MULTINUCLEAR NMR SPECTROSCOPY AND DFT CALCULATIONS<sup>3</sup>

#### 5.1 Introduction

Contemporary MAS NMR spectroscopy has matured to the point that it can directly probe complex biological systems such as protein assemblies, as has been demonstrated in previous chapters. Technological and methodological advancements in MAS NMR spectroscopy allowed its application in the study of materials such as polymers, organic and inorganic solids due to the presence of NMR-active nuclei across the periodic table.<sup>1</sup> NMR crystallography, the structural characterization of solid materials by the combination of NMR, diffraction techniques, and/or quantum chemical calculations, has been successfully used to characterize organic and inorganic materials.<sup>2,3</sup> Our group has expanded NMR crystallography for the characterization of bioinorganic solids containing half-integer quadrupolar spin  $^{51}\text{V}$  centers. The atomic-level structural and chemical characterization of biological vanadium complexes is important for the understanding of their biological functions.

---

<sup>3</sup> The study discussed in this chapter was conducted in collaboration with the groups of Professor Debbie Crans of Colorado State University, and Professor Amir Goldbourn of Tel Aviv University.

The work presented in this chapter demonstrates the applicability of NMR crystallography for the structural characterization of vanadium(V) bioinorganic complexes.<sup>4</sup>

Vanadium-containing biological macromolecules and bioinorganic complexes have found a variety of applications in catalysis, pharmaceutical industry, and biology; and their characterization is important for progress in all these areas. Vanadium oxides and coordination compounds catalyze numerous types of chemical reactions, including aerobic alcohol oxidation,<sup>5</sup> non-oxidative C-O bond breaking,<sup>6</sup> oxo-transfer reaction,<sup>7,8</sup> aerobic cleavage of C-C and C-H bonds,<sup>9,10</sup> and selective epoxidation of olefins.<sup>11,12</sup> Vanadium exhibits insulin-enhancing properties and has been explored for treatment of diabetes.<sup>13-18</sup> Vanadium(V) constitutes the active sites of vanadium-dependent haloperoxidases, catalyzing one-electron oxidation of halides to hypohalous acid, a reaction which has drawn significant interest in biotechnology applications.<sup>19-25</sup> Vanadium is also used in clean energy production, and the vanadium flow battery (VFB) is currently regarded as one of the leading energy storage systems.<sup>26-28</sup> The rich coordination chemistry of vanadium complexes formed from a wide array of ligands, results in a wide range of electronic structures and geometries.<sup>29</sup> Many physical methods are available for the characterization of geometric and electronic structure as well as chemical properties of vanadium-based systems. X-ray diffraction has played, and continues to play, a pivotal role in structural analysis of crystalline vanadium

---

<sup>4</sup> We have reported these findings in *Inorganic Chemistry (Li et al. (2015), Inorg. Chem., 54 (4), 1363-1374)*. The work discussed in this chapter is reprinted with permission from reference<sup>4</sup> with slight modifications. Copyright [2015] American Chemical Society.

complexes, particularly complexes with vanadium in its +5 oxidation state not amenable to EPR analysis. Unfortunately, many vanadium compounds either resist crystallization or are inherently noncrystalline, precluding their structural studies by diffraction techniques.<sup>30-35</sup> Development of methods for characterization of systems not accessible by X-ray crystallography is important and provides structural data on these challenging systems.

<sup>51</sup>V MAS NMR spectroscopy is a useful tool for site-specific characterization of V(V) sites in solids. Various aspects of the structure can be probed with high sensitivity and at atomic-level resolution: coordination geometry,<sup>16,36-44</sup> protonation states,<sup>45</sup> presence of paramagnetic sites and V(IV) species, as well as their proximity to V(V).<sup>46</sup> Protonation states of the metal and coordinated ligands are very important for understanding in detail catalytic processes and structures; however, information on protonation state for many systems cannot be obtained from X-ray diffraction due to the limited resolution of the structures or when a system under analysis is inherently noncrystalline. Over a period of a decade, our laboratory and others have developed a database of V(V) spectroscopic parameters and their relationship with structure and electronic properties in a wide range of vanadium-containing compounds.<sup>16,36,37,39-41,43,44,47-50</sup> From this body of work, our laboratory has identified empirical trends and dependencies of <sup>51</sup>V NMR parameters on coordination environment. However, to obtain detailed structural information, quantum chemical calculations are highly desirable, typically using density functional theory (DFT).<sup>16,36,38-44,47</sup> So far, the work in this area has mostly focused on establishing the validity of the combined <sup>51</sup>V MAS NMR/DFT approach for structural studies of vanadium compounds, predominantly on molecules whose X-ray structures are well established. DFT at the appropriate level

generally reproduces the experimental NMR parameters<sup>36,37,39-41,47,51</sup> including the  $^{51}\text{V}$  NMR observables, permitting direct identification of protonation states in bioinorganic complexes<sup>45</sup> and vanadium-dependent enzymes, haloperoxidases.<sup>47,52</sup>

Despite the successful use of  $^{51}\text{V}$  MAS NMR spectroscopic observables for structural characterization of vanadium(V)-based systems, it is challenging, if not impossible, to derive full three-dimensional structures of molecules on the basis of these parameters alone and in the absence of any other structural information. We have therefore explored the possibility of deriving 3D structural information on the basis of multiple NMR parameters measured from the NMR-active nuclei in the sample, using an approach termed NMR crystallography.<sup>53-55</sup> For these systems, NMR observables, such as dipolar couplings and anisotropic tensorial properties of the  $^{51}\text{V}$  nucleus and of the other atoms comprising the molecule (e.g.,  $^{15}\text{N}$ ,  $^{13}\text{C}$ ,  $^1\text{H}$ ,  $^{31}\text{P}$ , etc.), provide exquisite information on the geometric and electronic structure, and can be used as constraints for deriving the 3D structure of a compound using quantum chemical methods. The long-term goal of our work is to establish NMR crystallography for characterization of vanadium(V)-containing solids that are either noncrystalline or have unusual electronic structure and redox properties.<sup>37</sup>

In previous reports, our laboratory and others have shown that  $^{51}\text{V}$  quadrupolar interaction and chemical shift anisotropy (CSA) parameters are very sensitive probes of the local environment. Our group and others have also demonstrated the utility of double resonance methods for the measurement of internuclear distances between  $^{51}\text{V}$  and high-natural abundance spin-1/2 nuclei, such as  $^{31}\text{P}$ , in inorganic vanadium-based solids.<sup>56,57</sup> In this study, we expand the application of NMR crystallography to the next level by combining the  $^{51}\text{V}$  quadrupolar and CSA parameters with  $^{51}\text{V}$ - $^{15}\text{N}$

internuclear distances as well as with  $^{15}\text{N}$  CSA tensors and  $^{13}\text{C}$  isotropic chemical shifts. These parameters are used as structural constraints for the DFT-based structural calculations. We first validate this approach on ( $^{15}\text{N}$ -salicylideneglycinate)(benzhydroxamate)-oxovanadium(V) ( $\text{VO}^{15}\text{NGlySalbz}$ , Figure 5.1A) by demonstrating that the multinuclear NMR observables are accurate reporters of its three-dimensional structure. We then apply this strategy to a related compound (Methoxo)( $^{15}\text{N}$ -salicylidene-glycinato)oxovanadium(V) ( $\text{VO}^{15}\text{NGlySal}(\text{OCH}_3)$ ) in Figure 5.1A, whose 3D structure is unknown. This compound can adopt either a penta- or a hexacoordinate geometry, depending on whether a neutral  $\text{CH}_3\text{OH}$  molecule is coordinated directly to the vanadium. We demonstrate, on the basis of the multiple experimental  $^{51}\text{V}$ ,  $^{15}\text{N}$ , and  $^{13}\text{C}$  NMR observables and DFT calculations, that  $[\text{VO}^{15}\text{NGlySal}(\text{OCH}_3)]\cdot(\text{CH}_3\text{OH})$  contains a hexacoordinate vanadium, with methanol weakly coordinated to the vanadium center, at a distance of  $3.4\pm 0.4$  Å. The  $^{51}\text{V}$ - $^{15}\text{N}$  distances derived from the LA-REDOR experiment<sup>58</sup> are consistent with V-N being a single bond. The approach reported here establishes that NMR crystallography is effective for structural analysis of vanadium(V)-containing systems that are not amenable to single-crystal X-ray diffraction characterization. Furthermore, the characterization of the loosely bound methanol molecule is important to characterization of compounds that resist crystallization but contain co-precipitated solvent molecules.

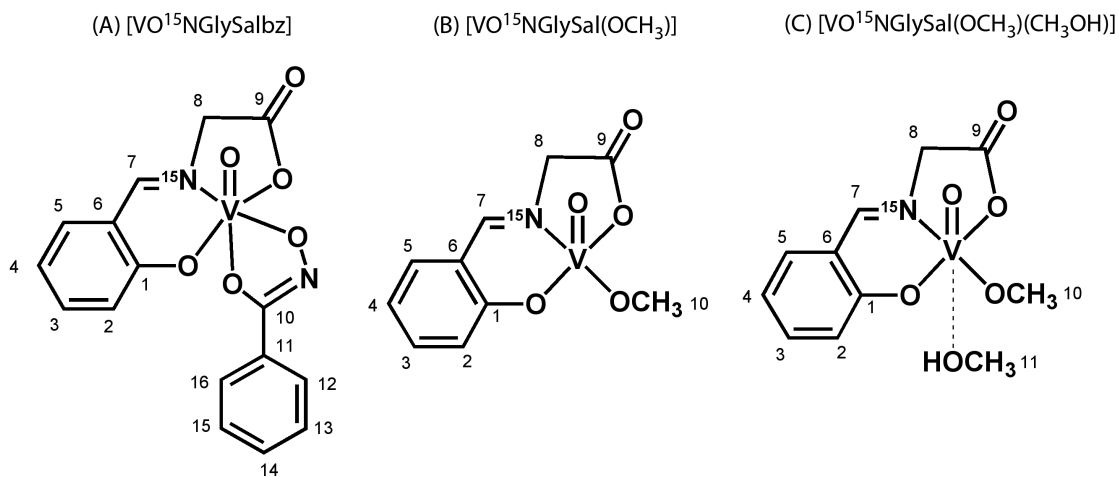


Figure 5.1: Molecular structure of vanadium compounds: (A)  $[\text{VO}^{15}\text{NglySalbz}]$ , (B)  $[\text{VO}^{15}\text{NglySal}(\text{OCH}_3)]$ , and (C)  $[\text{VO}^{15}\text{NglySal}(\text{OCH}_3)] \cdot (\text{CH}_3\text{OH})$ . The isotopically labeled  $^{15}\text{N}$  is marked in the structure. The carbon atom numbering corresponds to that in Table 5.3.

## 5.2 Materials and Experiments

### 5.2.1 Materials

$^{15}\text{N}$ -labeled oxovanadium complexes  $[\text{VO}^{15}\text{NglySalbz}]$  and  $[\text{VO}^{15}\text{NglySal}(\text{OCH}_3)] \cdot (\text{CH}_3\text{OH})$  used in this work were provided by our collaborator Dr. Pabitra B. Chatterjee at Colorado State University. The starting vanadium metal precursor  $[\text{VO}^{15}\text{NglySal}(\text{H}_2\text{O})]$  containing an  $^{15}\text{N}$ -labeled donor atom was synthesized following the previously described procedure,<sup>59,60,61</sup> where isotopically labelled glycine  $\text{H}_2^{15}\text{NCH}_2\text{COOH}$  was used in place of the natural abundance glycine containing  $^{13}\text{C}$  at natural abundance. The complexes  $[\text{VO}^{15}\text{NglySalbz}]$  and  $[\text{VO}^{15}\text{NglySal}(\text{OCH}_3)] \cdot (\text{CH}_3\text{OH})$  were prepared following the procedures for the corresponding vanadium(IV) complexes and their oxidation to a

vanadium(V) complex, which have been reported previously.<sup>60,61</sup> Solution <sup>1</sup>H NMR was used to confirm the synthesis of these materials.

### 5.2.2 <sup>51</sup>V, <sup>15</sup>N and <sup>13</sup>C MAS NMR Spectroscopy

The single-pulse excitation (SPE) <sup>51</sup>V MAS NMR spectra, <sup>13</sup>C cross-polarization MAS (CPMAS) spectra, and <sup>51</sup>V-<sup>15</sup>N LA-REDOR dephasing curves were acquired on a 9.4 T wide bore Tecmag Discovery spectrometer operating at Larmor frequencies of 400.2 MHz (<sup>1</sup>H), 105.2 MHz (<sup>51</sup>V), and 100.6 MHz (<sup>13</sup>C). These experiments were performed using a 3.2 mm Varian triple-resonance T3 probe. <sup>51</sup>V spectra for VO<sup>15</sup>NGlySalbz and [VO(<sup>15</sup>NGlySal)(OCH<sub>3</sub>)]·(CH<sub>3</sub>OH) were acquired at the MAS frequencies of 10, 13, 15 and 13, 17, and 20 kHz, respectively. <sup>13</sup>C CPMAS spectra were acquired at the MAS frequencies of 10 kHz and 17 kHz, respectively. The MAS frequency was controlled to ± 5 Hz by a Tecmag MAS controller. The temperature was set to +25 °C, and was controlled to ± 1°C by a Varian temperature controller. The magic angle was set by maximizing the number of rotational echoes observed in the <sup>23</sup>Na NMR free-induction decay of solid NaNO<sub>3</sub>.

The <sup>51</sup>V SPE experiment employed a non-selective excitation pulse width of 1.0 μs with an rf field of 62.5 kHz, the spectral width was set to 2.0 MHz, and a recycle delay of 1 s was used for all measurements. The total number of scans acquired for each compound depended on the MAS frequency and the amount of sample packed in the rotor, and ranged between 7,200 and 108,000. The spectra were processed by MestReNova. The isotropic chemical shifts were determined by the analyses of the spectra collected at the three different MAS frequencies and referenced with respect to a secondary reference, compound benzhydroxamato-{N-(2-oxiphenyl)-5,6-dibenzosalicylideneaminato}-oxovanadium(V) (dubbed SJZ0032<sup>36</sup>) whose

isotropic chemical shift was reported by us previously.<sup>36</sup> The NMR parameters, namely the <sup>51</sup>V quadrupolar coupling constant and quadrupolar anisotropy ( $C_Q$ ,  $\eta_Q$ ) as well as the reduced chemical shift anisotropy and asymmetry parameter of the chemical shift anisotropy (CSA) tensor ( $\delta_\sigma$ ,  $\eta_\sigma$ ) together with the Euler angles ( $\alpha$ ,  $\beta$ ,  $\gamma$ ) describing the relative orientations of the electric field gradient (EFG) and CSA tensors, were extracted by numerical simulations of the spinning sideband patterns using SIMPSON software package.<sup>62</sup>

In this work, we define the chemical shift parameters according to the Haeberlen-Mehring-Spiess convention,<sup>63-65</sup> where the three principal components of the CSA tensor,  $\delta_{xx}$ ,  $\delta_{yy}$  and  $\delta_{zz}$ , and the isotropic component  $\delta_{iso}$ , are defined according to  $|\delta_{xx} - \delta_{iso}| \leq |\delta_{yy} - \delta_{iso}| \leq |\delta_{zz} - \delta_{iso}|$ , and  $\delta_{iso} = (\delta_{xx} + \delta_{yy} + \delta_{zz})/3$ ,  $\delta_\sigma = \delta_{zz} - \delta_{iso}$ ; the asymmetry parameter  $\eta_\sigma = (\delta_{yy} - \delta_{xx})/(\delta_{zz} - \delta_{iso})$ . The EFG tensor parameters are  $C_Q = eQV_{ZZ}/h$  and  $\eta_Q = (V_{XX} - V_{YY})/V_{ZZ}$  where  $|V_{ZZ}| \geq |V_{YY}| \geq |V_{XX}|$  are the three components of the quadrupolar coupling tensor,  $e$  is the electronic charge,  $Q$  is the nuclear quadrupole moment and  $h$  is the Planck's constant.

In the <sup>13</sup>C CPMAS experiments, the <sup>1</sup>H 90° excitation pulse length was 2.8  $\mu$ s. The <sup>1</sup>H-<sup>13</sup>C cross-polarization was performed by applying a linear ramp (80% - 100%) on <sup>13</sup>C with the center of the rf field at 51 kHz, and a constant-amplitude rf field of 82 kHz on <sup>1</sup>H. A CP contact time of 3 ms was used. <sup>1</sup>H TPPM decoupling with rf strength of 90 kHz was used during acquisition. A total of 40,960 and 115,472 transients were accumulated for VO<sup>15</sup>NGlySalbz and [VO(<sup>15</sup>NGlySal)(OCH<sub>3</sub>)]·(CH<sub>3</sub>OH) samples, respectively; and the recycle delay was 2 s. The spectral width was set to 44.6 kHz.

Distance measurements were performed using the LA-REDOR experiment, the pulse sequence for which is shown in Figure 5.2. The long inversion pulse on the vanadium channel was set to 200  $\mu$ s, corresponding to two rotor periods at a MAS spinning rate of 10 kHz. The radio frequency field strengths were 46.8 kHz for the observed  $^{15}\text{N}$  nucleus and 48 kHz for the  $^{51}\text{V}$  nucleus. The data for the recoupling and reference experiments were collected in an alternating fashion, with one scan employing the recoupling pulse (giving the signal  $S$ ) followed by a second scan without recoupling (corresponding to  $S_0$ , the reference signal). The total LA-REDOR fraction was then calculated according to  $\Delta S/S_0 = (S_0 - S)/S_0$ . The recycle delay was 4 s. Spectra were recorded using a sample weight of 10-15 mg.

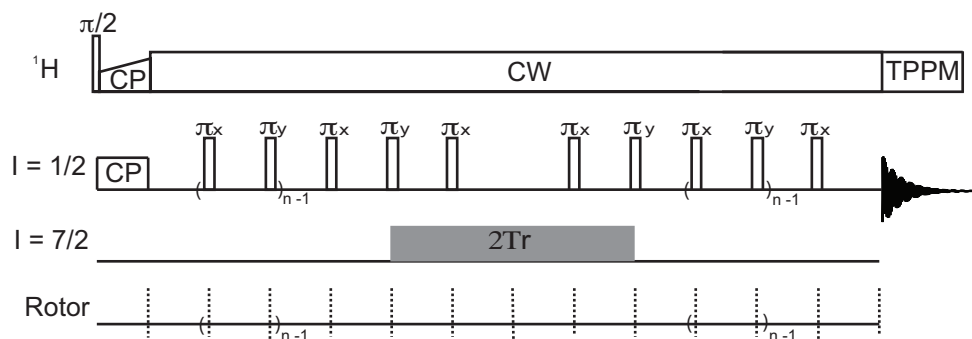


Figure 5.2: Low-alpha, low-amplitude rotational echo adiabatic passage double resonance (LA-REDOR) pulse sequence.

Numerical simulations of the LA-REDOR curves were performed using the program SIMPSON.<sup>62</sup> 320 REPULSION angles were used for powder averaging.<sup>66</sup> Curves were calculated as functions of dipolar coupling constants for specific values of  $C_Q(^{51}\text{V})$ ,  $\eta_Q(^{51}\text{V})$ ,  $\delta_\sigma(^{51}\text{V})$ ,  $\eta_\sigma(^{51}\text{V})$ ,  $\delta_\sigma(^{15}\text{N})$ .

The  $^{15}\text{N}$  ROCSA<sup>67</sup> experiments were carried out on a 14.1 T narrow bore Varian InfinityPlus solid-state NMR spectrometer operating at Larmor frequencies of 599.8 and 60.8 MHz for  $^1\text{H}$  and  $^{15}\text{N}$ , respectively. The spectra were acquired using a 1.6 mm MAS triple-resonance probe. The MAS frequency was set at 10 kHz and controlled within  $\pm 2$  Hz by a Varian MAS controller. ROCSA blocks were incorporated during the  $t_1$  period for  $^{15}\text{N}$  CSA evolution. The radio frequency field strength applied on the  $^{15}\text{N}$  channel during the ROCSA period was 75 kHz. The spectra were processed with NMRPipe.<sup>68</sup> The fitting of the experimental ROCSA spectra was done with SIMPSON using three variable parameters: reduced anisotropy  $\delta_\sigma$ , asymmetry parameter  $\eta_\sigma$ , and a line-broadening parameter.

### 5.2.3 Density Functional Theory (DFT) Calculations of NMR Parameters

Quantum chemical calculations for the structurally characterized VO<sup>15</sup>NGlySalbz complex were performed using density functional theory as implemented in Gaussian09.<sup>69</sup> The magnetic shielding and the electric field gradient tensors were computed using BLYP and B3LYP functionals with TZV and 6-311+G basis sets, using either the non-optimized X-ray geometry or geometry-optimized structure at the B3LYP/TZV level of theory, as summarized in Table 5.1 and 5.2. The  $^{51}\text{V}$  NMR parameters-  $\delta_\sigma$ ,  $\eta_\sigma$ ,  $C_Q$ ,  $\eta_Q$ ,  $\alpha$ ,  $\beta$ , and  $\gamma$ , were extracted using a home-written Mathematica program. The  $^{15}\text{N}$  and  $^{13}\text{C}$  CSA tensor parameters were extracted in an analogous fashion. The  $^{13}\text{C}$  chemical shifts were referenced by converting absolute magnetic shieldings  $\sigma_i$  into the chemical shift using the relation  $\delta_i = \sigma_{\text{ref}} - \sigma_i$ , with the value of  $\sigma_i$  determined by linear regression between calculated and experimental shifts for that structure.<sup>70</sup> The  $^{15}\text{N}$  chemical shifts were referenced to the N<sup>o</sup> of neutral histidine (41 ppm), whose absolute magnetic shielding tensors were calculated at the

same level of theory. The  $^{51}\text{V}$  chemical shifts are referenced to  $\text{VOCl}_3$  (0 ppm) whose absolute magnetic shielding tensors were calculated at the same level of theory for geometry-optimized structures. As the X-ray crystal structure of  $[\text{VO}(^{15}\text{NGlySal})(\text{OCH}_3)]\cdot(\text{CH}_3\text{OH})$  is not available, the Cartesian coordinates were obtained by B3LYP/TZV geometry optimization using the starting structure of  $\text{VO}_4^{3-}$  and incorporating the appropriate substituents. The calculations were conducted for both the distorted square pyramidal  $\text{VO}^{15}\text{NGlySal}(\text{OCH}_3)$  and distorted octahedral  $[\text{VO}(^{15}\text{NGlySal})(\text{OCH}_3)]\cdot(\text{CH}_3\text{OH})$  geometries. For the latter, the calculations were conducted as a function of the distance between the neutral ( $\text{CH}_3\text{OH}$ ) ligand and the vanadium center, in the range of 2.0 and 4.5 Å. In these calculations, the V-O distance was fixed and the geometry was optimized for each distance. The  $^{51}\text{V}$  and  $^{15}\text{N}$  NMR parameters were subsequently extracted from the calculated magnetic shielding and EFG tensors. As described in the subsequent sections, our results indicate that a methanol molecule is weakly coordinated to the vanadium, so that the compound is best represented by the chemical formula  $[\text{VO}(^{15}\text{NGlySal})(\text{OCH}_3)]\cdot(\text{CH}_3\text{OH})$ .

### 5.3 Results and Discussions

#### 5.3.1 $^{51}\text{V}$ , $^{15}\text{N}$ and $^{13}\text{C}$ Experimental NMR Parameters

The experimental  $^{51}\text{V}$  NMR spectra of  $[\text{VO}^{15}\text{NGlySalbz}]$  and  $[\text{VO}(^{15}\text{NGlySal})(\text{OCH}_3)]\cdot(\text{CH}_3\text{OH})$  acquired at three MAS frequencies each, are shown in Figure 5.3. The NMR parameters describing the quadrupolar tensors and chemical shift tensors were extracted from numerical simulations of the spectra and are summarized in Table 5.1. Interestingly,  $[\text{VO}^{15}\text{NGlySalbz}]$  and  $[\text{VO}(^{15}\text{NGlySal})(\text{OCH}_3)]\cdot(\text{CH}_3\text{OH})$  have very similar EFG tensors: the quadrupolar

coupling constants are 3.7 and 3.5 MHz, respectively, and the corresponding asymmetry parameters are 0.85 and 0.73.

At first glance, this quasi-agreement of the quadrupole coupling constants for the two materials may indicate that both compounds are hexacoordinate. In the case of the methoxy-derivative, a methanol molecule could potentially be coordinated to the vanadium center. Interestingly, the chemical shift tensors for the two compounds are very different. The  $^{51}\text{V}$  isotropic shifts are -405.3 and -528.9 ppm, and the corresponding reduced anisotropy parameters of the chemical shift tensors are -351.7 and -421.4 ppm, respectively. The relative deshielding of  $[\text{VO}^{15}\text{NGlySalbz}]$  by ca. 123 ppm with respect to  $[\text{VO}^{15}\text{NGlySal}(\text{OCH}_3)]\cdot(\text{CH}_3\text{OH})$  could be attributed to the redox non-innocent nature of the benzohydroxamate ligand.<sup>39</sup> It is worth noting that the principle axes of the EFG and chemical shift tensors, as represented by the Euler angles, see Table 5.1. Euler angles represent the angles of the rotations that transform chemical shift tensors into quadrupolar tensors.

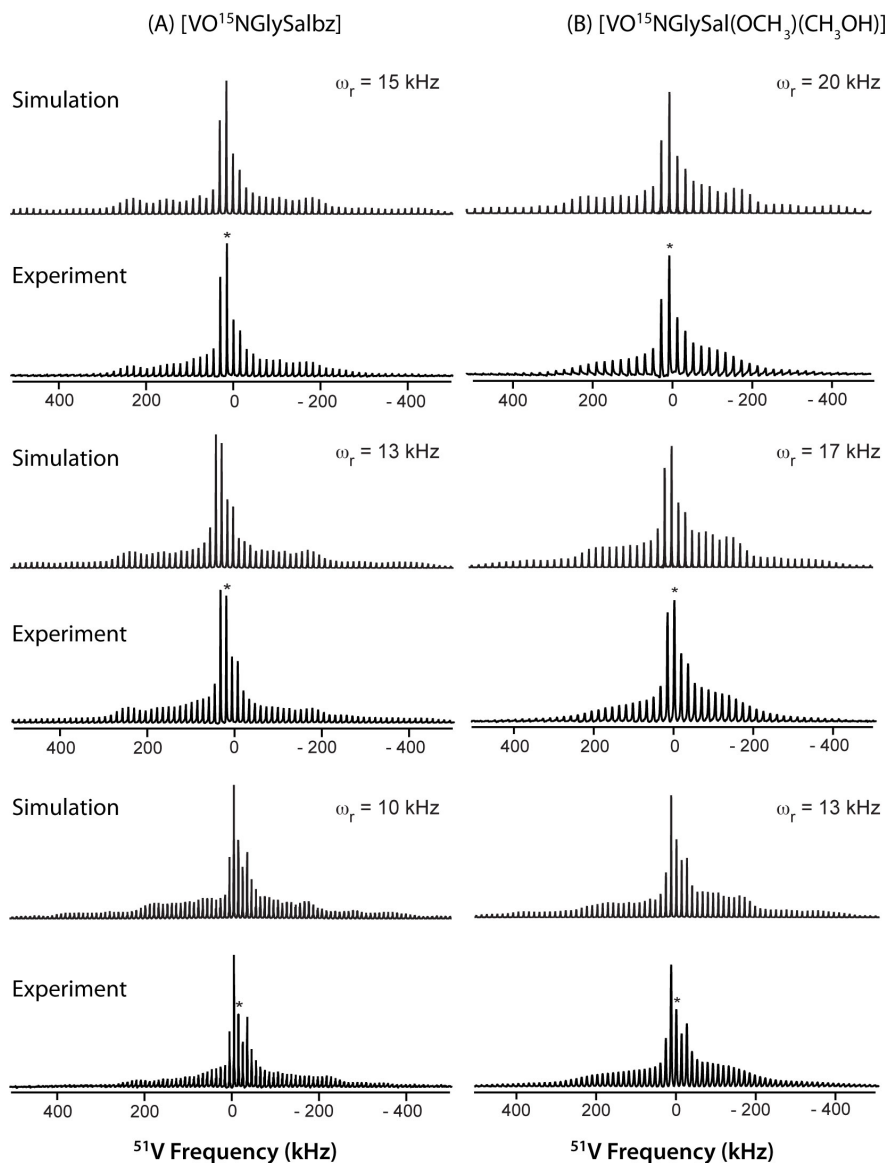


Figure 5.3:  $^{51}\text{V}$  MAS NMR spectra of (A)  $[\text{VO}^{15}\text{NGlySalbz}]$  and (B)  $[\text{VO}^{15}\text{NGlySal}(\text{OCH}_3)] \cdot (\text{CH}_3\text{OH})$  shown as a function of the MAS frequency. The experimental spectrum is displayed at the bottom, and simulated at the top of each panel. The MAS frequencies for the  $[\text{VO}^{15}\text{NGlySalbz}]$  spectra are: top,  $\nu_r = 15$  kHz; middle,  $\nu_r = 13$  kHz; and bottom,  $\nu_r = 10$  kHz. The MAS frequencies for the  $[\text{VO}^{15}\text{NGlySal}(\text{OCH}_3)] \cdot (\text{CH}_3\text{OH})$  spectra are: top,  $\nu_r = 20$  kHz; middle,  $\nu_r = 17$  kHz; and bottom,  $\nu_r = 13$  kHz. The best-fit parameters are indicated in Table 5.1. The spectra were acquired at the magnetic field of 9.4 T.

Table 5.1: Experimental and Computed  $^{51}\text{V}$  NMR Parameters for  $[\text{VO}^{15}\text{NGlySalbz}]$  and  $[\text{VO}^{15}\text{NGlySal}(\text{OCH}_3)]$ 

Compound	Method	$C_Q/\text{MHz}$	$\eta_Q$	$\delta_{\text{iso}}/\text{ppm}$	$\delta/\text{ppm}$	$\eta_a$	$\alpha/\text{degree}$	$\beta/\text{degree}$	$\gamma/\text{degree}$
<b><math>[\text{VO}^{15}\text{NGlySalbz}]</math></b>	<b>Experiment</b>	<b><math>3.7\pm 0.1</math></b>	<b><math>0.85\pm 0.05</math></b>	<b><math>-405.3\pm 5</math></b>	<b><math>-351.7\pm 5</math></b>	<b><math>0.36\pm 0.05</math></b>	<b><math>150\pm 30</math></b>	<b><math>60\pm 30</math></b>	<b><math>90\pm 30</math></b>
	BLYP/TZV	-4.0	0.53	-563.2	-375.2	0.07	41	36	-42
	BLYP/6-311+G	-4.8	0.6	-541.8	-376.0	0.06	39	37	-41
	B3LYP/TZV	-3.8	0.45	-784.2	-580.9	0.12	43	31	-42
	B3LYP/6-311+G	-4.7	0.56	-740.8	-573.0	0.1	41	33	-41
	BLYP/TZV (non-opt)	-5.4	0.87	-531.3	-348.9	0.06	-63.4	77.6	56.1
	B3LYP/TZV (non-opt)	-5.4	0.8	-744.6	-537.3	0.09	-67	75	58.6
<b><math>[\text{VO}^{15}\text{NGlySal}(\text{OCH}_3)_x]</math></b>	<b>Experiment</b>	<b><math>3.5\pm 0.1</math></b>	<b><math>0.73\pm 0.05</math></b>	<b><math>-528.9\pm 5</math></b>	<b><math>-421.4\pm 5</math></b>	<b><math>0.31\pm 0.05</math></b>	<b><math>0\pm 30</math></b>	<b><math>90\pm 30</math></b>	<b><math>90\pm 30</math></b>
$[\text{VO}^{15}\text{NGlySal}(\text{OCH}_3)]$	BLYP/TZV	-4.8	0.84	-711.9	-442.5	0.23	-54	115	58.7
	BLYP/6-311+G	-5.6	0.78	-692.5	-432.1	0.27	-56	119	59.4
	B3LYP/TZV	-4.7	0.9	-947.4	-642.4	0.06	-55	110	59.6
	B3LYP/6-311+G	-5.5	0.81	-902.1	-622.7	0.09	-56	115	59.3
$[\text{VO}^{15}\text{NGlySal}(\text{OCH}_3)]$ ( $\text{V-O}$ distance of 3.7 Å)	BLYP/TZV	3.1	0.79	-659.0	-432.2	0.19	90	29	71
	BLYP/6-311+G	-3.3*	0.98	-639.1	-425.7	0.19	-88	40	72
	B3LYP/TZV	3.1	0.73	-890.7	-620.2	0.16	89	20	71
	B3LYP/6-311+G	3.3	0.97	-845.1	-604.2	0.14	-88	31	71

\*The sign reversal for the  $C_Q$  in this case is due to the  $\eta_Q$  value being close to 1 and associated uncertainty in the sign of the quadrupolar coupling constant.

We have measured the  $^{15}\text{N}$  chemical shift tensor for both compounds, in a ROCSA experiment. The results are summarized in Table 5.2 and Figure 5.4. The experimentally determined isotropic chemical shifts for the two compounds differ merely by 4.1 ppm indicating a similar nitrogen coordination environment; the reduced anisotropy parameters differ by 16.6 ppm. In both cases the chemical shift tensors are rhombic.

Table 5.2: Experimental and Computed  $^{15}\text{N}$  NMR Parameters for  $[\text{VO}^{15}\text{NGlySalbz}]$  and  $[\text{VO}^{15}\text{NGlySal}(\text{OCH}_3)]$

compound	Method	$\delta_{\text{iso}}/\text{ppm}$	$\delta_{\sigma}/\text{ppm}$ ( $\pm 5$ )	$\eta_{\sigma}$ ( $\pm 0.05$ )
$[\text{VO}^{15}\text{NGlySalbz}]$	experiment	249.1	-193.3	0.69
	BLYP/TZV	263.2	-215.4	0.80
	BLYP/6-311+G	264.1	-214.6	0.82
	B3LYP/TZV	272.2	-224.3	0.79
	B3LYP/6-311+G	272.5	-223.1	0.81
	BLYP/TZV (non-opt)	253.4	-217.7	0.82
	B3LYP/TZV (non-opt)	259.3	-223.6	0.81
$[\text{VO}^{15}\text{NGlySal}(\text{OCH}_3)_x]$	experiment	253.2	-209.9	0.73
$[\text{VO}^{15}\text{NGlySalOCH}_3]$	BLYP/TZV	274.3	-229.0	0.82
	BLYP/6-311+G	275.1	-228.9	0.85
	B3LYP/TZV	282.1	-238.3	0.80
	B3LYP/6-311+G	282.5	-237.8	0.83
$[\text{VO}^{15}\text{NGlySal}(\text{OCH}_3)] \cdot (\text{CH}_3\text{OH})$ (V-O distance of 3.7 Å)	BLYP/TZV	267.7	-221.5	0.84
	BLYP/6-311+G	268.1	-221.1	0.86
	B3LYPTZV	275.5	-230.9	0.82
	B3LYP/6-311+G	275.6	-230.1	0.85

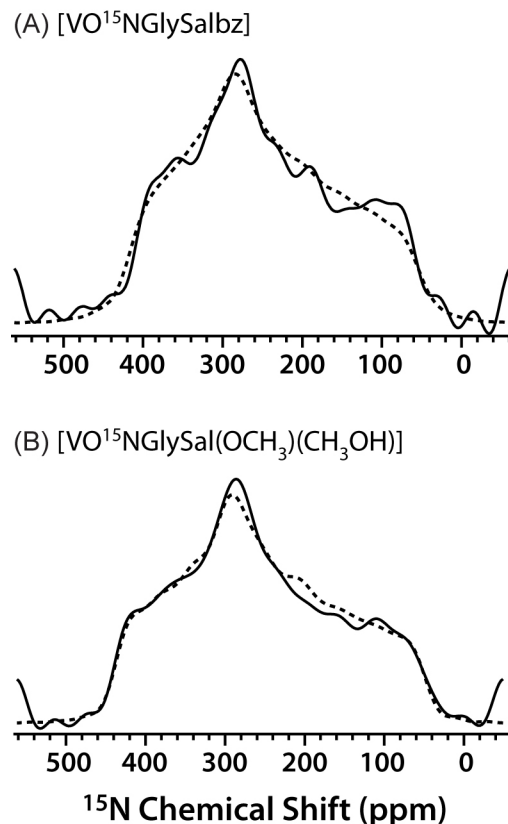


Figure 5.4: Experimental (solid line) and best-fit simulated (dashed line) ROCSA spectra for labeled  $^{15}\text{N}$  atom in (A)  $[\text{VO}^{15}\text{NGlySalbz}]$ , and (B)  $[\text{VO}^{15}\text{NGlySal}(\text{OCH}_3)](\text{CH}_3\text{OH})$ . The spectra were acquired at  $\nu_{\text{R}} = 10$  kHz and a magnetic field of 14.1 T. The experimental and SIMPSON best-fit  $^{15}\text{N}$  CSA parameters, as determined by the lowest RMSD, are shown in Table 5.2.

We have also recorded the  $^{13}\text{C}$  CPMAS spectra for both molecules, see Figure 5.5. The isotropic carbon chemical shifts are listed in Table 5.3. The chemical shift assignments presented in this table were performed on the basis of the density functional theory calculations. For the structurally characterized  $[\text{VO}^{15}\text{NGlySalbz}]$  the experimental and calculated shifts are in excellent agreement, except for those corresponding to the three carbon atoms directly bonded to nitrogens and for

ambiguities in the assignments for carbons 6, 11-13, and 15, whose chemical shifts overlap. In the case of  $[\text{VO}^{15}\text{NGlySal}](\text{OCH}_3) \cdot (\text{CH}_3\text{OH})$  the  $^{13}\text{C}$  shifts are in agreement with both penta- and hexacoordinate geometries according to the DFT calculations. The  $^{51}\text{V}$  and  $^{15}\text{N}$  parameters indicate that vanadium(V) adopts a hexacoordinate geometry with a methanol molecule weakly coordinated to the vanadium.

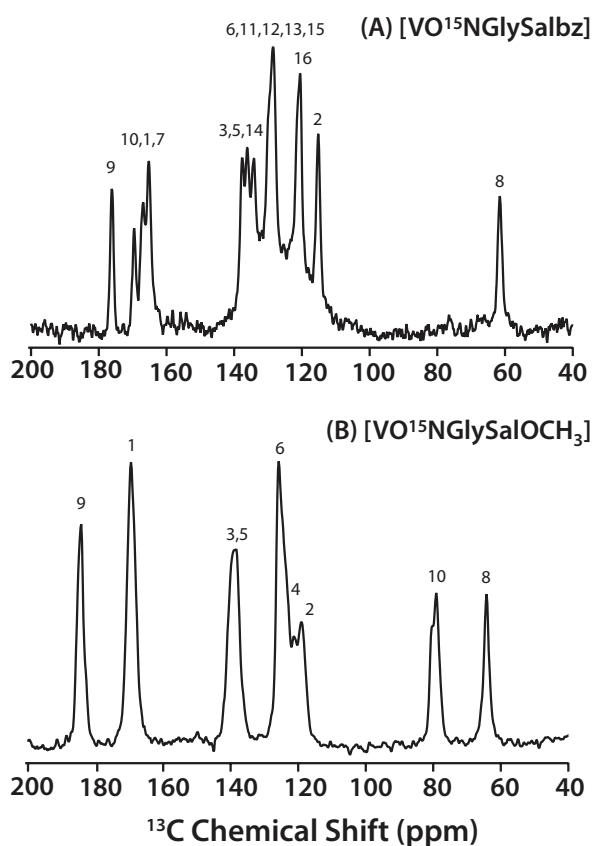


Figure 5.5:  $^{13}\text{C}$  CPMAS NMR spectra of (A)  $[\text{VO}^{15}\text{NGlySalbz}]$  and (B)  $[\text{VO}^{15}\text{NGlySal}](\text{OCH}_3) \cdot (\text{CH}_3\text{OH})$  acquired at the magnetic field of 9.4 T. The experimental chemical shift assignments were derived from DFT calculations and are listed in Table 5.3.

Table 5.3: Experimental and Computed (BLYP/TZV)  $^{13}\text{C}$  Isotropic Chemical Shifts for  $[\text{VO}^{15}\text{NGlySalbz}]$  and  $[\text{VO}^{15}\text{NGlySal}(\text{OCH}_3)]$ . The numbering of the carbon atoms is shown in Figure 5.1

Compound	Carbon Number	Experimental Chemical Shift (ppm) ( $\pm 0.5$ )	Calculated Chemical Shift (ppm)	
$[\text{VO}^{15}\text{NGlySalbz}]$	9	176.1	180.6	
	10	169.6	168.8	
	1	167.1	166.6	
	7	165.2	157.7	
	3	137.7	134.8	
	5	136.1	131.7	
	14	134.9	131.5	
	11*	128.9	131.2	
	12*	128.9	129.1	
	13*	128.9	128.7	
	15*	128.9	127.3	
	6*	120.9	124.2	
	16	120.9	123.3	
	4	120.9	119.1	
	2	115.2	117.0	
8*	61.5	70.6		
			<b>Penta-</b> $[\text{VO}^{15}\text{NGlySalOCH}_3]$	<b>Hexa-</b> $[\text{VO}^{15}\text{NGlySal}(\text{OCH}_3)] \cdot (\text{CH}_3\text{OH})$ (V-O distance 3.7 Å)
$[\text{VO}^{15}\text{NGlySal}(\text{OCH}_3)]$	9	182.9	183.9	183.1
	1	168.1	168.7	167.6
	7*	Missing	158.4	158.5
	3*	138.8	135.8	136.0
	5*	137.1	132.2	131.8
	6	124.6	124.6	123.5
	4	120.4	121.7	121.5
	2	119.0	118.8	118.5
	10	79.0	75.3	74.2
	8	64.3	67.9	68.0
11*	Missing	N/A	50.0	

\*Chemical shifts for these carbons could not be assigned unambiguously due to spectral overlap or missing peaks in the CPMAS spectra.

### 5.3.2 Distance Determination of $^{51}\text{V}$ - $^{15}\text{N}$ by LA-REDOR Experiments

For the two compounds under investigation, the  $^{51}\text{V}$  chemical shift anisotropies are substantial, which would impede accurate  $^{51}\text{V}$ - $^{15}\text{N}$  distance measurements by the commonly employed REAPDOR sequence.<sup>56,71</sup> Since the errors in distance estimates are as large as 10-15% (data not shown), we have pursued the recently developed LA-REDOR experiment.<sup>58</sup> This approach has been demonstrated to yield accurate distances even for quadrupolar sites possessing large quadrupolar and chemical shift interactions.<sup>72</sup>

In Figure 5.6, the experimental LA-REDOR data points and the simulated LA-REDOR curves are shown for  $[\text{VO}^{15}\text{NGlySalbz}]$  and  $[\text{VO}^{15}\text{NGlySal}(\text{OCH}_3)]\cdot(\text{CH}_3\text{OH})$ . The best-fit determined by minimizing the rmsd  $^{51}\text{V}$ - $^{15}\text{N}$  dipolar couplings are 300 Hz for  $[\text{VO}^{15}\text{NGlySalbz}]$  and 280 Hz for  $[\text{VO}^{15}\text{NGlySal}(\text{OCH}_3)]\cdot(\text{CH}_3\text{OH})$ , translating into the  $^{51}\text{V}$ - $^{15}\text{N}$  internuclear distances of 2.2 Å and 2.3 Å, respectively. The experimentally determined distance for  $[\text{VO}^{15}\text{NGlySalbz}]$  is within 5% of the 2.1 Å that derived from the X-ray structure. There is no X-ray structure for  $[\text{VO}^{15}\text{NGlySal}(\text{OCH}_3)]\cdot(\text{CH}_3\text{OH})$ , so we conducted a DFT geometry optimization at the B3LYP/TZV level of theory. See below. The geometry optimized structure reveals the  $^{51}\text{V}$ - $^{15}\text{N}$  distance of 2.15 Å within 7% of the DFT-derived distance.

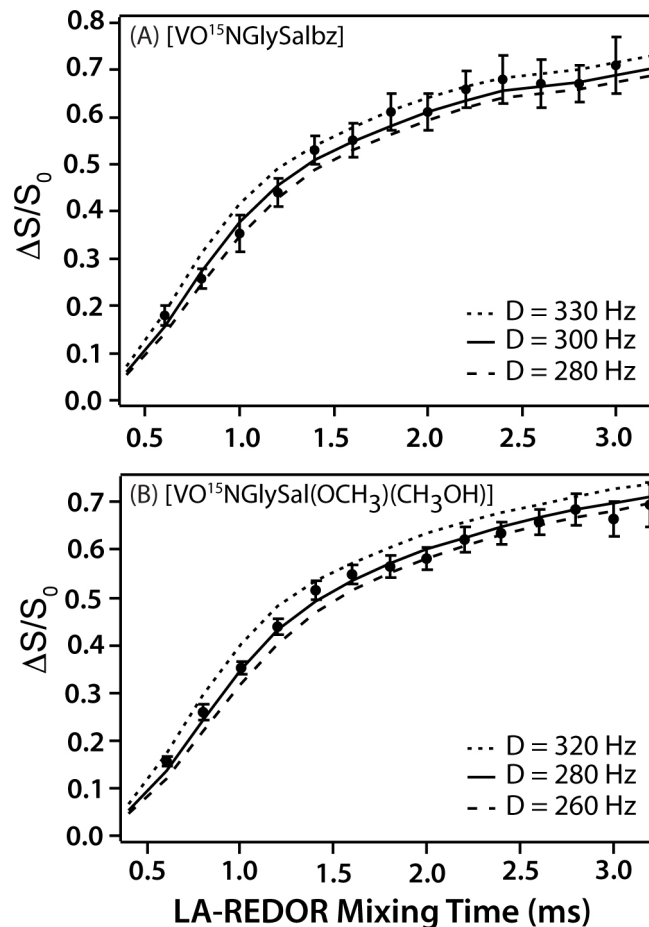


Figure 5.6: The LA-REDOR experimental data (filled circles) and simulated curves for (A)  $[\text{VO}^{15}\text{NGlySalbz}]$ , and (B)  $[\text{VO}^{15}\text{NGlySal}(\text{OCH}_3)] \cdot (\text{CH}_3\text{OH})$ . The LA-REDOR data were acquired at the magnetic field of 9.4 T. In (A), the simulated curves are depicted for  $D = 330$  Hz, 300 Hz, and 280 Hz, and the best-fit curve, as determined by the lowest RMSD, corresponds to  $D = 300 \pm 30$  Hz. In (B), simulated curves are shown for  $D = 320$  Hz, 280 Hz, and 260 Hz, and the best-fit curve corresponds to  $D = 280 \pm 40$  Hz. The simulations include the experimentally determined parameters describing the  $^{51}\text{V}$  and  $^{15}\text{N}$  EFG and CSA tensors:  $C_Q(^{51}\text{V})$ ,  $\eta_Q(^{51}\text{V})$ ,  $\delta_\sigma(^{51}\text{V})$ ,  $\eta_\sigma(^{51}\text{V})$ , and  $\delta_\sigma(^{15}\text{N})$ .

It is important to compare the above bond lengths in the context of the typical V-N bond distances. For instance, a triple bond in [(nacnac)V≡N(ODiP)] has been shown to be  $\sim 1.56 \text{ \AA}$ .<sup>73</sup> A terminal V=N double bond in hydrazido<sup>74</sup> and [N<sub>3</sub>N]V=NH complexes<sup>73</sup> is in the range of  $1.68 - 1.64 \text{ \AA}$ . In vanadium(V) bicyclic carbene–amide complex,<sup>75</sup> a terminal V-N single bond exists and its length is  $\sim 1.89 \text{ \AA}$ . In contrast, the non-terminal V-N bond length is significantly longer,  $\sim 2.11 \text{ \AA}$ , as has been shown in [VOCl<sub>2</sub>(CH<sub>3</sub>CN)(Hpycan)].<sup>76</sup> The vanadium-nitrogen bond length in the four-coordinated thionitrosyl complex of vanadium [(nacnac)V(NS)(OAr)] is  $\sim 1.68 \text{ \AA}$ ,<sup>77</sup> which clearly indicates that the V-N bond is not a *bona fide* triple bond but is instead either a double bond or has a partial triple bond character. When the donor nitrogen atom is coordinated to the vanadium center it results in a single V-N bond with the bond length around  $2.11 \text{ \AA}$ .<sup>78-80</sup>

Therefore, our results indicate that one can derive the V-N bond length (and bond order) based on the <sup>51</sup>V-<sup>15</sup>N LA-REDOR measurements. The bond order is often important for inferring the geometrical position of the coordinated nitrogen atom(s) (*cis* vs. *trans*) with respect to the terminal oxo group present in oxovanadium compounds.

### 5.3.3 Geometry Derivation Combining DFT Calculations and NMR Parameters

For quantum chemical calculations on [VO<sup>15</sup>NGlySalbz], we used the X-ray geometry as the starting structure, and conducted further geometry optimization at the B3LYP/TZV level. The NMR parameters were calculated using BLYP and B3LYP hybrid functionals and TZV and 6-311+G basis sets, on both the X-ray and geometry optimized structures. The results of the calculations of the <sup>51</sup>V, <sup>15</sup>N, and <sup>13</sup>C NMR parameters are summarized in Table 5.4, 5.5, and 5.6, respectively. For the

calculations of the  $^{51}\text{V}$  observables, the best agreement with the experiment is reached with the BLYP/TZV level of theory. Interestingly, the geometry-optimized structure yields remarkable agreement for the quadrupolar tensor, while the closest to the experimental chemical shift value is reached when the X-ray geometry is used without further optimization. If the B3LYP functional is used, the  $\delta_o$  value is grossly overestimated, by 185-229 ppm. It is also important to note that at all levels of theory, the  $^{51}\text{V}$  isotropic chemical shifts are in poor agreement with experiment: the deviations are 136/158 ppm for the BLYP, and 335/379 ppm for the B3LYP functionals (6-311+G/TZVP basis sets). That the calculated NMR parameters depend on the functional employed was confirmed previously.<sup>45</sup> Furthermore, as demonstrated by Bühl and coworkers, large deviations between experiment and theory are observed for isotropic chemical shifts, particularly for compounds with non-innocent ligands, and to reduce these discrepancies, advanced computationally expensive protocols are required.<sup>51,59</sup> The differences of the order of 136-158 ppm between experiment and theory at the BLYP level are in line with the previous reports,<sup>51</sup> while those yielded by the B3LYP functional are too large. On the basis of the above, we conclude that for the compounds under investigation the B3LYP functional does not yield accurate  $^{51}\text{V}$  chemical shift parameters. Therefore, even though we report and discuss the results of calculations for both functionals, we rely on the results of the BLYP-based calculations to derive structural information for  $[\text{VO}(^{15}\text{NGlySal})(\text{OCH}_3)]\cdot(\text{CH}_3\text{OH})$ .

The calculations of the  $^{15}\text{N}$  NMR parameters reveal similar behavior: the BLYP functional gives rise to the  $^{15}\text{N}$  CSA parameters, which are in much closer agreement with the experiment than those calculated at the B3LYP level. Interestingly, the calculated parameters do not depend to any significant extent on

whether the geometry-optimized or the X-ray structure is used (see Table 5.2). The difference between the experimental and the calculated  $^{15}\text{N}$   $\delta_c$  values is 21 ppm. We attribute this difference to the fact that we have conducted DFT calculations on a single molecule of  $[\text{VO}^{15}\text{NGlySalbz}]$ . It has been demonstrated that accurate chemical shift calculations in solids require taking into account the neighboring molecules in the crystal lattice.<sup>81</sup> At the moment such calculations are not feasible due to insufficient computational resources, but we will be attempting such studies in the future.

To reference the calculated  $^{13}\text{C}$  magnetic shieldings accurately, we followed the protocol reported by Emsley and colleagues, where the calculated absolute shieldings were corrected by a constant offset using linear regression of the data.<sup>70</sup> As shown in Figure 5.7, this procedure results in excellent agreement between the experimental and calculated  $^{13}\text{C}$  isotropic chemical shifts, permitting reliable assignments for  $[\text{VO}^{15}\text{NGlySalbz}]$ , except for carbons 6,11-13 and 15, whose chemical shifts overlap, and carbon 8 that is directly bonded to a nitrogen atom. (We note that we could not adopt a similar procedure for referencing the isotropic  $^{51}\text{V}$  and  $^{15}\text{N}$  chemical shifts because there is only one vanadium and one labeled nitrogen site in each molecule, and therefore we had to resort to reporting the isotropic chemical shift values with respect to a reference molecule, which introduces additional error, as discussed above.) Taking into consideration the overall good agreement between the experimental and calculated  $^{51}\text{V}$ ,  $^{15}\text{N}$ , and  $^{13}\text{C}$  NMR parameters, we conclude that the DFT-optimized structure for  $[\text{VO}^{15}\text{NGlySalbz}]$  is reliable.

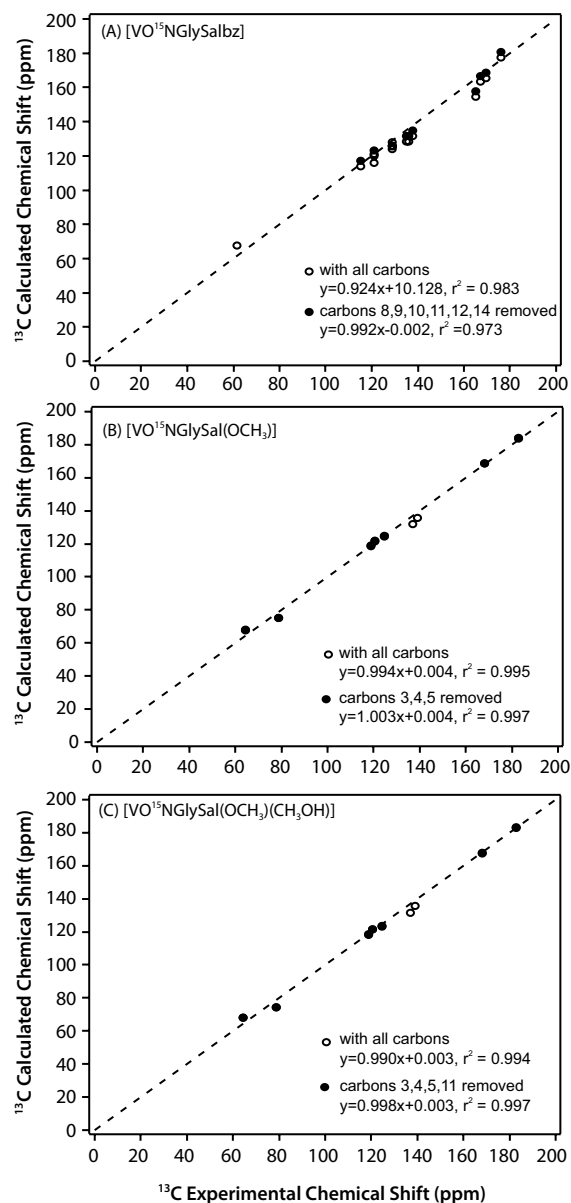


Figure 5.7: Correlation between calculated and experimental  $^{13}C$  isotropic chemical shifts in (A)  $[VO^{15}NGlySal(OCH_3)]$ , and (B)  $[VO(^{15}NGlySal)(OCH_3)] \cdot (CH_3OH)$ . In (B), the correlation is shown for pentacoordinate  $[VO^{15}NGlySalOCH_3]$  and in (C) for hexacoordinate  $[VO(^{15}NGlySal)(OCH_3)] \cdot (CH_3OH)$ . The empty and the filled circles represent all carbons and carbons with unambiguous chemical shift assignments, respectively. The linear fit equations are shown as legends on each graph. The isotropic shifts are summarized in Table 5.3.

We next turn our attention to  $[\text{VO}^{15}\text{NGlySal}(\text{OCH}_3)]\cdot(\text{CH}_3\text{OH})$ . Since no X-ray structure is available for this compound and its coordination geometry is not known *per se*, we have conducted DFT calculations by using the coordinates of  $\text{VO}_4^{3-}$  as the starting structure and incorporating the appropriate substituents, followed by geometry optimization at the B3LYP/TZV level. Using this method, we have generated two molecules: pentacoordinate  $[\text{VO}^{15}\text{NGlySalOCH}_3]$  and hexacoordinate  $[\text{VO}^{15}\text{NGlySal}(\text{OCH}_3)]\cdot(\text{CH}_3\text{OH})$ . For the latter, since the V---O distance is not known, we have conducted a series of calculations for distances fixed in the range of 2.0–4.5 Å, and optimized the geometry of the rest of the compound. The optimized geometries are shown in Figure 5.8.

For the pentacoordinate  $[\text{VO}^{15}\text{NGlySal}(\text{OCH}_3)]$ , significant differences are observed between the experimental and calculated  $^{51}\text{V}$  NMR parameters. The calculated absolute values of  $^{51}\text{V}$   $C_Q$  are in the range of 4.7 - 5.6 MHz depending on the method (vis-à-vis the experimental value of 3.5 MHz), suggesting that the actual molecule is not pentacoordinate. The calculated  $^{51}\text{V}$  isotropic chemical shift also agrees poorly with the experiment: depending on the method, the calculated values range between -692.5 and -947.4 ppm. Even though it has been reported previously that the calculated  $^{51}\text{V}$  isotropic chemical shifts are typically accurate to within 100-150 ppm, the deviations are too large to be explained by the errors of the DFT calculations (see the discussion for  $[\text{VO}^{15}\text{NglySalbz}]$  above).<sup>51</sup> The agreement for the reduced chemical shift anisotropy is significantly better: the calculations reveal a range of -442.5 to -642.4 ppm (vs. the experimental value of -421.5 ppm).

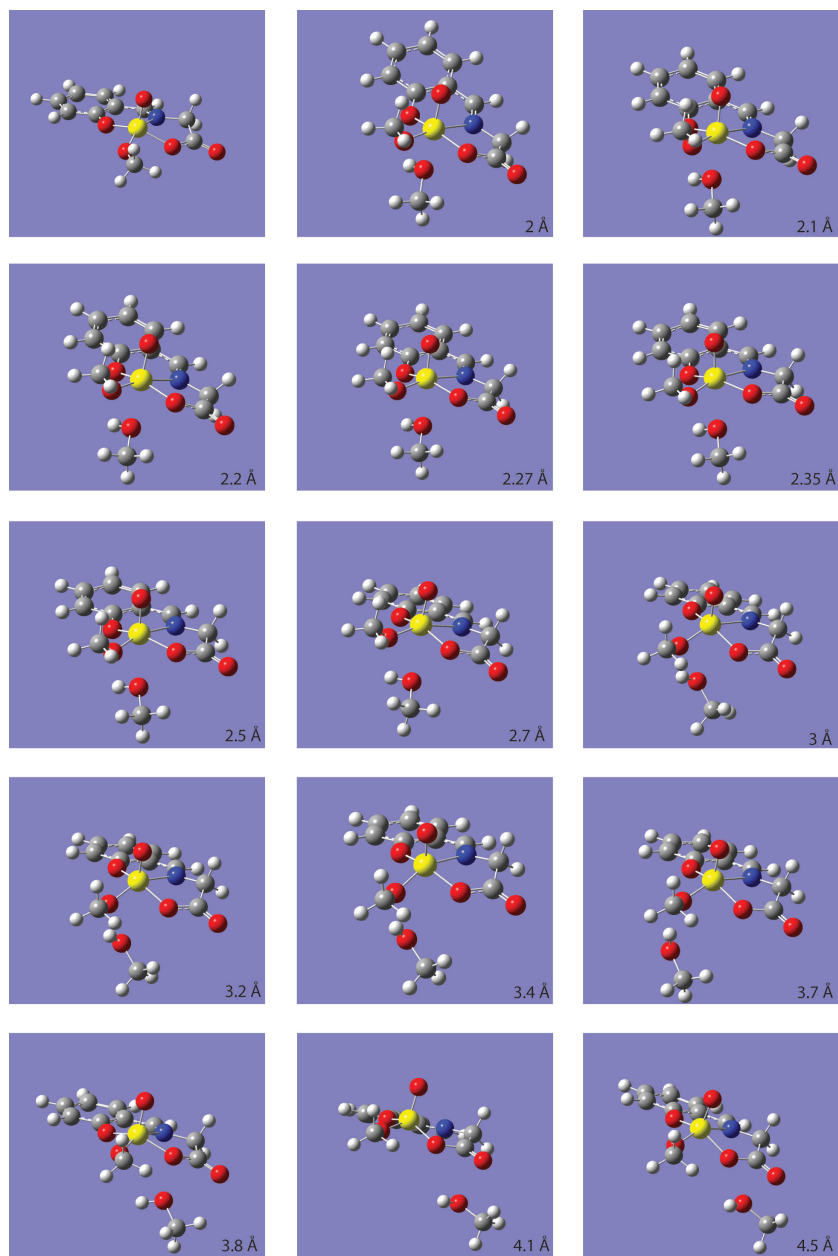


Figure 5.8: Structures of  $[\text{VO}^{15}\text{NglySal}(\text{OCH}_3)]$  and  $[\text{VO}^{15}\text{NglySal}(\text{OCH}_3)(\text{CH}_3\text{OH})]$  with  $\text{V}\cdots\text{OHCH}_3$  of different distances. Distances are marked in each structure. These structures are optimized with Gaussian09 at B3LYP/TZV theory level and are used for NMR parameters calculations.

The calculations with the distorted octahedral  $[\text{VO}^{15}\text{NglySal}(\text{OCH}_3)]\cdot(\text{CH}_3\text{OH})$  document a systematic dependence of the  $^{51}\text{V}$  NMR observables on the V---OHCH<sub>3</sub> distance, as summarized in Table 5.4. The results of the BLYP-based calculations indicate, for both the quadrupolar and the chemical shift tensors, that

- when methanol molecule is strongly coordinated to the vanadium center, the distance of 2-2.7 Å shows poor agreement between experiment and theory;
- as the V---OHCH<sub>3</sub> distance is increased up to 3-3.7 Å, the agreement between the calculated and the experimental parameters improves dramatically;
- the best agreement is attained at the V---OHCH<sub>3</sub> distance of 3-3.7 Å and the summary of the parameters is shown in Table 5.1; the calculated and experimental parameters agree within the error of the calculations;
- as the V---OHCH<sub>3</sub> distance is increased beyond 3.7 Å, the deviation between the calculated and experimental NMR observables systematically increases. At the distance of 4.5 Å, the calculated parameters are close to those of pentacoordinate  $[\text{VO}^{15}\text{NglySal}(\text{OCH}_3)]$ .

Table 5.4: Experimental and Computed  $^{51}\text{V}$  NMR Parameters for  $[\text{VO}^{15}\text{NGlySal}(\text{OCH}_3)]\cdot(\text{CH}_3\text{OH})$  as a Function of V---OHCH<sub>3</sub> Distance

V-CH <sub>3</sub> OH (Å)	C <sub>Q</sub> /MHz	η <sub>Q</sub>	δ <sub>iso</sub> /ppm	δ <sub>σ</sub> /ppm	η <sub>σ</sub>	α/degree	β/degree	γ/degree
<b>Experiment</b>	<b>3.5±0.1</b>	<b>0.73±0.05</b>	<b>-528.9±5</b>	<b>-421.4±5</b>	<b>0.31±0.05</b>	<b>0±30</b>	<b>90±30</b>	<b>90±30</b>
none	-4.8	0.84	-711.9	-442.5	0.23	-54.8	115	58.7
2	9.8	0.34	-591.8	-328	0.28	-16.1	137	13
2.1	6.8	0.44	-605	-328.8	0.27	-20.9	136	17.4
2.2	4.5	0.59	-617.2	-331.2	0.28	-25	133	22.1
2.27	3.3	0.77	-625.1	-333.8	0.28	-27.4	129	25.5
2.35	-2.3	0.91	-633.7	-337.5	0.28	-29.3	121	30
2.5	-1.6	0.75	-647.6	-347.5	0.27	-27.2	93.1	40.4
2.7	2	0.32	-659.4	-369.7	0.24	27.1	24.9	-58.6
3	3	0.61	-653.6	-425.8	0.18	72.4	40.1	88.6
3.2	3	0.65	-658.9	-435.8	0.17	77	36.6	80.5
3.4	3	0.66	-660.7	-434.9	0.18	83.9	30.1	72.2
3.7	3.1	0.79	-659	-432.2	0.19	89.7	29.4	71.3
3.8	4.1	0.8	-694.4	-431.4	0.27	-6.9	87.8	30.6
4.1	-4.1	0.99	-698.6	-436	0.25	-3.5	103	27
4.5	-4.6	0.77	-702.3	-441.9	0.19	15.5	123	14.6
<b>BLYP/6-311+G</b>								
V-CH <sub>3</sub> OH (Å)	C <sub>Q</sub> /MHz	η <sub>Q</sub>	δ <sub>iso</sub> /ppm	δ <sub>σ</sub> /ppm	η <sub>σ</sub>	α/degree	β/degree	γ/degree
<b>Experiment</b>	<b>3.5±0.1</b>	<b>0.73±0.05</b>	<b>-528.9±5</b>	<b>-421.4±5</b>	<b>0.31±0.05</b>	<b>0±30</b>	<b>90±30</b>	<b>90±30</b>
none	-5.6	0.78	-692.5	-432.1	0.27	-56.3	119	59.4
2	11.1	0.34	-572.4	-320.6	0.26	-15.6	137	13.4
2.1	7.8	0.44	-586.4	-320.1	0.26	-20.2	135	17.8
2.2	5.3	0.58	-598.9	-322	0.26	-24.2	132	22.3
2.27	3.9	0.73	-607.1	-324.4	0.27	-26.6	129	25.4
2.35	-2.7	1	-615.9	-328.3	0.27	-28.8	123	29.1
2.5	-1.9	0.65	-629.9	-339.2	0.26	-28	106	36.1
2.7	2	0.62	-640.2	-364.2	0.23	23.7	45.9	-51
3	3.2	0.81	-632	-421.7	0.17	77	52.9	83.3
3.2	3.2	0.86	-638	-430.1	0.17	81.6	50.7	77.3
3.4	3.2	0.88	-639.3	-428.5	0.19	87.7	43.8	72.1
3.7	-3.3	0.98	-639.1	-425.7	0.19	-87.9	39.8	72.3
3.8	4.6	0.89	-673	-422.7	0.32	-11.3	90.9	32.7
4.1	-4.8	0.9	-676.5	-426.8	0.3	-8	106	29.2
4.5	-5.4	0.67	-680.6	-431.7	0.23	11	127	18.3

B3LYP/TZV								
V-CH <sub>3</sub> OH (Å)	C <sub>Q</sub> /MH z	η <sub>Q</sub>	δ <sub>iso</sub> /ppm	δ <sub>σ</sub> /ppm	η <sub>σ</sub>	α/degree	β/degree	γ/degree
Experiment	3.5±0.1	0.73±0.0 5	-528.9±5	421.4± 5	0.31±0.0 5	0±30	90±30	90±30
none	-4.7	0.9	-947.4	-642.4	0.06	-54.7	110	59.6
2	9.9	0.33	-819.6	-480	0.21	-16.3	134	11.9
2.1	6.8	0.42	-832	-483.8	0.21	-21.2	133	16.1
2.2	4.4	0.57	-843.9	-489.1	0.21	-25.3	130	20.9
2.27	3.1	0.75	-851.7	-493.4	0.21	-27.5	125	24.8
2.35	-2.1	0.92	-860.2	-498.9	0.21	-29.1	116	30.9
2.5	-1.4	0.99	-874.3	-512.1	0.21	-25.6	73.8	47.2
2.7	2.1	0.1	-887.5	-541.4	0.2	33	15.4	-85.8
3	3.1	0.58	-883.2	-614.2	0.19	73.7	34.6	-87.3
3.2	3.1	0.6	-889.4	-624.5	0.18	77.8	29.3	83.1
3.4	3.1	0.6	-892	-622.6	0.17	83.9	20.8	72.6
3.7	3.1	0.73	-890.7	-620.2	0.16	89	19.5	70.6
3.8	4.2	0.71	-928.7	-626.4	0.11	-1.87	83.5	32.8
4.1	4.2	0.92	-933.4	-631.8	0.09	2.5	99.8	28.1
4.5	-4.5	0.84	-936.2	-635.6	0.06	22.7	122	13.9

B3LYP/6-311+G								
V-CH <sub>3</sub> OH (Å)	C <sub>Q</sub> /MH z	η <sub>Q</sub>	δ <sub>iso</sub> /ppm	δ <sub>σ</sub> /ppm	η <sub>σ</sub>	α/degree	β/degree	γ/degree
Experiment	3.5±0.1	0.73±0.0 5	-528.9±5	421.4± 5	0.31±0.0 5	0±30	90±30	90±30
none	-5.5	0.81	-902.1	-622.8	0.09	-56.2	115	59.3
2	11.3	0.32	-776.4	-465.2	0.2	-15.7	133	12.2
2.1	7.8	0.41	-789.6	-467.1	0.2	-20.3	132	16.4
2.2	5.2	0.55	-801.7	-471.4	0.2	-24.3	130	20.9
2.27	3.8	0.7	-809.7	-475.3	0.2	-26.5	126	24.4
2.35	2.6	0.97	-818.2	-480.9	0.2	-28.3	119	29
2.5	-1.8	0.79	-832.2	-494.8	0.2	-25	133	22.1
2.7	2.1	0.4	-843.7	-526.6	0.19	30	29.1	-78.6
3	3.3	0.74	-836.5	-600.5	0.18	78.7	45.4	87.3
3.2	3.3	0.79	-843.2	-609.5	0.17	82.8	42.2	79.4
3.4	3.3	0.82	-845.2	-607	0.16	88.3	34.7	72
3.7	3.3	0.97	-845.1	-604.2	0.14	-87.9	31.4	71.4
3.8	4.6	0.81	-881.9	-608.1	0.14	-7.02	87.2	35.2
4.1	-4.7	0.97	-885.7	-613.2	0.13	-2.76	103	30.7
4.5	-5.3	0.72	-888.9	-616.7	0.08	18.2	126	18.2

The dependence of  $C_Q$  on the V---OHCH<sub>3</sub> distance in [VO(<sup>15</sup>NGlySal)(OCH<sub>3</sub>)]·(CH<sub>3</sub>OH) can be explained by the analysis of the electrostatic potential (ESP) surfaces, Figure 5.9. When the distance is 2 Å, the ESP surfaces reveal large asymmetry in charge distribution arising from the axial ligands and giving rise to a large calculated  $C_Q$  of 9.8 MHz. This is in sharp disagreement with the experimental value of 3.5 MHz and can be ruled out. As the distance increases, the charge distribution becomes more symmetric, resulting in the systematic decrease of  $C_Q$  with the minimum value of -1.6 MHz observed at the V---OHCH<sub>3</sub> distance of 2.5 Å, and corresponding to the slightly distorted octahedral symmetry. As the distance is systematically increased, so is the asymmetry in the charge distribution, and at the distance of 4.5 Å,  $C_Q$  is -4.6 MHz, close to that of the pentacoordinate complex lacking a coordinated CH<sub>3</sub>OH molecule. The closest agreement between experimental and calculated  $C_Q$  is reached when the V---OHCH<sub>3</sub> distance is either 2.27 Å or 3.0–3.7 Å. The first case, where CH<sub>3</sub>OH is a *bona fide* ligand coordinated to the vanadium, can be ruled out on the basis of a dismal agreement between the calculated and experimental <sup>51</sup>V reduced anisotropy (See Table 5.4). On the other hand, when the V---OHCH<sub>3</sub> distance is in the range of 3.0–3.7 Å, the agreement between the calculated and experimental <sup>51</sup>V quadrupolar and chemical shift tensor parameters is excellent. Therefore, we conclude that the methanol molecule in [VO(<sup>15</sup>NGlySal)(OCH<sub>3</sub>)]·(CH<sub>3</sub>OH) plays the role of a crystallographic solvent and exhibits a weak electrostatic interaction with the vanadium.

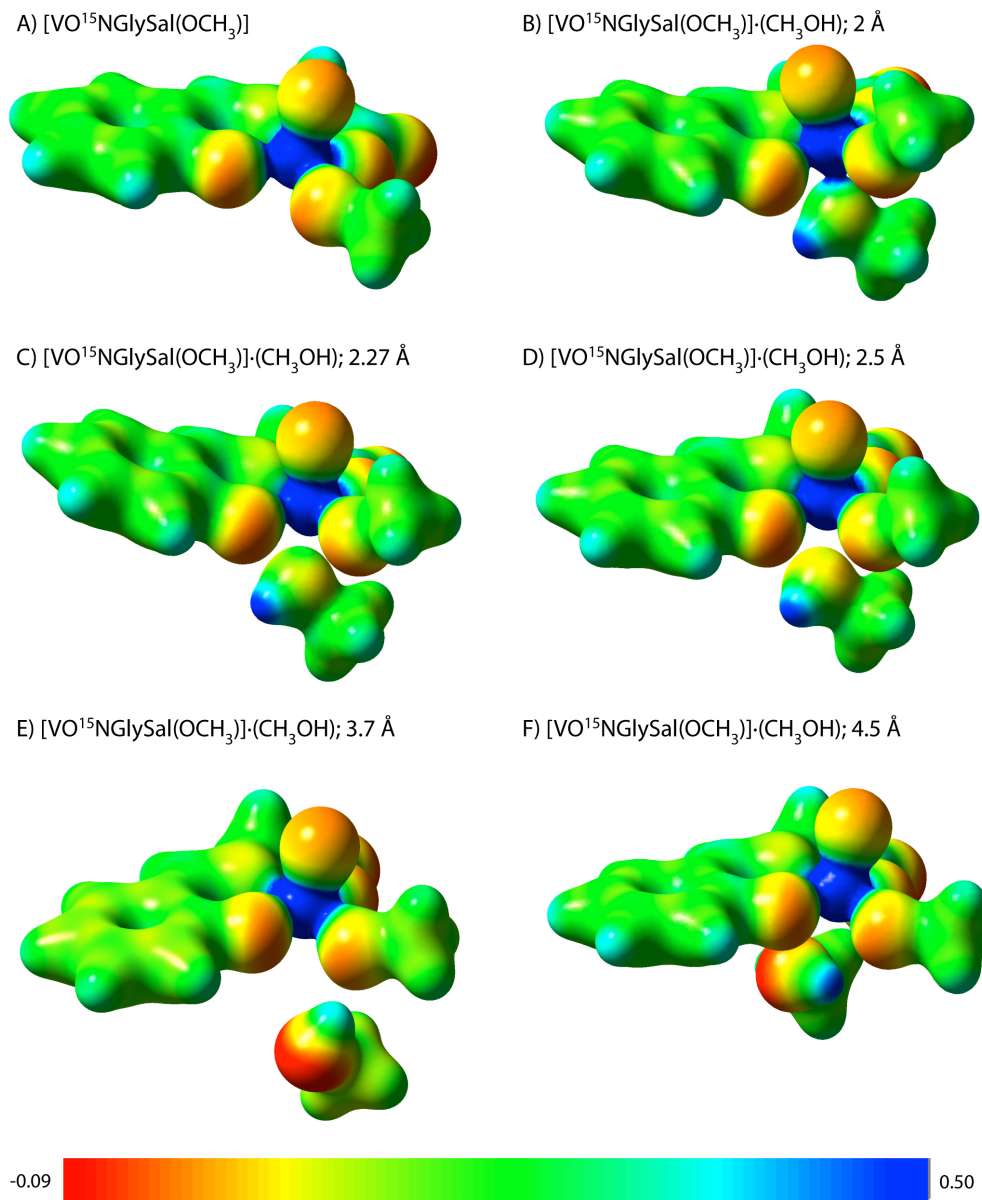


Figure 5.9: Image of the electrostatic potential (ESP) surfaces of  $[\text{VO}^{15}\text{NGlySal}(\text{OCH}_3)]$  (A) and  $[\text{VO}^{15}\text{NGlySal}(\text{OCH}_3)] \cdot (\text{CH}_3\text{OH})$  (B-F) generated in Gaussview from the total SCF density calculated by Gaussian at the BLYP/TZV level. For  $[\text{VO}^{15}\text{NGlySal}(\text{OCH}_3)] \cdot (\text{CH}_3\text{OH})$ , the ESP surfaces are plotted for structures where  $\text{V} \cdots \text{OHCH}_3$  distances were fixed at 2 Å (B), 2.27 Å (C), 2.5 Å (D), 3.7 Å (E), and 4.5 Å (F), and the geometries optimized. The regions of positive and negative charge are depicted in blue and red, respectively. The color legend is shown at the bottom.

Not surprisingly, the  $^{15}\text{N}$  NMR parameters are also sensitive to the coordination geometry, as summarized in Table 5.2. For the pentacoordinate  $[\text{VO}^{15}\text{NGlySalOCH}_3]$ , the isotropic chemical shift and reduced anisotropy computed at the BLYP level of theory are within 21.1-21.9 and 19-19.1 ppm of the corresponding experimental values. For the hexacoordinate  $[\text{VO}^{15}\text{NGlySal}(\text{OCH}_3)]\cdot(\text{CH}_3\text{OH})$ , the  $^{15}\text{N}$  chemical shift parameters show systematic dependence on the V---OHCH<sub>3</sub> distance, with the closest agreement between experiment and theory found for distances of 3–3.7 Å. The deviation between experiment and calculation at the BLYP level of theory is 12.2-14.8 and 9-11.6 ppm for  $\delta_{\text{iso}}$  and  $\delta_{\parallel}$ , respectively (see Table 5.2 and Table 5.5), which are much smaller discrepancies than for the pentacoordinate structure.

Finally, we have also examined the  $^{13}\text{C}$  isotropic chemical shifts for the pentacoordinate  $[\text{VO}^{15}\text{NGlySal}(\text{OCH}_3)]$  and the hexacoordinate  $[\text{VO}^{15}\text{NGlySal}(\text{OCH}_3)]\cdot(\text{CH}_3\text{OH})$  molecules. As shown in Figure 5.7 and summarized in Tables 5.3 and 5.6, the  $^{13}\text{C}$  isotropic chemical shift parameters are not sensitive enough to the coordination geometry, and very strong correlations are seen between the computed and experimental values, assuming both penta- and hexacoordinate structures. This is not particularly surprising, given the fact that there are no carbon atoms directly bonded to vanadium.

Table 5.5: Experimental and Computed  $^{15}\text{N}$  NMR Parameters for  $[\text{VO}^{15}\text{NGlySal}(\text{OCH}_3)]\cdot(\text{CH}_3\text{OH})$  as a Function of V---OHCH<sub>3</sub> Distance

V-CH <sub>3</sub> OH (Å)	BLYP/TZV			B3LYP/TZV			BLYP/6-311+G		
	$\delta_{\text{iso}}/\text{ppm}$	$\delta_{\sigma}/\text{ppm} (\pm 5)$	$\eta_{\sigma} (\pm 0.05)$	$\delta_{\text{iso}}/\text{ppm}$	$\delta_{\sigma}/\text{ppm} (\pm 5)$	$\eta_{\sigma} (\pm 0.05)$	$\delta_{\text{iso}}/\text{ppm}$	$\delta_{\sigma}/\text{ppm} (\pm 5)$	$\eta_{\sigma} (\pm 0.05)$
<b>Experiment</b>	<b>253.2</b>	<b>-209.9</b>	<b>0.73</b>	<b>253.2</b>	<b>-209.9</b>	<b>0.73</b>	<b>253.2</b>	<b>-209.9</b>	<b>0.73</b>
<b>none</b>	274.3	-229	0.82	282.1	-238.3	0.8	275.1	-228.9	0.85
<b>2</b>	280.3	-244.4	0.83	288.1	-252	0.81	280.2	-242.6	0.85
<b>2.1</b>	279.3	-243.4	0.82	288.1	-252	0.81	280.2	-242.6	0.85
<b>2.2</b>	278.5	-241.9	0.82	286.6	-250	0.8	278.7	-240	0.82
<b>2.27</b>	278.2	-240.9	0.82	286.4	-249.2	0.8	278.4	-239	0.84
<b>2.35</b>	278	-239.8	0.82	286.3	-248.4	0.8	278.3	-237.8	0.85
<b>2.5</b>	277.9	-237.8	0.84	286.3	-247	0.82	278	-236.4	0.86
<b>2.7</b>	275.4	-232.9	0.85	283.7	-242.4	0.83	275.6	-231.6	0.87
<b>3</b>	265.5	-220	0.84	273.5	-229.1	0.82	265.5	-218.9	0.86
<b>3.2</b>	265.4	-220	0.84	273.4	-229	0.82	265.6	-219.3	0.86
<b>3.4</b>	266.4	-220.3	0.84	274.2	-229.5	0.82	266.8	-219.8	0.86
<b>3.7</b>	267.7	-221.5	0.84	275.5	-230.9	0.82	268.1	-221.1	0.86
<b>3.8</b>	279.3	-238.5	0.77	287.7	-247.8	0.75	279.6	-237.4	0.79
<b>4.1</b>	279.1	-236.5	0.78	287.2	-245.9	0.76	279.4	-236.7	0.8
<b>4.5</b>	275.2	-228.8	0.82	282.7	-238	0.8	275.1	-227.9	0.83

Table 5.6: Experimental and Computed  $^{13}\text{C}$  NMR Parameters for  $[\text{VO}^{15}\text{NGlySalbz}]$  and  $[\text{VO}^{15}\text{NGlySal}(\text{OCH}_3)]$

Carbon Number*	Experimental Chemical Shift (ppm)	BLYP/TZV	BLYP/6-311+G	B3LYP/TZV	B3LYP/6-311+G
		Calculated Chemical Shift (ppm)			
<b><math>[\text{VO}^{15}\text{NGlySalbz}]</math></b>					
9	176.1	180.6	174.3	192.2	185.5
10	169.6	168.8	163	180.6	174.2
1	167.1	166.6	162.1	176	171
7	165.2	157.7	152.7	170	164.6
3	137.7	134.8	131.7	144.3	140.6
5	136.1	131.7	128	140.6	136.4
14	134.9	131.5	127.4	140.4	136
11**	128.9	131.2	126.2	138.6	134
12**	128.9	129.1	125.3	138.1	133.3
13**	128.9	128.7	125.3	136.7	132.9
15**	128.9	127.3	123.8	135.4	131.5
6**	120.9	124.2	119.8	132.1	127.4
16	120.9	123.3	118.9	130.7	126.1
4	120.9	119.1	115.8	126.8	123.1
2	115.2	116.9	112.7	125.1	120.5
8**	61.5	70.6	67.3	75.1	71.7
<b><math>[\text{VO}^{15}\text{NGlySal}(\text{OCH}_3)]</math></b>					
9	182.9	183.9	178.9	193.8	188
1	168.1	168.7	164.9	176.4	171.9
7**	Missing	158.4	155	169.7	165.6
3**	138.8	135.9	133.4	144.1	141
5**	137.1	132.2	129.9	140	136.9
6	124.6	124.6	120.8	130.2	126.1
4	120.4	121.7	120	128.3	125.9
2	119	118.8	116.2	126	122.9
10	78.9	75.3	73.9	79.4	77.7
8	64.3	68	65.5	70.9	68.2
<b><math>[\text{VO}^{15}\text{NGlySal}(\text{OCH}_3)(\text{CH}_3\text{OH})]</math></b>					
9	182.9	183.1	178.2	193.2	187.6
1	168.1	167.6	164.3	175.6	171.5
7**	Missing	158.5	155.4	170	166.1
3**	138.8	136	133.8	144.5	141.6
5**	137.1	131.8	129.4	139.7	136.7
6	124.6	123.5	120.2	129.4	125.7
4	120.4	121.5	119.5	128.3	125.5
2	119	118.5	115.6	125.9	122.5
10	78.9	74.2	73	78.1	76.6
8	64.3	68	65.8	71.3	68.8
11**	Missing	50	48.2	52.5	50.7

\*The numbering of the carbon atoms is shown in Figure 5.1.

\*\*Chemical shifts for these carbons could not be assigned unambiguously due to spectral overlap or missing peaks in the CPMAS spectra.

Taken together, these results illustrate the fact that in small molecules, the DFT methods have reached a level where reliable structural parameters can be generated in the absence of single-crystal X-ray data. Importantly, through a combination of experiment and theory we have been able to derive the local 3D structure of  $[\text{VO}(^{15}\text{NGlySal})(\text{OCH}_3)]\cdot(\text{CH}_3\text{OH})$  and found that the vanadium coordination sphere is expanded to include a neutral and weakly coordinated methanol molecule. The methanol is in the *trans* position with respect to the terminal oxo group, at a distance of 3.0-3.7 Å. Since the majority of five-coordinate vanadium compounds are square pyramidal,<sup>82</sup> the presence of a sixth weakly coordinated ligand provides some additional stability to the complex. The potential for such interaction exists, but not many methods are available to demonstrate such an interaction. On the other hand, it is also possible that such a weak interaction disrupts the order and crystallinity of the material. These findings suggest that NMR crystallography is a particularly powerful method for investigations into materials in which solvent interactions are weak and potentially interfere with crystallization of the material.

To take application of solid-state NMR to the next level we intend to include a combined experimental-MAS NMR and computational approach where the experimental NMR parameters are used as fixed metrics in a constrained DFT-based geometry minimization. The NMR parameters include  $^{51}\text{V}$ ,  $^{15}\text{N}$ ,  $^{13}\text{C}$ , and  $^1\text{H}$  tensorial interactions as well as internuclear distances. A similar approach has been successfully demonstrated on small organic molecules.<sup>70,81</sup> We anticipate that including  $^{51}\text{V}$  quadrupolar and chemical tensors is advantageous and will permit solving crystal structures of vanadium-based complexes in the absence of any single crystal X-ray information.

#### 5.4 Conclusions and Future Outlook

To make NMR crystallography a viable approach for determination of 3D structures in vanadium-containing bioinorganic solids, protocols must be developed where the experimental NMR parameters are utilized as constraints in the iterative DFT geometry optimization steps. To this end, we have explored the NMR crystallography approach for two vanadium(V)-containing complexes,  $[\text{VO}^{15}\text{NGlySalbz}]$  and  $[\text{VO}^{15}\text{NGlySal}(\text{OCH}_3)]\cdot(\text{CH}_3\text{OH})$ . In these studies we have demonstrated that the experimental  $^{51}\text{V}$ ,  $^{15}\text{N}$ , and  $^{13}\text{C}$  NMR parameters together with internuclear  $^{51}\text{V}$ - $^{15}\text{N}$  distances represent useful structural constraints that can be employed in the DFT calculations of 3D structures of vanadium compounds in the absence of single crystal X-ray information. Our results indicate that the internuclear  $^{51}\text{V}$ - $^{15}\text{N}$  distances report on the V-N bond order, which is one for both compounds investigated, and which are also important in deriving the oxidation state on the metal and its coordination geometry. For the compound,  $[\text{VO}^{15}\text{NGlySal}(\text{OCH}_3)]\cdot(\text{CH}_3\text{OH})$ , which has not previously been structurally characterized, we have shown that the methanol associated with the solid actually engages in a weak interaction with the vanadium, resulting in six-coordinate vanadium. These studies allow unambiguous determination of the coordination geometry and the three-dimensional structure in non-crystalline materials using geometrical and tensorial parameters as restraints in DFT structure calculations.

## REFERENCES

- (1) Polenova, T.; Gupta, R.; Goldbourn, A. *Anal. Chem.* **2015**, *87*, 5458.
- (2) Harris, K. R., Wasylishen, E. R., Duer, J. M. *NMR Crystallography*; John Wiley & Sons Ltd, 2009.
- (3) Martineau, C. *Solid State Nucl. Magn. Reson.* **2014**, *63-64*, 1.
- (4) Li, M. Y.; Yehl, J.; Hou, G. J.; Chatterjee, P. B.; Goldbourn, A.; Crans, D. C.; Polenova, T. *Inorg. Chem.* **2015**, *54*, 1363.
- (5) Hanson, S. K.; Baker, R. T.; Gordon, J. C.; Scott, B. L.; Silks, L. A.; Thorn, D. L. *J. Am. Chem. Soc.* **2010**, *132*, 17804.
- (6) Son, S.; Toste, F. D. *Angew. Chem. Int. Ed. Engl.* **2010**, *49*, 3791.
- (7) Hanson, S. K.; Baker, R. T.; Gordon, J. C.; Scott, B. L.; Sutton, A. D.; Thorn, D. L. *J. Am. Chem. Soc.* **2009**, *131*, 428.
- (8) Zhang, Y. P.; Holm, R. H. *Inorg. Chem.* **1990**, *29*, 911.
- (9) Vennat, M.; Herson, P.; Bregeault, J. M.; Shul'pin, G. B. *Eur. J. Inorg. Chem.* **2003**, 908.
- (10) El Aakel, L.; Launay, F.; Atlamsani, A.; Bregeault, J. M. *Chem. Commun.* **2001**, 2218.
- (11) Zhang, W.; Yamamoto, H. *J. Am. Chem. Soc.* **2007**, *129*, 286.
- (12) Mimoun, H.; Mignard, M.; Brechot, P.; Saussine, L. *J. Am. Chem. Soc.* **1986**, *108*, 3711.
- (13) Willsky, G. R.; Chi, L. H.; Godzala, M. *Coord. Chem. Rev.* **2011**, *255*, 2258.
- (14) Li, M.; Ding, W. J.; Smee, J. J.; Baruah, B.; Willsky, G. R.; Crans, D. C. *Biometals* **2009**, *22*, 895.

- (15) Pereira, M. J.; Carvalho, E.; Eriksson, J. W.; Crans, D. C.; Aureliano, M. J. *Inorg. Biochem.* **2009**, *103*, 1687.
- (16) Smee, J. J.; Epps, J. A.; Ooms, K. J. *Inorg. Biochem.* **2009**, *103*, 575.
- (17) Crans, D. C.; Yang, L. Q.; Jakusch, T.; Kiss, T. *Inorg. Chem.* **2000**, *39*, 4409.
- (18) Thompson, K. H.; Lichter, J.; Lebel, C.; Scaife, M. C.; McNeill, J. H.; Orvig, C. J. *Inorg. Biochem.* **2009**, *103*, 554.
- (19) Deboer, E.; Plat, H.; Tromp, M. G. M.; Wever, R.; Franssen, M. C. R.; Vanderplas, H. C.; Meijer, E. M.; Schoemaker, H. E. *Biotechnol. Bioeng.* **1987**, *30*, 607.
- (20) Coupe, E. E.; Smyth, M. G.; Fosberry, A.; Hall, R. M.; Littlechild, J. A. *Protein Expres. Purif.* **2007**, *52*, 265.
- (21) Butler, A.; Carter-Franklin, J. N. *Nat. Prod. Rep.* **2004**, *21*, 180.
- (22) Itoh, N.; Hasan, A. K. M. Q.; Izumi, Y.; Yamada, H. *Eur. J. Biochem.* **1988**, *172*, 477.
- (23) Carter-Franklin, J. N.; Butler, A. *J. Am. Chem. Soc.* **2004**, *126*, 15060.
- (24) Andersson, M.; Willetts, A.; Allenmark, S. *J. Org. Chem.* **1997**, *62*, 8455.
- (25) ten Brink, H. B.; Dekker, H. L.; Shoemaker, H. E.; Wever, R. *J. Inorg. Biochem.* **2000**, *80*, 91.
- (26) Ding, C.; Zhang, H. M.; Li, X. F.; Liu, T.; Xing, F. *J. Phys. Chem. Lett.* **2013**, *4*, 1281.
- (27) ; Vanadium and Batteries.
- (28) ; <http://greenbuildingelements.com/2013/07/10/hokkaido-to-utilize-60-mwh-vanadium-flow-battery-for-grid-storage/>.
- (29) Chatterjee, P. B.; Bhattacharya, K.; Chaudhury, M. *Coord. Chem. Rev.* **2011**, *255*, 2150.
- (30) Lapina, O. B.; Khabibulin, D. F.; Shubin, A. A.; Terskikh, V. V. *Prog. Nucl. Magn. Reson. Spectrosc.* **2008**, *53*, 128.
- (31) Plevin, M. J.; Bryce, D. L.; Boisbouvier, J. *Nat. Chem.* **2010**, *2*, 466.

- (32) Tran, T. T.; Herfort, D.; Jakobsen, H. J.; Skibsted, J. *J. Am. Chem. Soc.* **2009**, *131*, 14170.
- (33) Ellis, P. D.; Lipton, A. S. *Annu. Rep. NMR Spectrosc.* **2007**, *60*, 1.
- (34) Rovnyak, D.; Baldus, M.; Wu, G.; Hud, N. V.; Feigon, J.; Griffin, R. G. *J. Am. Chem. Soc.* **2000**, *122*, 11423.
- (35) Weiss, J. W. E.; Bryce, D. L. *J. Phys. Chem. A* **2010**, *114*, 5119.
- (36) Pooransingh, N.; Pomerantseva, E.; Ebel, M.; Jantzen, S.; Rehder, D.; Polenova, T. *Inorg. Chem.* **2003**, *42*, 1256.
- (37) Chatterjee, P. B.; Goncharov-Zapata, O.; Quinn, L. L.; Hou, G. J.; Hamaed, H.; Schurko, R. W.; Polenova, T.; Crans, D. C. *Inorg. Chem.* **2011**, *50*, 9794.
- (38) Goncharova-Zapata, O.; Chatterjee, P. B.; Hou, G. J.; Quinn, L. L.; Li, M. Y.; Yehl, J.; Crans, D. C.; Polenova, T. *Crystengcomm* **2013**, *15*, 8776.
- (39) Ooms, K. J.; Bolte, S. E.; Baruah, B.; Choudhary, M. A.; Crans, D. C.; Polenova, T. *Dalton Trans.* **2009**, 3262.
- (40) Bolte, S. E.; Ooms, K. J.; Polenova, T.; Baruah, B.; Crans, D. C.; Smee, J. J. *J. Chem. Phys.* **2008**, *128*, 052317.
- (41) Ooms, K. J.; Bolte, S. E.; Smee, J. J.; Baruah, B.; Crans, D. C.; Polenova, T. *Inorg. Chem.* **2007**, *46*, 9285.
- (42) Schweitzer, A.; Gutmann, T.; Wachtler, M.; Breitzke, H.; Buchholz, A.; Plass, W.; Buntkowsky, G. *Solid State Nucl. Magn. Reson.* **2008**, *34*, 52.
- (43) Fenn, A.; Wachtler, M.; Gutmann, T.; Breitzke, H.; Buchholz, A.; Lippold, I.; Plass, W.; Buntkowsky, G. *Solid State Nucl. Magn. Reson.* **2009**, *36*, 192.
- (44) Nica, S.; Buchholz, A.; Rudolph, M.; Schweitzer, A.; Wachtler, M.; Breitzke, H.; Buntkowsky, G.; Winfried, P. *Eur. J. Inorg. Chem.* **2008**, 2350.
- (45) Chatterjee, P. B.; Goncharov-Zapata, O.; Hou, G. J.; Dmitrenko, O.; Polenova, T.; Crans, D. C. *Eur. J. Inorg. Chem.* **2012**, 4644.
- (46) Ooms, K.; Polenova, T.; Shough, A. M.; Doren, D. J.; Nash, M. J.; Lobo, R. F. *J. Phys. Chem. C* **2009**, *113*, 10477.
- (47) Pooransingh-Margolis, N.; Renirie, R.; Hasan, Z.; Wever, R.; Vega, A. J.; Polenova, T. *J. Am. Chem. Soc.* **2006**, *128*, 5190.

- (48) Huang, W.; Todaro, L.; Yap, G. P.; Beer, R.; Francesconi, L. C.; Polenova, T. *J. Am. Chem. Soc.* **2004**, *126*, 11564.
- (49) Huang, W.; Todaro, L.; Francesconi, L. C.; Polenova, T. *J. Am. Chem. Soc.* **2003**, *125*, 5928.
- (50) Gutmann, T.; Schweitzer, A.; Wachtler, M.; Breitzke, H.; Blichholz, A.; Plass, W.; Buntkowsky, G. *Z. Phys. Chem.* **2008**, *222*, 1389.
- (51) Geethalakshmi, K. R.; Waller, M. P.; Buhl, M. *Inorg. Chem.* **2007**, *46*, 11297.
- (52) Polenova, T.; Pooransingh-Margolis, N.; Rehder, D.; Renirie, R.; Wever, R. In *Vanadium, The Versatile Metal*; Kustin, K., Crans, D. C., Costa-Pessoa, J., Eds.; Oxford University Press: ACS Publications, 2007, p 178.
- (53) Elena, B.; Pintacuda, G.; Mifsud, N.; Emsley, L. *J. Am. Chem. Soc.* **2006**, *128*, 9555.
- (54) Dutour, J.; Guillou, N.; Huguenard, C.; Taulelle, F.; Mellot-Draznieks, C.; Ferey, G. *Solid State Sci* **2004**, *6*, 1059.
- (55) Taulelle, F. *Solid State Sci* **2004**, *6*, 1053.
- (56) Huang, W.; Vega, A. J.; Gullion, T.; Polenova, T. *J. Am. Chem. Soc.* **2007**, *129*, 13027.
- (57) Lu, X. Y.; Lafon, O.; Trebosc, J.; Amoureux, J. P. *J. Magn. Reson.* **2012**, *215*, 34.
- (58) Nimerovsky, E.; Goldbourt, A. *J. Magn. Reson.* **2010**, *206*, 52.
- (59) Frausto, J. J. R.; Wootton, R.; Gillard, R. D. *J. Chem. Soc. A* **1970**, 3369.
- (60) Theriot, L. J.; Carlisle, G. O.; Hu, H. J. *J. Inorg. Nucl. Chem.* **1969**, *31*, 2841.
- (61) Liu, S. X.; Gao, S. *Inorg. Chim. Acta* **1998**, *282*, 149.
- (62) Bak, M.; Rasmussen, J. T.; Nielsen, N. C. *J. Magn. Reson.* **2000**, *147*, 296.
- (63) *Advances in Magnetic Resonance*; Academic Press: New York, 1976.
- (64) *Principles of High Resolution NMR in Solids*; Springer Verlag: Berlin, 1983.
- (65) *NMR Basic Principles and Progress*; Springer Verlag: Berlin, 1978; Vol. 15.

- (66) Bak, M.; Nielsen, N. C. *J. Magn. Reson.* **1997**, *125*, 132.
- (67) Chan, J. C. C.; Tycko, R. *J. Chem. Phys.* **2003**, *118*, 8378.
- (68) Delaglio, F.; Grzesiek, S.; Vuister, G. W.; Zhu, G.; Pfeifer, J.; Bax, A. *J. Biomol. NMR* **1995**, *6*, 277.
- (69) Frisch, M. J.; Trucks, G. W.; Schlegel, H. B.; Gaussian 09 ed.; Gaussian, Inc.: Wallingford, CT, 2009.
- (70) Baias, M.; Dumez, J. N.; Svensson, P. H.; Schantz, S.; Day, G. M.; Emsley, L. *J. Am. Chem. Soc.* **2013**, *135*, 17501.
- (71) Gullion, T. *Chem. Phys. Lett.* **1995**, *246*, 325.
- (72) Nimerovsky, E.; Goldbourt, A. *J. Magn. Reson.* **2012**, *225*, 130.
- (73) Cummins, C. C.; Schrock, R. R.; Davis, W. M. *Inorg. Chem.* **1994**, *33*, 1448.
- (74) Davies, S. C.; Hughes, D. L.; Konkol, M.; Richards, R. L.; Sanders, J. R.; Sobota, P. *Dalton Trans.* **2002**, 2811.
- (75) Mark, M.; Sandro, G.; Glenn, Y.; Louise, M. *Chem. Commun.* **1997**, 643.
- (76) Kabanos, T. A.; Keramidas, A. D.; Papaioannou, A.; Terzis, A. *Inorg. Chem.* **1994**, *33*, 845.
- (77) Tran, B. L.; Thompson, R.; Ghosh, S.; Gao, X. F.; Chen, C. H.; Baik, M. H.; Mindiola, D. J. *Chem. Commun.* **2013**, *49*, 2768.
- (78) Chatterjee, P. B.; Crans, D. C. *Inorg. Chem.* **2012**, *51*, 9144.
- (79) Broring, M.; Hell, C.; Bregier, F.; Burghaus, O.; Tejero, E. C. *Inorg. Chem.* **2007**, *46*, 5477.
- (80) Chatterjee, P. B.; Bhattacharya, S.; Audhya, A.; Choi, K. Y.; Endo, A.; Chaudhury, M. *Inorg. Chem.* **2008**, *47*, 4891.
- (81) Salager, E.; Stein, R. S.; Pickard, C. J.; Elena, B.; Emsley, L. *Phys. Chem. Chem. Phys.* **2009**, *11*, 2610.
- (82) Crans, D. C.; Tarlton, M. L.; McLauchlan, C. C. *Eur. J. Inorg. Chem.* **2014**.

**Appendix A**  
**COPYRIGHT LETTERS**

## NATURE PUBLISHING GROUP LICENSE TERMS AND CONDITIONS

Jul 16, 2016

---

This Agreement between Mingyue Li ("You") and Nature Publishing Group ("Nature Publishing Group") consists of your license details and the terms and conditions provided by Nature Publishing Group and Copyright Clearance Center.

License Number	3910941083912
License date	Jul 16, 2016
Licensed Content Publisher	Nature Publishing Group
Licensed Content Publication	Nature Reviews Molecular Cell Biology
Licensed Content Title	Tracking the ends: a dynamic protein network controls the fate of microtubule tips
Licensed Content Author	Anna Akhmanova and Michel O. Steinmetz
Licensed Content Date	Apr 1, 2008
Licensed Content Volume Number	9
Licensed Content Issue Number	4
Type of Use	reuse in a dissertation / thesis
Requestor type	academic/educational
Format	print and electronic
Portion	figures/tables/illustrations
Number of figures/tables/illustrations	1
High-res required	no
Figures	box 1
Author of this NPG article	no
Your reference number	
Title of your thesis / dissertation	STRUCTURAL AND DYNAMICS STUDIES OF MICROTUBULE-ASSOCIATED TAU AND KIF5B

ASSEMBLED WITH MICROTUBULES; NMR  
CRYSTALLOGRAPHY OF OXOVANADIUM (V)  
BIOINORGANICS: INSIGHTS FROM MAGIC  
ANGLE SPINNING NMR SPECTROSCOPY

Expected completion date Aug 2016

Estimated size (number  
of pages) 200

Requestor Location Mingyue Li  
Timberline Dr.

NEWARK, DE 19711  
United States  
Attn: Mingyue Li

Billing Type Invoice

Billing Address Mingyue Li  
Timberline Dr.

NEWARK, DE 19711  
United States  
Attn: Mingyue Li

Total 0.00 USD

#### Terms and Conditions

##### Terms and Conditions for Permissions

Nature Publishing Group hereby grants you a non-exclusive license to reproduce this material for this purpose, and for no other use, subject to the conditions below:

1. NPG warrants that it has, to the best of its knowledge, the rights to license reuse of this material. However, you should ensure that the material you are requesting is original to Nature Publishing Group and does not carry the copyright of another entity (as credited in the published version). If the credit line on any part of the material you have requested indicates that it was reprinted or adapted by NPG with permission from another source, then you should also seek permission from that source to reuse the material.
2. Permission granted free of charge for material in print is also usually granted for any electronic version of that work, provided that the material is incidental to the work as a whole and that the electronic version is essentially equivalent to, or substitutes for, the print

version. Where print permission has been granted for a fee, separate permission must be obtained for any additional, electronic re-use (unless, as in the case of a full paper, this has already been accounted for during your initial request in the calculation of a print run). NB: In all cases, web-based use of full-text articles must be authorized separately through the 'Use on a Web Site' option when requesting permission.

3. Permission granted for a first edition does not apply to second and subsequent editions and for editions in other languages (except for signatories to the STM Permissions Guidelines, or where the first edition permission was granted for free).
4. Nature Publishing Group's permission must be acknowledged next to the figure, table or abstract in print. In electronic form, this acknowledgement must be visible at the same time as the figure/table/abstract, and must be hyperlinked to the journal's homepage.
5. The credit line should read:  
Reprinted by permission from Macmillan Publishers Ltd: [JOURNAL NAME] (reference citation), copyright (year of publication)  
For AOP papers, the credit line should read:  
Reprinted by permission from Macmillan Publishers Ltd: [JOURNAL NAME], advance online publication, day month year (doi: 10.1038/sj.[JOURNAL ACRONYM].XXXXX)

**Note: For republication from the *British Journal of Cancer*, the following credit lines apply.**

Reprinted by permission from Macmillan Publishers Ltd on behalf of Cancer Research UK: [JOURNAL NAME] (reference citation), copyright (year of publication) For AOP papers, the credit line should read:

Reprinted by permission from Macmillan Publishers Ltd on behalf of Cancer Research UK: [JOURNAL NAME], advance online publication, day month year (doi: 10.1038/sj.[JOURNAL ACRONYM].XXXXX)

6. Adaptations of single figures do not require NPG approval. However, the adaptation should be credited as follows:

Adapted by permission from Macmillan Publishers Ltd: [JOURNAL NAME] (reference citation), copyright (year of publication)

**Note: For adaptation from the *British Journal of Cancer*, the following credit line applies.**

Adapted by permission from Macmillan Publishers Ltd on behalf of Cancer Research UK: [JOURNAL NAME] (reference citation), copyright (year of publication)

7. Translations of 401 words up to a whole article require NPG approval. Please visit <http://www.macmillanmedicalcommunications.com> for more information. Translations of up to a 400 words do not require NPG approval. The translation should be credited as follows:

Translated by permission from Macmillan Publishers Ltd: [JOURNAL NAME] (reference citation), copyright (year of publication).

**Note: For translation from the *British Journal of Cancer*, the following credit line applies.**

Translated by permission from Macmillan Publishers Ltd on behalf of Cancer Research UK: [JOURNAL NAME] (reference citation), copyright (year of publication)

We are certain that all parties will benefit from this agreement and wish you the best in the use of this material. Thank you.

Special Terms:  
v1.1

**Questions? [customercare@copyright.com](mailto:customercare@copyright.com) or +1-855-239-3415 (toll free in the US) or +1-978-646-2777.**

---

---

## NATURE PUBLISHING GROUP LICENSE TERMS AND CONDITIONS

Jul 16, 2016

This Agreement between Mingyue Li ("You") and Nature Publishing Group ("Nature Publishing Group") consists of your license details and the terms and conditions provided by Nature Publishing Group and Copyright Clearance Center.

License Number	3910941289916
License date	Jul 16, 2016
Licensed Content Publisher	Nature Publishing Group
Licensed Content Publication	Nature Reviews Molecular Cell Biology
Licensed Content Title	Kinesin superfamily motor proteins and intracellular transport
Licensed Content Author	Nobutaka Hirokawa, Yasuko Noda, Yosuke Tanaka and Shinsuke Niwa
Licensed Content Date	Oct 1, 2009
Licensed Content Volume Number	10
Licensed Content Issue Number	10
Type of Use	reuse in a dissertation / thesis
Requestor type	academic/educational
Format	print and electronic
Portion	figures/tables/illustrations
Number of figures/tables/illustrations	1
High-res required	no
Figures	figure 1
Author of this NPG article	no
Your reference number	
Title of your thesis /	STRUCTURAL AND DYNAMICS STUDIES OF

dissertation                      MICROTUBULE-ASSOCIATED TAU AND KIF5B  
ASSEMBLED WITH MICROTUBULES; NMR  
CRYSTALLOGRAPHY OF OXOVANADIUM (V)  
BIOINORGANICS: INSIGHTS FROM MAGIC  
ANGLE SPINNING NMR SPECTROSCOPY

Expected completion date Aug 2016

Estimated size (number of pages) 200

Requestor Location                      Mingyue Li  
Timberline Dr.

NEWARK, DE 19711  
United States  
Attn: Mingyue Li

Billing Type                                      Invoice

Billing Address                                      Mingyue Li  
Timberline Dr.

NEWARK, DE 19711  
United States  
Attn: Mingyue Li

Total    0.00 USD

#### Terms and Conditions

##### Terms and Conditions for Permissions

Nature Publishing Group hereby grants you a non-exclusive license to reproduce this material for this purpose, and for no other use, subject to the conditions below:

1. NPG warrants that it has, to the best of its knowledge, the rights to license reuse of this material. However, you should ensure that the material you are requesting is original to Nature Publishing Group and does not carry the copyright of another entity (as credited in the published version). If the credit line on any part of the material you have requested indicates that it was reprinted or adapted by NPG with permission from another source, then you should also seek permission from that source to reuse the material.
2. Permission granted free of charge for material in print is also usually granted for any electronic version of that work, provided that the material is incidental to the work as a whole and that the electronic

version is essentially equivalent to, or substitutes for, the print version. Where print permission has been granted for a fee, separate permission must be obtained for any additional, electronic re-use (unless, as in the case of a full paper, this has already been accounted for during your initial request in the calculation of a print run). NB: In all cases, web-based use of full-text articles must be authorized separately through the 'Use on a Web Site' option when requesting permission.

3. Permission granted for a first edition does not apply to second and subsequent editions and for editions in other languages (except for signatories to the STM Permissions Guidelines, or where the first edition permission was granted for free).
4. Nature Publishing Group's permission must be acknowledged next to the figure, table or abstract in print. In electronic form, this acknowledgement must be visible at the same time as the figure/table/abstract, and must be hyperlinked to the journal's homepage.
5. The credit line should read:  
Reprinted by permission from Macmillan Publishers Ltd: [JOURNAL NAME] (reference citation), copyright (year of publication)  
For AOP papers, the credit line should read:  
Reprinted by permission from Macmillan Publishers Ltd: [JOURNAL NAME], advance online publication, day month year (doi: 10.1038/sj.[JOURNAL ACRONYM].XXXXX)

**Note: For republication from the *British Journal of Cancer*, the following credit lines apply.**

Reprinted by permission from Macmillan Publishers Ltd on behalf of Cancer Research UK: [JOURNAL NAME] (reference citation), copyright (year of publication) For AOP papers, the credit line should read:

Reprinted by permission from Macmillan Publishers Ltd on behalf of Cancer Research UK: [JOURNAL NAME], advance online publication, day month year (doi: 10.1038/sj.[JOURNAL ACRONYM].XXXXX)

6. Adaptations of single figures do not require NPG approval. However, the adaptation should be credited as follows:

Adapted by permission from Macmillan Publishers Ltd: [JOURNAL NAME] (reference citation), copyright (year of publication)

**Note: For adaptation from the *British Journal of Cancer*, the following credit line applies.**

Adapted by permission from Macmillan Publishers Ltd on behalf of Cancer Research UK: [JOURNAL NAME] (reference citation), copyright (year of publication)

7. Translations of 401 words up to a whole article require NPG approval. Please visit <http://www.macmillanmedicalcommunications.com> for more information. Translations of up to a 400 words do not require NPG approval. The translation should be credited as follows:

Translated by permission from Macmillan Publishers Ltd: [JOURNAL NAME] (reference citation), copyright (year of publication).

**Note: For translation from the *British Journal of Cancer*, the following credit line applies.**

Translated by permission from Macmillan Publishers Ltd on behalf of Cancer Research UK: [JOURNAL NAME] (reference citation), copyright (year of publication)

We are certain that all parties will benefit from this agreement and wish you the best in the use of this material. Thank you.

Special Terms:

v1.1

**Questions? [customercare@copyright.com](mailto:customercare@copyright.com) or +1-855-239-3415 (toll free in the US) or +1-978-646-2777.**

---

---

## JOHN WILEY AND SONS LICENSE TERMS AND CONDITIONS

Jul 16, 2016

---

This Agreement between Mingyue Li ("You") and John Wiley and Sons ("John Wiley and Sons") consists of your license details and the terms and conditions provided by John Wiley and Sons and Copyright Clearance Center.

License Number	3910950011346
License date	Jul 16, 2016
Licensed Content Publisher	John Wiley and Sons
Licensed Content Publication	Protein Science
Licensed Content Title	Kinesin, 30 years later: Recent insights from structural studies
Licensed Content Author	Weiyi Wang,Luyan Cao,Chunguang Wang,Benoît Gigant,Marcel Knossow
Licensed Content Date	Jun 11, 2015
Licensed Content Pages	10
Type of use	Dissertation/Thesis
Requestor type	University/Academic
Format	Print and electronic
Portion	Figure/table
Number of figures/tables	2
Original Wiley figure/table number(s)	Figure 2 and Figure 6
Will you be translating?	No
Title of your thesis / dissertation	STRUCTURAL AND DYNAMICS STUDIES OF MICROTUBULE-ASSOCIATED TAU AND KIF5B

ASSEMBLED WITH MICROTUBULES; NMR  
CRYSTALLOGRAPHY OF OXOVANADIUM (V)  
BIOINORGANICS: INSIGHTS FROM MAGIC ANGLE  
SPINNING NMR SPECTROSCOPY

Expected completion date Aug 2016

Expected size (number of pages) 200

Requestor Location Mingyue Li  
Timberline Dr.

NEWARK, DE 19711  
United States  
Attn: Mingyue Li

Publisher Tax ID EU826007151

Billing Type Invoice

Billing Address Mingyue Li  
Timberline Dr.

NEWARK, DE 19711  
United States  
Attn: Mingyue Li

Total 0.00 USD

Terms and Conditions

**TERMS AND CONDITIONS**

This copyrighted material is owned by or exclusively licensed to John Wiley & Sons, Inc. or one of its group companies (each a "Wiley Company") or handled on behalf of a society with which a Wiley Company has exclusive publishing rights in relation to a particular work (collectively "WILEY"). By clicking "accept" in connection with completing this licensing transaction, you agree that the following terms and conditions apply to this transaction (along with the billing and payment terms and conditions established by the Copyright Clearance Center Inc., ("CCC's Billing and Payment terms and conditions"), at the time that you opened your RightsLink account (these are available at any time at <http://myaccount.copyright.com>).

**Terms and Conditions**

- The materials you have requested permission to reproduce or reuse (the "Wiley Materials") are protected by copyright.

- You are hereby granted a personal, non-exclusive, non-sub licensable (on a stand-alone basis), non-transferable, worldwide, limited license to reproduce the Wiley Materials for the purpose specified in the licensing process. This license, **and any CONTENT (PDF or image file) purchased as part of your order**, is for a one-time use only and limited to any maximum distribution number specified in the license. The first instance of republication or reuse granted by this license must be completed within two years of the date of the grant of this license (although copies prepared before the end date may be distributed thereafter). The Wiley Materials shall not be used in any other manner or for any other purpose, beyond what is granted in the license. Permission is granted subject to an appropriate acknowledgement given to the author, title of the material/book/journal and the publisher. You shall also duplicate the copyright notice that appears in the Wiley publication in your use of the Wiley Material. Permission is also granted on the understanding that nowhere in the text is a previously published source acknowledged for all or part of this Wiley Material. Any third party content is expressly excluded from this permission.
- With respect to the Wiley Materials, all rights are reserved. Except as expressly granted by the terms of the license, no part of the Wiley Materials may be copied, modified, adapted (except for minor reformatting required by the new Publication), translated, reproduced, transferred or distributed, in any form or by any means, and no derivative works may be made based on the Wiley Materials without the prior permission of the respective copyright owner. **For STM Signatory Publishers clearing permission under the terms of the [STM Permissions Guidelines](#) only, the terms of the license are extended to include subsequent editions and for editions in other languages, provided such editions are for the work as a whole in situ and does not involve the separate exploitation of the permitted figures or extracts**, You may not alter, remove or suppress in any manner any copyright, trademark or other notices displayed by the Wiley Materials. You may not license, rent, sell, loan, lease, pledge, offer as security, transfer or assign the Wiley Materials on a stand-alone basis, or any of the rights granted to you hereunder to any other person.
- The Wiley Materials and all of the intellectual property rights therein shall at all times remain the exclusive property of John Wiley & Sons Inc, the Wiley Companies, or their respective licensors, and your interest therein is only that of having possession of and the right to reproduce the Wiley Materials pursuant to Section 2 herein during the continuance of this Agreement. You agree that you own no right, title or interest in or to the Wiley Materials or any of the intellectual property rights therein. You shall have no rights hereunder other than the license as provided for above in Section 2. No right, license or interest to any trademark, trade name, service mark or other branding ("Marks") of WILEY or its licensors is granted hereunder, and you agree that you shall not assert any such right, license or interest with respect thereto
- **NEITHER WILEY NOR ITS LICENSORS MAKES ANY WARRANTY OR REPRESENTATION OF ANY KIND TO YOU OR ANY THIRD PARTY, EXPRESS, IMPLIED OR STATUTORY, WITH RESPECT TO THE MATERIALS OR THE ACCURACY OF ANY INFORMATION CONTAINED IN THE**

MATERIALS, INCLUDING, WITHOUT LIMITATION, ANY IMPLIED WARRANTY OF MERCHANTABILITY, ACCURACY, SATISFACTORY QUALITY, FITNESS FOR A PARTICULAR PURPOSE, USABILITY, INTEGRATION OR NON-INFRINGEMENT AND ALL SUCH WARRANTIES ARE HEREBY EXCLUDED BY WILEY AND ITS LICENSORS AND WAIVED BY YOU.

- WILEY shall have the right to terminate this Agreement immediately upon breach of this Agreement by you.
- You shall indemnify, defend and hold harmless WILEY, its Licensors and their respective directors, officers, agents and employees, from and against any actual or threatened claims, demands, causes of action or proceedings arising from any breach of this Agreement by you.
- IN NO EVENT SHALL WILEY OR ITS LICENSORS BE LIABLE TO YOU OR ANY OTHER PARTY OR ANY OTHER PERSON OR ENTITY FOR ANY SPECIAL, CONSEQUENTIAL, INCIDENTAL, INDIRECT, EXEMPLARY OR PUNITIVE DAMAGES, HOWEVER CAUSED, ARISING OUT OF OR IN CONNECTION WITH THE DOWNLOADING, PROVISIONING, VIEWING OR USE OF THE MATERIALS REGARDLESS OF THE FORM OF ACTION, WHETHER FOR BREACH OF CONTRACT, BREACH OF WARRANTY, TORT, NEGLIGENCE, INFRINGEMENT OR OTHERWISE (INCLUDING, WITHOUT LIMITATION, DAMAGES BASED ON LOSS OF PROFITS, DATA, FILES, USE, BUSINESS OPPORTUNITY OR CLAIMS OF THIRD PARTIES), AND WHETHER OR NOT THE PARTY HAS BEEN ADVISED OF THE POSSIBILITY OF SUCH DAMAGES. THIS LIMITATION SHALL APPLY NOTWITHSTANDING ANY FAILURE OF ESSENTIAL PURPOSE OF ANY LIMITED REMEDY PROVIDED HEREIN.
- Should any provision of this Agreement be held by a court of competent jurisdiction to be illegal, invalid, or unenforceable, that provision shall be deemed amended to achieve as nearly as possible the same economic effect as the original provision, and the legality, validity and enforceability of the remaining provisions of this Agreement shall not be affected or impaired thereby.
- The failure of either party to enforce any term or condition of this Agreement shall not constitute a waiver of either party's right to enforce each and every term and condition of this Agreement. No breach under this agreement shall be deemed waived or excused by either party unless such waiver or consent is in writing signed by the party granting such waiver or consent. The waiver by or consent of a party to a breach of any provision of this Agreement shall not operate or be construed as a waiver of or consent to any other or subsequent breach by such other party.
- This Agreement may not be assigned (including by operation of law or otherwise) by you without WILEY's prior written consent.

- Any fee required for this permission shall be non-refundable after thirty (30) days from receipt by the CCC.
- These terms and conditions together with CCC's Billing and Payment terms and conditions (which are incorporated herein) form the entire agreement between you and WILEY concerning this licensing transaction and (in the absence of fraud) supersedes all prior agreements and representations of the parties, oral or written. This Agreement may not be amended except in writing signed by both parties. This Agreement shall be binding upon and inure to the benefit of the parties' successors, legal representatives, and authorized assigns.
- In the event of any conflict between your obligations established by these terms and conditions and those established by CCC's Billing and Payment terms and conditions, these terms and conditions shall prevail.
- WILEY expressly reserves all rights not specifically granted in the combination of (i) the license details provided by you and accepted in the course of this licensing transaction, (ii) these terms and conditions and (iii) CCC's Billing and Payment terms and conditions.
- This Agreement will be void if the Type of Use, Format, Circulation, or Requestor Type was misrepresented during the licensing process.
- This Agreement shall be governed by and construed in accordance with the laws of the State of New York, USA, without regards to such state's conflict of law rules. Any legal action, suit or proceeding arising out of or relating to these Terms and Conditions or the breach thereof shall be instituted in a court of competent jurisdiction in New York County in the State of New York in the United States of America and each party hereby consents and submits to the personal jurisdiction of such court, waives any objection to venue in such court and consents to service of process by registered or certified mail, return receipt requested, at the last known address of such party.

#### **WILEY OPEN ACCESS TERMS AND CONDITIONS**

Wiley Publishes Open Access Articles in fully Open Access Journals and in Subscription journals offering Online Open. Although most of the fully Open Access journals publish open access articles under the terms of the Creative Commons Attribution (CC BY) License only, the subscription journals and a few of the Open Access Journals offer a choice of Creative Commons Licenses. The license type is clearly identified on the article.

##### **The Creative Commons Attribution License**

The [Creative Commons Attribution License \(CC-BY\)](#) allows users to copy, distribute and transmit an article, adapt the article and make commercial use of the article. The CC-BY license permits commercial and non-

##### **Creative Commons Attribution Non-Commercial License**

The [Creative Commons Attribution Non-Commercial \(CC-BY-NC\) License](#) permits use, distribution and reproduction in any medium, provided the original work is properly cited and is not used for commercial purposes.(see below)

**Creative Commons Attribution-Non-Commercial-NoDerivs License**

The [Creative Commons Attribution Non-Commercial-NoDerivs License](#) (CC-BY-NC-ND) permits use, distribution and reproduction in any medium, provided the original work is properly cited, is not used for commercial purposes and no modifications or adaptations are made. (see below)

**Use by commercial "for-profit" organizations**

Use of Wiley Open Access articles for commercial, promotional, or marketing purposes requires further explicit permission from Wiley and will be subject to a fee.

Further details can be found on Wiley Online Library

<http://olabout.wiley.com/WileyCDA/Section/id-410895.html>

**Other Terms and Conditions:**

**v1.10 Last updated September 2015**

**Questions? [customercare@copyright.com](mailto:customercare@copyright.com) or +1-855-239-3415  
(toll free in the US) or +1-978-646-2777.**

---

---

## ELSEVIER LICENSE TERMS AND CONDITIONS

Jul 16, 2016

---

This Agreement between Mingyue Li ("You") and Elsevier ("Elsevier") consists of your license details and the terms and conditions provided by Elsevier and Copyright Clearance Center.

License Number	3910950786084
License date	Jul 16, 2016
Licensed Content Publisher	Elsevier
Licensed Content Publication	Journal of Magnetic Resonance
Licensed Content Title	Ultra-high resolution in MAS solid-state NMR of perdeuterated proteins: Implications for structure and dynamics
Licensed Content Author	Bernd Reif
Licensed Content Date	March 2012
Licensed Content Volume Number	216
Licensed Content Issue Number	n/a
Licensed Content Pages	12
Start Page	1
End Page	12
Type of Use	reuse in a thesis/dissertation
Intended publisher of new work	other
Portion	figures/tables/illustrations
Number of figures/tables/illustrations	1
Format	both print and electronic
Are you the author of this	No

Elsevier article?  
 Will you be translating? No  
 Order reference number  
 Original figure numbers Figure 1  
 Title of your thesis/dissertation STRUCTURAL AND DYNAMICS STUDIES OF MICROTUBULE-ASSOCIATED TAU AND KIF5B ASSEMBLED WITH MICROTUBULES; NMR CRYSTALLOGRAPHY OF OXOVANADIUM (V) BIOINORGANICS: INSIGHTS FROM MAGIC ANGLE SPINNING NMR SPECTROSCOPY  
 Expected completion date Aug 2016  
 Estimated size (number of pages) 200  
 Elsevier VAT number GB 494 6272 12  
 Requestor Location Mingyue Li  
 Timberline Dr.  
 NEWARK, DE 19711  
 United States  
 Attn: Mingyue Li  
 Total 0.00 USD

#### Terms and Conditions

##### INTRODUCTION

1. The publisher for this copyrighted material is Elsevier. By clicking "accept" in connection with completing this licensing transaction, you agree that the following terms and conditions apply to this transaction (along with the Billing and Payment terms and conditions established by Copyright Clearance Center, Inc. ("CCC"), at the time that you opened your Rightslink account and that are available at any time at <http://myaccount.copyright.com>).

##### GENERAL TERMS

2. Elsevier hereby grants you permission to reproduce the aforementioned material subject to the terms and conditions indicated.

3. Acknowledgement: If any part of the material to be used (for example, figures) has appeared in our publication with credit or acknowledgement to another source, permission must also be sought from that source. If such permission is not obtained then that material may not be included in your publication/copies. Suitable acknowledgement to the source must be made, either as a footnote or in a reference list at the end of your publication, as follows:

"Reprinted from Publication title, Vol /edition number, Author(s), Title of article / title of

chapter, Pages No., Copyright (Year), with permission from Elsevier [OR APPLICABLE SOCIETY COPYRIGHT OWNER]." Also Lancet special credit - "Reprinted from The Lancet, Vol. number, Author(s), Title of article, Pages No., Copyright (Year), with permission from Elsevier."

4. Reproduction of this material is confined to the purpose and/or media for which permission is hereby given.

5. Altering/Modifying Material: Not Permitted. However figures and illustrations may be altered/adapted minimally to serve your work. Any other abbreviations, additions, deletions and/or any other alterations shall be made only with prior written authorization of Elsevier Ltd. (Please contact Elsevier at [permissions@elsevier.com](mailto:permissions@elsevier.com))

6. If the permission fee for the requested use of our material is waived in this instance, please be advised that your future requests for Elsevier materials may attract a fee.

7. Reservation of Rights: Publisher reserves all rights not specifically granted in the combination of (i) the license details provided by you and accepted in the course of this licensing transaction, (ii) these terms and conditions and (iii) CCC's Billing and Payment terms and conditions.

8. License Contingent Upon Payment: While you may exercise the rights licensed immediately upon issuance of the license at the end of the licensing process for the transaction, provided that you have disclosed complete and accurate details of your proposed use, no license is finally effective unless and until full payment is received from you (either by publisher or by CCC) as provided in CCC's Billing and Payment terms and conditions. If full payment is not received on a timely basis, then any license preliminarily granted shall be deemed automatically revoked and shall be void as if never granted. Further, in the event that you breach any of these terms and conditions or any of CCC's Billing and Payment terms and conditions, the license is automatically revoked and shall be void as if never granted. Use of materials as described in a revoked license, as well as any use of the materials beyond the scope of an unrevoked license, may constitute copyright infringement and publisher reserves the right to take any and all action to protect its copyright in the materials.

9. Warranties: Publisher makes no representations or warranties with respect to the licensed material.

10. Indemnity: You hereby indemnify and agree to hold harmless publisher and CCC, and their respective officers, directors, employees and agents, from and against any and all claims arising out of your use of the licensed material other than as specifically authorized pursuant to this license.

11. No Transfer of License: This license is personal to you and may not be sublicensed, assigned, or transferred by you to any other person without publisher's written permission.

12. No Amendment Except in Writing: This license may not be amended except in a writing signed by both parties (or, in the case of publisher, by CCC on publisher's behalf).

13. Objection to Contrary Terms: Publisher hereby objects to any terms contained in any purchase order, acknowledgment, check endorsement or other writing prepared by you, which terms are inconsistent with these terms and conditions or CCC's Billing and Payment terms and conditions. These terms and conditions, together with CCC's Billing and Payment terms and conditions (which are incorporated herein), comprise the entire agreement between you and publisher (and CCC) concerning this licensing transaction. In the event of any conflict between your obligations established by these terms and conditions and those established by CCC's Billing and Payment terms and conditions, these terms and conditions

shall control.

14. **Revocation:** Elsevier or Copyright Clearance Center may deny the permissions described in this License at their sole discretion, for any reason or no reason, with a full refund payable to you. Notice of such denial will be made using the contact information provided by you. Failure to receive such notice will not alter or invalidate the denial. In no event will Elsevier or Copyright Clearance Center be responsible or liable for any costs, expenses or damage incurred by you as a result of a denial of your permission request, other than a refund of the amount(s) paid by you to Elsevier and/or Copyright Clearance Center for denied permissions.

#### LIMITED LICENSE

The following terms and conditions apply only to specific license types:

15. **Translation:** This permission is granted for non-exclusive world **English** rights only unless your license was granted for translation rights. If you licensed translation rights you may only translate this content into the languages you requested. A professional translator must perform all translations and reproduce the content word for word preserving the integrity of the article.

16. **Posting licensed content on any Website:** The following terms and conditions apply as follows: Licensing material from an Elsevier journal: All content posted to the web site must maintain the copyright information line on the bottom of each image; A hyper-text must be included to the Homepage of the journal from which you are licensing at <http://www.sciencedirect.com/science/journal/xxxxx> or the Elsevier homepage for books at <http://www.elsevier.com>; Central Storage: This license does not include permission for a scanned version of the material to be stored in a central repository such as that provided by Heron/XanEdu.

Licensing material from an Elsevier book: A hyper-text link must be included to the Elsevier homepage at <http://www.elsevier.com>. All content posted to the web site must maintain the copyright information line on the bottom of each image.

**Posting licensed content on Electronic reserve:** In addition to the above the following clauses are applicable: The web site must be password-protected and made available only to bona fide students registered on a relevant course. This permission is granted for 1 year only. You may obtain a new license for future website posting.

17. **For journal authors:** the following clauses are applicable in addition to the above:

#### **Preprints:**

A preprint is an author's own write-up of research results and analysis, it has not been peer-reviewed, nor has it had any other value added to it by a publisher (such as formatting, copyright, technical enhancement etc.).

Authors can share their preprints anywhere at any time. Preprints should not be added to or enhanced in any way in order to appear more like, or to substitute for, the final versions of articles however authors can update their preprints on arXiv or RePEc with their Accepted Author Manuscript (see below).

If accepted for publication, we encourage authors to link from the preprint to their formal publication via its DOI. Millions of researchers have access to the formal publications on ScienceDirect, and so links will help users to find, access, cite and use the best available version. Please note that Cell Press, The Lancet and some society-owned have different preprint policies. Information on these policies is available on the journal homepage.

**Accepted Author Manuscripts:** An accepted author manuscript is the manuscript of an

article that has been accepted for publication and which typically includes author-incorporated changes suggested during submission, peer review and editor-author communications.

Authors can share their accepted author manuscript:

- immediately
  - o via their non-commercial person homepage or blog
  - o by updating a preprint in arXiv or RePEc with the accepted manuscript
  - o via their research institute or institutional repository for internal institutional uses or as part of an invitation-only research collaboration work-group
  - o directly by providing copies to their students or to research collaborators for their personal use
  - o for private scholarly sharing as part of an invitation-only work group on commercial sites with which Elsevier has an agreement
- after the embargo period
  - o via non-commercial hosting platforms such as their institutional repository
  - o via commercial sites with which Elsevier has an agreement

In all cases accepted manuscripts should:

- link to the formal publication via its DOI
- bear a CC-BY-NC-ND license - this is easy to do
- if aggregated with other manuscripts, for example in a repository or other site, be shared in alignment with our hosting policy not be added to or enhanced in any way to appear more like, or to substitute for, the published journal article.

**Published journal article (JPA):** A published journal article (PJA) is the definitive final record of published research that appears or will appear in the journal and embodies all value-adding publishing activities including peer review co-ordination, copy-editing, formatting, (if relevant) pagination and online enrichment.

Policies for sharing publishing journal articles differ for subscription and gold open access articles:

**Subscription Articles:** If you are an author, please share a link to your article rather than the full-text. Millions of researchers have access to the formal publications on ScienceDirect, and so links will help your users to find, access, cite, and use the best available version. Theses and dissertations which contain embedded PJAs as part of the formal submission can be posted publicly by the awarding institution with DOI links back to the formal publications on ScienceDirect.

If you are affiliated with a library that subscribes to ScienceDirect you have additional private sharing rights for others' research accessed under that agreement. This includes use for classroom teaching and internal training at the institution (including use in course packs and courseware programs), and inclusion of the article for grant funding purposes.

**Gold Open Access Articles:** May be shared according to the author-selected end-user license and should contain a [CrossMark logo](#), the end user license, and a DOI link to the formal publication on ScienceDirect.

Please refer to Elsevier's [posting policy](#) for further information.

18. **For book authors** the following clauses are applicable in addition to the above:

Authors are permitted to place a brief summary of their work online only. You are not allowed to download and post the published electronic version of your chapter, nor may you scan the printed edition to create an electronic version. **Posting to a repository:** Authors are permitted to post a summary of their chapter only in their institution's repository.

**19. Thesis/Dissertation:** If your license is for use in a thesis/dissertation your thesis may be submitted to your institution in either print or electronic form. Should your thesis be published commercially, please reapply for permission. These requirements include permission for the Library and Archives of Canada to supply single copies, on demand, of the complete thesis and include permission for Proquest/UMI to supply single copies, on demand, of the complete thesis. Should your thesis be published commercially, please reapply for permission. Theses and dissertations which contain embedded PJAs as part of the formal submission can be posted publicly by the awarding institution with DOI links back to the formal publications on ScienceDirect.

#### **Elsevier Open Access Terms and Conditions**

You can publish open access with Elsevier in hundreds of open access journals or in nearly 2000 established subscription journals that support open access publishing. Permitted third party re-use of these open access articles is defined by the author's choice of Creative Commons user license. See our [open access license policy](#) for more information.

#### **Terms & Conditions applicable to all Open Access articles published with Elsevier:**

Any reuse of the article must not represent the author as endorsing the adaptation of the article nor should the article be modified in such a way as to damage the author's honour or reputation. If any changes have been made, such changes must be clearly indicated.

The author(s) must be appropriately credited and we ask that you include the end user license and a DOI link to the formal publication on ScienceDirect.

If any part of the material to be used (for example, figures) has appeared in our publication with credit or acknowledgement to another source it is the responsibility of the user to ensure their reuse complies with the terms and conditions determined by the rights holder.

#### **Additional Terms & Conditions applicable to each Creative Commons user license:**

**CC BY:** The CC-BY license allows users to copy, to create extracts, abstracts and new works from the Article, to alter and revise the Article and to make commercial use of the Article (including reuse and/or resale of the Article by commercial entities), provided the user gives appropriate credit (with a link to the formal publication through the relevant DOI), provides a link to the license, indicates if changes were made and the licensor is not represented as endorsing the use made of the work. The full details of the license are available at <http://creativecommons.org/licenses/by/4.0>.

**CC BY NC SA:** The CC BY-NC-SA license allows users to copy, to create extracts, abstracts and new works from the Article, to alter and revise the Article, provided this is not done for commercial purposes, and that the user gives appropriate credit (with a link to the formal publication through the relevant DOI), provides a link to the license, indicates if changes were made and the licensor is not represented as endorsing the use made of the work. Further, any new works must be made available on the same conditions. The full details of the license are available at <http://creativecommons.org/licenses/by-nc-sa/4.0>.

**CC BY NC ND:** The CC BY-NC-ND license allows users to copy and distribute the Article, provided this is not done for commercial purposes and further does not permit distribution of the Article if it is changed or edited in any way, and provided the user gives appropriate credit (with a link to the formal publication through the relevant DOI), provides a link to the

license, and that the licensor is not represented as endorsing the use made of the work. The full details of the license are available at <http://creativecommons.org/licenses/by-nc-nd/4.0>. Any commercial reuse of Open Access articles published with a CC BY NC SA or CC BY NC ND license requires permission from Elsevier and will be subject to a fee.

Commercial reuse includes:

- Associating advertising with the full text of the Article
- Charging fees for document delivery or access
- Article aggregation
- Systematic distribution via e-mail lists or share buttons

Posting or linking by commercial companies for use by customers of those companies.

**20. Other Conditions:**

v1.8

**Questions? [customercare@copyright.com](mailto:customercare@copyright.com) or +1-855-239-3415 (toll free in the US) or +1-978-646-2777.**

---

---

**JOHN WILEY AND SONS LICENSE  
TERMS AND CONDITIONS**

Jul 16, 2016

---

This Agreement between Mingyue Li ("You") and John Wiley and Sons ("John Wiley and Sons") consists of your license details and the terms and conditions provided by John Wiley and Sons and Copyright Clearance Center.

License Number	3910950345061
License date	Jul 16, 2016
Licensed Content Publisher	John Wiley and Sons
Licensed Content Publication	Angewandte Chemie International Edition
Licensed Content Title	Ultrahigh Resolution in Proton Solid-State NMR Spectroscopy at High Levels of Deuteration
Licensed Content Author	Veniamin Chevelkov, Kristina Rehbein, Anne Diehl, Bernd Reif
Licensed Content Date	Apr 28, 2006
Licensed Content Pages	4
Type of use	Dissertation/Thesis
Requestor type	University/Academic
Format	Print and electronic
Portion	Figure/table
Number of figures/tables	1
Original Wiley figure/table number(s)	Figure 2
Will you be translating?	No
Title of your thesis / dissertation	STRUCTURAL AND DYNAMICS STUDIES OF MICROTUBULE-ASSOCIATED TAU AND KIF5B

ASSEMBLED WITH MICROTUBULES; NMR  
CRYSTALLOGRAPHY OF OXOVANADIUM (V)  
BIOINORGANICS: INSIGHTS FROM MAGIC ANGLE  
SPINNING NMR SPECTROSCOPY

Expected completion date Aug 2016

Expected size (number of pages) 200

Requestor Location Mingyue Li  
Timberline Dr.

NEWARK, DE 19711  
United States  
Attn: Mingyue Li

Publisher Tax ID EU826007151

Billing Type Invoice

Billing Address Mingyue Li  
Timberline Dr.

NEWARK, DE 19711  
United States  
Attn: Mingyue Li

Total 0.00 USD

#### Terms and Conditions

##### TERMS AND CONDITIONS

This copyrighted material is owned by or exclusively licensed to John Wiley & Sons, Inc. or one of its group companies (each a "Wiley Company") or handled on behalf of a society with which a Wiley Company has exclusive publishing rights in relation to a particular work (collectively "WILEY"). By clicking "accept" in connection with completing this licensing transaction, you agree that the following terms and conditions apply to this transaction (along with the billing and payment terms and conditions established by the Copyright Clearance Center Inc., ("CCC's Billing and Payment terms and conditions"), at the time that you opened your RightsLink account (these are available at any time at <http://myaccount.copyright.com>).

##### Terms and Conditions

- The materials you have requested permission to reproduce or reuse (the "Wiley Materials") are protected by copyright.

- You are hereby granted a personal, non-exclusive, non-sub licensable (on a stand-alone basis), non-transferable, worldwide, limited license to reproduce the Wiley Materials for the purpose specified in the licensing process. This license, **and any CONTENT (PDF or image file) purchased as part of your order**, is for a one-time use only and limited to any maximum distribution number specified in the license. The first instance of republication or reuse granted by this license must be completed within two years of the date of the grant of this license (although copies prepared before the end date may be distributed thereafter). The Wiley Materials shall not be used in any other manner or for any other purpose, beyond what is granted in the license. Permission is granted subject to an appropriate acknowledgement given to the author, title of the material/book/journal and the publisher. You shall also duplicate the copyright notice that appears in the Wiley publication in your use of the Wiley Material. Permission is also granted on the understanding that nowhere in the text is a previously published source acknowledged for all or part of this Wiley Material. Any third party content is expressly excluded from this permission.
- With respect to the Wiley Materials, all rights are reserved. Except as expressly granted by the terms of the license, no part of the Wiley Materials may be copied, modified, adapted (except for minor reformatting required by the new Publication), translated, reproduced, transferred or distributed, in any form or by any means, and no derivative works may be made based on the Wiley Materials without the prior permission of the respective copyright owner. **For STM Signatory Publishers clearing permission under the terms of the [STM Permissions Guidelines](#) only, the terms of the license are extended to include subsequent editions and for editions in other languages, provided such editions are for the work as a whole in situ and does not involve the separate exploitation of the permitted figures or extracts**, You may not alter, remove or suppress in any manner any copyright, trademark or other notices displayed by the Wiley Materials. You may not license, rent, sell, loan, lease, pledge, offer as security, transfer or assign the Wiley Materials on a stand-alone basis, or any of the rights granted to you hereunder to any other person.
- The Wiley Materials and all of the intellectual property rights therein shall at all times remain the exclusive property of John Wiley & Sons Inc, the Wiley Companies, or their respective licensors, and your interest therein is only that of having possession of and the right to reproduce the Wiley Materials pursuant to Section 2 herein during the continuance of this Agreement. You agree that you own no right, title or interest in or to the Wiley Materials or any of the intellectual property rights therein. You shall have no rights hereunder other than the license as provided for above in Section 2. No right, license or interest to any trademark, trade name, service mark or other branding ("Marks") of WILEY or its licensors is granted hereunder, and you agree that you shall not assert any such right, license or interest with respect thereto
- **NEITHER WILEY NOR ITS LICENSORS MAKES ANY WARRANTY OR REPRESENTATION OF ANY KIND TO YOU OR ANY THIRD PARTY, EXPRESS, IMPLIED OR STATUTORY, WITH RESPECT TO THE MATERIALS OR THE ACCURACY OF ANY INFORMATION CONTAINED IN THE**

MATERIALS, INCLUDING, WITHOUT LIMITATION, ANY IMPLIED WARRANTY OF MERCHANTABILITY, ACCURACY, SATISFACTORY QUALITY, FITNESS FOR A PARTICULAR PURPOSE, USABILITY, INTEGRATION OR NON-INFRINGEMENT AND ALL SUCH WARRANTIES ARE HEREBY EXCLUDED BY WILEY AND ITS LICENSORS AND WAIVED BY YOU.

- WILEY shall have the right to terminate this Agreement immediately upon breach of this Agreement by you.
- You shall indemnify, defend and hold harmless WILEY, its Licensors and their respective directors, officers, agents and employees, from and against any actual or threatened claims, demands, causes of action or proceedings arising from any breach of this Agreement by you.
- IN NO EVENT SHALL WILEY OR ITS LICENSORS BE LIABLE TO YOU OR ANY OTHER PARTY OR ANY OTHER PERSON OR ENTITY FOR ANY SPECIAL, CONSEQUENTIAL, INCIDENTAL, INDIRECT, EXEMPLARY OR PUNITIVE DAMAGES, HOWEVER CAUSED, ARISING OUT OF OR IN CONNECTION WITH THE DOWNLOADING, PROVISIONING, VIEWING OR USE OF THE MATERIALS REGARDLESS OF THE FORM OF ACTION, WHETHER FOR BREACH OF CONTRACT, BREACH OF WARRANTY, TORT, NEGLIGENCE, INFRINGEMENT OR OTHERWISE (INCLUDING, WITHOUT LIMITATION, DAMAGES BASED ON LOSS OF PROFITS, DATA, FILES, USE, BUSINESS OPPORTUNITY OR CLAIMS OF THIRD PARTIES), AND WHETHER OR NOT THE PARTY HAS BEEN ADVISED OF THE POSSIBILITY OF SUCH DAMAGES. THIS LIMITATION SHALL APPLY NOTWITHSTANDING ANY FAILURE OF ESSENTIAL PURPOSE OF ANY LIMITED REMEDY PROVIDED HEREIN.
- Should any provision of this Agreement be held by a court of competent jurisdiction to be illegal, invalid, or unenforceable, that provision shall be deemed amended to achieve as nearly as possible the same economic effect as the original provision, and the legality, validity and enforceability of the remaining provisions of this Agreement shall not be affected or impaired thereby.
- The failure of either party to enforce any term or condition of this Agreement shall not constitute a waiver of either party's right to enforce each and every term and condition of this Agreement. No breach under this agreement shall be deemed waived or excused by either party unless such waiver or consent is in writing signed by the party granting such waiver or consent. The waiver by or consent of a party to a breach of any provision of this Agreement shall not operate or be construed as a waiver of or consent to any other or subsequent breach by such other party.
- This Agreement may not be assigned (including by operation of law or otherwise) by you without WILEY's prior written consent.

- Any fee required for this permission shall be non-refundable after thirty (30) days from receipt by the CCC.
- These terms and conditions together with CCC's Billing and Payment terms and conditions (which are incorporated herein) form the entire agreement between you and WILEY concerning this licensing transaction and (in the absence of fraud) supersedes all prior agreements and representations of the parties, oral or written. This Agreement may not be amended except in writing signed by both parties. This Agreement shall be binding upon and inure to the benefit of the parties' successors, legal representatives, and authorized assigns.
- In the event of any conflict between your obligations established by these terms and conditions and those established by CCC's Billing and Payment terms and conditions, these terms and conditions shall prevail.
- WILEY expressly reserves all rights not specifically granted in the combination of (i) the license details provided by you and accepted in the course of this licensing transaction, (ii) these terms and conditions and (iii) CCC's Billing and Payment terms and conditions.
- This Agreement will be void if the Type of Use, Format, Circulation, or Requestor Type was misrepresented during the licensing process.
- This Agreement shall be governed by and construed in accordance with the laws of the State of New York, USA, without regards to such state's conflict of law rules. Any legal action, suit or proceeding arising out of or relating to these Terms and Conditions or the breach thereof shall be instituted in a court of competent jurisdiction in New York County in the State of New York in the United States of America and each party hereby consents and submits to the personal jurisdiction of such court, waives any objection to venue in such court and consents to service of process by registered or certified mail, return receipt requested, at the last known address of such party.

#### **WILEY OPEN ACCESS TERMS AND CONDITIONS**

Wiley Publishes Open Access Articles in fully Open Access Journals and in Subscription journals offering Online Open. Although most of the fully Open Access journals publish open access articles under the terms of the Creative Commons Attribution (CC BY) License only, the subscription journals and a few of the Open Access Journals offer a choice of Creative Commons Licenses. The license type is clearly identified on the article.

##### **The Creative Commons Attribution License**

The [Creative Commons Attribution License \(CC-BY\)](#) allows users to copy, distribute and transmit an article, adapt the article and make commercial use of the article. The CC-BY license permits commercial and non-

##### **Creative Commons Attribution Non-Commercial License**

The [Creative Commons Attribution Non-Commercial \(CC-BY-NC\) License](#) permits use, distribution and reproduction in any medium, provided the original work is properly cited and is not used for commercial purposes.(see below)

**Creative Commons Attribution-Non-Commercial-NoDerivs License**

The [Creative Commons Attribution Non-Commercial-NoDerivs License](#) (CC-BY-NC-ND) permits use, distribution and reproduction in any medium, provided the original work is properly cited, is not used for commercial purposes and no modifications or adaptations are made. (see below)

**Use by commercial "for-profit" organizations**

Use of Wiley Open Access articles for commercial, promotional, or marketing purposes requires further explicit permission from Wiley and will be subject to a fee.

Further details can be found on Wiley Online Library

<http://olabout.wiley.com/WileyCDA/Section/id-410895.html>

**Other Terms and Conditions:**

v1.10 Last updated September 2015

**Questions? [customercare@copyright.com](mailto:customercare@copyright.com) or +1-855-239-3415 (toll free in the US) or +1-978-646-2777.**

**RightsLink®**[Home](#)[Account Info](#)[Help](#)

**Title:** Proton to Carbon-13  
INEPT in Solid-State  
NMR Spectroscopy

**Author:** Bénédicte Elena, Anne  
Lesage, Stefan  
Steuernagel, et al

**Publication:** Journal of the  
American Chemical  
Society

**Publisher:** American Chemical  
Society

**Date:** Dec 1, 2005  
Copyright © 2005, American  
Chemical Society

Logged in as:  
Mingyue Li  
Account #:  
3001028616

[LOGOUT](#)

### PERMISSION/LICENSE IS GRANTED FOR YOUR ORDER AT NO CHARGE

This type of permission/license, instead of the standard Terms & Conditions, is sent to you because no fee is being charged for your order. Please note the following:

- Permission is granted for your request in both print and electronic formats, and translations.
- If figures and/or tables were requested, they may be adapted or used in part.
- Please print this page for your records and send a copy of it to your publisher/graduate school.
- Appropriate credit for the requested material should be given as follows: "Reprinted (adapted) with permission from (COMPLETE REFERENCE CITATION). Copyright (YEAR) American Chemical Society." Insert appropriate information in place of the capitalized words.
- One-time permission is granted only for the use specified in your request. No additional uses are granted (such as derivative works or other editions). For any other uses, please submit a new request.

If credit is given to another source for the material you requested, permission must be obtained from that source.

[BACK](#)[CLOSE WINDOW](#)

Copyright © 2016 [Copyright Clearance Center, Inc.](#) All Rights Reserved. [Privacy statement.](#) [Terms and Conditions.](#)

Comments? We would like to hear from you. E-mail us at [customercare@copyright.com](mailto:customercare@copyright.com)

## ELSEVIER LICENSE TERMS AND CONDITIONS

Jul 16, 2016

This Agreement between Mingyue Li ("You") and Elsevier ("Elsevier") consists of your license details and the terms and conditions provided by Elsevier and Copyright Clearance Center.

License Number	3910951066531
License date	Jul 16, 2016
Licensed Content Publisher	Elsevier
Licensed Content Publication	Progress in Nuclear Magnetic Resonance Spectroscopy
Licensed Content Title	Solid-state NMR and protein dynamics
Licensed Content Author	Alexey Krushelnitsky, Detlef Reichert
Licensed Content Date	31 October 2005
Licensed Content Volume Number	47
Licensed Content Issue Number	1-2
Licensed Content Pages	25
Start Page	1
End Page	25
Type of Use	reuse in a thesis/dissertation
Intended publisher of new work	other
Portion	figures/tables/illustrations
Number of figures/tables/illustrations	1
Format	both print and electronic
Are you the author of this Elsevier article?	No
Will you be translating?	No

Order reference number

Original figure numbers Figure 1

Title of your thesis/dissertation STRUCTURAL AND DYNAMICS STUDIES OF MICROTUBULE-ASSOCIATED TAU AND KIF5B ASSEMBLED WITH MICROTUBULES; NMR CRYSTALLOGRAPHY OF OXOVANADIUM (V) BIOINORGANICS: INSIGHTS FROM MAGIC ANGLE SPINNING NMR SPECTROSCOPY

Expected completion date Aug 2016

Estimated size (number of pages) 200

Elsevier VAT number GB 494 6272 12

Requestor Location Mingyue Li  
Timberline Dr.  
  
NEWARK, DE 19711  
United States  
Attn: Mingyue Li

Total 0.00 USD

Terms and Conditions

#### INTRODUCTION

1. The publisher for this copyrighted material is Elsevier. By clicking "accept" in connection with completing this licensing transaction, you agree that the following terms and conditions apply to this transaction (along with the Billing and Payment terms and conditions established by Copyright Clearance Center, Inc. ("CCC"), at the time that you opened your Rightslink account and that are available at any time at <http://myaccount.copyright.com>).

#### GENERAL TERMS

2. Elsevier hereby grants you permission to reproduce the aforementioned material subject to the terms and conditions indicated.

3. Acknowledgement: If any part of the material to be used (for example, figures) has appeared in our publication with credit or acknowledgement to another source, permission must also be sought from that source. If such permission is not obtained then that material may not be included in your publication/copies. Suitable acknowledgement to the source must be made, either as a footnote or in a reference list at the end of your publication, as follows:  
"Reprinted from Publication title, Vol /edition number, Author(s), Title of article / title of chapter, Pages No., Copyright (Year), with permission from Elsevier [OR APPLICABLE SOCIETY COPYRIGHT OWNER]." Also Lancet special credit - "Reprinted from The Lancet, Vol. number, Author(s), Title of article, Pages No., Copyright (Year), with

permission from Elsevier."

4. Reproduction of this material is confined to the purpose and/or media for which permission is hereby given.

5. Altering/Modifying Material: Not Permitted. However figures and illustrations may be altered/adapted minimally to serve your work. Any other abbreviations, additions, deletions and/or any other alterations shall be made only with prior written authorization of Elsevier Ltd. (Please contact Elsevier at [permissions@elsevier.com](mailto:permissions@elsevier.com))

6. If the permission fee for the requested use of our material is waived in this instance, please be advised that your future requests for Elsevier materials may attract a fee.

7. Reservation of Rights: Publisher reserves all rights not specifically granted in the combination of (i) the license details provided by you and accepted in the course of this licensing transaction, (ii) these terms and conditions and (iii) CCC's Billing and Payment terms and conditions.

8. License Contingent Upon Payment: While you may exercise the rights licensed immediately upon issuance of the license at the end of the licensing process for the transaction, provided that you have disclosed complete and accurate details of your proposed use, no license is finally effective unless and until full payment is received from you (either by publisher or by CCC) as provided in CCC's Billing and Payment terms and conditions. If full payment is not received on a timely basis, then any license preliminarily granted shall be deemed automatically revoked and shall be void as if never granted. Further, in the event that you breach any of these terms and conditions or any of CCC's Billing and Payment terms and conditions, the license is automatically revoked and shall be void as if never granted. Use of materials as described in a revoked license, as well as any use of the materials beyond the scope of an unrevoked license, may constitute copyright infringement and publisher reserves the right to take any and all action to protect its copyright in the materials.

9. Warranties: Publisher makes no representations or warranties with respect to the licensed material.

10. Indemnity: You hereby indemnify and agree to hold harmless publisher and CCC, and their respective officers, directors, employees and agents, from and against any and all claims arising out of your use of the licensed material other than as specifically authorized pursuant to this license.

11. No Transfer of License: This license is personal to you and may not be sublicensed, assigned, or transferred by you to any other person without publisher's written permission.

12. No Amendment Except in Writing: This license may not be amended except in a writing signed by both parties (or, in the case of publisher, by CCC on publisher's behalf).

13. Objection to Contrary Terms: Publisher hereby objects to any terms contained in any purchase order, acknowledgment, check endorsement or other writing prepared by you, which terms are inconsistent with these terms and conditions or CCC's Billing and Payment terms and conditions. These terms and conditions, together with CCC's Billing and Payment terms and conditions (which are incorporated herein), comprise the entire agreement between you and publisher (and CCC) concerning this licensing transaction. In the event of any conflict between your obligations established by these terms and conditions and those established by CCC's Billing and Payment terms and conditions, these terms and conditions shall control.

14. Revocation: Elsevier or Copyright Clearance Center may deny the permissions described in this License at their sole discretion, for any reason or no reason, with a full refund payable

to you. Notice of such denial will be made using the contact information provided by you. Failure to receive such notice will not alter or invalidate the denial. In no event will Elsevier or Copyright Clearance Center be responsible or liable for any costs, expenses or damage incurred by you as a result of a denial of your permission request, other than a refund of the amount(s) paid by you to Elsevier and/or Copyright Clearance Center for denied permissions.

#### LIMITED LICENSE

The following terms and conditions apply only to specific license types:

**15. Translation:** This permission is granted for non-exclusive world **English** rights only unless your license was granted for translation rights. If you licensed translation rights you may only translate this content into the languages you requested. A professional translator must perform all translations and reproduce the content word for word preserving the integrity of the article.

**16. Posting licensed content on any Website:** The following terms and conditions apply as follows: Licensing material from an Elsevier journal: All content posted to the web site must maintain the copyright information line on the bottom of each image; A hyper-text must be included to the Homepage of the journal from which you are licensing at <http://www.sciencedirect.com/science/journal/xxxxx> or the Elsevier homepage for books at <http://www.elsevier.com>; Central Storage: This license does not include permission for a scanned version of the material to be stored in a central repository such as that provided by Heron/XanEdu.

Licensing material from an Elsevier book: A hyper-text link must be included to the Elsevier homepage at <http://www.elsevier.com>. All content posted to the web site must maintain the copyright information line on the bottom of each image.

**Posting licensed content on Electronic reserve:** In addition to the above the following clauses are applicable: The web site must be password-protected and made available only to bona fide students registered on a relevant course. This permission is granted for 1 year only. You may obtain a new license for future website posting.

**17. For journal authors:** the following clauses are applicable in addition to the above:

#### Preprints:

A preprint is an author's own write-up of research results and analysis, it has not been peer-reviewed, nor has it had any other value added to it by a publisher (such as formatting, copyright, technical enhancement etc.).

Authors can share their preprints anywhere at any time. Preprints should not be added to or enhanced in any way in order to appear more like, or to substitute for, the final versions of articles however authors can update their preprints on arXiv or RePEc with their Accepted Author Manuscript (see below).

If accepted for publication, we encourage authors to link from the preprint to their formal publication via its DOI. Millions of researchers have access to the formal publications on ScienceDirect, and so links will help users to find, access, cite and use the best available version. Please note that Cell Press, The Lancet and some society-owned have different preprint policies. Information on these policies is available on the journal homepage.

**Accepted Author Manuscripts:** An accepted author manuscript is the manuscript of an article that has been accepted for publication and which typically includes author-incorporated changes suggested during submission, peer review and editor-author communications.

Authors can share their accepted author manuscript:

- immediately
  - o via their non-commercial person homepage or blog
  - o by updating a preprint in arXiv or RePEc with the accepted manuscript
  - o via their research institute or institutional repository for internal institutional uses or as part of an invitation-only research collaboration work-group
  - o directly by providing copies to their students or to research collaborators for their personal use
  - o for private scholarly sharing as part of an invitation-only work group on commercial sites with which Elsevier has an agreement
- after the embargo period
  - o via non-commercial hosting platforms such as their institutional repository
  - o via commercial sites with which Elsevier has an agreement

In all cases accepted manuscripts should:

- link to the formal publication via its DOI
- bear a CC-BY-NC-ND license - this is easy to do
- if aggregated with other manuscripts, for example in a repository or other site, be shared in alignment with our hosting policy not be added to or enhanced in any way to appear more like, or to substitute for, the published journal article.

**Published journal article (JPA):** A published journal article (PJA) is the definitive final record of published research that appears or will appear in the journal and embodies all value-adding publishing activities including peer review co-ordination, copy-editing, formatting, (if relevant) pagination and online enrichment.

Policies for sharing publishing journal articles differ for subscription and gold open access articles:

**Subscription Articles:** If you are an author, please share a link to your article rather than the full-text. Millions of researchers have access to the formal publications on ScienceDirect, and so links will help your users to find, access, cite, and use the best available version. Theses and dissertations which contain embedded PJAs as part of the formal submission can be posted publicly by the awarding institution with DOI links back to the formal publications on ScienceDirect.

If you are affiliated with a library that subscribes to ScienceDirect you have additional private sharing rights for others' research accessed under that agreement. This includes use for classroom teaching and internal training at the institution (including use in course packs and courseware programs), and inclusion of the article for grant funding purposes.

**Gold Open Access Articles:** May be shared according to the author-selected end-user license and should contain a [CrossMark logo](#), the end user license, and a DOI link to the formal publication on ScienceDirect.

Please refer to Elsevier's [posting policy](#) for further information.

18. **For book authors** the following clauses are applicable in addition to the above:

Authors are permitted to place a brief summary of their work online only. You are not allowed to download and post the published electronic version of your chapter, nor may you scan the printed edition to create an electronic version. **Posting to a repository:** Authors are

permitted to post a summary of their chapter only in their institution's repository.

**19. Thesis/Dissertation:** If your license is for use in a thesis/dissertation your thesis may be submitted to your institution in either print or electronic form. Should your thesis be published commercially, please reapply for permission. These requirements include permission for the Library and Archives of Canada to supply single copies, on demand, of the complete thesis and include permission for Proquest/UMI to supply single copies, on demand, of the complete thesis. Should your thesis be published commercially, please reapply for permission. Theses and dissertations which contain embedded PJAs as part of the formal submission can be posted publicly by the awarding institution with DOI links back to the formal publications on ScienceDirect.

#### **Elsevier Open Access Terms and Conditions**

You can publish open access with Elsevier in hundreds of open access journals or in nearly 2000 established subscription journals that support open access publishing. Permitted third party re-use of these open access articles is defined by the author's choice of Creative Commons user license. See our [open access license policy](#) for more information.

#### **Terms & Conditions applicable to all Open Access articles published with Elsevier:**

Any reuse of the article must not represent the author as endorsing the adaptation of the article nor should the article be modified in such a way as to damage the author's honour or reputation. If any changes have been made, such changes must be clearly indicated.

The author(s) must be appropriately credited and we ask that you include the end user license and a DOI link to the formal publication on ScienceDirect.

If any part of the material to be used (for example, figures) has appeared in our publication with credit or acknowledgement to another source it is the responsibility of the user to ensure their reuse complies with the terms and conditions determined by the rights holder.

#### **Additional Terms & Conditions applicable to each Creative Commons user license:**

**CC BY:** The CC-BY license allows users to copy, to create extracts, abstracts and new works from the Article, to alter and revise the Article and to make commercial use of the Article (including reuse and/or resale of the Article by commercial entities), provided the user gives appropriate credit (with a link to the formal publication through the relevant DOI), provides a link to the license, indicates if changes were made and the licensor is not represented as endorsing the use made of the work. The full details of the license are available at <http://creativecommons.org/licenses/by/4.0>.

**CC BY NC SA:** The CC BY-NC-SA license allows users to copy, to create extracts, abstracts and new works from the Article, to alter and revise the Article, provided this is not done for commercial purposes, and that the user gives appropriate credit (with a link to the formal publication through the relevant DOI), provides a link to the license, indicates if changes were made and the licensor is not represented as endorsing the use made of the work. Further, any new works must be made available on the same conditions. The full details of the license are available at <http://creativecommons.org/licenses/by-nc-sa/4.0>.

**CC BY NC ND:** The CC BY-NC-ND license allows users to copy and distribute the Article, provided this is not done for commercial purposes and further does not permit distribution of the Article if it is changed or edited in any way, and provided the user gives appropriate credit (with a link to the formal publication through the relevant DOI), provides a link to the license, and that the licensor is not represented as endorsing the use made of the work. The full details of the license are available at <http://creativecommons.org/licenses/by-nc-nd/4.0>. Any commercial reuse of Open Access articles published with a CC BY NC SA or CC BY

NC ND license requires permission from Elsevier and will be subject to a fee.  
Commercial reuse includes:

- Associating advertising with the full text of the Article
- Charging fees for document delivery or access
- Article aggregation
- Systematic distribution via e-mail lists or share buttons

Posting or linking by commercial companies for use by customers of those companies.

**20. Other Conditions:**

v1.8

**Questions? [customercare@copyright.com](mailto:customercare@copyright.com) or +1-855-239-3415  
(toll free in the US) or +1-978-646-2777.**



## ELSEVIER LICENSE TERMS AND CONDITIONS

Jul 16, 2016

This Agreement between Mingyue Li ("You") and Elsevier ("Elsevier") consists of your license details and the terms and conditions provided by Elsevier and Copyright Clearance Center.

License Number	3910951290185
License date	Jul 16, 2016
Licensed Content Publisher	Elsevier
Licensed Content Publication	Journal of Magnetic Resonance
Licensed Content Title	Broadband homonuclear correlation spectroscopy driven by combined R2nv sequences under fast magic angle spinning for NMR structural analysis of organic and biological solids
Licensed Content Author	Guangjin Hou, Si Yan, Julien Trébosc, Jean-Paul Amoureux, Tatyana Polenova
Licensed Content Date	July 2013
Licensed Content Volume Number	232
Licensed Content Issue Number	n/a
Licensed Content Pages	13
Start Page	18
End Page	30
Type of Use	reuse in a thesis/dissertation
Intended publisher of new work	other
Portion	figures/tables/illustrations
Number of figures/tables/illustrations	1

Format both print and electronic  
 Are you the author of this Elsevier article? No  
 Will you be translating? No  
 Order reference number  
 Original figure numbers Figure 1  
 Title of your thesis/dissertation STRUCTURAL AND DYNAMICS STUDIES OF MICROTUBULE-ASSOCIATED TAU AND KIF5B ASSEMBLED WITH MICROTUBULES; NMR CRYSTALLOGRAPHY OF OXOVANADIUM (V) BIOINORGANICS: INSIGHTS FROM MAGIC ANGLE SPINNING NMR SPECTROSCOPY  
 Expected completion date Aug 2016  
 Estimated size (number of pages) 200  
 Elsevier VAT number GB 494 6272 12  
 Requestor Location Mingyue Li  
 Timberline Dr.  
 NEWARK, DE 19711  
 United States  
 Attn: Mingyue Li  
 Total 0.00 USD

#### Terms and Conditions

##### INTRODUCTION

1. The publisher for this copyrighted material is Elsevier. By clicking "accept" in connection with completing this licensing transaction, you agree that the following terms and conditions apply to this transaction (along with the Billing and Payment terms and conditions established by Copyright Clearance Center, Inc. ("CCC"), at the time that you opened your Rightslink account and that are available at any time at <http://myaccount.copyright.com>).

##### GENERAL TERMS

2. Elsevier hereby grants you permission to reproduce the aforementioned material subject to the terms and conditions indicated.

3. Acknowledgement: If any part of the material to be used (for example, figures) has appeared in our publication with credit or acknowledgement to another source, permission must also be sought from that source. If such permission is not obtained then that material may not be included in your publication/copies. Suitable acknowledgement to the source must be made, either as a footnote or in a reference list at the end of your publication, as

follows:

"Reprinted from Publication title, Vol /edition number, Author(s), Title of article / title of chapter, Pages No., Copyright (Year), with permission from Elsevier [OR APPLICABLE SOCIETY COPYRIGHT OWNER]." Also Lancet special credit - "Reprinted from The Lancet, Vol. number, Author(s), Title of article, Pages No., Copyright (Year), with permission from Elsevier."

4. Reproduction of this material is confined to the purpose and/or media for which permission is hereby given.

5. Altering/Modifying Material: Not Permitted. However figures and illustrations may be altered/adapted minimally to serve your work. Any other abbreviations, additions, deletions and/or any other alterations shall be made only with prior written authorization of Elsevier Ltd. (Please contact Elsevier at [permissions@elsevier.com](mailto:permissions@elsevier.com))

6. If the permission fee for the requested use of our material is waived in this instance, please be advised that your future requests for Elsevier materials may attract a fee.

7. Reservation of Rights: Publisher reserves all rights not specifically granted in the combination of (i) the license details provided by you and accepted in the course of this licensing transaction, (ii) these terms and conditions and (iii) CCC's Billing and Payment terms and conditions.

8. License Contingent Upon Payment: While you may exercise the rights licensed immediately upon issuance of the license at the end of the licensing process for the transaction, provided that you have disclosed complete and accurate details of your proposed use, no license is finally effective unless and until full payment is received from you (either by publisher or by CCC) as provided in CCC's Billing and Payment terms and conditions. If full payment is not received on a timely basis, then any license preliminarily granted shall be deemed automatically revoked and shall be void as if never granted. Further, in the event that you breach any of these terms and conditions or any of CCC's Billing and Payment terms and conditions, the license is automatically revoked and shall be void as if never granted. Use of materials as described in a revoked license, as well as any use of the materials beyond the scope of an unrevoked license, may constitute copyright infringement and publisher reserves the right to take any and all action to protect its copyright in the materials.

9. Warranties: Publisher makes no representations or warranties with respect to the licensed material.

10. Indemnity: You hereby indemnify and agree to hold harmless publisher and CCC, and their respective officers, directors, employees and agents, from and against any and all claims arising out of your use of the licensed material other than as specifically authorized pursuant to this license.

11. No Transfer of License: This license is personal to you and may not be sublicensed, assigned, or transferred by you to any other person without publisher's written permission.

12. No Amendment Except in Writing: This license may not be amended except in a writing signed by both parties (or, in the case of publisher, by CCC on publisher's behalf).

13. Objection to Contrary Terms: Publisher hereby objects to any terms contained in any purchase order, acknowledgment, check endorsement or other writing prepared by you, which terms are inconsistent with these terms and conditions or CCC's Billing and Payment terms and conditions. These terms and conditions, together with CCC's Billing and Payment terms and conditions (which are incorporated herein), comprise the entire agreement between you and publisher (and CCC) concerning this licensing transaction. In the event of

any conflict between your obligations established by these terms and conditions and those established by CCC's Billing and Payment terms and conditions, these terms and conditions shall control.

14. **Revocation:** Elsevier or Copyright Clearance Center may deny the permissions described in this License at their sole discretion, for any reason or no reason, with a full refund payable to you. Notice of such denial will be made using the contact information provided by you. Failure to receive such notice will not alter or invalidate the denial. In no event will Elsevier or Copyright Clearance Center be responsible or liable for any costs, expenses or damage incurred by you as a result of a denial of your permission request, other than a refund of the amount(s) paid by you to Elsevier and/or Copyright Clearance Center for denied permissions.

#### LIMITED LICENSE

The following terms and conditions apply only to specific license types:

15. **Translation:** This permission is granted for non-exclusive world **English** rights only unless your license was granted for translation rights. If you licensed translation rights you may only translate this content into the languages you requested. A professional translator must perform all translations and reproduce the content word for word preserving the integrity of the article.

16. **Posting licensed content on any Website:** The following terms and conditions apply as follows: Licensing material from an Elsevier journal: All content posted to the web site must maintain the copyright information line on the bottom of each image; A hyper-text must be included to the Homepage of the journal from which you are licensing at <http://www.sciencedirect.com/science/journal/xxxxx> or the Elsevier homepage for books at <http://www.elsevier.com>; Central Storage: This license does not include permission for a scanned version of the material to be stored in a central repository such as that provided by Heron/XanEdu.

Licensing material from an Elsevier book: A hyper-text link must be included to the Elsevier homepage at <http://www.elsevier.com>. All content posted to the web site must maintain the copyright information line on the bottom of each image.

**Posting licensed content on Electronic reserve:** In addition to the above the following clauses are applicable: The web site must be password-protected and made available only to bona fide students registered on a relevant course. This permission is granted for 1 year only. You may obtain a new license for future website posting.

17. **For journal authors:** the following clauses are applicable in addition to the above:

#### Preprints:

A preprint is an author's own write-up of research results and analysis, it has not been peer-reviewed, nor has it had any other value added to it by a publisher (such as formatting, copyright, technical enhancement etc.).

Authors can share their preprints anywhere at any time. Preprints should not be added to or enhanced in any way in order to appear more like, or to substitute for, the final versions of articles however authors can update their preprints on arXiv or RePEc with their Accepted Author Manuscript (see below).

If accepted for publication, we encourage authors to link from the preprint to their formal publication via its DOI. Millions of researchers have access to the formal publications on ScienceDirect, and so links will help users to find, access, cite and use the best available version. Please note that Cell Press, The Lancet and some society-owned have different

preprint policies. Information on these policies is available on the journal homepage.

**Accepted Author Manuscripts:** An accepted author manuscript is the manuscript of an article that has been accepted for publication and which typically includes author-incorporated changes suggested during submission, peer review and editor-author communications.

Authors can share their accepted author manuscript:

- immediately
  - o via their non-commercial person homepage or blog
  - o by updating a preprint in arXiv or RePEc with the accepted manuscript
  - o via their research institute or institutional repository for internal institutional uses or as part of an invitation-only research collaboration work-group
  - o directly by providing copies to their students or to research collaborators for their personal use
  - o for private scholarly sharing as part of an invitation-only work group on commercial sites with which Elsevier has an agreement
- after the embargo period
  - o via non-commercial hosting platforms such as their institutional repository
  - o via commercial sites with which Elsevier has an agreement

In all cases accepted manuscripts should:

- link to the formal publication via its DOI
- bear a CC-BY-NC-ND license - this is easy to do
- if aggregated with other manuscripts, for example in a repository or other site, be shared in alignment with our hosting policy not be added to or enhanced in any way to appear more like, or to substitute for, the published journal article.

**Published journal article (JPA):** A published journal article (PJA) is the definitive final record of published research that appears or will appear in the journal and embodies all value-adding publishing activities including peer review co-ordination, copy-editing, formatting, (if relevant) pagination and online enrichment.

Policies for sharing publishing journal articles differ for subscription and gold open access articles:

**Subscription Articles:** If you are an author, please share a link to your article rather than the full-text. Millions of researchers have access to the formal publications on ScienceDirect, and so links will help your users to find, access, cite, and use the best available version. Theses and dissertations which contain embedded PJAs as part of the formal submission can be posted publicly by the awarding institution with DOI links back to the formal publications on ScienceDirect.

If you are affiliated with a library that subscribes to ScienceDirect you have additional private sharing rights for others' research accessed under that agreement. This includes use for classroom teaching and internal training at the institution (including use in course packs and courseware programs), and inclusion of the article for grant funding purposes.

**Gold Open Access Articles:** May be shared according to the author-selected end-user license and should contain a [CrossMark logo](#), the end user license, and a DOI link to the formal publication on ScienceDirect.

Please refer to Elsevier's [posting policy](#) for further information.

**18. For book authors** the following clauses are applicable in addition to the above: Authors are permitted to place a brief summary of their work online only. You are not allowed to download and post the published electronic version of your chapter, nor may you scan the printed edition to create an electronic version. **Posting to a repository:** Authors are permitted to post a summary of their chapter only in their institution's repository.

**19. Thesis/Dissertation:** If your license is for use in a thesis/dissertation your thesis may be submitted to your institution in either print or electronic form. Should your thesis be published commercially, please reapply for permission. These requirements include permission for the Library and Archives of Canada to supply single copies, on demand, of the complete thesis and include permission for Proquest/UMI to supply single copies, on demand, of the complete thesis. Should your thesis be published commercially, please reapply for permission. Theses and dissertations which contain embedded PJAs as part of the formal submission can be posted publicly by the awarding institution with DOI links back to the formal publications on ScienceDirect.

### **Elsevier Open Access Terms and Conditions**

You can publish open access with Elsevier in hundreds of open access journals or in nearly 2000 established subscription journals that support open access publishing. Permitted third party re-use of these open access articles is defined by the author's choice of Creative Commons user license. See our [open access license policy](#) for more information.

#### **Terms & Conditions applicable to all Open Access articles published with Elsevier:**

Any reuse of the article must not represent the author as endorsing the adaptation of the article nor should the article be modified in such a way as to damage the author's honour or reputation. If any changes have been made, such changes must be clearly indicated.

The author(s) must be appropriately credited and we ask that you include the end user license and a DOI link to the formal publication on ScienceDirect.

If any part of the material to be used (for example, figures) has appeared in our publication with credit or acknowledgement to another source it is the responsibility of the user to ensure their reuse complies with the terms and conditions determined by the rights holder.

#### **Additional Terms & Conditions applicable to each Creative Commons user license:**

**CC BY:** The CC-BY license allows users to copy, to create extracts, abstracts and new works from the Article, to alter and revise the Article and to make commercial use of the Article (including reuse and/or resale of the Article by commercial entities), provided the user gives appropriate credit (with a link to the formal publication through the relevant DOI), provides a link to the license, indicates if changes were made and the licensor is not represented as endorsing the use made of the work. The full details of the license are available at <http://creativecommons.org/licenses/by/4.0>.

**CC BY NC SA:** The CC BY-NC-SA license allows users to copy, to create extracts, abstracts and new works from the Article, to alter and revise the Article, provided this is not done for commercial purposes, and that the user gives appropriate credit (with a link to the formal publication through the relevant DOI), provides a link to the license, indicates if changes were made and the licensor is not represented as endorsing the use made of the work. Further, any new works must be made available on the same conditions. The full details of the license are available at <http://creativecommons.org/licenses/by-nc-sa/4.0>.

**CC BY NC ND:** The CC BY-NC-ND license allows users to copy and distribute the Article, provided this is not done for commercial purposes and further does not permit distribution of

the Article if it is changed or edited in any way, and provided the user gives appropriate credit (with a link to the formal publication through the relevant DOI), provides a link to the license, and that the licensor is not represented as endorsing the use made of the work. The full details of the license are available at <http://creativecommons.org/licenses/by-nc-nd/4.0>. Any commercial reuse of Open Access articles published with a CC BY NC SA or CC BY NC ND license requires permission from Elsevier and will be subject to a fee.

Commercial reuse includes:

- Associating advertising with the full text of the Article
- Charging fees for document delivery or access
- Article aggregation
- Systematic distribution via e-mail lists or share buttons

Posting or linking by commercial companies for use by customers of those companies.

#### 20. Other Conditions:

v1.8

**Questions? [customercare@copyright.com](mailto:customercare@copyright.com) or +1-855-239-3415 (toll free in the US) or +1-978-646-2777.**



RightsLink®

Home

Account Info

Help



**Title:** 1H-13C/1H-15N Heteronuclear Dipolar Recoupling by R-Symmetry Sequences Under Fast Magic Angle Spinning for Dynamics Analysis of Biological and Organic Solids

Logged in as:  
Mingyue Li  
Account #:  
3001028616

LOGOUT

**Author:** Guangjin Hou, In-Ja L. Byeon, Jinwoo Ahn, et al

**Publication:** Journal of the American Chemical Society

**Publisher:** American Chemical Society

**Date:** Nov 1, 2011

Copyright © 2011, American Chemical Society

**PERMISSION/LICENSE IS GRANTED FOR YOUR ORDER AT NO CHARGE**

This type of permission/license, instead of the standard Terms & Conditions, is sent to you because no fee is being charged for your order. Please note the following:

- Permission is granted for your request in both print and electronic formats, and translations.
- If figures and/or tables were requested, they may be adapted or used in part.
- Please print this page for your records and send a copy of it to your publisher/graduate school.
- Appropriate credit for the requested material should be given as follows: "Reprinted (adapted) with permission from (COMPLETE REFERENCE CITATION). Copyright (YEAR) American Chemical Society." Insert appropriate information in place of the capitalized words.
- One-time permission is granted only for the use specified in your request. No additional uses are granted (such as derivative works or other editions). For any other uses, please submit a new request.

If credit is given to another source for the material you requested, permission must be obtained from that source.

BACK

CLOSE WINDOW

Copyright © 2016 [Copyright Clearance Center, Inc.](#) All Rights Reserved. [Privacy statement](#). [Terms and Conditions](#). Comments? We would like to hear from you. E-mail us at [customer care@copyright.com](mailto:customer care@copyright.com)



# RightsLink®

[Home](#)
[Create Account](#)
[Help](#)


ACS Publications  
Most Trusted. Most Cited. Most Read.

**Title:**

NMR Crystallography for Structural Characterization of Oxovanadium(V) Complexes: Deriving Coordination Geometry and Detecting Weakly Coordinated Ligands at Atomic Resolution in the Solid State

**Author:**

Mingyue Li, Jenna Yehl, Guangjin Hou, et al

**Publication:**

Inorganic Chemistry

**Publisher:**

American Chemical Society

**Date:**

Feb 1, 2015

Copyright © 2015, American Chemical Society

[LOGIN](#)

If you're a **copyright.com user**, you can login to RightsLink using your copyright.com credentials. Already a **RightsLink user** or want to [learn more?](#)

### PERMISSION/LICENSE IS GRANTED FOR YOUR ORDER AT NO CHARGE

This type of permission/license, instead of the standard Terms & Conditions, is sent to you because no fee is being charged for your order. Please note the following:

- Permission is granted for your request in both print and electronic formats, and translations.
- If figures and/or tables were requested, they may be adapted or used in part.
- Please print this page for your records and send a copy of it to your publisher/graduate school.
- Appropriate credit for the requested material should be given as follows: "Reprinted (adapted) with permission from (COMPLETE REFERENCE CITATION). Copyright (YEAR) American Chemical Society." Insert appropriate information in place of the capitalized words.
- One-time permission is granted only for the use specified in your request. No additional uses are granted (such as derivative works or other editions). For any other uses, please submit a new request.

[BACK](#)
[CLOSE WINDOW](#)

Copyright © 2016 [Copyright Clearance Center, Inc.](#) All Rights Reserved. [Privacy statement](#). [Terms and Conditions](#).

Comments? We would like to hear from you. E-mail us at [customercare@copyright.com](mailto:customercare@copyright.com)